



**HAL**  
open science

# Nuclear Statistical Equilibrium for compact stars: modelling the nuclear energy functional

F. Aymard

► **To cite this version:**

F. Aymard. Nuclear Statistical Equilibrium for compact stars: modelling the nuclear energy functional. Nuclear Experiment [nucl-ex]. Université de Caen Normandie, 2015. English. NNT : . tel-01244647

**HAL Id: tel-01244647**

**<https://hal.in2p3.fr/tel-01244647>**

Submitted on 16 Dec 2015

**HAL** is a multi-disciplinary open access archive for the deposit and dissemination of scientific research documents, whether they are published or not. The documents may come from teaching and research institutions in France or abroad, or from public or private research centers.

L'archive ouverte pluridisciplinaire **HAL**, est destinée au dépôt et à la diffusion de documents scientifiques de niveau recherche, publiés ou non, émanant des établissements d'enseignement et de recherche français ou étrangers, des laboratoires publics ou privés.



Université de Caen Basse-Normandie

U.F.R. : Sciences

École doctorale : SIMEM

## Thèse de doctorat

Présentée et soutenue le 27 novembre 2015

par

**M. François Aymard**

en vue de l'obtention du

**Doctorat de l'Université de Caen Basse-Normandie**

Spécialité : Constituants Élémentaires et Physique Théorique

Titre :

# Nuclear Statistical Equilibrium for compact stars: modelling the nuclear energy functional

Directrice de thèse : Professeur **Francesca Gulminelli**

Membres du Jury :

M.	<b>Jerzy Dudek</b>	
Mme	<b>Francesca Gulminelli</b>	(Directrice de thèse)
M.	<b>Jérôme Margueron</b>	
Mme	<b>Constança Providência</b>	(Rapporteur)
Mme	<b>Adriana Raduta</b>	
M.	<b>Stefan Typel</b>	(Rapporteur)







# Abstract

The core collapse supernova is one of the most powerful known phenomena in the universe. It results from the explosion of very massive stars after they have burnt all their fuel. The hot compact remnant, the so-called proto-neutron star, cools down to become an inert catalyzed neutron star. The dynamics and structure of compact stars, that is core collapse supernovae, proto-neutron stars and neutron stars, are still not fully understood and are currently under active research, in association with astrophysical observations and nuclear experiments. One of the key components for modelling compact stars concerns the Equation of State. The task of computing a complete realistic consistent Equation of State for all such stars is challenging because a wide range of densities, proton fractions and temperatures is spanned.

This thesis deals with the microscopic modelling of the structure and internal composition of baryonic matter with nucleonic degrees of freedom in compact stars, in order to obtain a realistic unified Equation of State. In particular, we are interested in a formalism which can be applied both at sub-saturation and super-saturation densities, and which gives in the zero temperature limit results compatible with the microscopic Hartree-Fock-Bogoliubov theory with modern realistic effective interactions constrained on experimental nuclear data. For this purpose, we present, for sub-saturated matter, a Nuclear Statistical Equilibrium model which corresponds to a statistical superposition of finite configurations, the so-called Wigner-Seitz cells. Each cell contains a nucleus, or cluster, embedded in a homogeneous electron gas as well as a homogeneous neutron and proton gas. Within each cell, we investigate the different components of the nuclear energy of clusters in interaction with gases. The use of the nuclear mean-field theory for the description of both the clusters and the nucleon gas allows a theoretical consistency with the treatment at saturation and beyond. At densities above two-three times saturation, other degrees of freedom are expected to appear, which potentially lead to other consistency problems but this issue will not be treated in this thesis.

The thesis is divided into three parts.

In part I, we present the Nuclear Statistical Equilibrium model based on the grand canonical statistics and non-relativistic Skyrme interactions. Results at  $\beta$ -equilibrium are shown and the importance of the clusters distribution as well as a realistic treatment for the free energy model is discussed.

Part II investigates the functional behavior of the baryonic energy in the Wigner-Seitz cell within the Extended-Thomas-Fermi approximation. In particular, both bulk and surface in-medium effects are studied, and their dependence on cluster size and asymmetry as well as gas densities and asymmetry is investigated. A preliminary result of in-medium surface effects is presented within some approximations in the case of  $\beta$ -equilibrated matter.

In part III, we develop approximations in order to obtain a reliable analytical expression of the mass formula, directly linked to the functional form and parameters of the Skyrme interaction. In this part, we mainly focus on nuclei in vacuum, and analyse the different binding energy components in terms of bulk and surface properties, as well as isovector and isoscalar properties.

## Résumé

Les supernovæ à effondrement de cœur sont l'un des phénomènes connus les plus puissants de l'univers. Elles résultent de l'explosion d'étoiles très massives, ayant brûlé tout leur combustible. Le résidu chaud et compact, appelé proto-étoile à neutron, se refroidit pour devenir une étoile à neutrons, objet inerte. La dynamique et la structure des étoiles compactes, c'est-à-dire les supernovæ à effondrement de cœur, les proto-étoiles à neutrons et les étoiles à neutrons, ne sont pas encore complètement connues, et sont aujourd'hui au cœur d'intenses recherches, en association avec les observations astrophysiques et les expériences nucléaires. L'un des ingrédients clés de la modélisation d'étoile compacte concerne l'équation d'état. La difficulté de l'obtention d'une équation d'état réaliste et consistante pour tous ces objets stellaires réside dans le fait que l'on doit considérer une large variété de conditions thermodynamiques, c'est-à-dire des valeurs de densités, de fractions de protons et de températures, très différentes.

Le travail de cette thèse consiste à modéliser, à partir des degrés de libertés nucléoniques, la structure microscopique ainsi que la composition interne de la matière baryonique des étoiles compactes, afin d'obtenir une équation d'état réaliste et unifiée. En particulier, on est intéressé à utiliser un formalisme qui peut s'appliquer à des densités aussi bien sous-saturées que sur-saturées, et qui, à la limite thermodynamique de température nulle, est compatible avec les interactions effectives modernes et réalistes données par la théorie microscopique d'Hartree-Fock-Bogoliubov et contraintes par les expériences nucléaires. Pour atteindre cet objectif, on présente, pour la matière sous-saturée, un modèle en équilibre statistique nucléaire, qui correspond à une superposition statistique de configurations finies, appelées cellules de Wigner-Seitz. Chaque cellule contient un noyau, ou agrégat, baignant dans un gaz homogène d'électrons ainsi que dans un gaz homogène de neutrons et de protons. Au sein de chaque cellule, on étudie les différentes composantes de l'énergie nucléaire des agrégats en interaction avec les gaz. L'utilisation de la théorie nucléaire de champ moyen pour la description des agrégats ainsi que du gaz de nucléons permet de traiter de façon consistante la matière sous-saturée et la matière sur-saturée. À des densités de plus de deux-trois fois la densité de saturation, l'apparition de degrés de liberté supplémentaires pose de nouveau des problèmes de consistance théorique qui ne sont pas traités dans cette thèse.

La thèse est organisée selon trois parties.

Dans la partie I, on présente le modèle en équilibre statistique nucléaire, basé sur l'ensemble grand canonique et sur les interactions non relativistes de Skyrme. Des résultats en équilibre  $\beta$  sont présentés, et l'importance de la distribution en masse d'agrégats d'une part, et d'un traitement réaliste de l'énergie libre d'autre part, est discutée.

Dans la partie II, on étudie le comportement fonctionnel de l'énergie baryonique des cellules de Wigner-Seitz, en utilisant l'approximation de Thomas-Fermi étendue. En particulier, les effets de volume et de surface dus au milieu stellaire sont étudiés, et leurs dépendances en termes de taille et d'asymétrie du noyau, ainsi que de densité et d'asymétrie du gaz de nucléons sont analysées. Des résultats préliminaires de l'effet de l'interaction de surface du milieu sont présentés, sous hypothèse de certaines approximations et dans le cas de l'équilibre  $\beta$ .

Dans la partie III, on développe des approximations afin d'obtenir une expression analytique fiable de formule de masse, directement reliée à la forme fonctionnelle et aux paramètres de l'interaction de Skyrme. Dans cette partie, on se concentre principalement sur les noyaux dans le vide, et l'on analyse les différentes composantes de l'énergie de liaison en termes de propriétés de volume et de surface, ainsi que de propriétés isoscalaire et isovecteur.





# Remerciements / Acknowledgements

Je remercie tout d'abord le directeur, Dominique Durand, pour m'avoir accueilli au Laboratoire de Physique Corpusculaire et m'avoir ainsi permis d'y réaliser une thèse en physique théorique.

I would like to thank the jury members who carefully read this manuscript and agreed to come, from far away for most of them, to Caen for my defense. I have especially appreciated the referees -Constança Providência and Stefan Typel- having shown an interest in my work during the defense as well as during the conferences where we met. Je veux aussi remercier Adriana pour ses commentaires et corrections utiles.

I would also like to acknowledge the English professor Catharine Mason who helped me to overcome my difficulties in this language, at the beginning of my thesis, with pleasant and fruitful lessons, as well as at the end, by proof reading some parts of this manuscript.

Durant mes trois années de thèse, j'ai eu la chance d'être encadré par Francesca, envers qui je ne saurais assez exprimer ma gratitude. J'ai amplement apprécié la grande liberté que Francesca m'a accordé, que ce soit à propos de l'aménagement calendaire, ou de la participation aux conférences, événements de vulgarisation, enseignements, encadrements de stage, ou encore du choix des différentes problématiques de physique à développer. J'ai également apprécié la disponibilité permanente qu'elle a bien voulu m'accorder, y compris lors de ses périodes d'intenses enseignements. J'ai ainsi pu lui adresser de multiples questions, parfois élémentaires, sur lesquelles elle a pris la peine de s'y pencher minutieusement, jusqu'à m'en trouver convaincu. De ces abondantes discussions, j'ai pu m'imprégner des qualités pédagogiques étendues de Francesca, et j'espère que je saurai en conserver une influence majeure par la suite. Travailler avec Francesca fut un immense plaisir.

Je souhaite vivement exprimer toute mon estime à Adriana et Jérôme avec qui j'ai également travaillé. J'ai apprécié leur patience et leur diligence. Les échanges extrêmement intéressants que j'ai eu avec eux tout au long de ma thèse m'ont permis d'aborder mon sujet de thèse de points de vue différents.

Ces trois années de thèse m'ont profondément enrichi, tant d'un point de vue professionnel que personnel. Je conserverai donc, envers Adriana, Francesca et Jérôme, une dette particulière puisque ma décision de poursuivre en doctorat fut largement infléchie par mon stage de M1, lors duquel ils m'ont encadré.

Parce que travailler dans un environnement aussi agréable et convivial que l'est le LPC est une véritable chance, je tiens à remercier l'ensemble des membres du laboratoire.

J'ai assurément une pensée spéciale pour tous les thésards du laboratoire et d'ailleurs que j'ai rencontrés, et dont je ne peux faire une liste exhaustive.

Je voudrais néanmoins évoquer Claire et Matthieu R., que j'ai connus brièvement puisque de deux ans mes aînés. De la même année, j'ajouterai une mention spéciale au prolix Matthieu S.

Merci à Guillaume, Sylvain, Xavier, avec qui j'ai partagé d'innombrables bons moments durant ces trois années de thèse. Je remercie Xavier tout particulièrement pour avoir été un agréable colocataire lors d'une conférence de physique nucléaire. Merci à Sylvain pour sa gentillesse, ainsi que pour nos nombreuses discussions de physique. Je lui suis également reconnaissant pour les restaurants caennais que nous avons découvert. Guillaume aura su enjoliver ces années par son inhérent et sempiternel humour. Je l'en remercie ; et j'ai beaucoup apprécié les diverses veillées que nous avons eues.

Parmi les plus jeunes générations de thésards, je voudrais citer spécialement Lou, Baptiste, Thibault, avec qui j'ai aussi passé d'inoubliables moments. Je leur souhaite bon courage pour leur dernière année de thèse. Un grand merci spécial à l'éclairé Thibault pour son obligeance noctambulée.

Je suis reconnaissant pour toutes les discussions sérieuses, ainsi que celles qui l'étaient beaucoup moins, pour tous les moments de détente, et toutes les soirées, que j'ai partagés avec eux tous.

Enfin, je souhaite vivement remercier les membres de ma famille pour leur soutien. Naturellement, ma reconnaissance va expressément à mes parents qui m'ont continuellement encouragé et approuvé. Depuis l'aube de mon existence, ils ont su, incessamment, m'inciter vers le long et exigeant, mais ô combien gratifiant, chemin de l'Instruction.

Qu'ils voient dans l'accomplissement de ma thèse le reflet de leur enseignement.





# Contents

<b>General introduction</b>	<b>1</b>
<b>Part I: Finite temperature sub-saturation matter</b>	<b>25</b>
<b>I.1 Nuclear Statistical Equilibrium</b>	<b>28</b>
I.1.1 Grand canonical partition function . . . . .	28
I.1.1.a Statistical mechanics and stellar matter . . . . .	28
I.1.1.b Wigner-Seitz cells . . . . .	32
I.1.1.c The partition function . . . . .	35
I.1.2 Thermodynamic quantities . . . . .	41
<b>I.2 Modelling nuclear energetics</b>	<b>44</b>
I.2.1 Nucleon gas . . . . .	44
I.2.1.a Mean-field approach . . . . .	45
I.2.1.b Quantum mechanics expressions of densities . . . . .	47
I.2.1.c Effective Skyrme interaction . . . . .	49
I.2.1.d Homogeneous matter . . . . .	51
I.2.1.e Pairing effects in the BCS approximation . . . . .	52
I.2.2 Cluster energetics . . . . .	54
I.2.2.a Ground states energy . . . . .	54
I.2.2.b Degeneracy factor . . . . .	56
I.2.3 In-medium effects . . . . .	60
I.2.3.a Coulomb energy . . . . .	60
I.2.3.b Nuclear in-medium effects . . . . .	60
<b>I.3 Results at chemical equilibrium</b>	<b>63</b>
I.3.1 The numerical code . . . . .	63
I.3.2 Proton fractions . . . . .	64
I.3.3 Cluster distribution . . . . .	67
I.3.4 Average composition . . . . .	70

<b>Part II: Modelling the energetics of Wigner-Seitz cells</b>	<b>79</b>
<b>II.1 Quantum mechanics and semi-classical developments</b>	<b>82</b>
II.1.1 Mean field operator of the Skyrme interaction . . . . .	82
II.1.2 Semi-classical approximations . . . . .	84
<b>II.2 Density profile modelling</b>	<b>87</b>
II.2.1 Nuclei in vacuum . . . . .	87
II.2.1.a Profiles of symmetric nuclei . . . . .	88
i) Generalized Fermi function . . . . .	88
ii) Simple Fermi function . . . . .	91
iii) Comparison to HF calculations . . . . .	92
II.2.1.b Density profiles for asymmetric nuclei . . . . .	95
i) Fermi-Dirac ansatz . . . . .	95
ii) Isospin asymmetry inhomogeneities . . . . .	97
iii) Comparison to HF calculations . . . . .	98
II.2.1.c Decomposition of the energetics . . . . .	101
i) Surface energy . . . . .	102
ii) Surface symmetry energy . . . . .	103
iii) Curvature symmetry energy . . . . .	105
iv) Hints from Hartree-Fock . . . . .	107
II.2.2 Nuclei embedded in a nucleon gas . . . . .	108
II.2.2.a Density profiles and associated energy . . . . .	109
i) Fermi-Dirac density profiles . . . . .	109
ii) Bulk isospin asymmetry . . . . .	111
II.2.2.b Decomposition of the energetics: in-medium effects	113
<b>II.3 In-medium interactions</b>	<b>115</b>
II.3.1 Modifications of the bulk energy . . . . .	115
II.3.2 Modification of the surface energy . . . . .	117
II.3.3 Dependence on the effective interaction . . . . .	119
II.3.4 Effects of the in-medium corrections on neutron stars . . .	122
 <b>Part III: Analytical mass formula</b>	 <b>131</b>
<b>III.1 Symmetric nuclei</b>	<b>134</b>
III.1.1 Ground state energy . . . . .	135
III.1.2 Analytical expression for the diffuseness . . . . .	140
III.1.3 Decomposition of the surface energy . . . . .	142

---

<b>III.2 Asymmetric nuclei</b>	<b>148</b>
III.2.1 Decomposition of the nuclear energy . . . . .	149
III.2.2 Approximations for the isovector energy . . . . .	154
III.2.2.a No skin approximation . . . . .	154
III.2.2.b Gaussian approximations . . . . .	159
i) Global Gaussian approximation . . . . .	159
ii) Other Gaussian approximations . . . . .	161
iii) Isovector energy expression . . . . .	163
III.2.2.c Comparison to Hartree-Fock calculations . . . . .	169
III.2.3 Study of the different energy terms . . . . .	170
<b>III.3 Clusters embedded in a nucleon gas</b>	<b>179</b>
III.3.1 Nuclei beyond the drip lines . . . . .	180
III.3.2 Nucleon gas . . . . .	182
III.3.3 In-medium interactions . . . . .	183
<b>General Conclusions</b>	<b>191</b>
<b>A Analytical integrals of Fermi functions</b>	<b>201</b>
A.1 General formulae . . . . .	201
A.2 Expressions of a 3D integral as 1D integrals . . . . .	202
<b>B Analytical integrals of Gaussian</b>	<b>204</b>
<b>C Analytical expressions of the energy density derivatives</b>	<b>206</b>
C.1 Second derivatives of the energy density . . . . .	206
C.2 Expansions of the energy density first derivative . . . . .	208





# General introduction

## 1 Astrophysical context

Both the terms *supernova* and *neutron star* were first introduced by Walter Baade and Fritz Zwicky in 1934 [Baa34b; Baa34a].

The name *supernova* referred to a “remarkable type of giant novae” [Baa34b], a rare and very energetic cosmic phenomenon, characterized by a sudden and ephemeral burst in luminosity. The first SuperNova (SN) ever recorded is thought to have occurred in 185 CE. Chinese astronomers, who commented the event, called it a “guest star” [Zha06]. Due to the low SN event rate, only five or six galactic SN have been registered since 1000 CE, and extragalactic SN have only been observed for a century [Ber91a], including the most well-observed SN to date, located in the Large Magellanic Cloud and occurred in 1987.

Though Landau anticipated that the density of stellar matter may become “so great that atomic nuclei come in close contact, forming one gigantic nucleus” in 1932 [Lan32], it is also W. Baade and F. Zwicky who, only two years only after the discovery of the neutron [Cha32], first “advance[d] the view that supernovae represent the transitions from ordinary stars into *neutron stars*, which in their final stages consist of extremely closely packed neutrons” [Baa34a]. The existence of Neutron Stars (NS) however was observationally only proved in 1968, when radio pulsars were discovered [Hew68], and in the same year identified to NS [Gol68]. Since then, about 1800 neutron stars have been identified in all wavelengths from radio to  $\gamma$ -rays.

According to their spectroscopic properties, the SN have been classified into different groups. For the type Ia showing a lack of hydrogen lines but strong Silicon absorption lines, it is commonly accepted that they result from thermonuclear explosion of white dwarfs, leaving no compact remnant. The other explosion types are thought to be triggered by the core collapse of massive stars, eventually leading to a neutron star or a black hole. This thesis deals with the microscopic modelling of the structure and internal composition of baryonic matter in these Core Collapse Supernovae (CCSN) as well as their (hot) dense remnants, called Proto-Neutron Stars (PNS). A brief overview of the current understanding of the dynamics of these compact stars is sketched out in what follows.

### Core Collapse Supernovae

The first stage of the active life of a star consists in burning the hydrogen of its central part into helium. Other exothermic reactions take place in the star core contributing to the stellar nucleosynthesis, notably the CNO cycle. Their influence is however negligible in the balance in the star energy release for stars with mass and temperature similar to our sun. When  $\sim 90\%$  of the total star mass is converted, the inert helium core

contracts under gravitational force. For enough high-mass stars,  $M \gtrsim 4 M_{\odot}$ , the ignition temperature of helium into carbon and then into oxygen ( $T \sim 10^8$  K) is reached, and the star becomes a red giant. Following the same process, the most massive stars,  $M \gtrsim 10 M_{\odot}$ , can ignite their core elements up to the neon, magnesium, silicon, and finally iron ( $T \sim 10^9$  K  $\sim 0.1$  MeV). As a consequence of this burning sequence in stages, at the end of their lives, these massive stars, become red supergiants, develop an onion-like structure. Their central core is composed of iron and neutron-rich iron-group nuclei [Bet79], surrounded by shells of lower and lower burning elements (Si, O, C, He, H) up to possible inert hydrogen, at progressively lower temperatures and densities [Woo02; Lim06]. Such stars are called presupernova or progenitor of CCSN.

The Nickel and Iron isotopes being the most stable nuclei, that is having the highest binding energy per nucleon, their fusion is not possible and the chain of reactions in the core of the star ends. The inert core is thus sustained by the internal pressure of the matter, that is mainly by the degenerated electrons. There is therefore a critical mass, above which the gravitational force dominates the electron degeneracy pressure and the core contracts. This limiting value is given by the Chandrasekhar mass [Cha31] which depends on the electron fraction  $Y_e$ :

$$M_{Ch} = 1.457 (2Y_e)^2 M_{\odot}.$$

Corrections including temperature dependence can also be considered [Woo02]. According to the model calculations of stellar evolution which give similar final states of the core, characterized by central density  $\rho_c \sim 10^{10} \text{ g} \cdot \text{cm}^{-3} \sim 10^{-5} \text{ fm}^{-3}$ , temperature  $T_c \sim 1$  MeV, entropy  $s_c = 1$ , the electron fraction of the core is  $Y_e \sim 0.42 - 0.46$ , leading to a Chandrasekhar mass value of  $\sim 1.2 - 1.4 M_{\odot}$  [Arn77; Bet79]. When the mass of the iron core reaches this critical mass, it collapses under the overwhelming gravitational pressure, starting the so-called core collapse supernova (upper left panel of fig. 1). This process can be schematically divided into three stages.

In the first stage, the implosion, the dynamics is dominated by the electron fraction, mainly determined by the weak processes. Due to the increases in density and temperature during the collapse, electron captures on nuclei and free protons out of  $\beta$ -equilibrium occur and reduce the electron fraction. The neutrinos produced by these reactions are able to escape from the star as long as the density is below a critical density  $\rho_{crit} \sim 10^{-3} \text{ fm}^{-3}$ . Thus, pressure and energy are removed from the system and consequently the infall is accelerated. The endothermic reactions of photodissociation of iron group nuclei into alpha particles, and then of these alpha particles into neutrons and protons also accelerate the collapse. When the density reaches the critical density, the medium is no longer transparent to neutrinos: the neutrinos are trapped

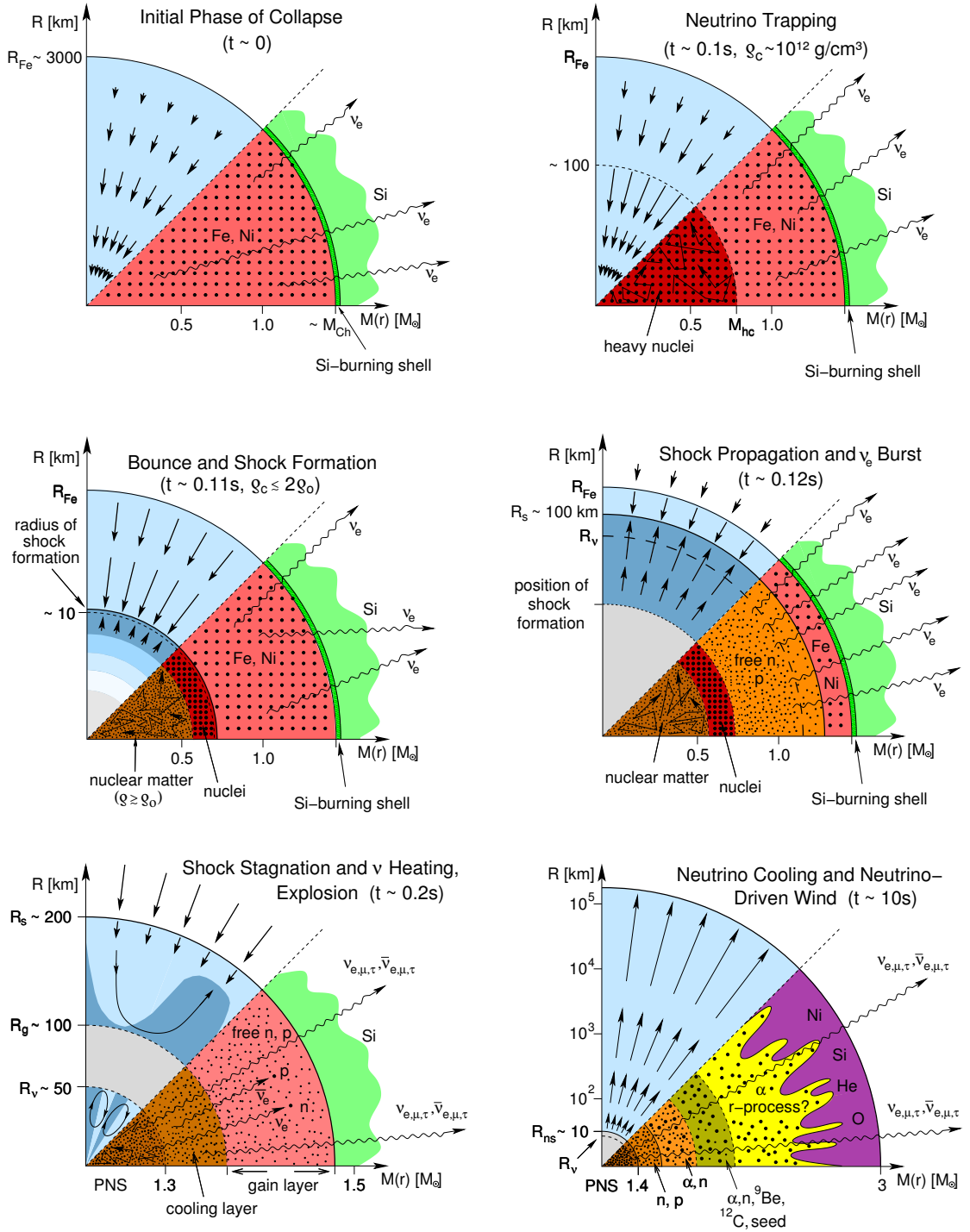


Figure 1: Schematic representation of the evolutionary stages of stellar core collapse.  $M_{hc}$  stands for the homologous inner core mass and  $R_{Fe}$ ,  $R_s$ ,  $R_{ns}$ , and  $R_\nu$  for the radii of the iron core, the shock, the neutron star, and the neutrinosphere, respectively. The arrows represent the velocity vectors. Figure from [Jan07].

and  $\beta$ -equilibrium is established [Bet90] (upper right panel of fig. 1). The infall is thus (quasi-)adiabatic and the collapse is homologous, meaning that it behaves as a unit, collapsing self-similarly. The core is divided into a homologous inner core which falls at subsonic velocity, and an outer core which falls at supersonic velocity, in which matter cannot communicate via pressure waves.

The second stage of CCSN corresponds to the bounce. It happens a few hundred milliseconds after the beginning of the infall, when the central baryonic density reaches about the nuclear saturation density  $\rho_{sat} \sim 0.16 \text{ fm}^{-3}$ , defined as the equilibrium density of non-charged homogeneous infinite baryonic matter (the so-called nuclear matter). Because of the high incompressibility of nuclear matter, the internal pressure sharply counterbalances the gravitational effects and the collapse suddenly stops in propagating waves in the homologous core. The outer core however continues to fall inwards at a supersonic speed. As a result, the pressure waves accumulate at the sonic surface, creating a shock wave, characterized by a discontinuity in pressure and matter velocity (middle left panel of fig. 1). The shock wave then propagates faster than the speed of sound through the rest of the iron core, and eventually reaches the envelope of the star (middle right panel of fig. 1).

The shock wave propagation induces the final stage, in which the outer layers are expelled out of the star, leading to the supernova explosion as well as a compact hot remnant at the center. However, the so-called prompt mechanism, for which it is assumed that the shock wave responsible for the explosion is caused only by the bounce, is known to be not energetic enough [Bet90]. Indeed, the shock wave loses energy through the photodissociation of the core nuclei into alpha particles and neutrons. Furthermore, since the neutrinos beyond the neutrinosphere, produced by electron captures, leave the star, they also contribute to the energy loss (middle right panel of fig. 1). The weakened shock thus finally stalls at several hundred kilometres from the core, while the matter behind the shock continues falling inwards, forming a proto-neutron star (PNS) (lower left panel of fig. 1). The exact dynamics of the explosion remains currently uncertain, and several mechanisms have been advanced, insisting on the importance of taking into account of hydrodynamical instabilities, rotation, magnetic field or g-mode oscillations [Bur06; Jan07]. In the delayed mechanism [Jan07], the shock is revived by the neutrinos emitted by the PNS a few seconds after the collapse halt, creating a region of high temperature and low density between the shock and outer layers which, by convection, allows the neutrino energy to be efficiently absorbed by the shock wave (lower left panel of fig. 1). When the explosion occurs, the outer layers of the stars are ejected (lower right panel of fig. 1), enriching the interstellar medium with the elements produced during the different burning stages, as well as during the supernova explosion

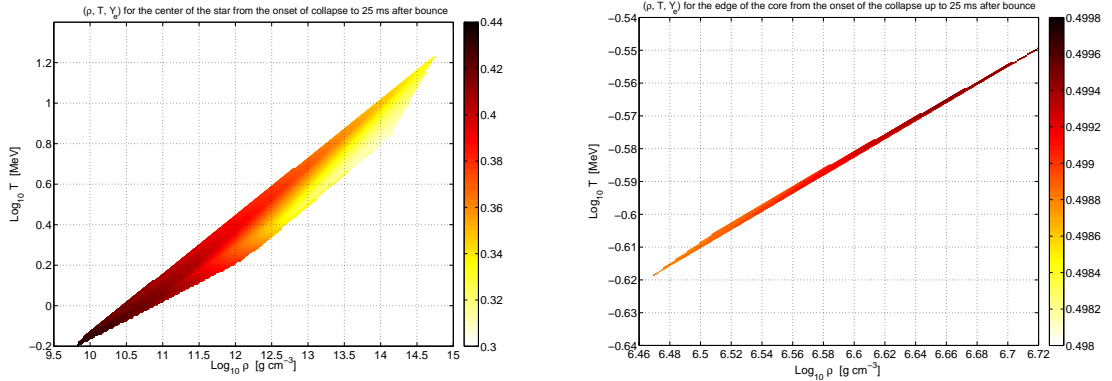


Figure 2: Baryonic density  $\rho_B$  (abscissa, log scale), temperature  $T$  (ordinate, log scale) and electron fraction  $Y_e$  (color, linear scale) ranges spanned by the core, in the center (left panel) and on the edge (right panel) of a  $15M_\odot$  presupernova. Figure from [Fan10].

(through s- and r-processes) [Woo02; Jan07].

Fig. 2 gives a general overview of the density, temperature and electron fraction ranges typically spanned during the collapse and the early post bounce, of the core center (left panel) and of the core edge (right panel). One can see that the SN matter is in extremely different conditions according to the star location and time after the beginning of the infall. More specifically, matter can be symmetric ( $Y_e = 0.5$ ) as well as neutron rich (up to  $Y_e \sim 0.3$ ), denser than the saturation density (up to  $\sim 3\rho_{sat}$ ) as well as much more diluted ( $\rho_B \sim 10^{-9} \text{ fm}^{-3}$ ), and spans two orders of magnitude in temperature ( $100 \text{ keV} \lesssim T \lesssim 10 \text{ MeV}$ ).

### From proto-neutron stars to neutron stars

The remaining PNS eventually leads to a neutron star (NS), or collapses into a black hole if it exceeds the NS maximum mass. The evolution onto a cold NS takes about a hundred years, passing through various stages of very different durations [Pra97]. As already mentioned, the very beginning of the PNS consists of the hot ( $T_c \sim 20 \text{ MeV}$ ) bounced homologous core of radius of  $\sim 10 - 20 \text{ km}$ , in which neutrinos are trapped. It accretes the outer low density matter, called the mantle, which corresponds to the region between the iron core and the stalling shock. The mantle is then deleptonized by electron captures, leading to a reduction of its pressure causing its collapse towards the core. About 10 seconds after, the neutrinos producing the core deleptonization diffuse to the surface, transferring most of their initial energy to the core matter. Thus the central temperature increases up to  $T_c \sim 50 \text{ MeV}$ . Less than a minute later, the core medium becomes transparent to neutrinos (which now are low-energy) and so cools down, reaching  $T_c \sim 5 \text{ MeV}$ . At that time, the neutrino emission rate substantially decreases,

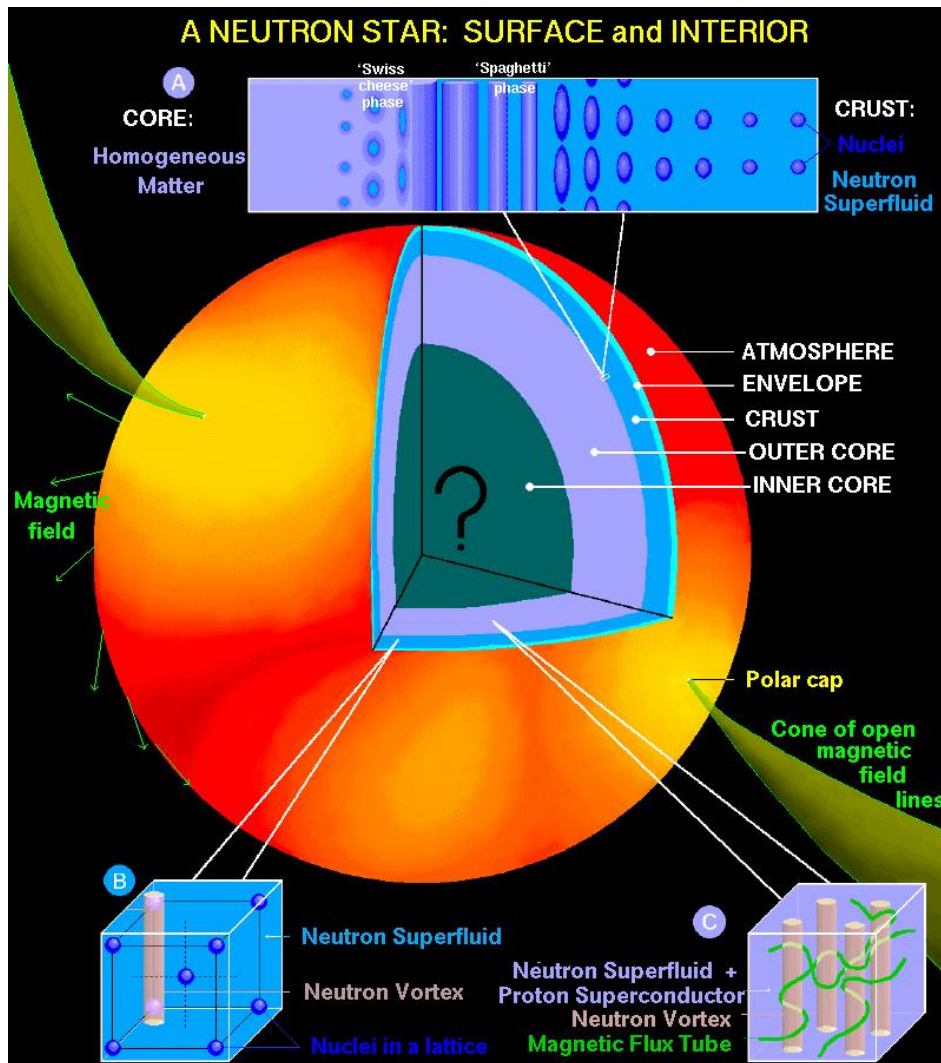


Figure 3: Schematic structure of neutron stars. Figure from [Pag06b].

as well as the core cooling speed.

The star crust also cools but less quickly, preventing the complete thermal equilibrium of the star for about a hundred years. When the neutron star is finally isothermal, its temperature is about a few tens of keV. It continues to slowly cool down, first by mainly emitting neutrinos and anti-neutrinos produced by beta decay and inverse beta decay at  $\beta$ -equilibrium, during tens of thousands of years; and then by thermal emission for a few million years.

A few hours after the collapse, the cold neutron star of  $T \sim 100$  keV is catalyzed, that is in its ground state. Fig. 3 represents its schematic structure from which we can distinguish six main regions. The thin external layers, called the atmosphere (a few

centimetres wide) and envelope (a few meters), are important in the determination of thermal emission. Towards the interior of the NS, the atoms are ionized, and the solid crust of 1–2 km wide is composed of clusterized nuclear matter in presence of an electron gas, in  $\beta$ -equilibrium. Due to electron captures, the matter is more neutron-rich with increasing density, further towards the interior of the star. The crust can be divided into two regions, the outer and the inner crusts. The border between them is determined by the density where nuclei are at the (stellar) neutron drip line, which is defined as the limit where the neutron separation energy, modified by the additional Coulomb interactions due to electrons, becomes negative.

In the outer crust of a few hundred meters wide, matter is then organized as a lattice of exotic nuclei in equilibrium with relativistic electrons; in the inner crust, nuclei, or clusters, are in addition immersed in a neutron gas. Though the crust only represents a small percent of the total NS mass, knowledge of it is essential in order to understand the NS dynamics, like cooling, accretion, glitches. Between the crust and the core, that is for densities between  $\sim 0.2\rho_{sat}$  and  $\rho_{sat}$ , highly non-spherical clusters appear, commonly called pasta phases. For densities above saturation, the core matter is homogeneous. We can distinguish the outer core, up to  $\sim 2\rho_{sat}$ , made of neutrons, protons, electrons, and muons, from the inner core for which its composition remains uncertain, due to the likely presence of other degrees of freedom, such as strangeness (e.g. hyperon), Bose condensates (e.g. pions, kaons) and/or deconfined quark matter (quark-gluon plasma).

## 2 Equation of State

Nuclear physics is a key component for the understanding of compact stars. The Equation of State (EoS) relates, in given conditions of temperature and densities, the macroscopic quantities of the star, such as the internal energy and the pressure, which determine the dynamics of CCSN, the evolution of the PNS, and the mass-radius relation of NS. Furthermore, the microscopic matter properties play an essential role for the structure of (P)NS, as well as for the CCSN nucleosynthesis, the electron capture rates which determine the electron fraction and the neutrino scattering governing the deleptonization processes and the cooling speed of (P)NS. The determination of a realistic consistent unified EoS for the wide ranges of density, temperature and asymmetry spanned during the CCSN and (P)NS cooling is however challenging.

At densities higher than saturation, that is during the core bounce and in the remnant (P)NS core, simple energetic arguments show that the EoS has to take into account exotic particles [Gle82]. Due to the additional strangeness degree of freedom, the appearance of phase transitions is predicted, with both relativistic [Sch00] and non-relativistic [Gul13] models. In ref. [Oer12], pions and hyperons have been taken into account in CCSN

simulations. Pions have been assumed to behave as a non-interacting free gas, and the hyperons interaction has been modelled with a non-relativistic potential. These particles are shown to play a non-negligible role in the pressure, energy, density, and sound speed during the CCSN. Furthermore, the presence of hyperons is expected to speed up the PNS cooling [Sch96]. Concerning a possible deconfined quark matter, a transition after the core bounce has been shown to produce a second shock [Sag09]. Quark-gluon plasma in the NS core is also known to strongly modify the NS mass-radius relation [Lat01].

All these different aspects are not treated in the present work. Indeed, this thesis is focused on matter where the density is below saturation, which is relevant for the (P)NS crust and the SN stages of core collapse and explosion. A general overview of sub-saturated EoS is given in what follows.

## Neutron star

Only the energy at zero temperature is required to describe the cold catalyzed Neutron Star. The modelling of the crust began in the early 1970s, in particular with the pioneering works of Baym *et al.* [Bay71a] and Negele and Vautherin [Neg73]. To describe the lattice of both the outer and inner crust, both works used the Wigner-Seitz (WS) cells as independent elementary constituents, each of them containing a nucleus located at the crystal site, a homogeneous electron gas and, in the inner crust, a homogeneous free neutrons gas. The size and asymmetry of the nucleus as well as the neutron gas density are determined by minimizing the energy of the WS cell, under some equilibrium constraints.

The analysis of [Bay71a] has been performed in separately treating the nuclear gas phase from the clusterized one. In this work, the pure neutron gas energy is evaluated within a density functional, and a compressible liquid-drop-like model is developed in the spirit of the Thomas-Fermi approximation in order to model the energy of the nucleus. The clusters energy is thus described using a bulk term, directly given by the energy density times its volume, and approximated surface terms, taking into account the energy modifications due to the gas. To evaluate the energy density entering the cluster bulk part, the authors use different formulas for extreme values (saturation/very low density and symmetric/neutron matter) and polynomial interpolations are employed for intermediate conditions. These severe approximations on the density functional however allow a consistent treatment of the energy of the free neutrons gas in the inner crust and of the clusters bulk part. The surface energy of the cluster, modified by the neutron gas, is evaluated starting from the Thomas-Fermi approximation and Fermi-Dirac density profiles. Assuming the clusters to be spherical, neglecting curvature effects, and making the rough assumption that the energy per particle is a linear function of the den-

sity when crossing the surface from gas to cluster, an analytical formula, proportional to  $A^{2/3}$  (with  $A$  the baryon number of the nucleus), has been proposed for the surface energy of a cluster embedded in a neutron gas. In this final result, the surface tension is treated as a free parameter to be adjusted to experimental data. The formula for the surface energy does not depend on the isospin and exhibits a decreasing behaviour with the neutron gas density. The main interaction term between the gas and the clusters is described by an excluded volume. In this work, shell and pairing effects have been neglected in both nuclei and the neutron gas.

The matter composition is then given by the minimization of the WS total energy with respect to the cluster size and asymmetry, the neutron gas, and the volume of the WS cell. The authors show that this amounts to minimizing the cluster energy per nucleon with respect to its size, within the constraints of chemical equilibrium and pressure equality between the neutron gas and clusterized phase, the whole matter being at  $\beta$ -equilibrium.

With this quasi-analytical model, the authors conclude that, with the increase of matter density, the number density of nuclei increases, as well as its number of protons, though the proton fraction decreases. Nuclei are shown to be present up to the saturation density. Matter is predicted to be homogeneous starting from a density slightly higher than saturation. This surprising result is due to the fact that, in that model, an instability against proton clustering already occurs at a baryonic density above saturation.

The other pioneering work [Neg73] is based on microscopic Hartree-Fock (HF) calculations which make it possible to directly calculate the total energy of the WS cell. No differentiation between the gas phase and the clusterized one is necessary in this framework. The authors use an energy density formula derived from a phenomenological effective two-body nucleon-nucleon interaction, taking into account the spin-orbit interaction of protons only, and neglecting pairing effects. The numerical solution of HF equations in spherical symmetry on a harmonic oscillator basis gives the optimal configuration for the single particle wave functions for a given total baryon number and cell volume. The ground state at a given density is then evaluated by the minimization of the WS cell energy varying the total baryon cell number of  $\beta$ -stable configurations.

As in the results of [Bay71a], the proton fraction is found to decrease with the increase of matter density, and density inhomogeneities corresponding to clusters are present up to densities close to saturation. The proton number however is shown to be very sensitive to the shell effects, since the observed values are only at closure shells. Furthermore, this proton number of the cell decreases close to the saturation density, contrary to the results of [Bay71a], for which it monotonically increases. This disagreement actually describes the same process, which is the transition of clusterized matter to homogeneous matter. In [Neg73], the transition is described as a decrease in the cluster size, leading to a final

disappearance of clusters, whereas in [Bay71a] the clusters are close enough to touch each others and therefore create a very large cluster, ultimately leading to homogeneous matter. Though leading to the same conclusion, these different mechanisms reflect a very different treatment of the in-modifications surface energy. Concerning the EoS, the authors of [Neg73] conclude that their analysis and the study of [Bay71a] are globally in agreement.

Superfluidity in the neutron star medium, neglected in the two previous studies, was first suggested in [Mig59]. This phenomenon is now known to play a crucial role during the cooling and thermalization of the (P)NS [Lat94; Gne01; For10], and on the so-called glitches in pulsars, which are commonly explained by the appearance and disappearance of superfluid vortices in the NS inner crust [Pet95; Pie14]. Pairing also has an effect on the structure of Wigner-Seitz cells, as it has been first investigated in [Bal05], within the HF BCS framework. In that work, pairing in the clustered phase is considered with the realistic phenomenological functional of [Fay00], and microscopic calculations based on the Brueckner theory are used to model the pairing of the free neutron gas. For consistency, a global energy density functional is built by matching the two functionals, making it possible to take into account a pairing at intermediate densities, corresponding to the cluster surface.

In that work, it is shown that both the neutron and proton superfluidity significantly modify the ground state structure of the inner crust. In particular, it was found that pairing correlations smooth the fluctuations in the energies. As a consequence, the competing ground state energy of different Wigner-Seitz configurations are very close, and the proton number of the WS cells is not necessarily at shell closure, contrary to [Neg73].

To obtain accurate results, the most recent works directly employ the measured masses for the outer crust composition. However, since current experimental data are not available up to the neutron drip line, realistic extrapolated models are required. In [Pea11], different Hartree-Fock Bogoliubov models have been tested in the unknown regions. Though the Equation of State is substantially the same, the composition varies considerably from one model to another, highlighting the uncertainties in the composition of the catalyzed outer crust. The outer crust has also been shown to be very sensitive to the precision of the nuclei mass. For example, in [Wol13], taking into account the recently measured mass of the isotope  $^{82}\text{Zn}$ , is shown to modify the NS composition by shifting the position of  $^{80}\text{Zn}$  and replacing  $^{82}\text{Zn}$  by  $^{78}\text{Ni}$  at a given depth inside the NS.

## Single Nucleus Approximation

The Equation of State for compact star matter at sub-saturated density and at finite temperature was first investigated within the so-called Single Nucleus Approximation (SNA). It is based on the assumption that, like at zero temperature, matter is made of a lattice of WS cells, each of them containing a unique cluster, immersed in an electron and free nucleon gas. The equilibrium is thus given by minimising the free energy of the WS cell. Such EoS were first developed in the late 1970's by Lamb *et al.* in the pioneering work [Lam78]. In each WS cell, the authors consider a heavy nucleus, an electron gas, free neutrons and protons, as well as an alpha-particle gas. The neutron and proton gases are always present at finite temperature because of the excited states of nucleons in the continuum. Due to the finite entropy contribution in the Wigner Seitz cell, light nuclei can also be present. Because of the specific binding energy of  ${}^4\text{He}$ , the authors assume that the alpha particles are dominant. The other difference with respect to zero temperature models is that  $\beta$ -equilibrium is not necessarily verified since equilibrium with respect to weak interactions is often not achieved within the collapse, explosion and cooling. As a consequence, the proton fraction is not constrained and, to obtain a complete EoS, the WS cell free energy has thus to be minimized at fixed total baryonic density and temperature, as well as at fixed proton fraction.

One of the main EoS widely used in CCSN simulations, and available at the on-line service CompOSE providing data tables from different EoS used in compact star physics [Com13], has been established by Lattimer and Swesty in [Lat91], based on [Lat85], in the continuity of the previous study [Lam78].

As already mentioned, the EoS of [Lat85; Lat91] considers nuclear matter as a mixture of one heavy nucleus, alpha particles and free nucleons in chemical equilibrium. This model treats the nuclei and the free nucleon gas separately. Neglecting pairing effects, the free energy of the homogeneous neutron and proton gas is described with a non-relativistic energy functional. Like in [Bay71a], the nuclear free energy of nuclei is decomposed into a bulk part, evaluated with the same energy functional as the one used for the nucleon gas, and a surface part, taking into account the modifications due to the nucleon gas. Based on Thomas-Fermi considerations, the authors have proposed an analytical formula for the surface free energy of the WS cell in evaluating the number of the surface nucleons and performing a fit on Thomas-Fermi and Hartree-Fock calculations. In particular, it is assumed that this formula does not depend on the asymmetry isospin of the gas phase, and the temperature dependence of the surface tension is parametrized with a function depending on the critical temperature of infinite nuclear matter. This approach ensures that the surface tension well vanishes at the thermodynamic critical temperature and mocks up the rapid increase of surface modes with available excitation

energy. The authors propose two surface energy formulas, one taking into account the neutron skin in [Lat85], while in [Lat91], the effect is neglected to simplify the equation, in order to make a direct implementation of their EoS in simulation codes possible. For the same reason, the Skyrme 1 initially used in [Lat85] is replaced by expansions around saturation density and around isospin symmetry in [Lat91], highlighting the usual nuclear coefficients of symmetric saturated matter. As a consequence, the density dependence of the symmetry energy is not very realistic. Alpha particles are simply treated as hard spheres forming an ideal Boltzmann gas, and the contribution of their excited states, which lie at very high energy  $E \sim 20$  MeV, is neglected. Finally, the interactions between the nuclei, alpha particles, and free nuclear gas is given by an excluded volume, and the alpha gas is assumed to not modify the surface interactions. This model also allows another geometry, and proposes corresponding formulas for the surface and Coulomb energy terms of the so-called bubble nuclei. Other possible geometries violating spherical symmetry (rods, slabs...) are not considered. The most favorable geometry between the sphere and the bubble is given by the configuration which minimizes the free energy. To determine if matter is homogeneous or clusterized, the authors perform Gibbs' phase rule, assuming the transition is first-order. They similarly consider alpha matter and nuclei without alpha matter at high densities.

The other EoS within the SNA and most commonly used in core-collapse simulations, also available on [Com13], has been developed by Shen *et al.* [She98]. In this model, the authors consider spherical nuclei embedded in a neutron and proton gas, but do not distinguish the clusterized phase from the gas one. Instead, a shape for the distribution profiles of neutrons and protons within the WS cell is assumed, depending on  $2 \times 4$  free parameters. Using the Thomas-Fermi approximation with these nucleon distributions, the total cell free energy is calculated with the relativistic mean-field theory TM1. In order to take into account inhomogeneity of nucleon distribution, an additional gradient-dependent term has been added in the energy density functional. The configuration corresponding to the equilibrium is then given by the parameters which minimize the free energy at fixed temperature and baryonic densities, which lead to a minimization over seven parameters in general, six if  $\beta$ -equilibrium is reached.

The main advantage of the two models previously presented, [Lat91] and [She98], is that, since they use the same framework to describe clusterized matter and the homogeneous nucleon gas, they provide a unified and consistent EoS for densities up to  $\sim 2\rho_{sat}$  (beyond which other degrees of freedom have to be taken into account). Nonetheless, a first-order phase transition is required to match sub-saturated matter to super-saturated matter, leading to a spurious discontinuity.

The two models also share the common limitation that the resulting equation of state

and matter composition are given in a tabulated form, and that the energy functional cannot be changed by the user. In both cases the energy functionals are somewhat obsolete and do not take into account the recent progress in the knowledge of the density dependence of the symmetry energy [EPJ14], nor the present estimation of the uncertainties associated to the functional. In this respect, the Lattimer and Swesty model [Lat91] appears slightly superior to the Shen one [She98] because the latter one is too stiff and with an overestimated spin-orbit coupling with respect to present constraints. From the viewpoint of the modelling, the opposite is true. Indeed, the two models widely differ by the choice of prescription of the interaction between the nuclear components, though, in principle, they both take into account the same physical effects. The model [Lat91] introduces an excluded volume by hand and develops approximations for the surface interactions which are not fully controlled, while in [She98], all these effects are evaluated within the Thomas-Fermi approximation. Another difference is that alpha particles are not considered in [She98] which poses a major limitation in this model. However, they have been implemented in more recent works using the same approach [She11].

### Nuclear Statistical Equilibrium

The SNA models presented in the previous section assume that matter at finite temperature can be represented by the most probable nucleus given by the minimization of the free energy of a WS cell. However, to determine the equilibrium, one should minimize the free energy of the total system made of a mixture of states, that is a mixture of different Wigner-Seitz cells. The models taking into account a full distribution of different clusters are known as Nuclear Statistical Equilibrium (NSE) models. It is clear and well known that the microscopic phenomena happening in CCSN and (P)NS cooling and thermalization, such as neutrino scattering and all the different weak rates governing the heat transfer, strongly depend on the nuclear species present in the stellar medium [Lan04; Mar04; Cab06; Pag06a]. The same is true for the modelling of out-of-equilibrium problems like accretion and r- and p-nucleosynthesis of heavy elements. Furthermore, the consideration of the distribution of matter composition may even affect the average quantities giving the EoS [Rad10; Buy13; Gul15] since the most probable configuration is not necessarily representative of the average one. The fact that the SNA matches neither with the average nor with the most probable nucleus predicted by NSE models [Sou09; Gul15], provides a strong motivation for considering a distribution of nuclei.

Different EoS within the NSE framework are currently being developed. All of them consider a mixture of nuclei, including light clusters and resonances, embedded in a nucleon gas. The Coulomb energy, including the electron screening, is evaluated within the spherical Wigner–Seitz approximation. We present a few NSE models in what follows,

and focus on the different nuclear energy prescriptions.

The NSE models were first investigated in the early 1980s. The work of El Eid and Hillebrandt [Eid80] is the third EoS used in supernova simulations. In this pioneering analysis, the authors assume that nuclei, in chemical equilibrium with a free neutron and proton gas, can be treated as a Boltzmann gas, neglecting any interaction and modification induced by the external nuclear gas. The multiplicity of a given nucleus, that is the number of the same nucleus specie in a volume unit is then simply given by the Boltzmann statistics multiplied by a temperature dependent degeneracy factor, to take into account the nuclei excited states. To evaluate the ground state binding energies, the authors use a droplet model mass formula [Mye69], making it possible to consider nuclei of any size and any proton fraction. In particular, very neutron-rich nuclei expected at  $\beta$ -equilibrium are taken into account. An analytical phenomenological formula is used to calculate the excited states of any nucleus. The temperature dependent energy density of the free interacting nucleons is evaluated in the Hartree approximation, with the simple Seyler and Blanchard two body interaction potential. For consistency, the parameters of this potential are chosen such that they are compatible with the mass formula used for nuclei. Because of the schematic treatment of the nucleon gas, this model can only be used at very low densities.

The Statistical Multifragmentation Model of Botvina and Mishustin [Bot10] adjusted into NSE and developed in the grand canonical ensemble, uses tabulated binding energies for the lightest nuclei  $A \leq 4$ . Otherwise, the model is based on a simple liquid-drop parametrization. The nuclei energy contains a bulk term ( $\propto A$ ) which depends on the nucleus proton fraction  $Z/A$  and an isoscalar surface term ( $\propto A^{2/3}$ ), thus neglecting curvature and isovector surface effects. The isoscalar terms phenomenologically depend on the temperature to take into account bulk and surface entropy for nuclei size  $A > 4$ . Pairing and shell effects are therefore neglected, but are expected to have little influence at the large temperatures for which this model is designed. An excluded volume effect is assumed to consider finite size of nuclei, but it is not included in the statistical weight of the different clusters and therefore only amounts to a renormalization of the nominal density. The light clusters of mass  $A \leq 4$  are treated with their ground state measured properties, that is their binding energy and spin degeneracy. Their excited states are neglected and their proper volume is used to consider excluded volume effects, which again do not enter in the thermodynamics. The neutron and proton gas is considered as a classical ideal gas such that, contrary to [Eid80], this model does not take into account nucleon-nucleon interactions. This simple model, limited to low densities since it neglects nuclear interactions between species, has the advantage that the coefficients of the cluster mass formula can be easily modified in order to explore certain aspects of

the nuclear interactions such as a possible modification of the symmetry energy due to the stellar medium.

The NSE model of Blinnikov *et al.* [Bli11] uses tabulated theoretical nuclear binding energies, covering 20,000 nuclei from  $A \geq 4$ . This limits the model to a global proton fraction larger than  $\sim 0.3$ . These predictions are based on a sophisticated mass formula composed of macroscopic and microscopic terms, and take into account deformation, pairing, and shell effects. The zero-temperature energy of the interacting nucleon gas is given by the same functional as [Bay71a]. In this model, the change of the nuclear surface energy due to the presence of the free nucleons is calculated by following the procedure of [Maz79]. An extra term  $\propto A^{2/3}$  is added, and the binding energy is modified in solving the pressure balance across the nuclear surface. The authors neglect bulk interactions such as the excluded volume approximation. Again, the approximate description of the nucleon gas prevents using the model at densities close to saturation, and in particular describing the transition from clusterized to uniform matter. The nuclei excited states are described by a temperature dependent degeneracy factor.

Another EoS, available at the online service [Com13] and recently used in simulations, has been developed within the grand canonical ensemble by Hempel and Schaffner-Bielich [Hem10]. This model is based on relativistic mean-field to describe the interacting nucleons gas as well as finite nuclei when the experimental masses have not been measured. As in the other models, the nuclei excited states are given by a temperature dependent degeneracy factor. The interaction between the nuclei and the nuclear gas is estimated with the excluded volume approximation, and no surface contribution is considered.

In the continuity of the work of [Rad10; Rad14; Gul15], the NSE model used in the present thesis, and presented in detail in part I, is based on non-relativistic Skyrme interactions to describe the nucleon gas, as well as finite nuclei when no experimental information is available. Besides the use of different nuclear interactions and excited states partition functions, the major difference of this model compared to [Hem10], is that no excluded volume effect is assumed, but a bulk modification energy shift due to the nuclear gas is consistently derived.

Globally, the width of the mass distributions in the NSE models can become larger than 100 units, indicating substantial differences to the SNA. It has also been shown that within NSE, the presence of clusterized matter starts at lower density [Bli11], and that the contribution of light clusters is very important and only poorly represented by alpha particles alone [Hem10]. Besides these global features, the different NSE models predict very different matter composition, mainly influenced by the choice of prescriptions used

to describe the nuclei ground state energy [Buy13]. In particular, mass formulas lead to smooth clusters distributions while using experimental data favour more specific nuclei, mainly linked to shell closures. Concerning the EoS, large differences between NSE and SNA as well as between the different NSE models themselves, occur at large temperatures  $T \gtrsim 5$  MeV and high densities  $\rho_B \sim 0.1\rho_{sat}$  [Buy13]. The cluster binding energy modifications due to the nuclear gas, neglected in most NSE models, have been shown to be important at low temperature  $T \lesssim 2$  MeV and high densities  $\rho_B \gtrsim 0.1\rho_{sat}$  [Buy13; Aym14].

### 3 Organisation of the thesis

In this thesis, we are interested in obtaining a realistic unified EoS for compact stars. We are thus seeking a formalism which can be applied both at sub-saturation and super-saturation densities, with and without beta equilibrium, and at any value for the temperature. In particular, the microscopic HF(B) treatment of the Wigner-Seitz cell should emerge as a natural  $T \rightarrow 0$  limit of the NSE model. For this purpose, we build an NSE model which can be viewed as a statistical superposition of individual Wigner-Seitz cells. Within each cell, we investigate the nuclear energetics of clusters in interaction with a nucleon gas present in sub-saturated matter. The use of the mean-field theory for the description of both the clusters and the nucleon gas allows us to be consistent with a treatment at densities above saturation, not studied in this work.

The thesis is divided into three parts. In part I, we present the NSE model based on the grand canonical statistics and non-relativistic Skyrme interactions. Results at  $\beta$ -equilibrium are shown and the importance of the cluster distributions as well as a realistic treatment for the energetics are discussed. Part II investigates the functional behavior of the baryonic energy in the Wigner-Seitz cell within the Extended-Thomas-Fermi approximation. In particular, the surface symmetry energy is discussed in detail, and its sign is shown to depend on the prescription used to decompose the total energy into bulk and surface terms. A bulk in-medium effect is consistently derived, replacing the excluded volume assumed in other models. Both bulk and surface in-medium effects are studied and their dependence in terms of cluster size and asymmetry as well as gas densities and asymmetry is investigated. A preliminary result of in-medium surface effects is presented within some approximations in the case of  $\beta$ -equilibrated matter. In part III, we develop approximations in order to obtain a reliable analytical expression of the mass formula directly linked to the functional form and parameters of the Skyrme interaction. This part of the work is not completely achieved and we mainly focus on nuclei in vacuum. This allows us to analyse the different mass components in terms of bulk and surface properties, as well as isovector and isoscalar properties. General

conclusions are then proposed.

At the end of each part, a brief summary is written in French.

# Résumé de l'introduction

Le travail de cette thèse consiste à modéliser de façon microscopique la structure et la composition interne des étoiles compactes, c'est-à-dire les supernovæ à effondrement de cœur, les proto-étoiles à neutrons et les étoiles à neutrons. Un bref panorama de la compréhension actuelle de la dynamique de ces objets stellaires est esquissé dans ce chapitre.

Après avoir consommé la plupart de leur hydrogène, les supergéantes rouges, étoiles très massives ( $M \gtrsim 10M_{\odot}$ ), présentent une structure en pelures d'oignon, de température et de densité de plus en plus faibles à mesure que l'on s'éloigne du centre de l'étoile. Leur cœur inerte, composé de fer et de noyaux riches en neutrons appartenant au groupe de fer [Bet79], est entouré de couches d'éléments en fusion, de plus en plus légers (Si, O, C, He, H), et éventuellement d'une couche externe d'hydrogène inerte [Woo02; Lim06]. Ces étoiles sont appelées pré-supernovæ, ou progéniteurs de supernovæ. Les isotopes du Nickel et du fer étant les noyaux les plus stables, ils ne peuvent pas fusionner. Ainsi les chaînes de réactions nucléaires sont stoppées dans le cœur des pré-supernovæ. Celui-ci est donc maintenu par la pression interne de la matière, principalement due aux électrons dégénérés, qui compense les effets gravitationnels et permet au cœur de rester à l'équilibre. Il existe une masse critique  $M_{Ch}$ , appelée masse de Chandrasekhar [Cha31], au-delà de laquelle cet équilibre est rompu, la gravitation dominant la pression de dégénérescence des électrons. La valeur de la masse de Chandrasekhar est prédite par les modèles actuels comme étant de l'ordre de  $\sim 1.2 - 1.4 M_{\odot}$  [Arn77; Bet79]. Quand la masse du cœur de fer atteint cette masse critique, le cœur s'effondre sur lui-même. Démarre alors ce que l'on appelle la supernova à effondrement de cœur. Ce processus peut être schématiquement divisé en trois étapes : l'implosion, le rebond et l'explosion (voir figure 1). La durée totale de la supernova est de l'ordre de quelques secondes. La matière de supernova est dans des conditions thermodynamiques extrêmement différentes, dépendant à la fois de sa localisation dans l'étoile et du temps écoulé depuis le début de l'implosion. Ainsi, la matière peut être symétrique ( $Y_e = 0.5$ ) ou bien très riche en neutrons (jusqu'à  $Y_e \sim 0.3$ ), plus dense que la saturation (jusqu'à  $\sim 3\rho_{sat}$ ) ou bien beaucoup plus diluée ( $\rho_B \sim 10^{-9} \text{ fm}^{-3}$ ), et la température varie de deux ordres

de grandeurs, passant de la centaine de keV à la dizaine de MeV (voir figure 2).

Le résidu chaud et compacte qui subsiste après l’explosion de la supernova est appelée la proto-étoile à neutrons. Elle évolue en étoile à neutrons ou en trou noir si l’équilibre n’est pas établi. Le refroidissement du résidu conduit à une étoile à neutrons, objet à température nulle. Cette évolution prend une centaine d’années, et passe par différentes étapes de différentes durées [Pra97]. Une centaine d’heures après l’explosion, l’étoile à neutrons (de température  $T \sim 100$  keV) est dans son état fondamental, et présente une structure que l’on peut schématiquement diviser en six régions (voir figure 3). Les régions étudiées dans cette thèse concernent la croûte externe, composée d’un réseau de noyaux de plus en plus riches en neutrons et en équilibre avec un gaz d’électrons relativistes, ainsi que la croûte interne dans laquelle les noyaux, ou agrégats, sont en plus immergés dans un gaz de neutrons. La limite entre la croûte externe et la croûte interne est déterminée par la ligne de limite de stabilité (stellaire) en neutron. Bien que la croûte ne représente qu’un faible pourcentage de la masse totale de l’étoile à neutrons, la connaissance de sa structure est importante afin de comprendre la dynamique des étoiles à neutrons comme son refroidissement, l’accrétion, ou bien le phénomène de glitch.

La physique nucléaire un ingrédient clé pour la compréhension des étoiles compactes. L’équation d’état établit un rapport entre les conditions thermodynamiques, c’est-à-dire la températures et les densités, et les quantités macroscopiques de l’étoile, notamment l’énergie interne et la pression. Ce sont ces quantités qui déterminent la dynamique des supernovæ à effondrement de cœur, l’évolution des proto-étoiles à neutrons, et la relation masse-rayon des étoiles à neutrons. Par ailleurs, les propriétés microscopiques de la matière jouent un rôle prépondérant dans la structure des (proto-)étoiles à neutrons, ainsi que dans la nucléosynthèse, les taux de capture d’électrons qui déterminent la fraction d’électrons dans la matière, et la diffusion des neutrinos qui gouvernent les processus de déleptonisation et la vitesse de refroidissement de la (proto-)étoile à neutrons. Cependant, établir une équation d’état unifiée, réaliste et consistante pour les intervalles de densité, de température et d’asymétrie explorés pendant l’effondrement, le rebond et l’explosion de la supernova, puis le refroidissement du résidu est un tâche difficile. Dans cette thèse, on se limite à la matière en-deçà de la saturation, c’est-à-dire la matière de la croûte des proto-étoiles à neutrons ainsi que la matière de supernova lors des étapes d’effondrement et d’explosion. Un panorama général des équations d’état de la matière sous-saturée est présenté dans ce chapitre.

Pour modéliser la structure des étoiles à neutrons, à température nulle, seule l’énergie est requise. Les premiers travaux de modélisation de la croûte d’étoile à neutrons ont été effectués dans les années 70, avec les papiers de Baym *et al.* [Bay71a] et de Negele et Vautherin [Neg73]. Dans ces travaux, la maille élémentaire du réseau d’agrégat est décrite par la cellule sphérique de Wigner-Seitz, contenant un unique noyau, le gaz homogène

d'électrons ainsi que le gaz homogène de neutrons libres dans la croûte interne. L'étude de la matière d'étoile, à densité totale donnée, se réduit ainsi à l'étude de la cellule de Wigner-Seitz. La taille et l'asymétrie d'isospin du noyau ainsi que la densité du gaz de neutrons sont déterminés en minimisant l'énergie de la cellule de Wigner-Seitz, avec la condition d'être à l'équilibre  $\beta$ . Plus récemment, il a été montré que la superfluidité des neutrons ainsi que celle des protons modifient significativement l'état fondamental de la structure de la croûte interne [Bal05]. On sait également que la composition de la croûte externe est très sensible à la connaissance et à la précision des masses nucléaires (voir par exemple [Wol13]). Ainsi, les modèles récents utilisent les masses mesurées pour déterminer la composition de la croûte externe. Cependant, comme les données expérimentales ne sont pas disponibles jusqu'à la ligne de limite de stabilité en neutron, des modèles réalistes extrapolés sont toujours nécessaires.

L'équation d'état de la matière sous-saturée d'étoiles compactes à température finie a été tout d'abord étudiée en utilisant l'approximation de noyau seul, dans les années 70 [Lam78]. Cette approximation est basée sur l'hypothèse que, comme à température nulle, la matière est organisée selon un réseau de cellules de Wigner-Seitz, chacune d'entre elles contenant un unique noyau, immergé dans un gaz d'électrons, un gaz de nucléons, ainsi qu'un gaz d'alpha. Due aux états excités de nucléons dans le continuum, les gaz de neutrons et de protons sont toujours présents à température finie. Des noyaux légers peuvent également être présents à cause de la contribution finie d'entropie. Comme l'hélium 4 présente une énergie de liaison spécifiquement importante, il est souvent supposé que les particules alpha sont dominantes et représentent bien la contribution des noyaux légers. La configuration d'équilibre est déterminé par la minimisation de l'énergie libre des cellules de Wigner-Seitz. Mais contrairement à la température nulle, l'équilibre  $\beta$  n'est pas nécessairement vérifié. En effet, l'équilibre par rapport aux interactions faibles n'est souvent pas réalisée durant l'implosion, l'explosion et le refroidissement. Ainsi, la fraction de proton n'est pas contrainte et pour obtenir une équation d'état complète, il est nécessaire de minimiser l'énergie libre à densité baryonique, température et fraction de proton fixes. Il existe deux équations d'états basées sur l'approximation de noyau seul qui sont couramment utilisées dans les codes de simulation de supernova [Lat91; She98].

Les modèles basés sur l'approximation de noyau seul supposent que la matière à température finie peut être représenté par le noyau le plus probable donné par la minimisation de l'énergie libre d'une cellule de Wigner-Seitz. Cependant, pour déterminer l'équilibre, il convient de minimiser l'énergie libre totale du système, faite d'un mélange d'états, c'est-à-dire un mélange de cellules de Wigner-Seitz différentes. Les modèles prenant en compte une distribution complète des différents agrégats sont appelés modèles en équilibre statistique nucléaire. Le premier d'entre-eux a été élaboré au début des années 80 [Eid80]. Il est évident et bien connu que les phénomènes microscopiques

qui se déroulent lors dans les supernovæ à effondrement de cœur ainsi que lors du refroidissement et de la thermalisation des (proto-)étoiles à neutrons, tels que la diffusion de neutrinos et tous les taux de réactions régissant le transfert de chaleur, dépendent fortement des espèces nucléaires présentes dans le milieu stellaire [Lan04; Mar04; Cab06; Pag06a]. C'est également le cas pour la modélisation des problèmes hors d'équilibre comme l'accrétion et la nucléosynthèse r(p) des éléments lourds. En outre, la prise en compte de la distribution de la composition de la matière peut même affecter les quantités moyennes donnant l'équation d'état [Rad10; Buy13; Gul15], puisque la configuration la plus probable n'est pas nécessairement représentative de celle moyennée. Le fait que la configuration prédite par les modèles d'approximation de noyau seul ne corresponde, ni à la moyenne, ni au noyau le plus probable prévu par les modèles en équilibre statistique nucléaire [Sou09; Gul15], fournit une forte motivation pour considérer une distribution de noyaux.

Différentes équations d'état en équilibre statistique nucléaire sont actuellement en cours d'élaboration [Bli11; Hem10; Gul15]. Ils considèrent tous un mélange de noyaux (incluant les noyaux légers et les résonances), immergés dans un gaz de nucléons. L'énergie de Coulomb, incluant l'écrantage des électrons, est évaluée par l'approximation (sphérique) de Wigner-Seitz. De façon générale, la largeur des distributions de masse dans les modèles en équilibre statistique nucléaire peut devenir plus grand que 100 unités, indiquant des différences substantielles par rapport aux modèles d'approximation de noyau seul. Il a également été montré que, dans ces modèles statistiques, la présence de matière agrégée débute à des densités inférieures [Bli11]. De plus, la contribution des noyaux légers est très importante et est assez mal représentée par des alpha seulement [Hem10]. En revanche, les différents modèles en équilibre statistique nucléaire prédisent des compositions de la matière très différentes, ce qui est principalement du aux choix différents de prescriptions utilisées pour décrire l'énergie de l'état fondamental des noyaux [Buy13]. En particulier, les formules de masse conduisent à des distributions de noyaux lissées, alors qu'en utilisant des données expérimentales, des noyaux plus spécifiques sont favorisés, principalement liés à des fermetures de couches. Concernant l'équation d'état, de grandes différences entre les deux types de modèles, ainsi qu'entre les différents modèles en équilibre statistique nucléaire eux-mêmes, apparaissent à hautes températures  $T \gtrsim 5$  MeV et à hautes densités  $\rho_B \sim 0.1\rho_{sat}$  [Buy13]. Il a également été montré que les modifications de l'énergie de liaison du noyau, dues au gaz de nucléons et négligées dans la plupart des modèles en équilibre statistique nucléaire, sont importantes à basse température  $T \lesssim 2$  MeV et à hautes densités  $\rho_B \gtrsim 0.1\rho_{sat}$  [Buy13; Aym14].

Dans cette thèse, nous nous intéressons à l'obtention d'une équation d'état réaliste et unifiée pour la matière d'étoiles compactes. Nous cherchons donc un formalisme qui peut être appliqué à la fois aux densités sous-saturée et sur-saturée, en et hors équilibre

beta, et à toute valeur de température. En particulier, le traitement microscopique Hartree-Fock(Bogoliubov) de la cellule de Wigner-Seitz devrait émerger comme une limite naturelle  $T \rightarrow 0$  du modèle en équilibre statistique nucléaire. À cette fin, nous construisons un modèle en équilibre statistique nucléaire qui peut être considéré comme une superposition statistique de cellules de Wigner-Seitz. Dans chaque cellule, nous étudions les énergies nucléaires de l'agrégat en interaction avec un gaz de nucléons présent dans la matière sous-saturée. L'utilisation de la théorie du champ moyen pour la description à la fois des agrégats et du gaz de nucléons nous permet d'être consistant avec un traitement à densités supérieures à la saturation, non étudiées dans ce travail.

La thèse est divisée en trois parties. Dans la partie I, nous présentons le modèle en équilibre statistique nucléaire basé sur l'ensemble statistique grand canonique, et sur les interactions non relativistes de Skyrme. Les résultats à équilibre  $\beta$  sont présentés et l'importance des distributions des agrégats ainsi que celle d'un traitement réaliste pour l'énergétique sont discutées. Dans la partie II, nous étudions le comportement fonctionnel de l'énergie baryonique dans la cellule de Wigner-Seitz en utilisant l'approximation de Thomas-Fermi étendue. En particulier, l'énergie de surface de symétrie est discutée en détail, et on montre que son signe dépend de la prescription utilisée pour décomposer l'énergie totale en termes de volume et de surface. Les effets de milieu de volume et de surface sont étudiés, et leur dépendance en termes de taille et d'asymétrie de l'agrégat ainsi que de la densité et de l'asymétrie du gaz est étudiée. Un résultat préliminaire des effets de milieu de surface est présenté, en utilisant certaines approximations dans le cas de la matière en équilibre  $\beta$ . Dans la partie III, nous développons des approximations dans le but d'obtenir une expression analytique fiable de la formule de masse, directement reliée à la forme fonctionnelle et aux paramètres de l'interaction de Skyrme. Cette partie du travail n'est pas complètement achevée, et nous nous concentrons principalement sur des noyaux dans le vide. Cela nous permet d'analyser les différents composants de l'énergie de liaison du noyau, en termes de propriétés de volume et de surface, ainsi que des propriétés isovectorielles et isoscalaires. Les conclusions générales sont ensuite présentées.

À la fin de chaque partie, un bref résumé est rédigé en français.



Part I:

Finite temperature sub-saturation  
matter

# Part introduction

This part deals with sub-saturated matter of Supernovae (SN) and Proto-Neutron Stars (PNS) at finite temperature.

As already discussed in the general introduction, clusterized matter can be modelled by separately treating the nuclei and the free nucleons, as it has been done in [Bay71a] at zero temperature. An alternative formulation within the density functional theory is to follow an entirely microscopic approach, like [Neg73], which is in principle more appealing since it does not require to artificially distinguish the bound nucleons from the unbound ones, and naturally takes into account the whole interaction between the clusterized phase and the more dilute one. For this reason, and due to the improving accuracy and predictive power of mean-field energy density functionals, microscopic Hartree-Fock(-Bogoliubov) methods are preferentially employed for the computation of the neutron star EoS [Gri11; Pea12; Pas13].

Finite temperature mean-field calculations have been also largely developed [Ons08; For10]. However, because of their computational cost, these microscopic calculations at finite temperature are not adapted to the large scale conditions spanned during SN and PNS dynamics. Therefore, we believe that models with cluster degrees of freedom are still nowadays the most appealing to study sub-saturated matter at finite temperature, as it was done in the past in the seminal works [Lat91; She98]. The strongest limitation of these hybrid models is that they assume a unique configuration for each thermodynamic condition  $(T, \rho_B, Y_p)$ , against the very principle of temperature in statistical mechanics, which corresponds to a mixture of different microscopic states. These Single Nucleus Approximation (SNA) models are essentially meant to calculate the average properties of matter.

To improve the model, especially in order to obtain the matter composition of utmost importance for the determination of microscopic phenomena, Nuclear Statistical Equilibrium (NSE) approaches are developed. They allow to take into account a full distribution of nuclei mass and asymmetry. The main current drawback of these models is that the interaction between the clusters and the gas is either neglected or at best approximated with the so-called excluded volume effect: the clusters and the gas do

---

not overlap in space and the cluster binding energy is not modified by the surrounding nucleons medium.

Another general issue is the problem of consistency between the models of supersaturated matter, commonly based on mean-field approaches, and the ones of sub-saturated matter where clusters have to be taken into account. Indeed, an Equation of State of both regions is required in order to study the dynamics and macroscopic properties of core collapse supernova and (proto-)neutron stars. Matching non-consistent sub-saturated and supersaturated models leads to non-physical discontinuities at the matching region. As a consequence, the mass-radius relation of neutron stars present large uncertainties on the radius (the mass being mainly constrained by the core) [Pro15], and the dynamics of CCSN can be spuriously modified [Oer13].

In this part, we develop an analytical unified theoretical formalism to describe clustered matter at finite temperature, based on the NSE approach, which is consistent with a supersaturation density model. The part is organised as follows. In chapter I.1, we present the grand canonical partition function used in order to obtain the NSE, from which the matter composition as well as the average thermodynamic quantities naturally arise. In chapter I.2, we detail how we evaluate the ingredients of the free energy entering the statistical model, that is the ground state energy of the Wigner-Seitz cells, as well as the modelling of its excited states. More specifically, we develop the free energy of the nucleon gas, the ground states and the excited states of the nuclei, and we introduce the interactions between the clusters and the free nucleons and electrons, which can be seen as an external stellar medium modifying the cluster self-energy. In this model, the in-medium effects are consistently treated with the gas and clusters modelling, and no excluded volume approximation is assumed. Results relevant for proto-neutron stars, that is at  $\beta$ -equilibrium and low temperatures, are shown in chapter I.3.

# Chapter I.1

## Nuclear Statistical Equilibrium

In this chapter, we develop the Nuclear Statistical Equilibrium model. We briefly present in section I.1.1 the partition function of the grand canonical ensemble for a model of nuclear free particles and clusters adequate for the description of supernovae and proto-neutron stars matter at sub-saturation density. We focus on the nuclear part and show that the degrees of freedom are naturally the Wigner-Seitz cells [Gul15]. Section I.1.2 gives the physical thermodynamic quantities calculated from the partition function, which lead to the equation of state (EoS).

### I.1.1 Grand canonical partition function

In this section, we extend the concept of Wigner-Seitz (WS) cells at finite temperature. Then using the thermodynamic limit and the WS approximation, we calculate the (baryonic) grand canonical partition function of sub-saturation matter, that is where the average baryon density is below the nuclear saturation density for symmetric matter,  $\rho_{sat} \sim 0.16 \text{ fm}^{-3}$ .

#### I.1.1.a Statistical mechanics and stellar matter

Compact stars are in static gravitational equilibrium, therefore their structure is determined by hydrostatics laws such as the spherical relativistic Tolman-Oppenheimer-Volkoff (TOV) equations [Tol39; Opp39]. As presented in the introduction, the structure of supernovae (SN) and proto-neutron stars (PNS) varies with time: the stellar dynamics induce reactions and internal motion of matter through convection, conduction and radiation. Therefore, the number densities  $\vec{\rho} = \{\rho_i\}$  of the different species  $i$  existing in stellar matter, as well as the temperature  $T$  are not homogeneous in space at any time of stellar evolution. However, their typical profiles change macroscopically [Sum08; Mar06], meaning that one can consider matter at given total average baryonic  $\rho_B$ , leptonic  $\rho_L$

and charge  $\rho_C$  densities and at a given temperature, as infinite matter. To explain this statement, let us consider for illustration the case of a (proto-)neutron-star in hydrostatic equilibrium. On the one hand, the degrees of freedom, that is the components of compact stars matter, the so-called Wigner-Seitz cells, have a size of the order of  $10 - 100$  fm. On the other hand, a change of a thousandth on the baryon density  $\Delta\rho_B/\rho_B \sim 10^{-3}$  typically gives, in spherical symmetry, a change on the star radius of  $\Delta r \gtrsim 10^{10}$  fm [Dat95]. Thus, neglecting this change of density, we can consider the matter density as a constant in layers with a thickness of  $10^{10}$  fm, that is a thickness which contains at least one billion WS cells. This simple order of magnitude calculation justifies the approximation to consider stellar matter at a given density as infinite matter, and thus the use of thermodynamics. The same considerations on the temperature profile and its variation with time allow to apply the laws of thermal equilibrium. Therefore, to study compact stars matter, we can focus on matter at the thermodynamic limit, at given  $(\vec{\rho}, T)$ , which physically corresponds to a location in the star and at a time of its evolution. Furthermore, the typical time of strong interaction is such that the corresponding chemical equilibrium is always achieved during compact stars dynamics, except for the very fast phenomena of accretion or during nucleosynthesis where the baryon density is too low. Concerning weak interactions, matter can be at  $\beta$ -equilibrium or out, depending on the space at time of stellar evolution, as discussed in the introduction. Therefore we will consider the thermodynamics conditions given by  $(\rho_B, T)$  when  $\beta$ -equilibrium is established, or  $(\rho_B, \rho_p, T)$  out of  $\beta$ -equilibrium (with  $\rho_p$  the proton density).

At the thermodynamic limit, if there are only short range interactions, all the ensembles are equivalent. This means that thermodynamics is unique, and that the physical properties of a system at equilibrium do not depend on the statistical ensemble which is used to describe it. In the case of compact stars, the electromagnetic interactions should in principle break the previous theorem since it is a long range interaction. However, the screening between protons and electrons provides an effective electromagnetic short range interaction (see section I.1.1.b), thus we can choose any ensemble. In this study, we consider the grand canonical ensemble where the temperatures  $T$ , the volume  $V_{tot}$ , and the chemical potentials  $\vec{\mu} = \{\mu_i\}$  of the species  $i$  are the fixed quantities. This ensemble is not expensive from the computational point of view, unlike other ensembles such as the canonical one [Gul12; Gul15]. For this reason, a grand canonical formulation appears more appealing and has been used in the NSE models [Bot10; Rad10; Hem10]. Indeed, the grand canonical ensemble allows to easily solve the self-consistent problems induced by the presence of nucleon gas and clusters within charge neutrality.

For a system of  $n$  species at temperature  $T$  in a volume  $V_{tot}$ , the grand canonical partition function is defined by the sum over the microscopic states  $K$  composed of  $A_{i,tot}^{(K)}$

particles for each species  $i = 1, \dots, n$

$$\mathcal{Z}_{tot}(\beta, \vec{\mu}) = \sum_{\{K\}} e^{-\beta(E_{tot}^{(K)} - \sum_i \mu_i A_{i,tot}^{(K)})}, \quad (\text{I.1})$$

with  $\beta = T^{-1}$ , and where  $E_{tot}^{(K)}$  is the total energy associated to the microscopic state  $K$  and  $\{\mu_i\}$  the grand canonical constraints. In sub-saturation matter on which we focus in this study, there are little number of species in addition of photons which can exist: only neutrons and protons in the baryonic sector and only electrons and positrons as well as neutrinos and anti-neutrinos in the leptonic sector. Indeed, increasing the number of degrees of freedom (including strangeness for example), is energetically beneficial only beyond the saturation density [Gle82]. Since there is no interaction between photons, neutrinos and the other elements, the total energy  $E_{tot}^{(K)}$  is simply the sum of the photons energy  $E_\gamma^{(K)}$ , the neutrinos energy  $E_\nu^{(K)}$ , and the other particles energy  $E_{n,p,e}^{(K)}$ , that is baryons, electrons and positrons. Thus the partition function eq. (I.1) can be factorized as

$$\mathcal{Z}_{tot}(\beta, \vec{\mu}) = \mathcal{Z}_{n,p,e}(\beta, \mu_n, \mu_p, \mu_{e^-}, \mu_{e^+}) \mathcal{Z}_\nu(\beta, \mu_\nu, \mu_{\bar{\nu}}) \mathcal{Z}_\gamma(\beta, \mu_\gamma). \quad (\text{I.2})$$

This decorrelation ensures that all the physical quantities, that is energy, pressure, entropy are additive. Considering the temperature and density range spanned in compact stars, the photons can be considered as an ultra-relativistic Bose gas in thermal equilibrium with the other particles [Lat91], thus their pressure  $p_\gamma$ , energy  $\epsilon_\gamma$  and entropy  $s_\gamma$  densities are the black body ones, that is

$$p_\gamma = \frac{\pi^2 T^4}{45}, \quad (\text{I.3a})$$

$$\epsilon_\gamma = \frac{3p_\gamma}{\rho_B}, \quad (\text{I.3b})$$

$$s_\gamma = \frac{4p_\gamma}{\rho_B T}, \quad (\text{I.3c})$$

with  $\rho_B$  the baryon density, and where we have considered the natural units  $k_B = \hbar = c = 1$ . For the same reason, (anti-)neutrinos as well as electrons and positrons are modelled as a relativistic Fermi gas in particle-antiparticle pair equilibrium ( $\mu_\nu = -\mu_{\bar{\nu}}$  and  $\mu_{e^-} = -\mu_{e^+} = \mu_e$ ) and in thermal equilibrium with nuclear matter [Lat91; Bay71b]. Introducing the spin degeneracy of electrons (neutrinos)  $g_i = g_e = 2$  ( $g_i = g_\nu = 1$ ) and their rest mass  $m_i = m_e$  ( $m_i = m_\nu = 0$ ), the corresponding net particle densities (that is the density of particles minus the density of antiparticles), pressure, energy and entropy

densities are respectively

$$\rho_i = \frac{g_i}{6\pi^2} \left[ \mu_i^3 + \mu_i \left( \pi^2 T^2 - \frac{3}{2} m_i^2 \right) \right], \quad (\text{I.4a})$$

$$p_i = \frac{g_i}{24\pi^2} \left[ \mu_i^4 + \mu_i^2 (2\pi^2 T^2 - 3m_i^2) + \pi^2 T^2 \left( \frac{7}{15} \pi^2 T^2 - \frac{1}{2} m_i^2 \right) \right], \quad (\text{I.4b})$$

$$\epsilon_i = \frac{g_i}{8\pi^2 \rho_B} \left[ \mu_i^4 + \mu_i^2 (2\pi^2 T^2 - m_i^2) + \pi^2 T^2 \left( \frac{7}{15} \pi^2 T^2 - \frac{1}{2} m_i^2 \right) \right], \quad (\text{I.4c})$$

$$s_i = \frac{g_i T}{6\rho_B} \left[ \mu_i^2 + \left( \frac{7}{15} \pi^2 T^2 - \frac{1}{2} m_i^2 \right) \right], \quad (\text{I.4d})$$

where  $i = e$  ( $i = \nu$ ) stands for electrons (neutrinos). When photons or neutrinos are present in the system, we can take into account them separately from the other components in adding eqs (I.3) and (I.4) to the corresponding baryon and electron quantities. When neutrinos are trapped during the CCSN (see general introduction), the chemical potential  $\mu_\nu$  is either determined by the dynamics, or by the  $\beta$ -equilibrium condition, whereas it is zero if the system is in the neutrino-free regime.

Thus we can focus on the partition function  $\mathcal{Z}_{n,p,e}$  of eq. (I.2), which stands for neutrons, protons and the net difference between electrons and positrons. In what follows, this net difference will be referred as electrons only. Because of Coulomb interaction, the baryons and electrons are not independent and the partition function cannot be, in principle, factorized. However, because of charge neutrality, the electron density is constrained to  $\rho_e = \rho_p = Z_{tot}^{(K)}/V_{tot}$ , with  $Z_{tot}^{(K)}$  the total protons number of the system. As a consequence, if we put all the Coulomb energy into the baryon energy  $E_b^{(K)}$ , this latter will depend on the densities of baryonic species ( $n, p$ ) only, and a factorization of the partition sums will hold. The energy  $E_{n,p,e}^{(K)}$  entering  $\mathcal{Z}_{n,p,e}$  thus reads  $E_{n,p,e}^{(K)} = E_b^{(K)} + E_e^{(K)} + E_{coul}^{(K)}$ , where  $E_e^{(K)}$  is the energy which gives the partition function associated to the quantities expressed in eqs. (I.4). This procedure allows to factorize  $\mathcal{Z}_{n,p,e}$  into a charge neutral electron partition function and a baryon partition function which holds both the nuclear and Coulomb interactions. The baryon grand canonical partition function thus reads

$$\mathcal{Z}_b(\beta, \mu_n, \mu_p) = \sum_{\{K\}} e^{-\beta(E_b^{(K)} + E_{coul}^{(K)} - N_{tot}^{(K)} \mu_n - Z_{tot}^{(K)} \mu_p)}, \quad (\text{I.5})$$

with  $N^{(K)}$  the total neutrons number of the system. In this equation, the Coulomb energy  $E_{coul}^{(K)}$  stands for electromagnetic interactions of electron-electron and electron-proton. Thus it depends on  $Z_{tot}^{(K)}$  as well as on the electron density  $\rho_e$ . Let us notice that we can deduce it from the electron chemical potential in inverting eq. (I.4a). We can see that though the quantities can be calculated separately, the interaction between electrons and protons implies a relation between their chemical potentials, and thus

reduce number of the grand canonical ensemble fixed variables.

### I.1.1.b Wigner-Seitz cells

We now detail how in compact stars, Wigner-Seitz cells can be introduced as the natural degrees of freedom. This means that each microscopic state  $K$  entering in the baryon partition function defined by eq. (I.5) can be expressed as a specific configuration of WS cells.

In neutron stars crust, that is at zero temperature, the system composition and characteristics are determined by minimizing its energy. It is clear that baryons are more bound if they are linked together to form a nucleus instead of a free Fermi gas. For this reason, there are no free nucleons at densities below drip lines. Like a crystal, matter is then organised as a network of nuclei immersed in an electron Fermi gas. Zero temperature implies that there is only one species of nuclei, corresponding to the ground state at the density considered. Similarly, in the inner crust where  $\beta$ -equilibrium implies that matter is so neutron rich that we are above the neutron drip line, matter is a lattice of one nucleus, surrounding by free electrons and free neutrons [Bay71b; Neg73]. Though the unbound neutrons would be evaporated in a lab, they remain in the star due to gravitational pressure. As far as the geometry is concerned, the energy is minimized for a body-centered cubic lattice [Wig34], and the global charge neutrality implies that each primitive cell, the so-called Wigner-Seitz cell, is also neutral [Wig34; Col60]. Thus, the energy of a system made of  $n$  cells is simply  $E_{tot} = nE_{WS}$ , and minimizing the total energy amounts to minimize the Wigner-Seitz cell energy  $E_{WS}$ .

At finite temperature, relevant for supernovae and proto-neutron stars crust, a natural extension consists in minimizing the WS cell free energy  $F_{WS}$ , in assuming that, like at zero temperature, matter is a lattice of one heavy nuclear species [Lat91; She98]. This Single Nucleus Approximation (SNA) is schematic and can be improved in considering a full distribution of different nuclei. Indeed, the detailed matter composition may affect the Equation of State (EoS), even if made of average quantities [Rad10; Gul15], as well as the nucleosynthesis of heavy elements [Lan04], the electron capture rates, the neutrino scattering through the core after bounce [Mar04; Cab06] and the cooling rate of neutron stars [Pag06a]. The Nuclear Statistical Equilibrium (NSE) models [Bot10; Hem10; Bli11; Rad14] are based on the Fisher conjecture that strong interactions in dilute matter is entirely exhausted by clusterization [Fis67]. The baryonic matter is then considered as a distribution of nuclei, the so-called clusters, in thermal equilibrium, and in chemical equilibrium with a free nucleon gas. At finite temperature, a gas of both neutrons and protons is systematically present, even at densities below drip lines because of the continuum of excited states of nuclei which can be reached at finite temperature, which would again imply nucleon evaporation if the system was not bound by gravity.

In the NSE models, though matter is not geometrically organized in a lattice structure, the WS cell concept can be extended as the smallest volume where the net electric charge is zero. We assume that, as in the case of a lattice, there is only one cluster in the WS cell, which is expected to be verified for low enough densities. In the limit where there is one species of nucleus in the system, this definition matches with the lattice one. However, even in that case, light nuclei are expected to be present. In SNA models [Lat91; She98] a representative alpha gas is considered. A more recent and sophisticated study [Typ10] has shown that alpha particles are formed at the nucleus surface of WS cells. In [Ava12], other light particles ( $^2\text{H}$ ,  $^3\text{H}$  and  $^3\text{He}$ ) have been separately added in the Wigner-Seitz cell. The advantage of the NSE approach is that considering light nuclear species is natural and they are all taken into account without special effort, though the Coulomb energy between the nuclei is disregarded and the nuclear interaction with the surrounding medium might be severely approximated.

Within each Wigner-Seitz cell, we make the standard approximation that the gas is homogeneous. This approximation is inspired by the numerical results of microscopic calculations [Bal05; Pea12; Pas13; Gri14]. Moreover, these works have shown that the polarisation of the nuclear gas is small such that it can be accounted in cluster models as an in-medium modification of the surface tension [Bay71a; Lat85], which are introduced in chapter I.2 and studied in details in part II. Concerning the electron gas, self-consistent calculations have shown that, because of the high electron incompressibility, the homogeneous approximation is excellent for all densities [Mar05]. In agreement with the general fact that finite temperature corresponds to a mixture of states, NSE models can be seen as a mixture of clusters of different sizes and asymmetries embedded in a homogeneous electron gas and a homogeneous nucleon gas, that is a mixture of WS cells with the same gases. This amounts to consider that the electrons and the unbound nucleons of the WS cells are free particles in the whole medium, consequently forming homogeneous gases. Besides, since the cells are electrically neutral, they do not interact, and so matter can be modelled as an ideal gas of WS cells. Wigner-Seitz cells are thus natural degrees of freedom of the system.

The chemical equilibrium between the nucleon gas and the clusters mentioned above, is a result of the strong interaction which reorganises matter much faster than does the dynamics of supernovae and proto-neutron stars. Within the SNA, the equilibrium simply means that, in each WS cell since they are the same, the gas chemical potentials of neutrons and of protons are equal to the cluster ones. However, in the NSE models, the equilibrium must be globally calculated, taking into account of all the different clusters. As a result, there is no chemical equilibrium in each WS cell, and the total numbers of neutrons  $N_{WS}$  and protons  $Z_{WS}$  in each cell are different, whereas the gas densities of protons and neutrons ( $\rho_{g,p}, \rho_{g,n}$ ) are the same.

For this reason, it is convenient to define the cluster in the WS cell with a volume  $V_{WS}$  as the bound nucleons, corresponding to the extra particles with respect to the particles belonging to the nucleon gas, with neutron  $N_g = \rho_{g,n}V_{WS}$  and proton  $Z_g = \rho_{g,p}V_{WS}$  numbers [Pap13]. These extra neutrons  $N_e$  and protons  $Z_e$  of the so-called e-cluster are then

$$\begin{aligned} N_e &= N_{WS} - \rho_{g,n}V_{WS}, \\ Z_e &= Z_{WS} - \rho_{g,p}V_{WS}, \end{aligned} \quad (\text{I.6})$$

where the volume of the WS cell is fixed by the charge neutrality condition:

$$V_{WS} = \frac{Z_e}{\rho_p - \rho_{g,p}}. \quad (\text{I.7})$$

In this equation,  $\rho_p = Z_{tot}/V_{tot}$  is the average proton density of the global (infinite) system. Another definition of the cluster, called the r-cluster, is possible by considering the distribution of nucleons in space [Pap13]: the r-clusters correspond to the more dense central part of the WS cell. its particle numbers ( $N, Z$ ) are related to the e-cluster ones by the relations

$$\begin{aligned} N_e &= N \left( 1 - \frac{\rho_{g,n}}{\rho_{sat,n}(\delta)} \right), \\ Z_e &= Z \left( 1 - \frac{\rho_{g,p}}{\rho_{sat,p}(\delta)} \right), \end{aligned} \quad (\text{I.8})$$

where  $\rho_{sat,n(p)}(\delta)$  is the neutron (proton) saturation density of nuclear matter at the bulk isospin asymmetry  $\delta$ . The study of this bulk isospin asymmetry  $\delta = 1 - 2\rho_{sat,p}/\rho_{sat}$ , corresponding to the nuclear (asymmetric) matter associated to a WS cell configuration, is detailed in part II, and determined by eqs. (II.62) and (II.63). Let us only anticipate that the bulk asymmetry  $\delta$  of a nucleus in vacuum differs from the nucleus global asymmetry  $I = 1 - 2Z/A$  due to neutron skin and Coulomb effects. Concerning nuclei immersed in a gas, the presence of unbound nucleons with an asymmetry  $\delta_g = 1 - 2\rho_{g,p}/\rho_g$  different from the cluster one also modifies the bulk asymmetry  $\delta$ .

Let us notice that without gas, the two definitions given by eqs (I.6) and (I.8) are equivalent. It is also important to observe that the definitions (I.8) simply ensure particle number conservation and do not imply any specific density profile in the Wigner-Seitz cell. The shape of the density profile will however be essential to determine the nuclear energetics, as we will see in detail in part II. In what follows, we will see that we need the two definitions: the e-clusters have to be considered in the statistical model to avoid double counting of the single-particle states whereas, because of the non-linearity of the

nuclear energy density with the density, the r-clusters are required to properly have the energetics.

### I.1.1.c The partition function

Using the Wigner-Seitz cells as degrees of freedom, a microscopic state  $K$  in the volume  $V_{tot} \rightarrow \infty$  is characterized by the  $\mathcal{N}^{(K)} \rightarrow \infty$  WS cells present in the system. By introducing an index  $k$  for each cell, the total numbers of particles involved in the partition function eq. (I.5) are

$$\begin{aligned} N_{tot}^{(K)} &= \sum_{k=1}^{\mathcal{N}^{(K)}} \left( N_e^{(k)} + \rho_{g,n} V_{WS}^{(k)} \right) = \sum_{k=1}^{\mathcal{N}^{(K)}} N_e^{(k)} + \rho_{g,n} V_{tot}, \\ Z_{tot}^{(K)} &= \sum_{k=1}^{\mathcal{N}^{(K)}} \left( Z_e^{(k)} + \rho_{g,p} V_{WS}^{(k)} \right) = \sum_{k=1}^{\mathcal{N}^{(K)}} Z_e^{(k)} + \rho_{g,p} V_{tot}. \end{aligned} \quad (\text{I.9})$$

In the grand canonical ensemble, these particle numbers are free to vary, that is neither the particle numbers of the different cells  $(N_e^{(k)}, Z_e^{(k)})$  nor the total number of WS cells  $\mathcal{N}^{(K)}$  are fixed. On the contrary, the baryon chemical equilibrium implies that the homogeneous gas densities  $\rho_{g,q}$  ( $q = n, p$ ) are fixed by the external chemical potentials  $\mu_q$ ; these densities are therefore the same in all the cells  $k$  and do not depend on the configuration  $K = \{k\}$ . Therefore, the gas quantities can be put out of the sum over the cell  $k$  by using the relation  $V_{tot} = \sum_{k=1}^{\mathcal{N}^{(K)}} V_{WS}^{(k)}$ , as it has been done to obtain the second equalities of eqs. (I.9)

Concerning the energy terms of the partition function eq. (I.5), since the WS cells do not interact with each other, it can be expressed as the sum of the nuclear and Coulomb energy due to electrons of each WS cell  $E_{WS}^{(k)} = E_b^{(k)} + E_{coul}^{(k)}$ , such that

$$E_b^{(K)} + E_{coul}^{(K)} = \sum_{k=1}^{\mathcal{N}^{(K)}} E_{WS}^{(k)} = \sum_{k=1}^{\mathcal{N}^{(K)}} E_b^{(k)} + E_{coul}^{(k)}. \quad (\text{I.10})$$

In each WS cell  $k$ , the nuclear energy of the homogeneous nucleon gas  $E_{gas}^{(k)}$  can be highlighted in introducing the in-medium cluster energy  $E_{cl,m}^{(k)}$ , which stands for the in-vacuum nucleus energy  $E_{cl}^{(k)}$  and its nuclear interaction with the gas  $\delta E^{(k)}$ , such that

$$E_b^{(k)} = E_{cl,m}^{(k)} + E_{gas}^{(k)} = E_{cl}^{(k)} + \delta E^{(k)} + E_{gas}^{(k)}. \quad (\text{I.11})$$

By introducing the gas energy of the whole system  $E_{gas}^{(K)} = \sum_{k=1}^{\mathcal{N}^{(K)}} E_{gas}^{(k)}$  of the configuration  $K$ , and using the expressions (I.9), (I.10) and (I.11) into the baryon partition

function eq. (I.5), we obtain

$$\begin{aligned} \mathcal{Z}_b(\beta, \mu_p, \mu_n) &= \sum_{\{K\}} \exp \left[ -\beta \left( E_{gas}^{(K)} - \rho_{g,n} V_{tot} \mu_n - \rho_{g,p} V_{tot} \mu_p \right) \right] \cdot \\ &\quad \cdot \prod_{k=1}^{\mathcal{N}^{(K)}} \exp \left[ -\beta \left( E_{cl,tot}^{(k)} - N_e^{(k)} \mu_n - Z_e^{(k)} \mu_p \right) \right], \end{aligned} \quad (\text{I.12})$$

with  $E_{cl,tot}^{(k)} = E_{cl}^{(k)} + E_{coul}^{(k)} + \delta E^{(k)}$  the energy corresponding to the cluster modified by the stellar medium. From eq. (I.12), we can see that the gas and the clusters are decorrelated. Indeed, a configuration  $K$  is a specific state of  $\mathcal{N}^{(K)}$  clusters on the one hand, and of gas energy  $E_{gas}^{(K)}$  of the other hand, that is

$$\sum_{\{K\}} = \sum_{\{E_{gas}^{(K)}\}} \sum_{\{\mathcal{N}^{(K)}\}}. \quad (\text{I.13})$$

The separated sum over the gas energy leads to the definition of the gas partition function  $\mathcal{Z}_{gas}(\beta, \mu_p, \mu_n)$  in introducing the average gas energy at given temperature and densities  $E_{gas} = \sum_{\{E_{gas}^{(K)}\}} E_{gas}^{(K)} e^{-\beta E_{gas}^{(K)}} / \sum_{\{E_{gas}^{(K)}\}} e^{-\beta E_{gas}^{(K)}}$  and its associated entropy  $S_{gas}(E_{gas})$  such that

$$\begin{aligned} \mathcal{Z}_{gas}(\beta, \mu_p, \mu_n) &= \sum_{\{E_{gas}^{(K)}\}} \exp \left[ -\beta \left( E_{gas}^{(K)} - \rho_{g,n} V_{tot} \mu_n - \rho_{g,p} V_{tot} \mu_p \right) \right] \\ &= \exp \left[ -\beta V_{tot} \left( \mathcal{H}_{gas} - T s_{gas}(\mathcal{H}_{gas}) - \rho_{g,n} \mu_n - \rho_{g,p} \mu_p \right) \right], \end{aligned} \quad (\text{I.14})$$

with  $\mathcal{H}_{gas} = E_{gas}/V_{tot}$  the average gas energy density and  $s_{gas}(\mathcal{H}_{gas}) = S_{gas}(E_{gas})/V_{tot}$  its associated entropy. The expressions of the gas energy and entropy densities are developed in section I.2.1. The baryon partition function is then factorized as

$$\mathcal{Z}_b(\beta, \mu_p, \mu_n) = \mathcal{Z}_{gas}(\beta, \mu_p, \mu_n) \mathcal{Z}_{cl}(\beta, \mu_p, \mu_n), \quad (\text{I.15})$$

where  $\mathcal{Z}_{cl}(\beta, \mu_p, \mu_n)$  is the partition function of the clusters

$$\mathcal{Z}_{cl}(\beta, \mu_p, \mu_n) = \sum_{\{\mathcal{N}\}} \prod_{k=1}^{\mathcal{N}} \exp \left[ -\beta \left( E_{cl,tot}^{(k)} - N_e^{(k)} \mu_n - Z_e^{(k)} \mu_p \right) \right]. \quad (\text{I.16})$$

Since we have put the nuclear interaction between the cluster and the gas into the cluster energy, the so-called cluster partition function eq. (I.16) stands for the statistical function of the clusters modified by the stellar medium. In what follows, we show how we can express this partition function as a factorization of independent single partition

functions of Wigner-Seitz cells. Since the gas configurations do not enter the cluster partition function, each  $k = 1, \dots, \mathcal{N}^{(K)}$  WS cell can be associated to a well defined type  $i$  characterized by the cluster particle numbers  $i = (N_e^{(i)}, Z_e^{(i)})$  only.

Let us first consider the simple case where the  $n_i^{(\mathcal{N})}$  WS cells of a type  $i$  are identical. This amounts to disregard the internal structure of the clusters, corresponding to spin, momentum and excited states which can be different in the different cells of the same type  $i$ . In this simplified model, each configuration of  $\{\mathcal{N}\}$  is only determined by the numbers  $\{n_i^{(\mathcal{N})}\}$  of  $i$ -types cells:  $\sum_{\{\mathcal{N}\}} = \sum_{\{n_i\}}$ . In that case, equation (I.16) is similar to the standard grand canonical description of independent and identical particles occupying single-particle states  $i$ . The WS cells act as the particles, and the different single-particle states correspond to the different WS cell types  $i$ , with the associated energy  $E_{cl,tot}^{(i)}$ , with the occupation state number  $n_i^{(\mathcal{N})}$ . In gathering the WS cells  $\{k\}$  of a same type  $i$  in eq. (I.16), the grand canonical partition function of identical WS cells  $i$  reads

$$\begin{aligned} \mathcal{Z}_{cl}^{id}(\beta, \mu_p, \mu_n) &= \sum_{\{n_i\}} \prod_{k_1=1}^{n_1} \prod_{k_2=1}^{n_2} \dots \prod_{k_i=1}^{n_i} \dots e^{-\beta(E_{cl,tot}^{(k_1)} - N_e^{(k_1)} \mu_n - Z_e^{(k_1)} \mu_p)} \\ &\quad e^{-\beta(E_{cl,tot}^{(k_2)} - N_e^{(k_2)} \mu_n - Z_e^{(k_2)} \mu_p)} \dots e^{-\beta(E_{cl,tot}^{(k_i)} - N_e^{(k_i)} \mu_n - Z_e^{(k_i)} \mu_p)} \dots \\ &= \sum_{\{n_i\}} \exp \left[ -\beta \sum_i n_i \left( E_{cl,tot}^{(i)} - N_e^{(i)} \mu_n - Z_e^{(i)} \mu_p \right) \right]. \end{aligned} \quad (\text{I.17})$$

Since the total numbers  $\mathcal{N} = \sum_i n_i^{(\mathcal{N})}$  can freely vary, the sums over the state occupations  $\{n_i\}$  are independent:  $\sum_{\{n_i\}} = \sum_{n_1} \sum_{n_2} \dots \sum_{n_i} \dots$ . Then, observing that  $n_i$  only appears in the  $i$ -th term of eq. (I.17), we recover the well known factorization of the total grand canonical partition into partition functions of single states  $\mathcal{Z}_{cl}^{id,(i)}(\beta, \mu_p, \mu_n)$ :

$$\mathcal{Z}_{cl}^{id}(\beta, \mu_p, \mu_n) = \prod_i \mathcal{Z}_{cl}^{id,(i)}(\beta, \mu_p, \mu_n), \quad (\text{I.18})$$

with

$$\mathcal{Z}_{cl}^{id,(i)}(\beta, \mu_p, \mu_n) = \sum_n \exp \left[ -\beta n \left( E_{cl,tot}^{(i)} - N_e^{(i)} \mu_n - Z_e^{(i)} \mu_p \right) \right]. \quad (\text{I.19})$$

Let us now turn to our system which is more sophisticated. Indeed, the Wigner-Seitz cells of a type  $i$ , though characterized by the same cluster species  $(N_e^{(i)}, Z_e^{(i)})$  are not identical, because of their internal degrees of freedom which are spin, center-of-mass momentum and energy state (ground state or excited state). In what follows, we will index them by the general notation  $j(i)$ . Let us notice that the cluster energy now depends on  $j(i)$ . As in the previous simpler case, we can consider that a configuration of  $\{\mathcal{N}\}$  is given by the  $\{n_i^{(\mathcal{N})}\}$  and gather the WS cells  $\{k\}$  of a same type  $i$ , thus the

sum  $\sum_{\{\mathcal{N}\}} \prod_{k=1}^{\mathcal{N}}$  of eq. (I.16) leads to the same sum  $\sum_{\{n_i\}} \prod_{k_1=1}^{n_1} \prod_{k_2=1}^{n_2} \cdots \prod_{k_i=1}^{n_i} \cdots$  as previously. However, a state  $i$  is now given by different states  $j(i)$ , which means that, in eq. (I.16), we have to consider

$$\sum_{\{n_i\}} \prod_{k_1=1}^{n_1} \prod_{k_2=1}^{n_2} \cdots \prod_{k_i=1}^{n_i} \cdots \sum_{j(k_1)} \sum_{j(k_2)} \cdots \sum_{j(k_i)} \cdots e^{-\beta(E_{cl,tot}^{(j(k_1))} - N_e^{(k_1)} \mu_n - Z_e^{(k_1)} \mu_p)} \\ e^{-\beta(E_{cl,tot}^{(j(k_2))} - N_e^{(k_2)} \mu_n - Z_e^{(k_2)} \mu_p)} \cdots e^{-\beta(E_{cl,tot}^{(j(k_i))} - N_e^{(k_i)} \mu_n - Z_e^{(k_i)} \mu_p)} \cdots,$$

In this expression, we can see that the accessible internal states  $j(i)$  are independently taken into account for each WS cell  $k_i$ . This means that for each state  $i$ , the degrees of degeneracy  $j(i)$  of the  $n_i$  WS cells is counted  $n_i!$  times. Therefore, to obtain the correct counting, we have to divide the partition sum by the number of cell permutations of the states  $i$ , that is  $n_i!$ . Then, the cluster partition function eq. (I.16) reads

$$\mathcal{Z}_{cl}(\beta, \mu_p, \mu_n) = \prod_i \sum_n \frac{1}{n!} \left( \sum_{j(i)} \exp \left[ -\beta \left( E_{cl,tot}^{(j(i))} - N_e^{(i)} \mu_n - Z_e^{(i)} \mu_p \right) \right] \right)^n, \quad (\text{I.20})$$

where we can recognise an exponential into its series form, leading to

$$\ln \mathcal{Z}_{cl}(\beta, \mu_p, \mu_n) = \sum_i \ln \mathcal{Z}_{cl}^{(i)}(\beta, \mu_p, \mu_n), \quad (\text{I.21})$$

with

$$\ln \mathcal{Z}_{cl}^{(i)}(\beta, \mu_p, \mu_n) = \sum_{j(i)} e^{-\beta(E_{cl,tot}^{(j(i))} - N_e^{(i)} \mu_n - Z_e^{(i)} \mu_p)} \quad (\text{I.22})$$

the partition function of the single WS cell  $i$ .

In eqs. (I.18) and eqs. (I.21), we have shown that the grand canonical partition functions in both cases, namely when considering identical WS cells  $\mathcal{Z}_{cl}^{id}$ , and when taking into account the internal states  $\mathcal{Z}_{cl}$ , can be factorized into independent single-cell or single-cluster partition functions. Let us notice that this factorization is due to the hypothesis of non-interaction of the WS cells. We also remark that the fact that the total system is divided in non-interacting subsystems ensures statistical ensemble equivalence [Hov49; Yan52].

However, the single-cell partition functions eqs. (I.19) and (I.22) exhibit two very different behaviors. Indeed, the single-cell partition function of identical WS cells  $\mathcal{Z}_{cl}^{id,(i)}$  is the sum of the Boltzmann factors of different states, whereas taking into account the internal degrees of freedom of the WS cells, it is the logarithm of the single-cell partition function  $\mathcal{Z}_{cl}^{(i)}$  which is the sum of the Boltzmann factors. This comes from the fact that

in this latter case,  $\mathcal{Z}_{cl}^{(i)}$  is a mixture of different states  $j(i)$ , and therefore can be in turn factorized as a product of single partition functions  $\mathcal{Z}_{cl}^{id,j(i)}$ , apart from the factors  $n!$  which prevent double counting of the different indistinguishable states.

In our system, the internal degrees of freedom  $j(i)$  are given by the cluster center-of-mass momentum  $\mathbf{p}^{j(i)}$  and the internal energy  $E^{*,j(i)}$  of the in-vacuum nucleus as well as the correction  $\delta E^{*,j(i)}$  due to the interaction with the gas. Let us notice that considering cluster center-of-mass momentum is correct for temperatures above the solid-gas transition. At lower temperatures where the system is a lattice and which we will not study, one should replace these translational degrees of freedom by vibrational ones. The energy of a cluster  $i$  in the specific state  $j(i)$  is thus:

$$E_{cl,tot}^{(j(i))} = E_{vac}^{(i)} + mA_e^{(i)} + \frac{(\mathbf{p}^{j(i)})^2}{2mA_e^{(i)}} + E^{*,j(i)} + E_{coul}^{(i)} + \delta E_{GS}^{(i)} + \delta E^{*,j(i)}, \quad (\text{I.23})$$

with  $A_e^{(i)} = N_e^{(i)} + Z_e^{(i)}$  the mass of the e-cluster,  $m$  the average mass of a nucleon,  $E_{vac}^{(i)}$  the ground state binding energy of the cluster  $i$  in vacuum,  $\delta E_{GS}^{(i)}$  the ground state energy of the in-medium interactions between the cluster and the nucleon gas. Consequently, the sum over the internal states in eq. (I.22)  $\sum_{j(i)} \exp[-\beta E_{cl,tot}^{(j(i))}]$  turns into two independent sums

$$\sum_{\mathbf{p}^{j(i)}} \exp\left[-\beta \frac{(\mathbf{p}^{j(i)})^2}{2mA_e^{(i)}}\right] \sum_{E^{*,j(i)}} \exp[-\beta E^{*,j(i)}] \sum_{\delta E^{*,j(i)}} \exp[-\beta \delta E^{*,j(i)}].$$

The cluster center of mass motion is a plane wave over the whole volume  $V_{tot}$ . The sum  $\sum_{\mathbf{p}^{j(i)}}$  is thus given by the plane wave density of states  $V_{tot}/(2\pi)^3 \int d\mathbf{p}$ , and the Gaussian integral reads

$$\sum_{\mathbf{p}^{j(i)}} \exp\left[-\beta \frac{(\mathbf{p}^{j(i)})^2}{2mA_e^{(i)}}\right] = \left(\frac{mA_e^{(i)}}{2\pi\beta}\right)^{3/2} V_{tot}. \quad (\text{I.24})$$

We can notice that the available volume for the center of mass is the whole volume, and there is no excluded volume effect.

Concerning the cluster energy degeneracy, the specific cases  $E^{*,j(i)} = 0$  denotes the cluster ground state and leads to the spin degeneracy  $(2J_{GS}^{(i)} + 1)$ . The sum over the cluster states is thus

$$g_\beta^{(i)} = \sum_{E^{*,j(i)}} \exp[-\beta E^{*,j(i)}] = (2J_{GS}^{(i)} + 1) + g_\beta^{*,(i)}, \quad (\text{I.25})$$

where we have defined the temperature dependent degeneracy factor of excited states

$$g_{\beta}^{*,(i)} = \sum_{E^{*,j(i)} \neq 0} \exp \left[ -\beta E^{*,j(i)} \right], \quad (\text{I.26})$$

which stands for the occupied states Boltzmann factor number due to excitations at finite temperature. The models used in the present work, in order to obtain explicit expressions of the different cluster quantities introduced above, are detailed in section I.2.2.

Similarly, the sum over  $\delta E^{*,j(i)}$  gives a degeneracy factor which can be put into an entropy term in defining the average energy  $\delta E^{(i)}$  due to the interaction between the gas and the cluster  $i$ :

$$\sum_{\delta E^{*,j(i)}} \exp \left[ -\beta \left( \delta E_{GS}^{(i)} + \delta E^{*,j(i)} \right) \right] = \exp^{-\beta \left[ \delta E^{(i)} - TS(\delta E^{(i)}) \right]}. \quad (\text{I.27})$$

The expressions of these interactions components are introduced in section I.2.3 and the energy  $\delta E^{(i)}$  at zero temperature is investigated in part II.

To summarize, at the thermodynamic limit, the baryonic partition function per unit volume  $\ln z_b = \lim_{V_{tot} \rightarrow \infty} \ln \mathcal{Z}_b / V_{tot}$  reads, using eqs. (I.15) and (I.21)

$$\ln z_b(\beta, \mu_p, \mu_n) = \ln z_{gas}(\beta, \mu_p, \mu_n) + \sum_{N,Z} \ln z_{cl}^{NZ}(\beta, \mu_p, \mu_n), \quad (\text{I.28})$$

where we have used the characterization of the WS cell  $i$  by its particle numbers  $N^{(i)}$  and  $Z^{(i)}$ , such that  $\sum_i = \sum_{N,Z}$ . Let us notice that the relations between the e-clusters and r-clusters, eqs. (I.8), show that, for a given nucleon gas, we can equivalently characterize a WS cell by the bound particles ( $N_e^{(i)}, Z_e^{(i)}$ ) or by the r-cluster particles ( $N^{(i)}, Z^{(i)}$ ). The nuclear matter partition function per unit volume entering eq. (I.28) is, according to eq. (I.14),

$$\ln z_{gas}(\beta, \mu_p, \mu_n) = -\beta \mathcal{H}_{gas} + s_{gas}(\mathcal{H}_{gas}) + \beta \rho_{g,n} \mu_n + \beta \rho_{g,p} \mu_p, \quad (\text{I.29})$$

and the single-cluster partition function per unit volume reads, with eqs. (I.22)-(I.25),

$$\begin{aligned} \ln z_{cl}^{NZ}(\beta, \mu_p, \mu_n) &= \lim_{V_{tot} \rightarrow \infty} \frac{1}{V_{tot}} \sum_{j(N,Z)} e^{-\beta (E_{cl,tot}^{(j(N,Z))} - N_e \mu_n - Z_e \mu_p)} \\ &= \left( \frac{mA_e}{2\pi\beta} \right)^{3/2} \left[ (2J_{GS}(N, Z) + 1) + g_{\beta}^*(N, Z) \right] \cdot \\ &\quad \cdot e^{-\beta (E_{vac}(N,Z) + E_{cout}(N,Z,\rho_e) + \delta F(N,Z,\rho_{g,n},\rho_{g,p}) - N_e \tilde{\mu}_n - Z_e \tilde{\mu}_p)}, \end{aligned} \quad (\text{I.30})$$

where we have defined the auxiliary chemical potentials  $\tilde{\mu}_q = \mu_q - m$  which exclude

the rest mass contribution (recall that we use  $c = 1$ ), and the average free energy  $\delta F = \delta E - TS(\delta E)$  of the cluster  $(N, Z)$ .

## I.1.2 Thermodynamic quantities

In this section, we show that from the baryonic grand canonical chemical potential eqs. (I.28)-(I.30), we can calculate the stellar matter composition, as well as the associated average physical quantities which, summed to the other components eq. (I.2), establish the so-called Equation of State.

In the grand canonical ensemble at the thermodynamic limit, the average nucleon densities  $\rho_{q=n,p}$  are

$$\rho_n = \frac{\partial \ln z(\beta, \mu_p, \mu_n)}{\partial (\beta \mu_n)} = \rho_{g,n} + \rho_{cl,n} \quad (\text{I.31})$$

$$\rho_p = \frac{\partial \ln z(\beta, \mu_p, \mu_n)}{\partial (\beta \mu_p)} = \rho_{g,p} + \rho_{cl,p}, \quad (\text{I.32})$$

where the cluster densities are defined as

$$\rho_{cl,n} = \sum_{N,Z} N_e \ln z_{cl}^{NZ}(\beta, \mu_p, \mu_n), \quad (\text{I.33})$$

$$\rho_{cl,p} = \sum_{N,Z} Z_e \ln z_{cl}^{NZ}(\beta, \mu_p, \mu_n). \quad (\text{I.34})$$

Let us notice that because of the Coulomb interaction, the energy  $E_{coul}$  depends on the electron density  $\rho_e = \rho_p$ , implying that the evaluation of the proton density is required to calculate the single-cluster partition function  $\ln z_{cl}^{NZ}$ . Equation (I.32) is therefore a self-consistent problem and its numerical resolution is explained in section I.3.1.

Introducing the multiplicity  $n_{NZ}$  per unit volume of clusters  $(N, Z)$ , that is the number of WS cells characterized by the cluster  $(N, Z)$  per unit volume, the densities are by definition (cf. eqs. (I.9))  $\rho_n = \rho_{g,n} + \sum_{N,Z} n_{NZ} N_e$  and  $\rho_p = \rho_{g,p} + \sum_{N,Z} n_{NZ} Z_e$  which, using eqs. (I.31) and (I.32) leads to

$$n_{NZ} = \ln z_{cl}^{NZ}(\beta, \mu_p, \mu_n). \quad (\text{I.35})$$

The matter composition is thus determined by the single-cluster partition functions. Let us remark that we can equivalently work with the isoscalar and isovector chemical potentials  $\mu = \mu_n + \mu_p$  and  $\mu_3 = \mu_n - \mu_p$ . The associated average densities are then

$$\rho_B = \frac{\partial \ln z(\beta, \mu, \mu_3)}{\partial (\beta \mu)} = \rho_g + \sum_{N,Z} n_{NZ} A_e = \rho_n + \rho_p \quad (\text{I.36})$$

$$\rho_3 = \frac{\partial \ln z(\beta, \mu, \mu_3)}{\partial (\beta \mu_3)} = \rho_{g,3} + \sum_{N,Z} n_{NZ} (N_e - Z_e) = \rho_n - \rho_p, \quad (\text{I.37})$$

with  $\rho_g = \rho_{g,n} + \rho_{g,p}$  and  $\rho_{g,3} = \rho_{g,n} - \rho_{g,p}$ .

The baryonic average energy density  $\varepsilon_b$  of the total system is, in the grand canonical ensemble,

$$\begin{aligned} \varepsilon_b &= - \left. \frac{\partial \ln z(\beta, \mu_p, \mu_n)}{\partial \beta} \right|_{(\beta \mu_p, \beta \mu_n)} \\ &= \mathcal{H}_{gas} + \sum_{N,Z} n_{NZ} \left( mA_e + \frac{3}{2}T + E_{vac}(N, Z) \right. \\ &\quad \left. + E_{coul}(N, Z, \rho_e) + E^*(N, Z) + \delta E(N, Z, \rho_{g,n}, \rho_{g,p}) \right), \end{aligned} \quad (\text{I.38})$$

where we have defined the temperature dependent average cluster excited energy as

$$E^*(N, Z) = \frac{1}{g_\beta(N, Z)} \sum_{E^*(N, Z)} E^*(N, Z) \exp[-\beta E^*(N, Z)]. \quad (\text{I.39})$$

In equation (I.38), we can recognise the average thermal energy  $3/2T$ , in agreement with the equipartition theorem for a classical gas. The other terms come from the internal properties of the clusters, thus we define the average cluster internal energy density as

$$\begin{aligned} \varepsilon_{cl}^{int} &= \sum_{N,Z} n_{NZ} \left( mA_e + E_{vac}(N, Z) \right. \\ &\quad \left. + E_{coul}(N, Z, \rho_e) + E^*(N, Z) + \delta E(N, Z, \rho_{g,n}, \rho_{g,p}) \right). \end{aligned} \quad (\text{I.40})$$

The baryonic average density energy eq. (I.38) is then simply

$$\varepsilon_b = \mathcal{H}_{gas} + \varepsilon_{cl}^{int} + \frac{3}{2}T n_{cl}, \quad (\text{I.41})$$

with  $n_{cl} = \sum_{N,Z} n_{NZ}$  the total multiplicity per unit volume, that is the number of WS cells in a volume unit.

Similarly, we can calculate the baryonic pressure

$$\begin{aligned} p_b &= \frac{\partial \ln \mathcal{Z}(\beta, \mu_p, \mu_n)}{\beta \partial V_{tot}} = T \ln z_b(\beta, \mu_p, \mu_n) \\ &= -\mathcal{H}_{gas} + T s_{gas}(\mathcal{H}_{gas}) + T n_{cl} + \mu_n \rho_{g,n} + \mu_p \rho_{g,p}. \end{aligned} \quad (\text{I.42})$$

as well as the baryonic average entropy density of the system

$$s_b = \beta p_b + \beta e_b - \beta \rho_n \mu_n - \beta \rho_p \mu_p = s_{gas}(\mathcal{H}_{gas}) + s_{cl}, \quad (\text{I.43})$$

where we have introduced the cluster entropy density as

$$s_{cl} = \beta \varepsilon_{cl}^{int} + \frac{5}{2} n_{cl} - \beta \mu_n \rho_{cl,n} - \beta \mu_p \rho_{cl,p}. \quad (\text{I.44})$$

## Chapter I.2

# Modelling nuclear energetics

In order to evaluate the baryonic grand partition function developed in chapter I.1 which is required to obtain the matter composition and the Equation of State, we need to know the nuclear energy of the Wigner-Seitz cells and its associated entropy, as well as the Coulomb energy due to electrons. It is important to stress once again that the presence of different WS cells in a given thermodynamic condition means that a well defined value of the gas density and composition, that is a set  $(\rho_{g,n}, \rho_{g,p})$  can be associated to any cluster species  $(N, Z)$ , and not only to the one given by the equality of chemical potentials. We thus need to model any nucleus  $(N, Z)$  in any gas  $(\rho_{g,n}, \rho_{g,p})$  at many temperatures. For this reason, systematic microscopic calculations are far too computationally expensive, and very hard to perform. Indeed to get different cluster compositions, a very large system containing many Wigner-Seitz cells should be considered in a variational calculation. This has been done in the literature only for highly simplified classical models [Hor04], or using severe approximations [Séb11]. It is therefore highly preferable to consider analytical or quasi-analytical expressions. As we discuss in this chapter, this can be done (within some approximation) by separating the cluster and the gas contribution.

In section I.2.1, we present (non-charged) nuclear matter within the effective Skyrme interaction, which gives the nucleon gas energy density of stellar matter. Concerning the in-vacuum cluster energetics, the issues specific to matter of compact stars, and especially of neutron stars, are discussed in section I.2.2. The interactions between the clusters and the stellar medium,  $\delta F$  and  $E_{coul}$ , are introduced in section I.2.3. (A thorough study of the nuclear in-medium interaction energy at zero temperature is made in part II.)

### I.2.1 Nucleon gas

The average energy density  $\mathcal{H}_{gas}$  of the nucleon gas present in compact stars is developed in this section. We consider only the nuclear interaction since the Coulomb energy has

been put into the cluster partition function. To model nuclear matter, we present the self-consistent mean-field approximation, and consider effective Skyrme interactions. To take into account pairing effects, which are beyond mean-field correlations, we briefly introduce in a second step the BCS theory. The corresponding gas entropy density  $s_{gas}$  is also given.

### I.2.1.a Mean-field approach

Let us consider a system of  $N$  fermions interacting via a Hamiltonian  $\hat{H}_{true}$ . The energy  $E_I$  corresponding to a given state  $|\Psi_I\rangle$  is then  $E_I = \langle \Psi_I | \hat{H}_{true} | \Psi_I \rangle$ . We introduce the independent fermions state at the same energy  $E_I$  which is given by a Slater determinant

$$|\Phi_I\rangle = \prod_{i=1}^N a_{\ell_i}^\dagger |0\rangle, \quad (\text{I.45})$$

where  $\{\ell_i^i\}$  stands for a set of good quantum numbers of particles  $i$  in the state  $I$ . That is, the kets  $\{|\ell_i^i\rangle = a_{\ell_i}^\dagger |0\rangle\}$  are the  $N$  single particle-states of the system in the state  $|\Phi_I\rangle$ . For weak correlations, we can make the assumption that  $|\Psi_I\rangle \approx |\Phi_I\rangle$ , that is we consider that the particles are independent. However, they still are in interaction via  $\hat{H}_{true}$ . The previous hypothesis can be generalized at finite temperature which is a mixture of states:

$$|\Psi_I\rangle \approx \sum_K c_K^{(I)} |\Phi_K\rangle. \quad (\text{I.46})$$

We define the mean-field Hamiltonian operator  $\hat{H}_I^{MF}$  of the independent particles in the state  $|\Psi_I\rangle$  by

$$\hat{H}_I^{MF} |\ell_i^i\rangle = e_{\ell_i} |\ell_i^i\rangle, \quad (\text{I.47})$$

with  $\{e_{\ell_i}\}$  the energies to be specified of the  $N$  independent (but still interacting) particles  $\{|\ell_i^i\rangle\}$ . Because the mean-field Hamiltonian depends on the system state  $|\Psi_I\rangle$ , eq. (I.47) is a self-consistent problem. So we have replaced the original correlated  $N$ -body problem with a self-consistent problem of independent particles.

We define the density matrix  $\hat{D}_{\Psi_I}$  as the  $N$ -body projection onto the state  $|\Psi_I\rangle$ , that is

$$\hat{D}_{\Psi_I} = |\Psi_I\rangle \langle \Psi_I| = \sum_{K,K'} c_K^{(I)} c_{K'}^{(I)*} |\Phi_K\rangle \langle \Phi_{K'}|, \quad (\text{I.48})$$

where we have used eq. (I.46). Because at equilibrium  $[\hat{H}_I^{MF}, \hat{D}_{\Psi_I}] = 0$ , we can choose the orthonormal basis  $\{|\Phi_K\rangle\}$  that diagonalises both the Hamiltonian  $\hat{H}_I^{MF}$  and the

projection  $\hat{D}_{\Psi_I}$ . Hence the  $(K, K')$  entries of  $\hat{D}_{\Psi_I}$  are  $\hat{D}_{\Psi_I}^{KK'} = p_K^{(I)} \delta_{KK'}$ , with  $p_K^{(I)} = |c_K^{(I)}|^2$  the probability to reach the state  $K$ :

$$\hat{D}_{\Psi_I} = \sum_K p_K^{(I)} |\Phi_K\rangle \langle \Phi_K|. \quad (\text{I.49})$$

Using the closure relation, one can easily show that the expectation value of any operator  $\hat{A}$  can be expressed thanks to the density matrix as follows:

$$\langle \hat{A} \rangle_{\Psi_I} = \text{Tr} \left( \hat{D}_{\Psi_I} \hat{A} \right). \quad (\text{I.50})$$

Taking the  $(N-1)$ -partial trace  $\text{Tr}_{2\dots N}$  of the projection  $\hat{D}_{\Psi_I}$ , the 1-body density operator  $\hat{\rho}_{\Psi_I}^{(1)} = \hat{\rho}_{\Psi_I}$  is defined as

$$\hat{\rho}_{\Psi_I} = N \text{Tr}_{2\dots N} \hat{D}_{\Psi_I}, \quad (\text{I.51})$$

which is also diagonal by the previous choice of the basis. Moreover, because of the orthonormalization of the wave functions, that is  $\text{Tr} \hat{D}_{\Psi_I} = 1$ , the trace of the 1-body density matrix is the particles number of the system:  $\text{Tr} \hat{\rho}_{\Psi_I} = N$ .

In  $\mathbf{r}$ -space, the matrix elements are

$$D_{\Psi_I}(\mathbf{r}_1, \dots, \mathbf{r}_N; \mathbf{r}'_1, \dots, \mathbf{r}'_N) = \langle \mathbf{r}_N \dots \mathbf{r}_1 | \hat{D}_{\Psi_I} | \mathbf{r}'_1 \dots \mathbf{r}'_N \rangle = \Psi_I^*(\mathbf{r}'_1, \dots, \mathbf{r}'_N) \Psi_I(\mathbf{r}_1, \dots, \mathbf{r}_N), \quad (\text{I.52})$$

so in particular the 2-point density function is

$$\rho_{\Psi_I}(\mathbf{r}, \mathbf{r}') = \langle \mathbf{r} | \hat{\rho}_{\Psi_I} | \mathbf{r}' \rangle = N \int d\mathbf{r}_2 \dots d\mathbf{r}_N \Psi_I^*(\mathbf{r}', \mathbf{r}_2, \dots, \mathbf{r}_N) \Psi_I(\mathbf{r}, \mathbf{r}_2, \dots, \mathbf{r}_N), \quad (\text{I.53})$$

where we have expressed the trace of eq. (I.51) as the  $N-1$  integrals. In eq. (I.53), the wave functions  $\Psi_I(\mathbf{r}, \mathbf{r}_2, \dots, \mathbf{r}_N)$  are the sum of  $\Phi_I(\mathbf{r}, \mathbf{r}_2, \dots, \mathbf{r}_N)$  as defined in eq. (I.49). Notice that a sum over spin states has also to be included, which is omitted for now, to simplify the notations. Using equation (I.45), we obtain, in  $\mathbf{r}$ -space:

$$\Phi_I(\mathbf{r}, \mathbf{r}_2, \dots, \mathbf{r}_N) = \hat{\mathcal{A}}_N \{ \varphi_{1_I}(\mathbf{r}) \varphi_{2_I}(\mathbf{r}_2) \dots \varphi_{N_I}(\mathbf{r}_N) \}, \quad (\text{I.54})$$

where  $\varphi_{\ell_I}(\mathbf{r}) = \langle \mathbf{r} | \ell_I \rangle$ , and  $\hat{\mathcal{A}}_N$  is the antisymmetric operator of  $N$  fermions. Using the normalisations and the Pauli exclusion principle, that is  $\langle \ell_I | \ell'_I \rangle = \delta_{\ell_I \ell'_I}$ , as well as the closure relations  $\int d\mathbf{r}_n |\varphi_{\ell_I}(\mathbf{r}_n)|^2 = 1$ , equation (I.53) reads

$$\rho_{\Psi_I}(\mathbf{r}, \mathbf{r}') = \varphi_I(\mathbf{r}) \varphi_I^*(\mathbf{r}'), \quad (\text{I.55})$$

with  $|\varphi_I\rangle$  the 1-body ket which can be expressed on an arbitrary basis  $|j\rangle$  of the one-body

Hilbert space as

$$|\varphi_I\rangle = \sum_j d_j^I |j\rangle. \quad (\text{I.56})$$

So the 2-point density function is  $\rho_{\Psi_I}(\mathbf{r}, \mathbf{r}') = \sum_j n_j^I \langle \mathbf{r} | j \rangle \langle j | \mathbf{r}' \rangle$ , with  $n_j^I = |d_j^I|^2$  the site occupation number. By identification with equation (I.53), the 1-body density operator is then the projection onto the 1-particle state  $|\varphi_I\rangle$

$$\hat{\rho}_{\Psi_I} = |\varphi_I\rangle \langle \varphi_I| = \sum_j n_j^I |j\rangle \langle j|, \quad (\text{I.57})$$

which is equivalent to

$$\hat{\rho}_{\Psi_I} = \sum_{ij} \rho_{\Psi_I}^{ij} a_i^\dagger a_j \quad (\text{I.58})$$

with  $\rho_{\Psi_I}^{ij} = \langle i | \hat{\rho}_{\Psi_I} | j \rangle$ .

To shorten the notations, we will skip the detailed “ $I$ ” and “ $\Psi_I$ ” in the following sections.

### I.2.1.b Quantum mechanics expressions of densities

As in nuclear matter we consider two types of fermions, we have two independent 1-body density operators, denoted  $\hat{\rho}_q$ , with  $q = n$  for neutrons,  $q = p$  for protons. Introducing the occupation number  $n_q^{\zeta, s}$  of the state  $|s, \zeta\rangle$  of the  $q$ -type particle, where  $s$  is the spin and  $\zeta$  the other quantum numbers, the two-body densities are

$$\rho_q(\mathbf{r}, \mathbf{r}') = \sum_{\zeta, s} n_q^{\zeta, s} \langle \zeta, s; \mathbf{r} | \hat{\rho}_q | \mathbf{r}'; s, \zeta \rangle = \sum_{\zeta, s} n_q^{\zeta, s} \varphi_q(\mathbf{r}; s, \zeta) \varphi_q^*(\mathbf{r}'; s, \zeta), \quad (\text{I.59})$$

with  $\varphi_q(\mathbf{r}; s, \zeta) = \langle \mathbf{r} | s, \zeta \rangle$ . The standard local  $q$ -particle density is thus

$$\rho_q(\mathbf{r}) = \rho_q(\mathbf{r}, \mathbf{r}') \Big|_{\mathbf{r}'=\mathbf{r}} = \sum_{\zeta, s} n_q^{\zeta, s} |\varphi_q(\mathbf{r}; s, \zeta)|^2. \quad (\text{I.60})$$

Similarly, we can define the 2-point kinetic densities  $\tau_q(\mathbf{r}, \mathbf{r}')$  via the momentum operator  $\hat{\mathbf{p}} = -i\hbar \nabla_{\mathbf{r}}$  [Bra85]:

$$\tau_q(\mathbf{r}, \mathbf{r}') = \frac{1}{\hbar^2} \sum_{\zeta, s} n_q^{\zeta, s} \langle \zeta, s; \mathbf{r} | \hat{\mathbf{p}} \hat{\rho}_q \hat{\mathbf{p}} | \mathbf{r}'; s, \zeta \rangle = \nabla_{\mathbf{r}} \nabla_{\mathbf{r}'} \sum_{\zeta, s} n_q^{\zeta, s} \varphi_q(\mathbf{r}; s, \zeta) \varphi_q^*(\mathbf{r}'; s, \zeta), \quad (\text{I.61})$$

where we recognize the 2-point density function eq. (I.59). The local kinetic function is then simply

$$\tau_q(\mathbf{r}) = \tau_q(\mathbf{r}, \mathbf{r}')|_{\mathbf{r}'=\mathbf{r}} = \nabla_{\mathbf{r}} \nabla_{\mathbf{r}'} \rho_q(\mathbf{r}, \mathbf{r}')|_{\mathbf{r}=\mathbf{r}'} = \sum_{\zeta, s} n_q^{\zeta s} |\nabla_{\mathbf{r}} \varphi_q(\mathbf{r}; s, \zeta)|^2. \quad (\text{I.62})$$

By introducing the Pauli matrix operator  $\hat{\sigma}$ , we can also define the 2-point spin-orbit density vectors [Ben03]

$$\mathbf{J}_q(\mathbf{r}, \mathbf{r}') = \frac{1}{2\hbar} \sum_{\zeta s} n_q^{\zeta s} \langle \zeta s, \mathbf{r} | \hat{\mathbf{p}} \hat{\rho}_q \times \hat{\sigma} | \mathbf{r}', s \zeta \rangle + cc, \quad (\text{I.63})$$

where “ $cc$ ” stands for the complex conjugate. In inserting the closure relation  $\sum_{s'} |s'\rangle \langle s'|$  and defining the matrix elements  $\sigma_{s's} = \langle s' | \hat{\sigma} | s \rangle$ , eq. (I.63) reads

$$\mathbf{J}_q(\mathbf{r}, \mathbf{r}') = -\frac{i}{2} \nabla_{\mathbf{r}} \sum_{\zeta} \sum_{ss'} n_q^{\zeta s} \varphi_q(\mathbf{r}; s, \zeta) \varphi_q^*(\mathbf{r}'; s', \zeta) \times \sigma_{s's} + cc. \quad (\text{I.64})$$

The usual 1-point spin-orbit density vectors are then

$$\mathbf{J}_q(\mathbf{r}) = \mathbf{J}_q(\mathbf{r}, \mathbf{r}) = -\frac{i}{2} \left[ (\nabla_{\mathbf{r}} - \nabla_{\mathbf{r}'} ) \times \mathbf{s}_q(\mathbf{r}, \mathbf{r}') \right] \Big|_{\mathbf{r}=\mathbf{r}'}, \quad (\text{I.65})$$

where the spin density is

$$\mathbf{s}_q(\mathbf{r}, \mathbf{r}') = \langle \mathbf{r} | \hat{\rho}_q \hat{\sigma} | \mathbf{r}' \rangle = \sum_{\zeta s} n_q^{\zeta s} \langle \zeta, s; \mathbf{r} | \hat{\sigma} | \mathbf{r}', s, \zeta \rangle. \quad (\text{I.66})$$

We can notice that all these local densities, eqs. (I.60), (I.62) and (I.65), which are the ingredients used in the Skyrme energy density (see eq. (I.68)), are expressed as a function of the 1-body density operators  $\hat{\rho}_q$ . This means that the energy density can be expressed as a functional of  $\hat{\rho}_q$ , that is

$$\frac{\langle \hat{H}_{true} \rangle}{V} = \frac{E[\hat{\rho}_n, \hat{\rho}_p]}{V} = \mathcal{H}[\hat{\rho}_n, \hat{\rho}_p]. \quad (\text{I.67})$$

The fact that the energy depends only of the 1-body density is very intuitive for the kinetic part of the Hamiltonian. Indeed, it is a 1-body operator that depends on the number of particles in the system. However, for any 2-body potential operator, it is expected to depend on the 2-body density. Actually, one can show that, in the case of independent fermions we are considering, the  $M$ -body density operators can be formally expressed as an antisymmetric function of an  $M$ -product of 1-body density  $\hat{\rho}_q$ , leading to the dependence of equation (I.67) [Rin80]. The dependence of the energy

density on 1-body densities only is of course a strong approximation, entirely due to our hypothesis of weak correlations which allowed us to express the exact  $N$ -body ket as a single Slater determinant. This approximation is known as the self-consistent mean-field approximation.

### I.2.1.c Effective Skyrme interaction

The Skyrme formalism [Sky56] belongs to the models which treat many-body problems by using non-relativistic effective density dependent nucleon-nucleon (NN) interactions in the self-consistent mean-field approximation. Unlike the Gogny models, the Skyrme functional parametrization is based on zero range interactions [Vau72], though finite-range corrections have been added [Pet95]. The free parameters, usually labelled  $t_i, x_i, \alpha, W_0$ , are fitted to reproduce a large set of experimental data, such as mass and radii of stable nuclei, fission barriers, energies of giant resonances, as well as ab initio calculations of symmetric and asymmetric nuclear matter. According to the selection of these constraints, the parameterization of the Skyrme interactions is not unique and therefore, there exist many different parameters sets [Dan09; Dut12]. Although all Skyrme forces are usually fitted to reproduce well the saturation energy and density of symmetric nuclear matter which are experimentally accessible, they differ significantly in both the isoscalar and isovector densities dependence. In this study we are particularly concerned by neutron-rich matter present in (proto-)neutron stars; therefore we use for most of our calculations the SLy interactions which are specifically fitted to heavy neutron-rich nuclei ground states and properties of neutron matter.

The main drawback of phenomenological functionals is that, since the microscopic details of the interaction are not considered, there is no clear relations between the fitted parameters and the specific physical properties of the many-body nuclear system. As a consequence, many parameters are strongly correlated. However, the structure of the Skyrme density functional has the great advantage that the variables characterizing infinite nuclear matter can be analytically expressed [Cha97]. (We use this specificity in part III.)

The standard Skyrme expression for the energy density is [Cha98]

$$\begin{aligned} \frac{\langle \hat{H}_{true} \rangle}{V} &= \frac{E[\hat{\rho}_n, \hat{\rho}_p]}{V} = \mathcal{H}[\hat{\rho}_n, \hat{\rho}_p] = \mathcal{H}(\mathbf{r}) \\ &= \mathcal{K}(\mathbf{r}) + \mathcal{H}_0(\mathbf{r}) + \mathcal{H}_3(\mathbf{r}) + \mathcal{H}_{eff}(\mathbf{r}) + \mathcal{H}_{fin}(\mathbf{r}) + \mathcal{H}_{so}(\mathbf{r}) + \mathcal{H}_{sg}(\mathbf{r}). \quad (\text{I.68}) \end{aligned}$$

In this expression,  $\mathcal{K}$  is the non-relativistic kinetic energy and  $\mathcal{H}_0(\mathbf{r})$  the zero-range potential interaction.  $\mathcal{H}_3(\mathbf{r})$  is the density dependent term which dominates the interaction at high density, therefore it can be seen as an effective term going beyond NN interactions and effectively accounting for  $N$ -body forces. The modification of the nucleon effective

mass  $m_q^* = (\partial\mathcal{H}/\partial\tau_q)^{-1}/2$  is taken into account by the effective term  $\mathcal{H}_{eff}$ . Finally, the effects of finite size, required to model finite nuclei energy are taken into account by the finite-range correction  $\mathcal{H}_{fin}$ , as well as spin-orbit  $\mathcal{H}_{so}$  and spin-gradient  $\mathcal{H}_{sg}$  interactions. Their expressions are

$$\mathcal{K} = \frac{\hbar^2}{2m}\tau, \quad (\text{I.69a})$$

$$\mathcal{H}_0 = C_0\rho^2 + D_0\rho_3^2, \quad (\text{I.69b})$$

$$\mathcal{H}_3 = (C_3\rho^2 + D_3\rho_3^2)\rho^\alpha, \quad (\text{I.69c})$$

$$\mathcal{H}_{eff} = C_{eff}\rho\tau + D_{eff}\rho_3\tau_3, \quad (\text{I.69d})$$

$$\mathcal{H}_{fin} = C_{fin}(\nabla\rho)^2 + D_{fin}(\nabla\rho_3)^2, \quad (\text{I.69e})$$

$$\mathcal{H}_{so} = C_{so}\mathbf{J} \cdot \nabla\rho + D_{so}\mathbf{J}_3 \cdot \nabla\rho_3, \quad (\text{I.69f})$$

$$\mathcal{H}_{sg} = C_{sg}\mathbf{J}^2 + D_{sg}\mathbf{J}_3^2, \quad (\text{I.69g})$$

where we have used the isoscalar and isovector densities  $\rho = \rho_n + \rho_p$  and  $\rho_3 = \rho_n - \rho_p$ , and similarly introduced the isoscalar  $\tau$  ( $\mathbf{J}$ ) and isovector  $\tau_3$  ( $\mathbf{J}_3$ ) kinetic densities (spin-orbit density vectors). The coefficients  $C_i$  and  $D_i$  of eqs. (I.69), respectively associated with the isoscalar and isovector contributions, are expressed as functions of the usual Skyrme parameters  $t_i$  and  $x_i$ , as well as  $W_0$  which independently parametrizes the spin-orbit interaction. We have [Cha98]

$$C_0 = \frac{3}{8}t_0 \quad D_0 = -\frac{1}{8}t_0[2x_0 + 1] \quad (\text{I.70a})$$

$$C_3 = \frac{1}{16}t_3 \quad D_3 = -\frac{1}{48}t_3[2x_3 + 1] \quad (\text{I.70b})$$

$$C_{eff} = \frac{1}{16}[3t_1 + t_2(4x_2 + 5)] \quad D_{eff} = \frac{1}{16}[t_2(2x_2 + 1) - t_1(2x_1 + 1)] \quad (\text{I.70c})$$

$$C_{fin} = \frac{1}{64}[9t_1 - t_2(4x_2 + 5)] \quad D_{fin} = -\frac{1}{64}[3t_1(2x_1 + 1) - t_2(2x_2 + 1)] \quad (\text{I.70d})$$

$$C_{so} = \frac{3}{4}W_0 \quad D_{so} = \frac{1}{4}W_0 \quad (\text{I.70e})$$

$$C_{sg} = \frac{1}{32}[t_1(1 - 2x_1) - t_2(1 + 2x_2)] \quad D_{sg} = \frac{1}{32}[t_1 - t_2]. \quad (\text{I.70f})$$

Let us notice that there are several Skyrme models which require additional parameters [Agr06; Cha09]. In particular a series of BSk functionals specifically optimized to astrophysical applications has been recently proposed by the Bruxelles group [Gor10]. In this thesis we do not aim at a complete model comparison, this is why we will stick to standard Skyrme functionals as described above.

### I.2.1.d Homogeneous matter

Let us specify the previous equations for homogeneous infinite matter which are relevant for the free nucleon part of compact stars that we can assimilate to a homogeneous nuclear gas. In this case, the energy density eq. (I.68) is simpler since the particle density gradients vanish, as well as the spin-orbit density vectors  $\mathbf{J}_q$ , as we can easily see from eq. (I.65). The energy density is then a function of particle and kinetic densities only. In homogeneous matter, the fermion functions eq. (I.56)  $\varphi_q(\mathbf{r}; s)$  are the superposition of an infinite number of plane waves. In the continuous limit corresponding to infinite nuclear matter, it reads

$$\varphi_q(\mathbf{r}; s) = \int d\mathbf{k} \alpha^s(\mathbf{k}) e^{-i\mathbf{k} \cdot \mathbf{r}}, \quad (\text{I.71})$$

with  $|\alpha^s(\mathbf{k})|^2 = 1/(8\pi^3)$ , such that the fermion functions are normalized. The particle densities, eq. (I.59) are then

$$\rho_q(\mathbf{r}) = \sum_s \frac{1}{8\pi^3} \int_0^\infty 4\pi k^2 n_q(k) dk = \frac{1}{\pi^2} \int_0^\infty k^2 n_q(k) dk = \rho_q, \quad (\text{I.72})$$

where  $n_q(k)$  is the Fermi distribution of fermions  $q = n, p$  at finite temperature and within the nuclear potential  $U_q[\hat{\rho}_n, \hat{\rho}_p] = \partial\mathcal{H}[\hat{\rho}_n, \hat{\rho}_p]/\partial\rho_q$ :

$$n_q(k) = \left\{ 1 + \exp \left[ \beta \left( \frac{k^2}{2m_q^*} + U_q[\hat{\rho}_n, \hat{\rho}_p] - \tilde{\mu}_q \right) \right] \right\}^{-1}. \quad (\text{I.73})$$

Introducing the auxiliary shifted chemical potentials  $\mu_q^{aux} = \tilde{\mu}_q - U_q$ , the densities eqs. (I.72) can be written as regular Fermi integrals. Equations (I.72) then establish a coupled self-consistent problem since the effective mass  $m_q^*$  depends on the densities  $\rho_n$  and  $\rho_p$ . For each couple  $(\mu_n^{aux}, \mu_p^{aux})$ , a unique solution  $(\rho_n, \rho_p)$  can be found.

The kinetic densities eqs (I.62) can be calculated, taking the gradient of the functions  $\varphi_q(\mathbf{r}; s)$

$$\tau_q(\mathbf{r}) = \frac{1}{\pi^2} \int_0^\infty k^4 n_q(k) dk = \tau_q. \quad (\text{I.74})$$

This equation defines a new self-consistent problem since, for given  $(\mu_n, \mu_p)$ , the potentials  $U_q$  depend on  $\tau_q$ .

The associated entropy is simply

$$s_q = -\frac{1}{\pi^2} \int dk k^2 \left[ n_q(k) \ln(n_q(k)) + (1 - n_q(k)) \ln(1 - n_q(k)) \right]. \quad (\text{I.75})$$

Let us notice that in the limit of zero temperature, these previous integrals are analytical, leading to simplifications. Indeed, the Fermi distribution tends to a Heaviside step function, such that

$$\rho_q = \frac{1}{\pi^2} \int_0^{k_{Fq}} k^2 dk = \frac{k_{Fq}^3}{3\pi^2} = \rho_{0q}, \quad (\text{I.76})$$

where  $k_{Fq}(\rho_n, \rho_p)$  are the Fermi momenta. The kinetic densities can then be expressed as a function of the associated density  $\rho_{0q}$

$$\tau_q = \frac{1}{\pi^2} \int_0^{k_{Fq}} k^2 (-ik)(ik) dk = \frac{3}{5} (3\pi^2)^{2/3} \rho_{0q}^{5/3} = \tau_{0q}, \quad (\text{I.77})$$

such that the second self-consistency between  $\tau_q$  and  $U_q$  vanishes at zero temperature. The entropy eq. (I.75) is zero, as expected.

### I.2.1.e Pairing effects in the BCS approximation

Superfluidity [Mig59] in the (proto-)neutron stars crust which arises at low temperatures, is a key component for the understanding of glitches [Pie14], thermalization time [For10], and cooling properties [Lat94; Gne01]. Present studies of crust superfluidity at finite temperature are always done solving Hartree-Fock-Bogoliubov (HFB) equations in the Single Nucleus Approximation. In this section, we introduce the residual effect of pairing correlations in the homogeneous matter component of the NSE model, using the local Bardeen, Cooper, Schrieffer (BCS) approximation [Bar57]. In sections I.2.2 and II.1, we will show how to implement superfluidity into the cluster energetics, as well as in the interaction between the bound nucleons and the gas.

In the BCS approximation, the energy pairing gap  $\Delta(T, \rho_n, \rho_p)$ , and the effective pairing interaction are linked by [Lan80; Bur14]

$$v_{\pi,q}(\rho_n, \rho_p) = -4\pi^2 \left\{ \int_0^{k_\Lambda} dk \frac{k^2}{\xi_q} [1 - 2f_q(k, \Delta)] \right\}^{-1}, \quad (\text{I.78})$$

with  $\xi_q = p^2/(2m_q^*) - \mu_q^{aux}$ . In turn, the Fermi distribution  $f_q(k, \Delta)$  of eq. (I.78) depends on the pairing gap as follows [Lan80]:

$$f_q(k, \Delta) = \frac{1}{2} \left[ 1 - \frac{\xi_q}{E_{q,\Delta}} \tanh \left( \frac{\beta E_{q,\Delta}}{2} \right) \right]. \quad (\text{I.79})$$

In this equation,  $E_{q,\Delta} = \sqrt{\xi_q^2 + \Delta^2}$  is the energy including the pairing gap. As in section I.2.1.d, eq. (I.78) defines a coupled self-consistent problem since the effective mass  $m_q^*$  depends on the densities  $\rho_n$  and  $\rho_p$ . Owing to the zero range of the pairing interaction,

a cutoff  $k_\Lambda/(2m) = 16$  MeV has to be introduced in the gap equations (I.78) to avoid divergences [Cha10; Bur14]. The set of equations is closed if the pairing gap or the pairing interaction is known. In a consistent treatment, one should in principle derive the mean-field and pairing functionals from the particle-hole and particle-particle matrix elements of the same effective nuclear interaction [Rin80]. In practical applications however this is seldom done, and a phenomenological pairing interaction is independently adjusted to experimental data.

Within this procedure, the density dependence of the pairing strength  $v_{\pi,q}(\rho_n, \rho_p)$  remains very poorly known, and it is usually assumed that it only depends on the density of the considered particles  $q$ . A usual phenomenological parametrization is [Ber91b; Cha10]

$$v_{\pi,q}(\rho_n, \rho_p) = v_\pi(\rho_q) = V_\pi \left[ 1 - \eta \left( \frac{2\rho_q}{\rho_{sat}} \right)^a \right], \quad (\text{I.80})$$

with  $\rho_{sat}$  the saturation density of symmetric nuclear matter, and where  $V_\pi$ ,  $\eta$  and  $a$  are adjustable parameters. These parameters are fitted to experimental data to reproduce the pairing gap of finite nuclei. Since our application consists in describing infinite nuclear matter, it is more realistic to fit them imposing to reproduce the pairing gap of nuclear matter as obtained in ab initio calculations of zero temperature pure neutron matter [Cao06a; Bur14]. This prescription has been made in [Bur14]. Using the pairing gap calculated with Brueckner-Hartree-Fock (BHF) and equation (I.78) to evaluate the pairing strength, the results of the fit performed in [Bur14] give:  $V_\pi = 1157.51$  MeV,  $\eta = 0.884$  and  $a = 0.256$ . Then, inverting eq. (I.78) allows to calculate the pairing gap energy for any density, isospin and temperature.

To take into account pairing effects in the gas component of the NSE model [Bur15], we have to add the energy density  $\mathcal{H}_\pi$ , associated to the interaction eq. (I.80), to the Skyrme energy density eq. (I.68) [Bur14]:

$$\mathcal{H}_\pi(\rho_n, \rho_p, \tilde{\rho}_n, \tilde{\rho}_p) = \frac{1}{4} \sum_{q=n,p} v_\pi(\rho_q) \tilde{\rho}_q^2, \quad (\text{I.81})$$

with  $\tilde{\rho}_q = 2\Delta(T, \rho_q)/v_\pi(\rho_q)$  the so-called anomalous density. Moreover, since the pairing affects the particle distributions, we have to consistently replace the Fermi distributions eq. (I.73) entering in the nucleon density eq. (I.72) and the kinetic energy density eq. (I.74) by the Fermi distributions including pairing eq. (I.79). We can notice that the nuclear potentials  $U_q$  then get a contribution from the pairing energy density  $\partial\mathcal{H}_\pi/\partial\rho_q$ . The entropy including pairing is given by eq. (I.75), with the following Fermi distribu-

tion [Lan80]

$$n_q(k, \Delta) = \left\{ 1 + \exp [\beta E_{q,\Delta}] \right\}^{-1}. \quad (\text{I.82})$$

## I.2.2 Cluster energetics

We now turn to the in-vacuum cluster component entering the cluster partition functions eq. (I.30), that is the ground state energy  $E_{vac}(N, Z)$ , as well as the temperature dependent degeneracy factor  $g_\beta(N, Z)$ .

### I.2.2.a Ground states energy

At zero temperature the variational problem reduces to the energy minimisation. For this reason, the composition of neutron star outer crusts are known to be largely sensitive to precision measurements of nuclear masses [Pea11; Kre13; Wol13]. This statement stays true at low temperatures. Indeed, in that case entropy is dominated by energy such that the states mixture is very reduced. As a consequence, only few low-lying excited states are occupied, and the cluster distribution is very narrow such that there are few species as well (see results in chap I.3).

In order to correctly model proto-neutron stars outer crust, we thus need to have nuclei ground states energy as precise as possible, and a natural choice is to directly take experimental information. To do so, we use the NUBASE2012 data of [Aud12], publicly available in electronic format. In this database, all nuclei for which some experimental information is known are considered, and extrapolations based on the trends of neighbouring nuclei give estimated values for nuclei masses close to the measured ones.

However, this database is far from being exhaustive enough for our purpose: much of compact stars composition matter is dominated by clusters which are beyond current experimental data. Indeed, the presence of electrons modifies the drip lines since the electrons energy have to be considered in the evaluation of the neutron/proton separation energy. Moreover, interactions with the nucleon gas modify the binding energy of the cluster. At  $\beta$ -equilibrium, the clusters can be much more neutron-rich than measured nuclei, and the most probable nuclei lay above the drip line (modified by the electrons) in the inner crust [Neg73]. Therefore we need a model able to extrapolate the currently known mass formula for a very wide range of nuclear sizes and proton fractions.

Unfortunately, the most precise models currently available, that is HFB, cannot be used into the NSE model. Indeed, besides computational cost problems which can be overtaken in building a mass table [Pea11], there is a principle reason. On the contrary of the Single Nucleus Approximation and ab initio calculations, the NSE implies that each cluster is not at beta equilibrium with the surrounding nucleon gas. This means

that, except for the outer crust at low temperatures where the gas is negligible, all the configurations cannot be reproduced by variational calculations.

The high computational cost of HF calculations has motivated the wide use of the so-called Extended-Thomas-Fermi (ETF) method which is a semi-classical approximation of HF [Ons08]. On the contrary to HF calculations, the density profile is variationally determined in the ETF approximation. If a parametrized profile is used instead of the variational one, excited configurations can be probed. More specifically, the gas density and the cluster size are decorrelated, since the parametrized profile allows for a continuous variation of the nucleon gas density within each WS cell. The energy density calculated within the Extended-Thomas-Fermi approximation and the use of a parametrized profile is thus a way to evaluate the energy of an arbitrary WS cell configuration, that is a cluster of any size and asymmetry immersed in a nucleon gas of any density and any asymmetry. This method is detailed in part II where it is used to calculate both the clusters ground state energy as well as its interactions with the unbound nucleons. To be implemented in the NSE model, one needs then to build a very wide in-medium mass table depending on the cluster size and proton fraction as well as on the gas density and isospin asymmetry. This has the disadvantage to make difficult a complete and systematic interaction study. Furthermore, this table should be often enough in order to take into account the improvements of the interactions. To solve this inconvenience, we have tried to develop analytical formulas of the ETF, which in addition give clear insight on the functional dependence of nuclear energies. (This work is presented in part III.)

In view of these problems, simpler analytical liquid-drop approaches have been employed to evaluate the in-vacuum ground state energy in most of the NSE models [Bot10; Hem10; Rad10]. For the numerical results of this part, we use for the smooth part of nuclear masses a liquid-drop-like parametrization based on mean-field Skyrme models [Dan09]:

$$E_{LDM}(A, I) = a_v A - a_s A^{2/3} - a_v^a \left( 1 + \frac{a_v^a}{a_s^a A^{1/3}} \right)^{-1} A I^2, \quad (\text{I.83})$$

where  $I = (N - Z)/A$  is the global isospin asymmetry of the cluster ( $N, Z$ ). In this equation, the parameters  $a_v$ ,  $a_s$ ,  $a_v^a$ ,  $a_s^a$  have been extracted from a fit of mass and neutron-proton radii differences obtained in HF calculations in an uncharged semi-infinite geometry. In this parametrization, the isoscalar part  $E_{LDM}(N, Z = N)$  contains bulk and surface contributions only, while the isovector part takes into account additional curvature and beyond contributions. This specific point as well as the global accuracy of eq. (I.83) is discussed in chapter II.2. Using eq. (I.83) has the advantage to consistently treat the cluster ground state energy and the nucleon gas. Indeed, the parametrizations have been fitted for a large number of different Skyrme interactions [Dan09] which can

also be used to calculate the gas energy (sec. I.2.1.c). As a consequence, the same interaction model can be used to compute the crust and the core of (proto)-neutron star. This point is important, because most equations of state used in the neutron star literature use matching procedures to join the sub-saturation crust part with the supersaturation core part, treated with a different mean-field model [Gri14]. At variance with these inconsistent treatments, our equations of state can be classified as “unified” [Pea12].

To take into account pairing effects, the smooth part of the nuclear energy, eq. (I.83), is supplemented in the case of even mass nuclei with the common simple phenomenological pairing term,  $\Delta_\pi(A) = \pm 12\delta_\pi\sqrt{A}$ , with  $\delta_\pi = 1$  for even-even nuclei and  $\delta_\pi = -1$  for odd-odd nuclei [Lil01; Hey04]. Let us notice that there are phenomenological indications that the pairing term should scale with  $A^{-1/3}$  and depend on the isospin  $I$  [Men10]. However, the parametrization proposed in [Men10] turns out to behave wrong for very asymmetric nuclei, far from the fit region. Since these nuclei are the most abundant in the stellar context, we have chosen the more standard isospin independent term. Let us however notice that this treatment of pairing in the nuclear mass is not consistent with the one of the nucleon gas detailed in sec. I.2.1.e. This point needs to be improved in the future to have a completely unified equation of state.

Finally, taking into account the Coulomb interaction (due to protons only), the in-vacuum nucleus energy is given by

$$E_{vac}(N, Z) = E_{LDM}(A, I) + a_c \frac{Z^2}{A^{1/3}} + \Delta_\pi(A), \quad (\text{I.84})$$

with  $a_c = 0.69 \text{ MeV}$  the Coulomb parameter.

Let us remark that this prescription disregards shell effects which are important at low temperatures. Though for temperatures above  $T \sim 2 \text{ MeV}$ , our model is expected to be realistic since these non-smooth effects rapidly vanish with temperature, shell effects need to be implemented in the future to obtain a reliable EoS at low temperatures. A way to consider them is to use Strutinsky’s shell corrections [Ons08].

### I.2.2.b Degeneracy factor

For light nuclei where the excited states are discrete, we take the  $N_{exp}$  values of the excited energy  $E_{j_{exp}}^*$  and of the associated degeneracy  $g_{j_{exp}}$  from the NUBASE2012 data [Aud12], such that the temperature dependent degeneracy factor entering in the partition function eq. (I.29) reads, according to (I.25),

$$g_\beta^{exp}(N, Z) = (2J_{GS}^{exp}(N, Z) + 1) + \sum_{j_{exp}}^{N_{exp}(N, Z)} g_{j_{exp}}(N, Z) \exp \left[ -\beta E_{j_{exp}}^*(N, Z) \right]. \quad (\text{I.85})$$

In the numerical results, these experimental data are used for cluster size up to the mass of  $A = 10$ , because the experimental information on individual excited states is obviously incomplete going towards the continuum, and the continuum part of the spectrum appears at lower energy when the nuclear mass increases. Only for masses of the order of 10 or less, the set of discrete measured excited states can be safely taken as a complete description of nuclear spectroscopy below the nucleon separation energy. Therefore, for higher masses an explicit treatment of the density of states is needed. In that case, the degeneracy factor reads:

$$g_{\beta}(N, Z, \rho_e) = (2J_{GS} + 1) + \int_{E_1^*}^{S_{n(p)}} dE \rho_{N,Z}^*(E) \exp -\beta E. \quad (\text{I.86})$$

In this equation,  $J_{GS}$  is arbitrarily taken at 0 if the ground-state spin is not experimentally known, and the lower bound  $E_1^*$  corresponds to the first excited state energy and is assumed to be equal to the pairing gap  $\Delta_{\pi}(A)$  for even-even nuclei and 0 otherwise. To avoid double counting with nucleon gas, the upper limit of the integral is the minimum between the neutron  $S_n$  and the proton  $S_p$  separation energies above which all the cluster nucleons are not bound. This constraint is also applied to the degeneracy factor of light nuclei, built out of discrete levels. Introducing the cluster energy modified by the electron screening (see eq. (I.105)),  $E_{cl}(N, Z, \rho_e) = E_{vac}(N, Z) + E_{coul}(N, Z, \rho_e)$ , the separation energies read

$$S_n(N, Z, \rho_e) = E_{cl}(N - 1, Z, \rho_e) - E_{cl}(N, Z, \rho_e), \quad (\text{I.87})$$

$$S_p(N, Z, \rho_e) = E_{cl}(N, Z - 1, \rho_e) - E_{cl}(N, Z, \rho_e). \quad (\text{I.88})$$

As previously, the non-screened energy part is taken from experimental data if available, and evaluated by eq. (I.84) otherwise. Let us notice that, for consistency, the same prescription is employed for the two energies  $E_{cl}$  entering the separation energies  $S_{n(p)}$ . For the level density of the nucleus  $\rho_{N,Z}^*(E)$  of eq. (I.86), we take the realistic formula fitted from a very large sample of experimental data of ref. [Egi05]:

$$\rho_{N,Z}^*(E) = \begin{cases} \rho_{N,Z}^+(E) = \frac{\exp \left[ 2\sqrt{a_{N,Z}} \left( E - E_{N,Z}^{fit} \right) \right]}{12\sqrt{2}\sigma_{N,Z} a_{N,Z}^{1/4} \left( E - E_{N,Z}^{fit} \right)^{5/4}}, & \text{if } E \geq \frac{25}{16a_{N,Z}} + E_{N,Z}^{fit}, \\ \rho_{N,Z}^-(E) = \rho_{N,Z}^+ \left( \frac{25}{16a_{N,Z}} + E_{N,Z}^{fit} \right), & \text{otherwise.} \end{cases} \quad (\text{I.89})$$

In what follows, we give the expressions of the different quantities entering eq. (I.89), as developed in [Egi05; Egi06], and comment how we adapt them when no experimental data are available. The spin cut-off and level density parameter are respectively:

$$\sigma_{N,Z}^2 = 0.0146 A^{5/3} \frac{1 + \sqrt{1 + 4a_{N,Z} (E - E_{N,Z}^{fit})}}{2a_{N,Z}}, \quad (\text{I.90})$$

$$a_{N,Z} = (q_1 A - q_2 A^2) \cdot \left\{ 1 + \frac{S(N, Z) - \Delta_{N,Z}}{E - E_{N,Z}^{fit}} \left[ 1 - e^{q_3 (E - E_{N,Z}^{fit})} \right] \right\}, \quad (\text{I.91})$$

with the fitted parameters  $q_1 = 0.127 \text{ MeV}^{-1}$ ,  $q_2 = 9.05 \cdot 10^{-5} \text{ MeV}^{-1}$  and  $q_3 = -0.006 \text{ MeV}^{-1}$ , and where  $S(N, Z)$  is the non-smooth part of the ground state energy, that is mainly pairing shell effects. In [Egi05], this shell correction  $S(N, Z)$  is obtained subtracting from the experimental mass a simple liquid-drop formula:

$$\begin{aligned} S(N, Z) &= M_{exp}(N, Z) - M_{LD}(N, Z) \\ &= M_{exp}(N, Z) - (Nm_n + Zm_p + B_{LD}(N, Z)), \end{aligned} \quad (\text{I.92})$$

where the binding energy is

$$\frac{B_{LD}}{A}(N, Z) = -a_{vol} + a_{surf} A^{-1/3} + \left( a_{vol}^{sym} - a_{surf}^{sym} A^{2/3} \right) I^2 + \frac{3e^2}{5r_0} Z^2 A^{-4/3}, \quad (\text{I.93})$$

with  $a_{vol} = 15.65 \text{ MeV}$ ,  $a_{surf} = 17.63 \text{ MeV}$ ,  $a_{vol}^{sym} = 27.72 \text{ MeV}$ ,  $a_{surf}^{sym} = 25.60 \text{ MeV}$ , and  $r_0 = 1.233 \text{ fm}$ . In our NSE model, the non-smooth part  $S(N, Z)$  of clusters for which there is no experimental data, is given by our prescription of pairing effect sec. I.2.2.a:  $S(N, Z) = \Delta_\pi(A)$ .

The pairing energy gap  $\Delta_{N,Z} \neq \Delta_\pi$  a priori, entering eq. (I.91), is defined in [Egi05; Egi06] from the so-called deuteron pairing term  $P_d(N, Z)$ :

$$\Delta_{N,Z} = \begin{cases} + \frac{1}{2} P_d(N, Z) & \text{for even-even,} \\ 0 & \text{for even-odd,} \\ - \frac{1}{2} P_d(N, Z) & \text{for odd-odd,} \end{cases} \quad (\text{I.94})$$

with the deuteron pairing defined as the derivative of the deuteron separation energy  $S_d(N, Z)$ :

$$P_d(N, Z) = \pm \frac{1}{2} \left[ S_d(N+1, Z+1) - S_d(N, Z) \right]$$

$$= \pm \frac{1}{2} \left[ 2M_{exp}(N, Z) - M_{exp}(N+1, Z+1) - M_{exp}(N-1, Z-1) \right], \quad (\text{I.95})$$

where  $+$  ( $-$ ) stands for even (odd) proton number. From eq. (I.95), we can justify eq. (I.94) in observing that the deuteron pairing  $P_d(N, Z)$  corresponds to the non-smooth energy differences. Indeed, if we assume that the nuclei mass can simply be decomposed as

$$M(N, Z) \approx Am + f(I)A + g(A, I) + \Delta(N, Z), \quad (\text{I.96})$$

with  $f(I)A$  the bulk energy,  $g(A, I)$  the smooth surface and curvature part,  $\Delta(N, Z)$  the non-smooth contributions due to pairing effects, the deuteron pairing reads

$$P_d(N, Z) \approx \pm \frac{1}{2} \left[ 2\Delta(N, Z) - \Delta(N+1, Z+1) - \Delta(N-1, Z-1) \right], \quad (\text{I.97})$$

where we have assumed that  $2g(A, I) \approx g(A+2, I) + g(A-2, I)$ . Taking a constant gap  $\Delta(N, Z) \approx \delta_\pi \Delta$  for the neighbouring considered nuclei, the different combinations of even/odd neutrons and protons give eq. (I.94). If the experimental masses do not exist, we can therefore use our own pairing prescription:  $\Delta_{N,Z} = \Delta_\pi(A)$ , and  $P_d(N, Z) = 2|\Delta_\pi(A)|$ .

Finally,  $E_{N,Z}^{fit}$  is a fitted parameter, given by [Egi05; Egi06]:

$$E_{N,Z}^{fit} = p_1 - \frac{1}{2} P_d(N, Z) + p_4 \frac{dS}{dA} \quad \text{for even-even}, \quad (\text{I.98})$$

$$E_{N,Z}^{fit} = p_2 - \frac{1}{2} P_d(N, Z) + p_5 \frac{dS}{dA} \quad \text{for } Z \text{ even, } N \text{ odd}, \quad (\text{I.99})$$

$$E_{N,Z}^{fit} = p_2 + \frac{1}{2} P_d(N, Z) - p_5 \frac{dS}{dA} \quad \text{for } N \text{ even, } Z \text{ odd}, \quad (\text{I.100})$$

$$E_{N,Z}^{fit} = p_3 + \frac{1}{2} P_d(N, Z) + p_4 \frac{dS}{dA} \quad \text{for odd-odd}, \quad (\text{I.101})$$

$$(\text{I.102})$$

with  $p_1 = -0.48$  MeV,  $p_2 = -0.57$  MeV,  $p_3 = -0.24$  MeV,  $p_4 = 0.29$  MeV,  $p_5 = 0.70$  MeV, and  $dS/dA$  the discrete derivative of shell effects

$$\frac{dS}{dA} = \frac{1}{4} \left[ S(Z+1, N+1) - S(Z-1, N-1) \right]. \quad (\text{I.103})$$

Though fitted to experimental data, this sophisticated model has been developed such that it is reasonable to expect that it remains valid at high asymmetries. Indeed, the level of reproduction of the measured densities of states is the same for nuclei included

in the fit and nuclei which were not [Egi05].

### I.2.3 In-medium effects

We now focus on the in-medium effects, that is the Coulomb energy due to interaction with electrons  $E_{coul}$  and the additional free energy due the interaction with the nucleon gas  $\delta F$  of eq. (I.30).

#### I.2.3.a Coulomb energy

A Wigner-Seitz cell whether defined in the lattice at zero temperature within the SNA, or generalized at finite temperature in the NSE, is a nearly spherical polyhedron in the body centered cubic lattice [Cha05]. To evaluate the Coulomb electron screening energy  $E_{coul}$ , we make the so-called Wigner-Seitz approximation [Wig34] according to which the WS cell is a perfect sphere, with an effective radius  $R_{WS}$ . This approximation, also made to evaluate the gas energy of the WS cells, is known to little change the energy [Cha07].

Assuming the nucleus as a hard sphere of proton density  $\rho_{sat,p}(\delta)$ , two distinct regions can be distinguished, corresponding to inside the nucleus where the charge density is  $\rho_c = \rho_{sat,p}(\delta) + \rho_{g,p} - \rho_e$  and outside the nucleus where  $\rho_c = \rho_{g,p} - \rho_e$ . Then the electric flux  $\mathcal{E}(r)$  is analytically given in reverting the Gauss's law in the spherical approximation, and in considering vacuum outside the WS cell. The total Coulomb energy of the cell is then simply given by

$$E_{coul}^{cell} = 2\pi \int_0^{R_{WS}} dr V(r) \rho_c(r) r^2, \quad (\text{I.104})$$

where  $V(r)$  is the potential associated to  $\mathcal{E}(r)$ . Neglecting the proton gas density  $\rho_{g,p}$  compared with the electron one  $\rho_e$ , we obtain the Coulomb interaction energy in the Wigner-Seitz approximation due to electrons [Lat85]:

$$E_{coul}(A, Z, \delta, \rho_e) = a_c \frac{Z^2}{A^{1/3}} \left[ \frac{1}{2} \frac{\rho_e}{\rho_{sat,p}(\delta)} - \frac{3}{2} \left( \frac{\rho_e}{\rho_{sat,p}(\delta)} \right)^{1/3} \right]. \quad (\text{I.105})$$

In this equation, we have neglected the surface Coulomb energy, coming from the finite diffusivity of the proton density profile.

#### I.2.3.b Nuclear in-medium effects

Let us turn to the free energy  $\delta F = \delta E - T\delta S$  due to nuclear interaction between the unbound nucleons and the cluster. According to section I.1.1.c, the WS cell free energy

is

$$F_{WS}(A, Z, \rho_{g,n}, \rho_{g,p}) = F_{vac}(A, Z) + f_{gas}(\rho_{g,n}, \rho_{g,p})V_{WS} + \delta F + E_{coul}(N, Z, \rho_e), \quad (\text{I.106})$$

or, equivalently,

$$F_{WS}(A, Z, \rho_{g,n}, \rho_{g,p}) = F_e(A, Z, \rho_{g,n}, \rho_{g,p}) + f_{gas}(\rho_{g,n}, \rho_{g,p})V_{WS} + E_{coul}(N, Z, \rho_e), \quad (\text{I.107})$$

with  $F_e$  the free energy of the e-cluster defined as the ensemble of bound nucleons. If we consider the cluster as a hard sphere of constant nucleon density, the e-cluster free energy is thus equal to the in-vacuum nucleus free energy from which is removed the free energy of the gas inside the cluster. As clusters have a finite diffuseness, we introduce the free energy hard sphere correction  $\delta F_s$  such that

$$F_e(A, Z, \rho_{g,n}, \rho_{g,p}) = F_{vac}(A, Z) - f_{gas}(\rho_{g,n}, \rho_{g,p})V_{cl} + \delta F_s(A, Z, \rho_{g,n}, \rho_{g,p}). \quad (\text{I.108})$$

In this equation,  $V_{cl} = A/\rho_{sat}(\delta)$  is the hard sphere equivalent volume of the cluster. Using eqs. (I.106), (I.107) and (I.108), the nuclear in-medium free energy reads

$$\delta F(A, Z, \rho_{g,n}, \rho_{g,p}) = \delta F_b(A, Z, \rho_{g,n}, \rho_{g,p}) + \delta F_s(A, Z, \rho_{g,n}, \rho_{g,p}), \quad (\text{I.109})$$

where we have introduced the bulk free energy

$$\delta F_b(A, Z, \rho_{g,n}, \rho_{g,p}) = -\frac{f_{gas}(\rho_{g,n}, \rho_{g,p})}{\rho_{sat}(\delta)} A. \quad (\text{I.110})$$

These relations will be derived for the energy from ETF considerations in part II. In particular, we will show that the in-medium bulk energy at zero temperature  $\delta E_b = -\mathcal{H}_{gas}(\rho_{g,n}, \rho_{g,p})A/\rho_{sat}(\delta)$  depends in a complex non-linear way on the asymmetry of both the cluster and the gas, such that no general conclusions can be drawn on systematic effects of the medium. It is also pointed out that  $\delta E_b$  exhausts the whole bulk energy, and the non-negligible extra energy  $\delta E_s$  is due to in-medium surface and curvature effects.

Let us notice that in all the equations of this section, we have used the particle numbers of the r-clusters, corresponding to more dense central part of the WS cell, and not of the e-clusters, which are defined as the bound nucleons. For example, the in-vacuum energy  $E_{vac}$  is a function of the r-particles  $A$  and  $Z$ . Let us stress that this is not an arbitrary choice, but comes from mean-field considerations which imply that the energy density is a non-linear functional of nucleon density. As a consequence, the energy of an r-space region is not equal to the sum of the energy of bound nucleons on the one hand, and unbound nucleons on the other hand, since both contribute to the nucleon density of the same r-space region. The correct energetics thus depends on the

r-particles ( $A, Z$ ).

## Chapter I.3

# Results at chemical equilibrium

In this chapter, we present some results at  $\beta$ -equilibrium and low temperatures, relevant for the slow cooling stage of proto-neutron stars outer and inner crust. These results have been obtained by solving the NSE model developed in chapter I.1. Unless explicitly specified, we use the equations of chapter I.2, without considering pairing effects in the gas, sec. I.2.1.e. Its implementation is a work in progress [Bur15]. The in-medium surface effects  $\delta F_s$  though potentially important, have been also neglected for these preliminary results. (They are studied in part II.)

In section I.3.1, we first present the numerical code which allows to solve our NSE model. The total proton fraction which is constrained by the  $\beta$ -equilibrium is discussed in section I.3.2 and the cluster distribution is investigated in section I.3.3. More specifically, we emphasize that different species are almost always present in matter, even at low temperatures  $T \lesssim 500$  keV. In section I.3.4, we compare average matter composition based on different cluster ground states energy prescriptions and show that, as expected, the experimental masses as well as an extrapolation model are required.

### I.3.1 The numerical code

On the contrary of the SNA, the Nuclear Statistical Equilibrium model does not need to minimise any quantity since the variational character of the approach is inherent to the construction of the partition function eq. (I.5). Solving the NSE thus amounts to properly determine the conjugate variables to the fixed quantities  $(\mu_n, \mu_p)$ , that is the gas densities and the (per volume) cluster multiplicities  $n_{NZ}(A, Z, \rho_{g,n}, \rho_{g,p}, \rho_p)$  eq. (I.35). The main challenge is that these quantities define several self-consistencies. The numerical code used to solve the NSE is briefly explained in what follows.

Noticing that the cluster distribution  $\{n_{NZ}\}$  depends on the gas components because of the nuclear interaction  $\delta F_b$ , it is natural to first calculate the gas partition function.

For a given set  $(\beta, \mu_n, \mu_p)$ , the self-consistent equations of nuclear matter eqs (I.72) and (I.74) are solved by iterations, using the 2-dimension Newton-Raphson method. This method allows to find, using quasi-analytical derivatives, the roots of the function  $f(\mu_q^{calc}) = \mu_q^{calc} - \mu_q$ , with  $\mu_q^{calc}$  the calculated quantities in inverting the Fermi distributions. Because of the phase transition of non-charged nuclear matter, three different densities may be found. In what follows, we assume working at total low densities and we choose if necessary the lowest gas densities.

Because of charge neutrality, we need to know a priori the total proton density  $\rho_p$  to calculate the cluster components  $n_{NZ}$  which, in their turn allow to calculate  $\rho_p$ , according to eq. (I.34). We could solve this self-consistency at this point, but since the physical conditions of compact star matter, that is the dynamics time and the position inside the star, are not related to the chemical potentials but to the average densities, it is more interesting to directly work with the average total densities  $(\rho_n, \rho_p)$  as first inputs. Thus knowing these densities allows to directly calculate the composition matter  $\{n_{NZ}\}$ , and the calculated total densities  $\rho_q^{calc} = \sum_{N,Z} N n_{NZ}$  are compared with the inputs. Again the 2-dimension Newton-Raphson method allows to find the roots of  $f(\rho_q^{calc}) = \rho_q^{calc} - \rho_q$ . The NSE model is solved and the average quantities can be calculated via the equations of sec. I.1.2.

For matter at  $\beta$ -equilibrium without neutrinos, that is

$$\Delta\mu = \mu_n - \mu_p - \mu_e = 0, \quad (\text{I.111})$$

an additional constraint is added, which establishes a relation between the two total densities  $\rho_n$  and  $\rho_p$ . From a practical point of view, the global code strategy can be sketched as follows: imposing a temperature and a total density, a first value of the total proton fraction  $Y_p = \rho_p/\rho_B$  is guessed. For iteratively found chemical potentials, the corresponding gas component is calculated, then the cluster one, until convergence on the assumed proton fraction. This procedure is repeated in increasing (decreasing)  $Y_p$  for positive (negative)  $\Delta\mu$ . The  $\beta$ -equilibrium solution is found by binary search.

In the following sections, we present results at  $\beta$ -equilibrium and low temperatures  $T \leq 2$  MeV for some representative densities relevant for outer and inner crust of proto-neutron stars, using experimental masses when available, and the Skyrme interaction SLy4 [Cha98] for both the nucleon gas and the cluster ground state energy eq. (I.84) when there are no experimental data.

### I.3.2 Proton fractions

The result of  $\beta$ -equilibrium eq. (I.111) giving the relation between the average proton fraction  $Y_p = \rho_p/\rho_B$  and the average baryon density  $\rho_B$  is displayed in figure I-1(a)

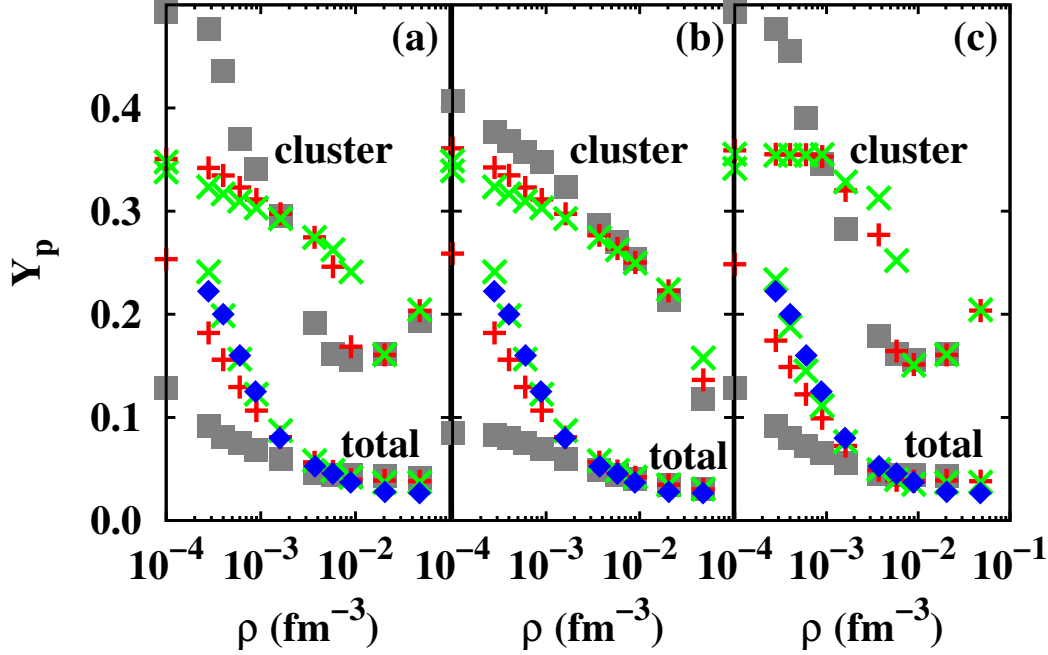


Figure I-1: Average cluster (upper symbols) and total (lower symbols) proton fraction as a function of the baryon density, for different temperatures  $T = 2$  MeV (grey square),  $T = 1$  MeV (red plus), and  $T = 500$  keV (green cross). Panel a): calculations using experimental data when available and parametrizations (I.83) and (I.86) otherwise; panel b): calculations using parametrizations (I.83) and (I.86) only; panel c): calculations using experimental data only. Total proton fraction at zero temperature from [Neg73] are given for comparison (blue diamond).

(labelled “total”), for different temperatures. We can see that the higher the density, the less temperature dependent the proton fraction. Globally, we recover the feature of monotonic increase of neutron richness with increasing density. As a consequence, the cluster proton fraction  $\rho_{cl,p}/\rho_{cl} = \sum_{NZ} Z_e n_{NZ} / \sum_{NZ} A_e n_{NZ}$  (upper symbols, labelled “cluster”) is also decreasing, except at the highest density. This last observation can be understood from the matter composition (see sec. I.3.4).

The decrease of total proton fraction with density, specific to  $\beta$ -equilibrium, is due to the electrons, and can be explained as follows. Considering the  $\beta$ -equilibrium condition  $\mu_n = \mu_p + \mu_e$  reached for a given density  $\rho_B$ , an increase  $\delta\rho_B$  of the baryon density implies increase of both the proton and the electron densities, that is the corresponding chemical potentials are modified by  $\delta\mu_p > 0$  and  $\delta\mu_e > 0$ . As a consequence of  $\beta$ -equilibrium, the neutron chemical potential modification due to the variation  $\delta\rho_B$  is  $\delta\mu_n = \delta\mu_p + \delta\mu_e$ , that is  $\delta\mu_n > \delta\mu_p > 0$ , which means that the neutron density increase

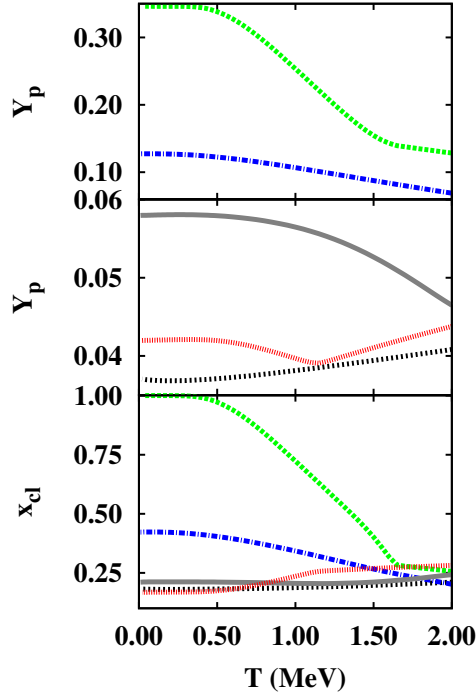


Figure I-2: Total proton fraction (upper and central panels) and cluster fraction (lower panel) as a function of temperature, for different densities. Green dashed lines:  $\rho_B = 1.0 \cdot 10^{-4} \text{ fm}^{-3}$ ; blue dashed-dotted lines:  $\rho_B = 9.0 \cdot 10^{-4} \text{ fm}^{-3}$ ; grey full lines:  $\rho_B = 3.7 \cdot 10^{-3} \text{ fm}^{-3}$ ; red dotted lines:  $\rho_B = 9.0 \cdot 10^{-3} \text{ fm}^{-3}$ ; Black short-dashed lines:  $\rho_B = 4.8 \cdot 10^{-2} \text{ fm}^{-3}$ ;

is more important than the proton one, leading to a decrease of the proton fraction. This neutron enrichment process can thus be simply understood as the consequence of the charge neutrality and the Pauli exclusion principle of electrons, which implies that for each extra proton, an extra electron occupying higher level energy density has to be added, favouring neutrons over pairs of protons and electrons. Therefore the proton fraction of matter at  $\beta$ -equilibrium in the neutrino-free regime is dominated by electrons properties and can be expected to not depend much on the details of the nuclear interactions, as we now turn to show.

For comparison, the zero temperature results of the pioneering work [Neg73] are also displayed in fig. I-1(a) (blue diamond). In this model, the WS cell nuclear energy is calculated with the Hartree-Fock method based on a simple energy functional. We can see that our results at low temperatures ( $T = 500 \text{ keV}$ , green cross) are in a very good agreement with [Neg73], corroborating the dominance of the relativistic electron gas used in both models. More generally, we can conclude that the proton fraction is largely independent of the nuclear interaction as it has been shown in [Rad14], and of the nuclear details of the clusters model. This statement is confirmed in figs. I-1(b) and I-1(c).

In panel (b), the calculations have been made using only the cluster parametrizations eqs. (I.84) and (I.89) respectively for the ground states energy and for the excited states. In panel (c), we consider clusters only with experimental data [Aud12]. These less sophisticated and very different prescriptions lead to very close total proton fraction whereas the average clusters proton fraction, thus the matter composition, is different (upper symbols of each panel).

The temperature dependence of the total proton fraction is displayed in the upper and central panels of fig. I-2, for several densities. For the same densities, the lower panel of the figure shows the cluster fraction  $x_{cl} = \rho_{cl}/\rho_B$  as a function of the temperature. We can see that for the lowest density considered  $\rho_B = 1.0 \cdot 10^{-4} \text{ fm}^{-3}$  (green dashed curve),  $x_{cl} \simeq 1$  at low temperatures, meaning that there is no gas. Therefore this density corresponds to the outer crust. The other displayed densities are relevant for the inner crust. From fig. I-2, we can observe that the total proton fraction is non-monotonic with temperature: at low densities, it decreases whereas at high densities it slightly increases (black dashed lines). To understand this behaviour, we need to investigate the matter composition (see sec. I.3.4).

### I.3.3 Cluster distribution

The specificity of the NSE model is that it allows different species of clusters to coexist at the same physical conditions, leading to a distribution represented by the set of multiplicities  $\{n_{NZ}\}$  eq. (I.35). From these quantities, we can define the multiplicities of charge  $n_Z = \sum_A n_{(A-Z)Z}$  (respectively of mass  $n_A = \sum_Z n_{(A-Z)Z}$ ) which stand for the number of r-clusters of charge  $Z$  (respectively of mass  $A$ ) in a volume unit. Let us notice that we could also define the multiplicities of e-clusters. But since the r-clusters are relevant for the energetics, we choose to study them in what follows.

The mass distribution (at  $\beta$ -equilibrium) is given in fig. I-3, for different temperatures and densities. Panel (a) shows the results for the inner layer of the outer crust, and panels (b), (c) and (d) represent increasingly deep regions in the inner crust, where the nucleon gas density increases. Globally, we can see two separate peaks: a large one at medium-heavy masses and a sharper one at light masses, and their respective weights depend on both the temperature and the density. The large spread of heavy clusters comes from the flat minimum of binding energy as a function of  $N$  and  $Z$ , whereas only a few light nuclei are favoured due to detailed nuclear structure properties that lead to huge binding energy variations in these few-body systems.

This general bimodal behaviour signs the competition between two opposite effects which are energy and entropy. Indeed, the light clusters, though less bound than the heavy ones, are favoured by their entropy part associated to their translational motion,

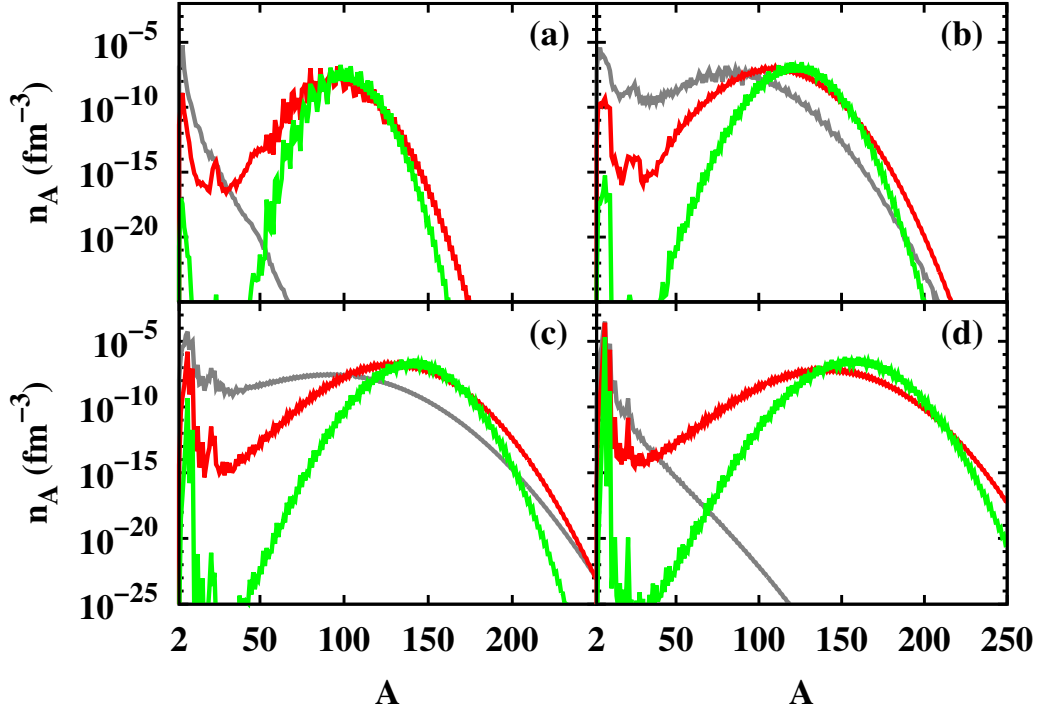


Figure I-3: Mass distribution for different temperatures  $T = 2$  MeV (grey),  $T = 1$  MeV (red), and  $T = 500$  keV (green). Panel a):  $\rho_B = 1.0 \cdot 10^{-4} \text{ fm}^{-3}$ ; panel b):  $\rho_B = 9.0 \cdot 10^{-4} \text{ fm}^{-3}$ ; panel c):  $\rho_B = 3.7 \cdot 10^{-3} \text{ fm}^{-3}$ ; panel d):  $\rho_B = 9.0 \cdot 10^{-3} \text{ fm}^{-3}$ .

eq. (I.24). The available volume for the center of mass does not depend on the cluster size. Consequently, a system made of  $N$  bound particles has the exact same entropy as 1 particle,  $\propto V_{tot}$ , whereas the entropy of  $N$  free particles is  $\propto V_{tot}^N$ . This simple argument explains why, for a given density, we can observe in fig. I-3, that the light clusters become dominant with increasing temperatures. For this reason, at  $T = 2$  MeV, there is almost no heavy clusters. More specifically, we can see in panels (a) and (d) that the peak at large size has disappeared, meaning that the entropy completely dominates over the binding energy. On the contrary, at low temperatures where the energy is dominant, the distribution of clusters is sharper, in agreement with the zero temperature limit for which only the most bound cluster survives.

Concerning the density dependence, the main effect is to shift the distribution to heavier clusters. This is due to the  $\beta$ -equilibrium condition which leads to a decrease of the proton fraction with density (fig. I-1). This extra neutron-richness affects both the cluster and the unbound components and this balance leads to populate more neutron-rich, thus heavier clusters. Clusters at higher densities are therefore more neutron-rich, thus less bound, leading to a smaller binding energy per nucleon difference with light clusters. This is why the entropy factor is at high densities more dominant for lower

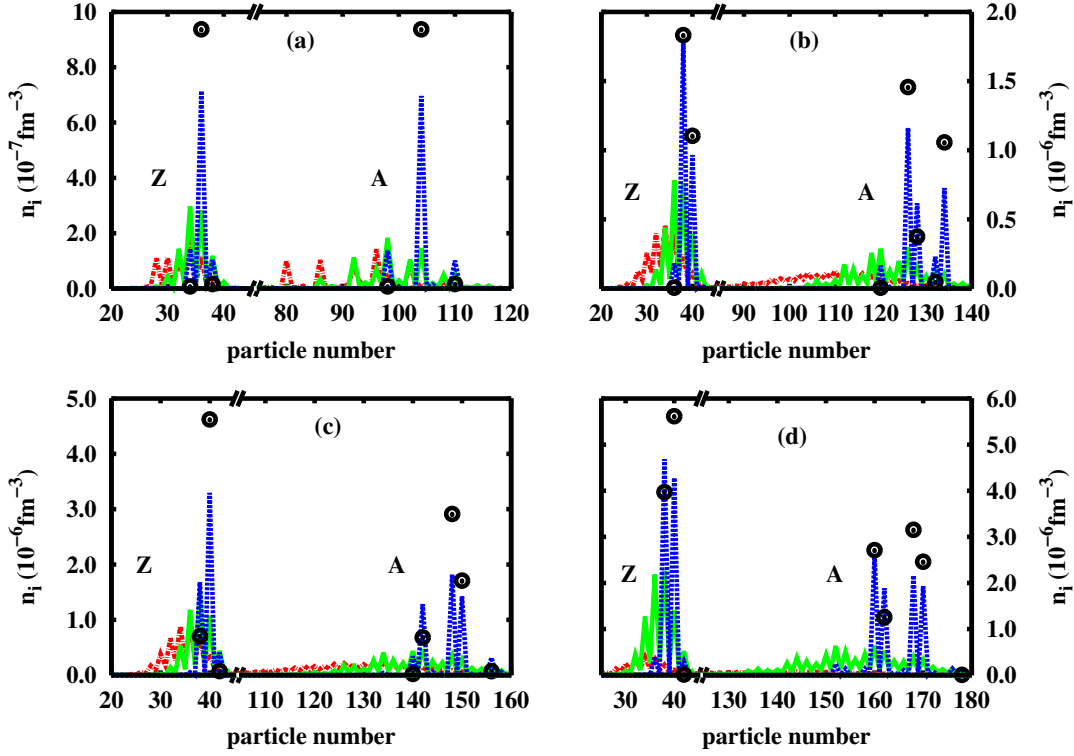


Figure I-4: Charge  $n_Z$  (left curves of each panel) and mass  $n_A$  (right curves of each panel) distributions for different temperatures  $T = 1 \text{ MeV}$  (red dash dotted lines),  $T = 500 \text{ keV}$  (green full lines),  $T = 100 \text{ keV}$  (blue dashed lines), and  $T = 40 \text{ keV}$  (black circles). Panel a):  $\rho_B = 1.0 \cdot 10^{-4} \text{ fm}^{-3}$ ; panel b):  $\rho_B = 9.0 \cdot 10^{-4} \text{ fm}^{-3}$ ; panel c):  $\rho_B = 3.7 \cdot 10^{-3} \text{ fm}^{-3}$ ; panel d):  $\rho_B = 9.0 \cdot 10^{-3} \text{ fm}^{-3}$ .

temperatures than in the case of lower densities. This clearly appears from fig. I-3: increasing density makes the light clusters dominant.

The mass distribution  $n_A$  and the charge distribution  $n_Z$  of the heavy clusters are displayed in linear scale in fig I-4 for the same densities as in fig I-3. The previous temperatures  $T = 1 \text{ MeV}$  and  $500 \text{ keV}$  are shown again as well as very low temperatures  $T = 100 \text{ keV}$  (blue dashed lines) and  $T = 40 \text{ keV}$  (black symbols). Globally, at temperatures below  $1 \text{ MeV}$ , only even-even nuclei are present, reflecting the important contribution of pairing effects in the ground state energy.

Unlike the mass distributions, the charge ones are not shifted in the inner crust: the cluster proton number is always around 40. This stability can be explained by the cancellation of two opposite effects. On the one side, the increase of density favours more charged clusters since the Coulomb interaction is screened by the increased electron gas density. On the other hand, the neutron enrichment induced by the  $\beta$ -equilibrium condition increases the isovector (repulsive) interaction (term in  $I^2$  in eq. (I.83)), which

limits the asymmetry, thus the charge, of the cluster. Let us notice that since supernovae matter is out of  $\beta$ -equilibrium, much massive clusters can exist during the collapse.

At low densities, the distributions of fig. I-4(a) exhibit several dominant clusters for temperatures above 100 keV (blue dashed lines). It is only at very low temperatures ( $T = 40$  keV) that only one specie remains and that the SNA can be safely applied. For higher densities however (panels (b), (c), (d)), the distributions in charge and in mass are multivalued for any temperature. Let us also observe in the figure that the most probable cluster  $(N_m, Z_m)$ , defined by the multiplicity maximum  $n_{N_m Z_m} = \max_{NZ} (n_{NZ})$ , is modified at low temperatures, especially between 500 keV and 100keV.

These results give indications that 40 keV in the inner crust and 100 keV in the outer crust are not low enough temperatures to be considered as zero temperature as far as the composition is concerned. Considering the low proton fractions, the binding energy of the nuclei considered are calculated with the parametrization eq. (I.84), where shell effects are not taken into account. This is an important limitation at these low temperatures and shell corrections have definitely to be applied to have realistic predictions [Ons08]. However it is interesting to remark that the dominance of  $Z = 40$  is kept if more sophisticated mass formulas containing shell effects are used, like for instance the Duflo-Zucker model [Ons08; Gor13; Gul15]. The non-smooth additional energy reduces the number of species. However, due to the competition of different shell closures, different bimodalities between highly different nuclear species (namely  $N = 50$  and  $N = 82$ ) appear [Gul15]. This means that, even adding shell effects, it is still very important to account for the whole NSE distribution even at very low temperatures.

### I.3.4 Average composition

In order to study general behaviours as a function of temperature and density, it is convenient to introduce quantities summarizing the matter composition. From the bimodal distributions (fig. I-3), we can conclude that the average cluster size  $\sum_{NZ} A n_{NZ} / \sum_{NZ} n_{NZ}$  and charge  $\sum_{NZ} Z n_{NZ} / \sum_{NZ} n_{NZ}$  are not necessarily representative of the clusters present in the matter. We thus introduce the most probable cluster  $(A_m, Z_m)$ . These quantities are displayed in fig. I-5 (symbols) as a function of the temperature for the four densities previously studied. The average cluster particle numbers (lines) are also plotted to give the weighting between the light clusters species and the medium-heavy ones.

We globally recover the general behaviours described in sec. I.3.3: at high temperatures, light nuclei dominate (where the average and most probable cluster nucleon numbers coincide), whereas at low temperatures, it is the heavy clusters which do. However, for a large domain of intermediate temperatures which depend on the density considered, the average mass and size (lines) show that heavy and light clusters coexist and neither

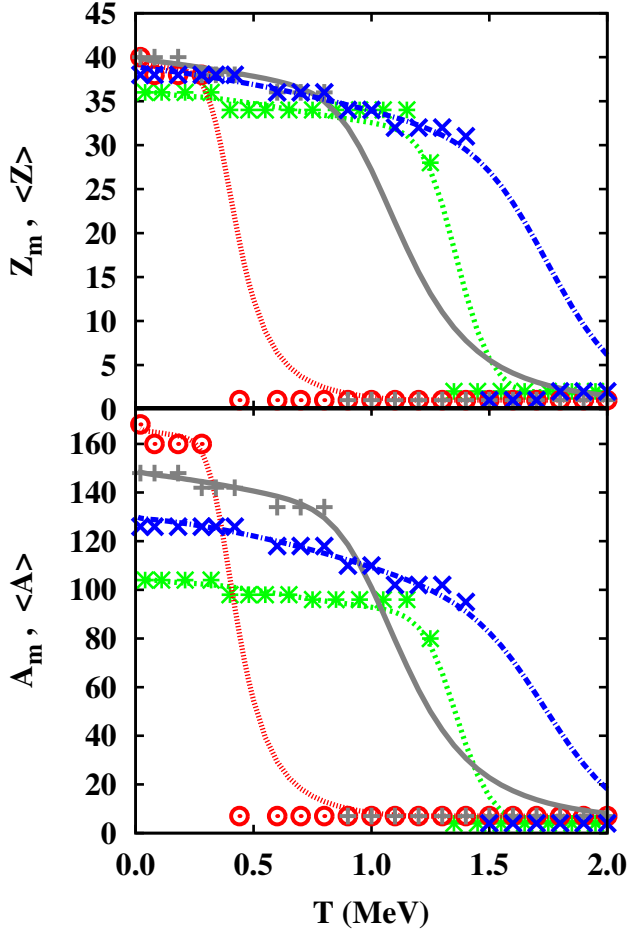


Figure I-5: Most probable (symbols) and average (lines) charge (upper panel) and mass (lower panel) as a function of the temperature, for different densities. Green dashed lines and stars:  $\rho_B = 1.0 \cdot 10^{-4} \text{ fm}^{-3}$ ; blue dashed-dotted lines and crosses:  $\rho_B = 9.0 \cdot 10^{-4} \text{ fm}^{-3}$ ; grey full lines and plus symbols:  $\rho_B = 3.7 \cdot 10^{-3} \text{ fm}^{-3}$ ; red dotted lines and circles:  $\rho_B = 9.0 \cdot 10^{-3} \text{ fm}^{-3}$ .

of them can be neglected. This is why most of SNA models considered heavy clusters in chemical equilibrium with, in addition to the nucleon gas, a light nuclei gas, usually made of alpha particles [Lam78; Lat91; She11]. We indeed recover  ${}^4\text{He}$  particles at low densities and high temperatures ( $\rho_B = 10^{-4} \text{ fm}^{-3}$  (green star) for  $T \gtrsim 1.3 \text{ MeV}$  and  $\rho_B = 9 \cdot 10^{-4} \text{ fm}^{-3}$  (blue cross) for  $T \gtrsim 1.8 \text{ MeV}$ ). However because of the very low total proton fraction at high densities, nuclei cannot be symmetric and we find that light clusters are essentially  ${}^7\text{H}$ . The binding energy of this specific nucleus has been estimated by [Aud12] at 0.940 keV per nucleon, and it is the considered heaviest bound isotope of hydrogen, as well as the nucleus richest in neutrons of the database. Though not very bound, it appears to dominate over WS cells made of alpha particles. Indeed, in that

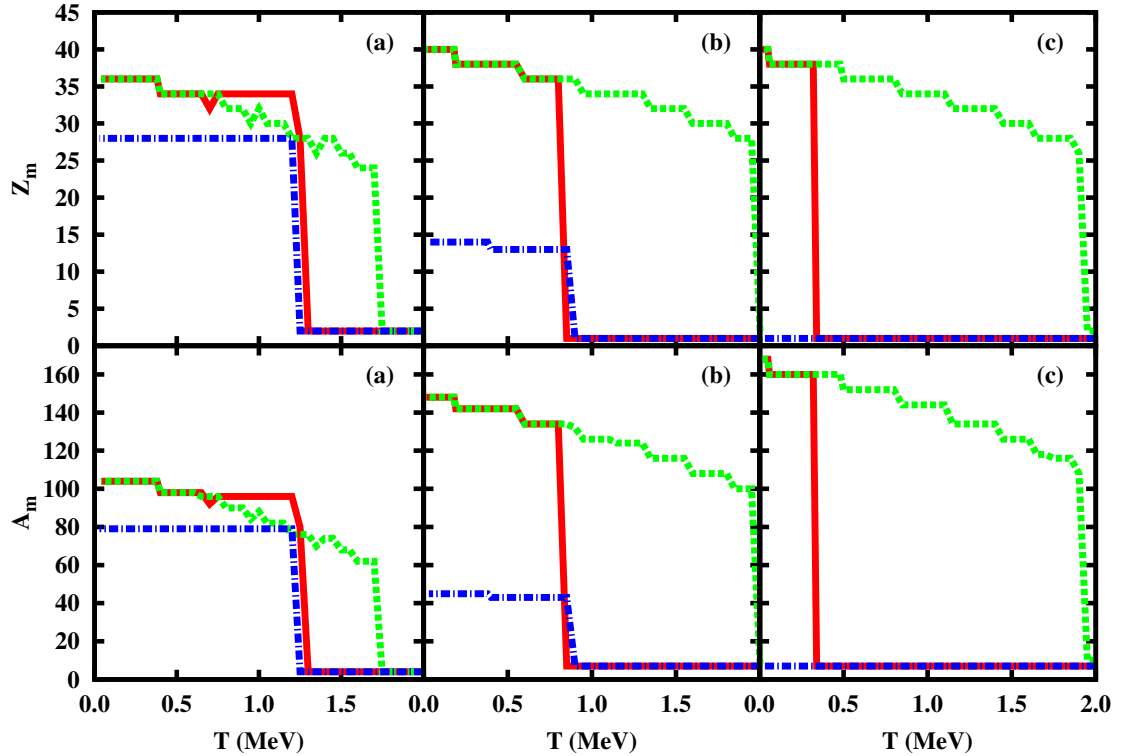


Figure I-6: Most probable charge (upper panels) and mass (lower panels), as a function of the temperature, calculated with three prescriptions: using experimental data when available and parametrizations (I.83) and (I.86) otherwise (red full lines), using parametrizations (I.83) and (I.86) only (dashed green lines), using experimental data only (dashed-dotted blue lines). Panels a):  $\rho_B = 1.0 \cdot 10^{-4} \text{ fm}^{-3}$ ; Panels b):  $\rho_B = 3.7 \cdot 10^{-3} \text{ fm}^{-3}$ ; Panels c):  $\rho_B = 9.0 \cdot 10^{-3} \text{ fm}^{-3}$ .

case, a denser neutron gas should be present at higher density to recover the correct total proton fraction, and such configurations correspond to an increased total energy with respect to the ones containing neutron-rich resonances. Therefore, the neutron richest clusters, which can be seen as light gas resonances, are favoured over other nuclei.

To corroborate this statement, we have calculated in fig. I-6 the most probable clusters predicted by the NSE using only the experimental database [Aud12] (dashed-dotted blue lines) and using only the Skyrme-based parametrizations (dashed green lines). We recall that these different mass models give the same total proton fraction (see sec. I.3.2). The red full lines of fig. I-6 are our standard results which mix both experimental data and parametrizations. As expected at the lowest considered proton fractions, heavy clusters at low temperatures are exclusively given by the parametrizations (the green dashed and full red lines coincide), reflecting the fact that the available nuclei from [Aud12] are not neutron-rich enough. At low densities, (panel (a)), the light clusters predicted by

the parametrization only also give  ${}^4\text{He}$ . However, they differ from the mixed model at higher densities: they predict  ${}^8\text{He}$  (panel (b)) and  ${}^{10}\text{He}$  (panel c) at 2 MeV. Though in quantitative disagreement, the qualitative behaviour is similar to the one obtained using the experimental database: in order to minimize the energy, neutron-rich light clusters are favoured over symmetric ones.

This statement may be revised when adding the surface in-medium interaction  $\delta F_s$ . Indeed, light particles having diffuse surface are expected to be very sensitive to surface corrections which are completely neglected in these calculations. More generally, in-medium effects for these light resonances might not be realistically treated in a mean-field approach like ours, which is essentially based on local density approximations. For this reason, it will be very interesting to include in the model the in-medium binding-energy shifts calculated from microscopic models [Typ10; Hem11]. Pairing interaction in the gas might also have an influence in decreasing the energy difference between WS cells made of symmetric clusters in high neutron gas density and neutron rich clusters in low neutron gas density.

From this detailed analysis of matter composition, we can explain the non monotonicity of the total proton fraction observed in sec. I.3.2. Indeed, comparing the behaviours of fig. I-2 with the dominant clusters fig. I-5, interesting correlations can be established. On the one hand, at low densities  $\rho_B \leq 3 \cdot 10^{-3} \text{ fm}^{-3}$  (blue, green and grey curves), heavy clusters are present at almost every temperature.  $\beta$ -equilibrium is thus established within clusterized matter, leading to a decrease of the proton fraction with temperature. A particular behavior is obtained at  $\rho_B = 10^{-4} \text{ fm}^{-3}$  (green lines) for  $T \gtrsim 1.6 \text{ MeV}$ , where  ${}^4\text{He}$  completely dominate matter (fig. I-5). This leads to a change of slope in the proton fraction in fig. I-2. On the other hand, at the higher density  $\rho_B = 9 \cdot 10^{-3} \text{ fm}^{-3}$ , the matter composition switches from heavy clusters at  $T \lesssim 0.4 \text{ MeV}$  to only light resonances  ${}^7\text{H}$  at  $T \gtrsim 1.1 \text{ MeV}$ , which corresponds to the minimum of the proton fraction. For the highest density  $\rho_B = 4.8 \cdot 10^{-2} \text{ fm}^{-3}$ , only displayed in fig. I-2, where we can see the monotonic increase of proton fraction, we have checked that  ${}^7\text{H}$  are always dominant. Therefore, the non-monotonicity of the total proton fraction is due to the fact that matter switches from a  $\beta$ -equilibrium dominated by heavy clusters, to a  $\beta$ -equilibrium dominated by loosely bound light resonances and free particles. These light clusters have an energetics similar to the nucleon gas for which the proton fraction increases with temperature.

# Part conclusions

In this part, we have considered a Nuclear Statistical Equilibrium (NSE) model based on the grand canonical partition function for a system composed of electrons, photons, neutrinos, protons, neutrons, and clusters of all sizes and isospin composition, in thermal and chemical equilibrium with respect to the strong interaction. The self-interaction of the proton and neutron gas is considered in the self-consistent mean-field approach, while clusters are modelled as an ideal gas with the only interaction given by the Coulomb screening effect of the electron gas. The interaction between the clusters and the free particles is split in a bulk and a surface part. For the preliminary results shown in this part, only the bulk part has been included. The grand-canonical partition sum can be factorized into its leptonic, photonic, and baryonic components. Since the first ones are very well known, we have particularly focussed on the baryonic sector, which can naturally be factorized in independent Wigner-Seitz cells partition functions. In turn, they can be split into a homogeneous component and a cluster. To model the large variety of clusters taken into account in the NSE, we have introduced quasi-analytical formulas for the different physical quantities entering the free energy. The cluster properties have been directly evaluated by experimental data when there exist. Otherwise, a liquid-drop-like binding energy has been chosen to be consistent with the effective Skyrme interaction used for the homogeneous nucleon gas. Since the mean-field entropy is known to give a very poor description of nuclear spectroscopy, the cluster excited states have been estimated on a realistic formula, fitted on a wealth of experimental data.

Using the SLy4 effective interaction for both the free nucleons and the nucleus part of the Wigner-Seitz cells, we have shown results relevant for proto-neutron stars crust, that is at  $\beta$ -equilibrium and low temperatures. We have shown that the total proton fraction is mainly constrained by the  $\beta$ -equilibrium condition, and therefore does not depend much on the details of the mass model. Concerning matter composition, we have seen that due to the competition between energy and entropy, either light or heavy clusters can be dominant, but they often coexist. This bimodal distribution implies that NSE models need both experimental data and extrapolated parametrizations. Indeed, due to the low proton fractions typically encountered in the stellar medium, there is no

mass information for the heavy clusters of the inner crust and the inner layer of the outer crust. A parametrized mass model has therefore to be employed, and consistency with the free-particle treatment as well as the requirement of having a unified equation of state for the crust and the core of neutron stars require that this mass model is compatible with the effective interaction used to describe the free particles. On the other hand, such mean-field models have poor performances concerning light clusters, and for them the use of experimental data appears mandatory.

We have shown that a wide distribution of clusters survives even at very low temperatures, such that NSE models are required to realistically describe proto-neutron stars matter even at low temperatures  $T \sim 500$  keV. Even below this temperature, temperature effects should not be neglected since the most probable cluster can change when decreasing temperature. Finally, we have found that the light clusters are not systematically alpha particles. Indeed, because of low proton fractions, very asymmetric light resonances seem to be more favoured. This last result should be taken with caution since cluster surface in-medium modifications which are expected to be especially important for light nuclei at low temperatures have been disregarded. Further investigations with improved models are highly desirable.

# Résumé de la partie I

Cette partie traite de la matière sous-saturée de supernovæ et de proto-étoiles à neutrons à température finie.

Comme déjà indiqué dans l'introduction générale, la matière agrégée peut être modélisée en traitant séparément les noyaux et les nucléons libres, comme cela a été fait dans [Bay71a] à température nulle. Une formulation alternative utilisant la théorie de la fonctionnelle de la densité consiste à suivre une approche entièrement microscopique, comme [Neg73]. Cette approche est en principe plus avenante car il n'est pas nécessaire de distinguer artificiellement les nucléons liés de ceux non-liés. Toute l'interaction entre la phase agrégée et celle plus diluée est donc naturellement prise en compte. Pour cette raison, et également en raison de l'augmentation de la précision et du pouvoir prédictif des fonctionnelles de densité d'énergie de champ moyen, les méthodes microscopiques Hartree-Fock (Bogoliubov) sont préférentiellement utilisées pour le calcul de l'équation d'état d'étoiles à neutrons [Gri11; Pea12; Pas13].

Les calculs de champ-moyen à température finie ont également été largement développés [Ons08; For10]. Toutefois, en raison de leur coût de calcul, ces calculs microscopiques à température finie ne sont pas adaptés aux très grands intervalles de conditions thermodynamiques explorées pendant la dynamique des supernovæ à effondrement de cœur et celle des proto-étoiles à neutrons. Par conséquent, nous croyons que les modèles avec les agrégats pris comme degrés de liberté sont encore de nos jours le plus avenant pour étudier la matière sous-saturée à température finie, comme cela a été fait dans le passé [Lat91; She98]. La limitation la plus importante de ces modèles hybrides est qu'ils supposent une configuration unique pour chaque condition thermodynamique  $(T, \rho_B, Y_p)$ , ce qui va à l'encontre du principe même de la température en mécanique statistique, qui correspond à un mélange de différents états microscopiques. Ces modèles basés sur l'approximation de noyau seul sont essentiellement destinés à calculer les propriétés moyennes de la matière.

Pour améliorer le modèle, en particulier afin d'obtenir la composition de la matière, de la plus haute importance pour la détermination des phénomènes microscopiques, des approches en équilibre statistique nucléaire sont développées. Ils permettent de prendre

en compte une complète distribution en masse et en asymétrie de noyaux. Le principal inconvénient actuel de ces modèles est que l'interaction entre les agrégats et le gaz de nucléons est, soit négligé ou au mieux approchée avec le dit effet de volume exclu: les agrégats et le gaz ne se chevauchent pas dans l'espace, et l'énergie de liaison de l'agrégat n'est pas modifiée par les nucléons libre du milieu stellaire.

Dans cette partie, nous avons considéré un modèle en équilibre statistique nucléaire basé sur la fonction de partition grand canonique pour un système composé d'électrons, de photons, de neutrinos, de protons et de neutrons, ainsi que d'agrégats de toutes tailles et composition d'isospin, en équilibres thermique et chimique par rapport à l'interaction forte. L'auto-interaction des gaz de protons et de neutrons est considéré via l'approche du champ moyen auto-cohérent, tandis que les agrégats sont modélisés comme un gaz parfait, dont la seule interaction est l'effet d'écrantage Coulombien du gaz d'électrons. L'interaction entre les agrégats et les particules libres est divisée en un terme de volume et un de surface. Pour les résultats préliminaires présentés dans cette partie, seule la partie de volume a été incluse. La fonction de partition grand-canonique peut être factorisée en ses composantes leptonique, photonique, et baryonique. Comme les deux premiers sont très bien connus, nous avons étudié le secteur baryonique, dont la fonction de partition se factorise naturellement en fonctions de partitions de cellules de Wigner-Seitz indépendantes. À leurs tours, elles peuvent être divisées en une partie homogène et un agrégat. Pour modéliser la grande variété d'agrégats pris en compte dans le modèle statistique, nous avons introduit des formules quasi-analytiques pour les différentes grandeurs physiques qui entrent dans l'énergie libre. Les propriétés de l'agrégat ont été directement évaluées par les données expérimentales lorsqu'elles existent. Sinon, une formule sophistiquée de goutte de liquide a été choisie pour décrire l'énergie de liaison, de sorte qu'elle soit compatible avec l'interaction effective de Skyrme utilisée pour le gaz homogène de nucléons. Comme l'entropie de champ-moyen est connue pour donner une description très pauvre de la spectroscopie nucléaire, les états excités des agrégats ont été évalués par une formule réaliste, ajustée sur un très grand nombre de données expérimentales.

En utilisant l'interaction effective SLy4 à la fois pour les nucléons libres et pour le noyau des cellules de Wigner-Seitz, nous avons montré des résultats pertinents pour la croûte des proto-étoiles à neutrons, c'est-à-dire en équilibre  $\beta$  et à basses températures. Nous avons montré que la fraction totale de protons est principalement contrainte par la condition de l'équilibre  $\beta$ , et ne dépend donc pas beaucoup des détails du modèle de masse. En ce qui concerne la composition de la matière, nous avons vu qu'en raison de la concurrence entre énergie et entropie, les noyaux soit légers soit lourds peuvent être dominants, mais ils coexistent souvent. Cette distribution bimodale implique que les modèles en équilibre statistique nucléaire ont besoin à la fois des données expérimentales

et de paramétrisations extrapolées. En effet, en raison des faibles fractions de protons généralement rencontrées dans le milieu stellaire, il n'y a aucune information de masse pour les agrégats lourds présents dans la croûte interne et la couche intérieure de la croûte externe des proto-étoiles à neutrons. Un modèle de masse paramétré doit donc être utilisé, et la consistance avec le traitement des particules libres ainsi que l'exigence d'avoir une équation d'état unifiée pour la croûte et le noyau des étoiles à neutrons implique que le modèle de masse doit être compatible avec l'interaction effective utilisée pour décrire les particules libres. D'autre part, ces modèles de champ moyen ont des performances médiocres concernant les noyaux légers ; leurs propriétés semblent donc devoir être nécessairement directement évaluées par les données expérimentales.

Nous avons montré qu'une large distribution d'agrégats survit même à des températures très basses ; les modèles en équilibre statistique nucléaire sont donc nécessaires pour décrire de façon réaliste la matière des proto-étoiles à neutrons, même à basse température  $T \sim 500$  keV. Même en-deçà de cette température, les effets de température ne devraient pas être négligés puisque l'agrégat le plus probable peut changer lorsque la température diminue. Enfin, nous avons constaté que les noyaux légers ne sont pas systématiquement des particules alpha. En effet, en raison des faibles fractions de protons, des faibles résonances très asymétriques semblent être plus favorisées. Ce dernier résultat doit être pris avec prudence, car les modifications de milieu de surface qui sont censés être particulièrement importants pour les noyaux légers à basses températures ont été ignorés. D'autres études avec des modèles améliorés sont fortement souhaitables.

Part II:

Modelling the energetics of  
Wigner-Seitz cells

# Part introduction

The semi-classical Thomas Fermi (TF) -also called Local Density Approximation (LDA)- and Extended-Thomas-Fermi (ETF) approaches to the density functional theory were largely used in the 80's for nuclear structure [Bra85; Tre86; Cen90] as well as astrophysical applications [Sur84; Pi86]. Two motivations of searching for approximations of the microscopic mean-field theory with effective interactions were advanced. On the one side, this semi-classical theory is quasi-analytical and thus has the advantage to highlight the functional dependence of nuclear energies and density profiles. This provides physical insights of the nuclei energetics which cannot be achieved with the numerical resolution of Hartree-Fock (HF) equations. On the other side, the computational resources at that time made systematic HF calculations very hard to perform with reliable numerical error bars. The exponential progress of numerical computing in the next two decades made this motivation obsolete, and nowadays, mean-field and beyond-mean field large-scale nuclear structure calculations [Was12] are routinely performed.

However in the recent years, a renewed interest towards the ETF theory has appeared [Ons08; Pot13; Lee10], particularly in the context of the description of stellar matter. This is largely due to the new challenges which are opened to the field and the needs for a microscopic description of the very exotic nuclear species which are expected to exist in stellar matter. Indeed, as explained in part I, a complete and microscopic description of stellar matter at sub-saturation densities and at finite temperature implies the evaluation of a very large data base of ground states and excited nuclear configurations which are not directly accessible to variational HF calculations, or are too expensive for large-scale calculations [New09].

In this condition, microscopic mean-field or beyond mean-field approaches cannot realistically be applied for a description of stellar matter in finite temperature. Then, recent models which account for the statistical distribution of nuclei rather use experimental information or simple Liquid-drop formulas for nuclear masses. Doing so, they do not consider in-medium modifications to the nuclear cluster energies [Hem10; Buy13; Fur13]. Indeed, in these models, apart from an excluded volume, the clusters are not affected by the other surrounding nucleons, that is their ground state energies are the

same in the medium as in vacuum. This approximation is clearly very severe at densities comparable to the saturation density. Therefore, the simpler ETF approach can be viewed as an interesting compromise to correctly include in-medium effects to cluster properties, and at the same time provide simple quasi-analytical expressions that can be implemented in a complete modelization of the stellar matter problem.

In this part, we present an ETF based model which, in a quasi-analytical way, provides nuclear clusters energies for ground state and excited state configurations, using parametrized nuclei density profiles. With this model, we can calculate the total energy of a Wigner-Seitz cell with an arbitrary composition in terms of cluster size and charge, and unbound nucleon density and asymmetry, in consistently taking into account all the in-medium effects, including the surface effects neglected in part I. We will focus on the ground state energy modification  $\delta E$ , and so we will not explicitly consider temperature in this part. However, we will consider any nucleus  $(A, Z)$  in any nucleon gas  $(\rho_g, \delta_g)$ , independently of chemical equilibrium between nuclei and gas, since this equilibrium is a posteriori given by the NSE model (see part I).

This part is organised as follows. In chapter [II.1](#), we introduce the semi-classical LDA and ETF formalisms which allow to express the Skyrme functional as a function of the nucleon densities only. In chapter [II.2](#), we present the modelling of the nuclear density profiles employed within the ETF. This parametrization is compared to HF calculations in order to test and quantify the accuracy of both the density profile model and the ETF approximation. We can then extract the in-medium effects which are presented in chapter [II.3](#). First applications on neutron stars are also shown.

## Chapter II.1

# Quantum mechanics and semi-classical developments

In this chapter, we develop the semi-classical (Extended-)Thomas-Fermi approximations which allow to express the Skyrme functional as a function of particle densities and their derivatives only. Using the Skyrme energy density eq. (I.68), we detail in section II.1.1 how to obtain from quantum mechanics the associated mean field operator and potentials which are involved in the semi-classical approximations. In section II.1.2, we give the expressions of the isoscalar and isovector kinetic densities  $\tau$  and  $\tau_3$  and spin-orbit density vectors  $\mathbf{J}$  and  $\mathbf{J}_3$  within both the LDA and the ETF approximations. This approach allows to express these local densities, and thus the energy density eq. (I.68), as a function of the particle densities and their derivatives only.

### II.1.1 Mean field operator of the Skyrme interaction

The semi-classical approximation expressions for the kinetic and spin-orbit densities are found from potentials associated to the energy density functional [Bra85]. In what follows, we detail how to define and calculate them, by using the notations of section I.2.1.a.

From equation (I.67), we can see that a variation of  $\delta\hat{\rho}_q$  implies a variation of  $\delta\mathcal{H}$  as follows

$$\begin{aligned}\delta\mathcal{H}[\hat{\rho}_n, \hat{\rho}_p] &= \sum_{q=n,p} \int d\mathbf{r} \frac{\delta\mathcal{H}[\hat{\rho}_n(\mathbf{r}), \hat{\rho}_p(\mathbf{r})]}{\delta\hat{\rho}_q(\mathbf{r})} \delta\hat{\rho}_q(\mathbf{r}) \\ &= \sum_q \int d\mathbf{r} \sum_{ij} H_{qji}^{MF}(\mathbf{r}) \delta\rho_{qij}(\mathbf{r}),\end{aligned}\tag{II.1}$$

where the mean field operators  $\hat{H}_q^{MF}$  have been defined as  $H_{qij}^{MF} = \delta\mathcal{H}/\delta\rho_{qji}$ . Equation

(II.1) can be rewritten as the useful relation

$$\delta\mathcal{H}[\hat{\rho}_n, \hat{\rho}_p] = \text{Tr} \left\{ \hat{H}_q^{MF} \delta\hat{\rho}_q \right\} \quad (\text{II.2})$$

with the sum over  $q$  is implicit. In our case, from equation (I.68), we can distinguish four distinct dependences:  $\mathcal{H}[\hat{\rho}_q] = \mathcal{H}(\rho_q, \nabla\rho_q, \tau_q, \mathbf{J}_q)$ , so equation (II.1) reads

$$\delta\mathcal{H}[\hat{\rho}_n, \hat{\rho}_p] = \int d\mathbf{r} \frac{\partial\mathcal{H}}{\partial\rho_q} \delta\rho_q + \frac{\partial\mathcal{H}}{\partial\nabla\rho_q} \delta\nabla\rho_q + \frac{\partial\mathcal{H}}{\partial\tau_q} \delta\tau_q + \frac{\partial\mathcal{H}}{\partial\mathbf{J}_q} \delta\mathbf{J}_q. \quad (\text{II.3})$$

Let us write this equation in the form of equation (II.2), as a trace.

Using the definition of the densities  $\rho_q(\mathbf{r})$  from equation (I.59), it straightforwardly comes  $\delta\rho_q = \sum_{\zeta, s} n_q^{\zeta s} \langle \zeta s, \mathbf{r} | \delta\hat{\rho}_q | \mathbf{r}, s \zeta \rangle$ , and then the first term of equation (II.3) is

$$\int d\mathbf{r} \frac{\partial\mathcal{H}}{\partial\rho_q} \delta\rho_q = \int d\mathbf{r} \sum_{\zeta, s} n_q^{\zeta s} \langle \zeta s, \mathbf{r} | \frac{\partial\mathcal{H}}{\partial\rho_q} \delta\hat{\rho}_q | \mathbf{r}, s \zeta \rangle = \text{Tr} \left\{ \frac{\partial\mathcal{H}}{\partial\rho_q} \delta\hat{\rho}_q \right\}. \quad (\text{II.4})$$

Using the relation  $\delta\nabla\rho_q = \nabla\delta\rho_q = \nabla(\delta\rho_q) - \delta\rho_q\nabla\cdot$ , the total gradient part vanishes because of boundary conditions that impose  $\delta\rho_q(\mathbf{r}_{bc}) = 0$ , so the second term of equation (II.3) reads

$$\begin{aligned} \int d\mathbf{r} \frac{\partial\mathcal{H}}{\partial\nabla\rho_q} \delta\nabla\rho_q &= - \int d\mathbf{r} \sum_{\zeta, s} n_q^{\zeta s} \langle \zeta s, \mathbf{r} | \delta\hat{\rho}_q \nabla \frac{\partial\mathcal{H}}{\partial\nabla\rho_q} | \mathbf{r}, s \zeta \rangle \\ &= - \text{Tr} \left\{ \nabla \left( \frac{\partial\mathcal{H}}{\partial\nabla\rho_q} \right) \delta\hat{\rho}_q \right\}. \end{aligned} \quad (\text{II.5})$$

Similarly, the term in  $\delta\tau_q$  in equation (II.3) leads to

$$\begin{aligned} \int d\mathbf{r} \frac{\partial\mathcal{H}}{\partial\tau_q} \delta\tau_q &= \int d\mathbf{r} \frac{1}{\hbar^2} \sum_{\zeta, s} n_q^{\zeta s} \langle \zeta s, \mathbf{r} | \frac{\partial\mathcal{H}}{\partial\tau_q} \hat{\mathbf{p}} \delta\hat{\rho}_q \hat{\mathbf{p}} | \mathbf{r}, s \zeta \rangle \\ &= \frac{1}{\hbar^2} \text{Tr} \left\{ \hat{\mathbf{p}} \frac{\partial\mathcal{H}}{\partial\tau_q} \hat{\mathbf{p}} \delta\hat{\rho}_q \right\}, \end{aligned} \quad (\text{II.6})$$

where we have used the invariance of the trace under cyclic permutations. Finally, the term in  $\delta\mathbf{J}_q$  in equation (II.3) becomes

$$\begin{aligned} \int d\mathbf{r} \frac{\partial\mathcal{H}}{\partial\mathbf{J}_q} \delta\mathbf{J}_q &= \int d\mathbf{r} \frac{1}{2\hbar} \sum_{\zeta, s} n_q^{\zeta s} \langle \zeta s, \mathbf{r} | \frac{\partial\mathcal{H}}{\partial\mathbf{J}_q} \hat{\mathbf{p}} \delta\hat{\rho} \times \hat{\boldsymbol{\sigma}} | \mathbf{r}, s \zeta \rangle + cc \\ &= \frac{1}{2\hbar} \text{Tr} \left\{ \left[ \frac{\partial\mathcal{H}}{\partial\mathbf{J}_q} \hat{\mathbf{p}} + \hat{\mathbf{p}} \left( \frac{\partial\mathcal{H}}{\partial\mathbf{J}_q} \right) \right] \times \hat{\boldsymbol{\sigma}} \delta\hat{\rho}_q \right\}, \end{aligned} \quad (\text{II.7})$$

where we have interchanged the variation of the density operator  $\delta\hat{\rho}_q$  and the Pauli ma-

trix operator  $\hat{\sigma}$  using  $\sum_s \langle s | \delta \hat{\rho}_q \hat{\sigma} | s \rangle = \sum_{ss'} \langle s | \delta \hat{\rho}_q | s' \rangle \langle s' | \hat{\sigma} | s \rangle = \sum_{ss'} \langle s' | \hat{\sigma} | s \rangle \langle s | \delta \hat{\rho}_q | s' \rangle = \sum_s \langle s | \hat{\sigma} \delta \hat{\rho}_q | s \rangle$ , as well as the anticommutativity of the cross product for the complex conjugate.

With equations (II.3)–(II.7), we obtain

$$\begin{aligned} \delta \mathcal{H}[\hat{\rho}_n, \hat{\rho}_p] = & \text{Tr} \left\{ \left[ \frac{\partial \mathcal{H}}{\partial \rho_q} - \nabla \left( \frac{\partial \mathcal{H}}{\partial \nabla \rho_q} \right) + \frac{1}{\hbar^2} \hat{\mathbf{p}} \frac{\partial \mathcal{H}}{\partial \tau_q} \hat{\mathbf{p}} \right. \right. \\ & \left. \left. + \frac{1}{2\hbar} \left[ \frac{\partial \mathcal{H}}{\partial \mathbf{J}_q} \hat{\mathbf{p}} + \hat{\mathbf{p}} \left( \frac{\partial \mathcal{H}}{\partial \mathbf{J}_q} \right) \right] \times \hat{\sigma} \right] \delta \hat{\rho}_q \right\}. \end{aligned} \quad (\text{II.8})$$

By identification with eq. (II.2), we obtain the 1-body mean field operators

$$\hat{H}_q^{MF} = \frac{1}{2m} \hat{\mathbf{p}} f_q(\mathbf{r}) \hat{\mathbf{p}} + V_q(\mathbf{r}) + \frac{1}{2\hbar} [\mathbf{W}_q \hat{\mathbf{p}} + \hat{\mathbf{p}} (\mathbf{W}_q)] \times \hat{\sigma}, \quad (\text{II.9})$$

where we have introduced the effective mass factors  $f_q(\mathbf{r}) = m/m_q^*(\mathbf{r})$  ( $m_q^*(\mathbf{r})$  are the effective masses), the local potentials  $V_q(\mathbf{r})$  and the spin-orbit potentials  $\mathbf{W}_q(\mathbf{r})$  as follows

$$f_q(\mathbf{r}) = \frac{2m}{\hbar^2} \frac{\partial \mathcal{H}}{\partial \tau_q} = 1 + \frac{2m}{\hbar^2} (C_{eff\rho} \pm D_{eff\rho_3}), \quad (\text{II.10a})$$

$$\begin{aligned} V_q(\mathbf{r}) = & \frac{\partial \mathcal{H}}{\partial \rho_q} - \nabla \left( \frac{\partial \mathcal{H}}{\partial \nabla \rho_q} \right) \\ = & 2C_0\rho \pm 2D_0\rho_3 + (2C_3\rho \pm 2D_3\rho_3) \rho^\alpha + \alpha\rho^{\alpha-1} (C_3\rho^2 + D_3\rho_3^2) \\ & + C_{eff\tau} \pm D_{eff\tau_3} - 2C_{fin} \nabla^2 \rho \mp 2D_{fin} \nabla^2 \rho_3 - C_{so} \nabla \cdot \mathbf{J} \mp D_{so} \nabla \cdot \mathbf{J}_3, \end{aligned} \quad (\text{II.10b})$$

$$\mathbf{W}_q(\mathbf{r}) = \frac{\partial \mathcal{H}}{\partial \mathbf{J}_q} = C_{so} \nabla \rho \pm D_{so} \nabla \rho_3 + 2C_{sg} \mathbf{J} \pm 2D_{sg} \mathbf{J}_3, \quad (\text{II.10c})$$

where the  $\pm$  and  $\mp$  stand for the neutron (above) or proton (below) quantities.

## II.1.2 Semi-classical approximations

To approximate the kinetic densities  $\tau_q$  and the spin-orbit density vectors  $\mathbf{J}_q$ , we use the well known Wigner-Kirkwood expansions in  $\hbar$ , a method developed in the 30' [Wig32; Kir33; Uhl36]. The semi-classical expansion of quantum mechanics is based on the idea that quantum effects do not modify too much the classical action, that is for systems where the relevant quantities with the dimension of an action are much larger than  $\hbar$ . This is why one can formally treat  $\hbar$  as a small quantity and perform a formal expansion in powers of it. The limit  $\hbar \rightarrow 0$  gives the classical limit. Let us notice that this is analogous to the non-relativistic limit in which one treats  $c$  as a large quantity and performs an expansion in inverse powers of  $c$ . The semi-classical approximation

of quantum mechanics consists in evaluating the corresponding path integral with the saddle point approximation around the classical action, that is at  $\hbar = 0$ .

In this paragraph, we will only quote the results up to the second order in  $\hbar$  (a detailed demonstration can be found for instance in [Gra79]):

$$\tau_q(\mathbf{r}) = \tau_{0q}(\mathbf{r}) + \tau_{2q}(\mathbf{r}) + O(\hbar^4) \quad (\text{II.11a})$$

$$\mathbf{J}_q(\mathbf{r}) = \mathbf{J}_{0q}(\mathbf{r}) + \mathbf{J}_{2q}(\mathbf{r}) + O(\hbar^4), \quad (\text{II.11b})$$

where the subscripts “0” (“2”) stand for the 0<sup>th</sup> (2<sup>nd</sup>) order term of the expansion in  $\hbar$ . The classical limit, that is the 0<sup>th</sup>, is given by [Bra85]:

$$\tau_{0q}(\mathbf{r}) = \frac{3}{5}(3\pi^2)^{2/3}\rho_q(\mathbf{r})^{5/3} \quad (\text{II.12a})$$

$$\mathbf{J}_{0q}(\mathbf{r}) = \mathbf{0}. \quad (\text{II.12b})$$

We can see that we recover the relations obtained in section I.2.1.d, in the case of homogeneous matter. That is why this is called the Local Density Approximation (LDA). Indeed, eqs. (II.12) mean that at each point of a given density  $\rho(r) = \rho^*$ , matter has the same energy density as a piece of infinite homogeneous matter at the same density  $\rho = \rho^*$ . It is interesting to observe that this classical limit, also called Thomas-Fermi (TF) approximation, is exact in the case of infinite fermionic matter since it corresponds to a state where finite size quantum corrections, that is shell effects, completely vanish. The semi-classical expansion is therefore expected to be a good approximation for large nuclei.

The first quantum corrections to the previous approximation are given by the 2<sup>nd</sup>  $\hbar$ -terms [Bra85]:

$$\tau_{2q}(\mathbf{r}) = \tau_{2q}^l(\mathbf{r}) + \tau_{2q}^{nl}(\mathbf{r}) + \tau_{2q}^{so}(\mathbf{r}), \quad (\text{II.13a})$$

$$J_{2q} = -\frac{2m}{\hbar^2}\rho_q\frac{W_q}{f_q}, \quad (\text{II.13b})$$

with

$$\tau_{2q}^l = \frac{1}{36}\frac{(\nabla\rho_q)^2}{\rho_q} + \frac{1}{3}\Delta\rho_q \quad (\text{II.14a})$$

$$\tau_{2q}^{nl} = \frac{1}{6}\frac{\nabla\rho_q\nabla f_q}{f_q} + \frac{1}{6}\rho_q\frac{\Delta f_q}{f_q} - \frac{1}{12}\rho_q\left(\frac{\nabla f_q}{f_q}\right)^2 \quad (\text{II.14b})$$

$$\tau_{2q}^{so} = \frac{1}{2}\left(\frac{2m}{\hbar^2}\right)^2\rho_q\left(\frac{W_q}{f_q}\right)^2. \quad (\text{II.14c})$$

Let us notice that the spin-orbit potentials  $W_q$  involved in eqs (II.13) and (II.14), are

expressed as a function of the spin-orbit currents (cf eq. (II.10)). So the relation between the spin currents and the gradient of the densities is in principle obtained in solving the 2x2 system of eqs. (II.10c) and (II.13b). However, in several Skyrme interactions (such as SIII, SLy4, SGII), the spin-gradient terms are neglected, that is  $C_{sg} = D_{sg} = 0$ . In that case, the spin-orbit currents are simply linearly related to the particle density gradients. For the following applications, we will only consider Skyrme forces with parameters optimized on phenomenological information in the absence of such spin-gradient terms. Therefore in what follows, we will not consider the spin-gradient interaction. We will also neglect pairing interaction. Let us notice that it can be simply taken into account in considering a different pairing strength  $v_\pi$  eq. (I.80) at each point of the density profile, that is depending on the corresponding density [Bur15].

This 2<sup>nd</sup> order Extended-Thomas-Fermi (ETF) approximation, given by eqs (II.13), allows to take into account a part of spin-orbit interaction and shell effects. In chapter II.2, we will compare this approximation with HF calculations in which these quantum effects are not approximated.

## Chapter II.2

# Density profile modelling

In the (E)TF approximation, non-local terms are entirely replaced by particle densities and their gradients. As a consequence, the energy functional eq. (I.68) solely depends on the local particle densities. Thus, the energy of any arbitrary nuclear configuration can be calculated if the density profiles  $\rho_q$  are given through a parametrized form. In this chapter, two types of such parametrizations are investigated and compared. We first focus on nuclei in vacuum (section II.2.1) where these two parametrizations are compared with HF calculations. We also present an application of the model to the study of the functional dependence of the symmetry energy on the nuclear mass. In a two-component nuclear system, we show that an explicit comparison to HF calculations can help to eliminate the ambiguity in the decomposition between surface and bulk energy, and we analyze the well known problem of the sign of the surface symmetry energy [Mye85]. In section II.2.2, we extend the previous model to the case of nuclei embedded in a nucleon gas. We recover the definitions of e- and r-clusters introduced in part I. The bulk isospin asymmetry is discussed.

### II.2.1 Nuclei in vacuum

In this section, we consider nuclei in vacuum. We present different density profiles ansatz of symmetric and asymmetric nuclei and discuss their accuracy. The definition of the density profiles allows calculating the nuclear energy using the ETF approximation. Moreover, the ETF expansion naturally leads to a decomposition of the total nuclear energy into different components (isoscalar and isovector terms, and bulk, surface and curvature parts) which usually enter nuclear mass formulas. The derivation of these different terms from a microscopic theory will shed light on the physical meaning of these terms.

### II.2.1.a Profiles of symmetric nuclei

Let us first consider a locally symmetric matter distribution, that is characterized by a single density profile which is supposed to be identical for protons and neutrons. In this case,  $\rho_3 = 0$ , and the energy density eq. (I.68) reads

$$\mathcal{H}[\rho] = h[\rho] + \frac{\hbar^2}{2m} f(\tau_2^l + \tau_2^{nl}) + C_{fin} (\nabla\rho)^2 + V_{so} \frac{\rho}{f} (\nabla\rho)^2, \quad (\text{II.15})$$

where we have highlighted the local energy density

$$h[\rho] = \frac{\hbar^2}{2m} f\tau_0 + C_0\rho^2 + C_3\rho^{\alpha+2}, \quad (\text{II.16})$$

with  $\tau_0 = 3/5 (3\pi^2/2)^{2/3} \rho^{5/3}$ , and the effective mass

$$f = 1 + \kappa\rho \quad \text{with} \quad \kappa = \frac{2m}{\hbar^2} C_{eff}. \quad (\text{II.17})$$

The second order  $\hbar^2$ -terms of eq. (II.15) are, for symmetric matter,

$$\tau_2^l = \frac{1}{36} \frac{(\nabla\rho)^2}{\rho} + \frac{1}{3} \Delta\rho, \quad (\text{II.18a})$$

$$\tau_2^{nl} = \frac{1}{6} \frac{\nabla\rho \nabla f}{f} + \frac{1}{6} \rho \frac{\Delta f}{f} - \frac{1}{12} \rho \left( \frac{\nabla f}{f} \right)^2, \quad (\text{II.18b})$$

$$V_{so} = -\frac{1}{2} \frac{2m}{\hbar^2} C_{so}^2, \quad (\text{II.18c})$$

where  $V_{so}$  is the symmetric spin-orbit potential.

#### i) Generalized Fermi function

The ground state configuration of a nucleus can be obtained from the variational calculation under the constraint of a finite number of nucleons  $A$

$$0 = \delta \left\{ \int d\mathbf{r} \mathcal{H}[\rho(\mathbf{r})] + \lambda \left[ A - \int d\mathbf{r} \rho(\mathbf{r}) \right] \right\} = \int d\mathbf{r} \left( \frac{\delta \mathcal{H}[\rho]}{\delta \rho} \delta \rho - \lambda \delta \rho \right), \quad (\text{II.19})$$

where  $\lambda$  is a Lagrange multiplier imposing the correct particle number which corresponds to the chemical potential as we will see. Since  $\mathcal{H}$  is a function of  $\rho$ ,  $\nabla\rho$  and  $\Delta\rho$ , equation (II.19) gives the following single Euler-Lagrange equation

$$\frac{\partial \mathcal{H}}{\partial \rho} - \nabla \cdot \frac{\partial \mathcal{H}}{\partial \nabla \rho} + \Delta \frac{\partial \mathcal{H}}{\partial \Delta \rho} = \lambda, \quad (\text{II.20})$$

where we have used the *fundamental lemma of calculus of variations*, and the boundary conditions  $\delta\rho_q(\mathbf{r}_{bc}) = 0$  and  $\delta\nabla\rho(\mathbf{r}_{bc}) = \mathbf{0}$  for factorizing  $\delta\rho$ . Substituting eq. (II.15) into the Euler-Lagrange equation, and using the  $\hbar^2$ -order in the ETF expansion eqs. (II.18), straightforwardly leads to

$$\lambda = \frac{dh}{d\rho} + C_{\nabla}(\nabla\rho)^2 + C_{\Delta}\Delta\rho, \quad (\text{II.21})$$

with

$$C_{\nabla}(\rho) = \frac{1}{36} \frac{\hbar^2}{2m} \left( \frac{1}{\rho} + 3\kappa^2 \frac{\rho}{f^2} \right) - \frac{V_{so}}{f^2}, \quad (\text{II.22a})$$

$$C_{\Delta}(\rho) = \frac{1}{3} \frac{\hbar^2}{2m} \left( -\frac{1}{6\rho} + \frac{7}{3}\kappa - \frac{\kappa}{2f} \right) - 2C_{fin} - 2V_{so} \frac{\rho}{f}. \quad (\text{II.22b})$$

This equation was solved, within a simplified energy functional and in the semi-infinite slab geometry, in ref. [Tre86]. A numerical solution of the Euler-Lagrange equations for finite nuclei, employing more general density functionals, including the Coulomb interaction and possibly  $\hbar^4$ -terms in the semi-classical expansion, is as numerical demanding as the resolution of the HF equations. For this reason, trial density profiles containing only a few variational parameters are often employed [Bra85; Tre86; Cen90; Ons08; Pot13; Lee10]. In particular, in ref. [Tre86], it was shown that a density profile presenting the correct asymptotic behaviors in the one-dimensional system, is given by the Generalized Fermi-Dirac (GFD) distribution. In what follows, we demonstrate this property in the case of the more elaborated functional that we use.

We can easily evaluate the Lagrange multiplier  $\lambda$  in the case of homogeneous infinite matter. In the symmetric case, the density reached is the saturation density  $\rho_{sat}$ . The variational principle  $\delta\{E - \lambda_{sat}A\} = 0$ , divided by the volume or by the particle number, leads to

$$\left. \frac{\partial\mathcal{H}}{\partial\rho} \right|_{\rho_{sat}} = \lambda_{sat} = \left. \frac{\mathcal{H}}{\rho} \right|_{\rho_{sat}}, \quad (\text{II.23})$$

showing that the Lagrange parameter  $\lambda_{sat}$  is the chemical potential of nuclear matter. We can notice that the equality (II.23) gives the value of the equilibrium density  $\rho_{sat}$ . Using eq. (II.15), we obtain the Lagrange parameter

$$\lambda_{sat} = \left. \frac{\partial h}{\partial\rho} \right|_{\rho=\rho_{sat}} = \frac{\hbar^2}{2m} \left( \frac{3\pi^2}{2} \right)^{2/3} \rho_{sat}^{2/3} \left[ 1 + \frac{8}{5}\kappa\rho_{sat} \right] + 2C_0\rho_{sat} + (\alpha + 2)C_3\rho_{sat}^{\alpha+1} \quad (\text{II.24})$$

$$= \frac{\hbar}{\rho} \Big|_{\rho=\rho_{sat}} = \frac{\hbar^2}{2m} \left( \frac{3\pi^2}{2} \right)^{2/3} \rho_{sat}^{2/3} \frac{3}{5} [1 + \kappa\rho_{sat}] + C_0\rho_{sat} + C_3\rho_{sat}^{\alpha+1}. \quad (\text{II.25})$$

We can notice that in the absence of interaction, we recover the well-known Fermi energy of a kinetic gas of fermions:  $\lambda_{sat} = \mu_F = \partial h / \partial \rho = \hbar^2 / 2m (3\pi^2 \rho / 2)^{2/3}$ , as well as the energy per particle  $\lambda_{sat} = e = h / \rho = 3/5 \mu_F$ . In that non-interacting case, equality (II.23) implies that  $\rho_{sat} = 0$ , simply meaning that matter exist at finite density without interaction.

Let us consider (symmetric) semi-infinite matter. Though the Euler-Lagrange equation (II.21) is not analytically solvable, we can constrain the density profile from the asymptotic behaviors. In the limit of vacuum ( $x > 0$ ), eq. (II.15) reads

$$\lambda_{sat} = \frac{1}{36} \frac{\hbar^2}{2m} \left[ \left( \frac{\rho'}{\rho} \right)^2 - 2 \frac{\rho''}{\rho} \right], \quad (\text{II.26})$$

which gives

$$\rho(x) \propto e^{-x/a_{out}} \quad \text{with} \quad a_{out} = \sqrt{-\frac{\hbar^2}{2m} \frac{1}{36\lambda_{sat}}}. \quad (\text{II.27})$$

Similarly, linearising eq. (II.15) around  $\rho_{sat}$  leads to

$$\delta\rho(x) \propto e^{x/a_{in}} \quad \text{with} \\ a_{in} = \sqrt{\frac{9}{K_{sat}} \left( \frac{\hbar^2}{2m} \frac{1}{3} \left[ \frac{1}{6} - \frac{7}{3} \kappa\rho_{sat} + \frac{1}{2} \frac{\kappa\rho_{sat}}{f_{sat}} \right] + 2C_{fin}\rho_{sat} + 2V_{so} \frac{\rho_{sat}^2}{f_{sat}} \right)}, \quad (\text{II.28})$$

with  $K_{sat} = 9\rho_{sat}^2 \partial^2(h/\rho) / \partial \rho^2 |_{\rho_{sat}}$  the nuclear matter incompressibility at saturation density. To fulfill the two previous asymptotic behaviours, the density profile can be represented via a Generalized Fermi-Dirac function

$$\rho(x) = \rho_{sat} F_\nu(x) \quad \text{with} \quad F_\nu(x) = \left( 1 + e^{x/a_\nu} \right)^{-\nu}, \quad (\text{II.29})$$

which presents the limiting behaviours  $\lim_{x \rightarrow -\infty} \rho(x) = \rho_{sat} (1 - \nu e^{x/a_\nu})$  and  $\lim_{x \rightarrow +\infty} \rho(x) = \rho_{sat} e^{-\nu x/a_\nu}$ . Identifying these equalities with eqs (II.27) and (II.28), we obtain analytical expressions for the parameters:

$$a_\nu = a_{in} \quad ; \quad \nu = \frac{a_{in}}{a_{out}} = \frac{6a_\nu}{\hbar} \sqrt{-2m\lambda_{sat}}. \quad (\text{II.30})$$

For spherical nuclei, we can assume that the density profile is also a Generalized

Fermi-Dirac distribution, involving an extra parameter  $R_\nu$  related to the size the nucleus:

$$\rho_{GFD}(r) = \frac{\rho_{sat}}{(1 + \exp [(r - R_\nu)/a_\nu])^\nu}. \quad (\text{II.31})$$

Concerning the parameter  $\rho_{sat}$ , it is justified to use the saturation density of nuclear matter, since it corresponds to the solution of the Euler-Lagrange equation in the limit of infinitely extended nuclei. Concerning the diffuseness, we will keep eq. (II.30) since there is no analytical solution of the Euler-Lagrange equation in spherical symmetry. The other parameter  $R_\nu$  can be unequivocally related to the particle number

$$A = 4\pi \int_0^\infty dr \rho_{GFD}(r) r^2, \quad (\text{II.32})$$

which can be approximated, assuming  $e^{-R_\nu/a_\nu} \ll 1$ , that is  $a \lesssim R$  [Kri81]:

$$A = \frac{4}{3}\pi\rho_{sat}R_\nu^3 \left[ 1 + 3\eta_\nu^{(0)} \frac{a_\nu}{R_\nu} + 6\eta_\nu^{(1)} \left( \frac{a_\nu}{R_\nu} \right)^2 + 3\eta_\nu^{(2)} \left( \frac{a_\nu}{R_\nu} \right)^3 \right], \quad (\text{II.33})$$

where the  $\eta_\nu^{(i)}$  are defined in appendix A.1, and given in table A.1. If, in addition, we assume  $a_\nu \ll R_\nu$ , this expression can be inverted giving at third order in the leptodermous expansion:

$$\begin{aligned} \frac{R_\nu}{R_{HS}} &\simeq 1 - \eta_\nu^{(0)} \frac{a}{R_{HS}} + \left[ \left( \eta_\nu^{(0)} \right)^2 - 2\eta_\nu^{(1)} \right] \left( \frac{a}{R_{HS}} \right)^2 \\ &- \left[ \frac{2}{3} \left( \eta_\nu^{(0)} \right)^3 - 2\eta_\nu^{(0)}\eta_\nu^{(1)} + \eta_\nu^{(2)} \right] \left( \frac{a}{R_{HS}} \right)^3 + O \left( \left( \frac{a}{R_{HS}} \right)^4 \right), \end{aligned} \quad (\text{II.34})$$

where  $R_{HS} = (3A/4\pi\rho_{sat})^{1/3}$  is the equivalent homogeneous sphere radius.

In conclusion, the parameters of the GFD ansatz given by the parametric form (II.31) can be determined in the following way:  $\rho_{sat}$  is the saturation density of nuclear matter,  $a_\nu$  is given by eq. (II.28),  $\nu$  is given by eq. (II.30) and  $R_\nu$  is given by eq. (II.34).

## ii) Simple Fermi function

The variational approach presented in the previous section allows an analytical determination of the nuclear energy for symmetric nuclei. Unfortunately, the generalization of these equations to asymmetric nuclei as well as to nuclei embedded in nucleon gas is highly non-trivial [Kri83], unless severe approximations are assumed. Since our aim is to have a model which can be applied for exotic nuclei as well as for dilute nuclear clusters present in the supernovae and (proto-)neutron star crust, we present in this section a simpler density profile form, still inspired by the solution of the Euler-Lagrange equa-

tions, but explicitly optimized on Hartree-Fock calculations. Another proposition will be developed in part III.

In the experimental analysis of measured density profiles, it is customary to use a simple  $\nu = 1$  Fermi-Dirac (FD) functional form [Val81]:

$$\rho(r) = \frac{\rho_{sat}}{1 + \exp[(r - R)/a]}. \quad (\text{II.35})$$

Similarly to the previous GFD model, the parameter  $\rho_{sat}$  can be identified with the saturation density, due to the limit of infinitely large nuclei, and the radius parameter related to the particle number  $A$  is given by eq. (II.34), with  $\nu = 1$ :

$$R = R_{HS} \left[ 1 - \frac{\pi^2}{3} \left( \frac{a}{R_{HS}} \right)^2 + O \left( \left( \frac{a}{R_{HS}} \right)^4 \right) \right]. \quad (\text{II.36})$$

The diffuseness parameter  $a$  of the total density profile has been fitted on HF calculations and in the case of symmetric nuclei, giving  $a = C_1 = 0.54$  fm [Pap13]. We will see in sections II.2.1.b and II.2.2 that this simple model can be easily generalized for asymmetric nuclei with nucleons gas.

### iii) Comparison to HF calculations

With the density profiles eq. (II.31) or (II.35), the nuclear ground state energy is straightforwardly calculated as

$$E(A) = \int \mathcal{H}[\rho(r)] d^3r, \quad (\text{II.37})$$

where the energy density  $\mathcal{H}[\rho(r)]$  is given by eq. (II.15) and by the semi-classical expansions eqs. (II.12) and (II.13). In this chapter we will use a numerical integration of eq. (II.37) in spherical symmetry, but analytical solutions will be sought for in part III.

The quality of both the ETF approximation and the density profiles ansatz can be judged by comparing the (G)FD distributions and the associated energies to HF calculations performed with the same nuclear effective interaction. For these numerical applications, we will use in this section the SLy4 Skyrme nuclear interaction [Cha98]. We first compare the GFD (II.31) and FD (II.35) ansatz density profiles for symmetric nuclei, showing the minor role of the parameter  $\nu$  as well as the limitations of the variational approach.

Figure II-1 shows the density profiles, the density multiplied by  $r^2$  and the gradient of the density multiplied by  $r^2$  for some symmetric nuclei. In all cases, the GFD (II.31) and FD (II.35) ansatz density profiles are compared to Hartree-Fock calculations in spherical symmetry. All the HF results presented in this thesis were kindly provided by J. Margueron. Double magic nuclei are considered in the left part of the figure, while

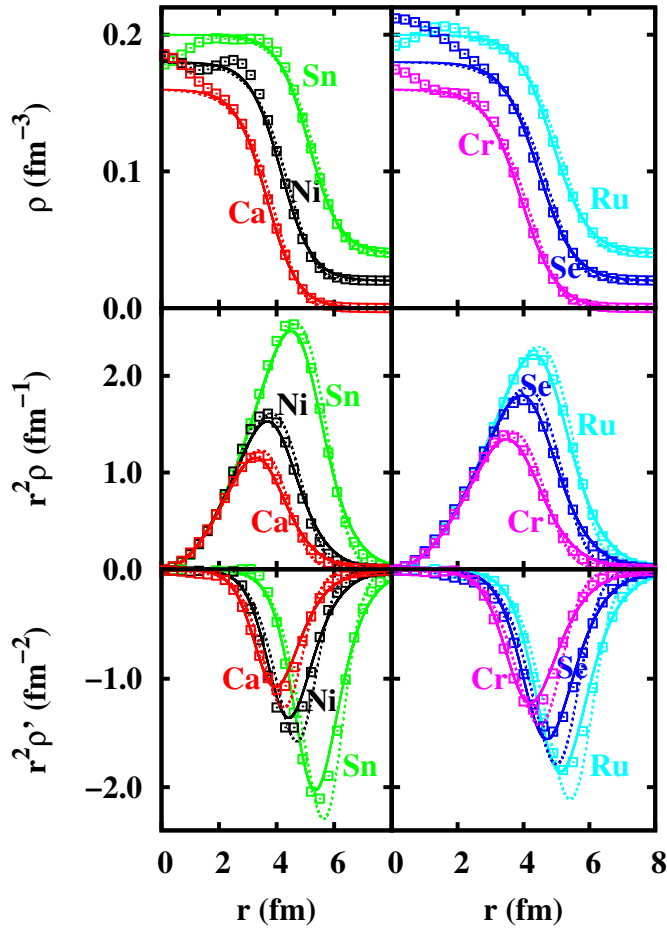


Figure II-1: Density profiles (upper panel), corresponding particle numbers (central panel) and density derivative profile times  $r^2$  (lower panel) of different magic (left side,  $^{40}\text{Ca}$ ,  $^{56}\text{Ni}$  and  $^{100}\text{Sn}$ ) and open-shell (right side,  $^{48}\text{Cr}$ ,  $^{68}\text{Se}$ ,  $^{88}\text{Ru}$ ) even-even symmetric nuclei. Symbols: spherical HF calculations. Dashed lines: GFD model eq. (II.31). Full lines: FD model eq. (II.35). On the upper panel, a vertical shift of  $\delta\rho = 0.02$  ( $0.04$ )  $\text{fm}^{-3}$  is applied to the density profiles of  $^{56}\text{Ni}$  and  $^{68}\text{Se}$  ( $^{100}\text{Sn}$  and  $^{88}\text{Ru}$ ) to better separate the different curves. Figure published in [Aym14].

open shells ones are plotted in the right part.

We can see on the upper panel that both the FD and the GFD distributions can reproduce the HF density profiles with the same accuracy and the diffuseness of the nuclear surface is equally well reproduced by the two ansatz. Microscopic density profiles show ripples in the central density which are cannot be reproduced by a (G)FD distribution. However, these structures are not expected to influence the energetics of the system in an important way, because of the volume element in the energy integral. Moreover such structures are largely due to the single particle wave function form of the one body density, and disappear if correlations beyond mean-field are accounted for.

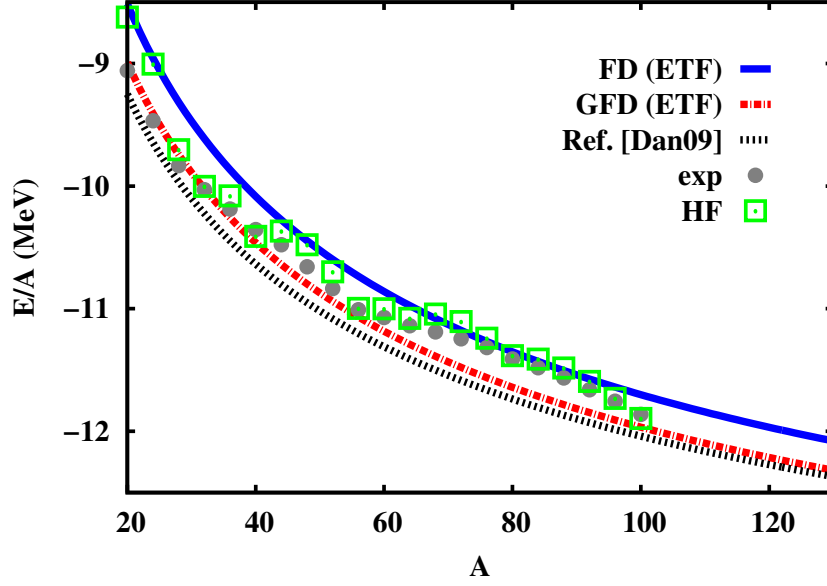


Figure II-2: Energy per nucleon of  $N = Z$  nuclei as a function of the mass number. squares: HF calculations. circles: experimental data from [NuD14]. Full blue line: FD model. Dashed red line: GFD model. Dotted black line: results from ref. [Dan09]. Figure published in [Aym14].

Therefore we are not interested in modelling them.

We also show the densities and the gradients of the densities multiplied by  $r^2$  in the central and lower panels of fig. II-1, which are the ingredients of the integrand of the energy eq. (II.37). Interesting enough, the GFD functional form does not give a better reproduction of the microscopic calculations than the simpler FD one. It is clear from this figure that the FD profile is enough to reproduce the features of the microscopic calculations. In particular we can see that the fall-off of the density in the HF calculation is very well described by an exponential behavior. Conversely, it was shown in ref. [Cen90] that the variational ETF solution exhibits a slower polynomial decrease when the  $\hbar^4$ -terms are included. This is an argument suggesting that we can safely neglect these higher order terms.

The satisfactory performance of the (G)FD model is confirmed and quantified by fig. II-2, which displays the nuclear energy per particle of symmetric nuclei as a function of their mass number  $A$ . For consistency, the same Coulomb energy as obtained in HF is subtracted from the experimental nuclear masses, taken from [NuD14].

We can see that the GFD profiles systematically produce more binding than the FD ones, as expected from the wider variational space associated to this functional form. The energies obtained using the GFD ansatz are in good agreement with both the microscopic calculations and the measured masses for magic nuclei (that is, the local minima in the

figure). However, the other nuclei are overbound. This overbinding is known to be due to the absence of fourth-order terms in the ETF functional [Cen90]. The simpler FD model without variational parameter underbinds magic nuclei, but it leads to an overall good agreement with the microscopic calculations. These results are consistent with previous findings comparing FD and GDF ansatz profiles [Cen90].

The results of the liquid-drop-like slab parametrization [Dan09] of eq. (I.83), using the same SLy4 functional [Cha98], are also displayed in fig. II-2. We can see that the variational ETF calculation correctly converges towards the slab estimation (I.83) for very large mass numbers, where curvature corrections to the surface energies due to the spherical geometry are becoming negligible. As we will discuss in detail in part III, the functional form given by eq. (II.37) naturally contains curvature effects. The difference between eq. (II.37) and eq. (I.83) is mostly due to the missing curvature term in eq. (I.83). For light nuclei, eq. (I.83) therefore tends to overestimate the binding.

From the ensemble of results in figs. II-1 and II-2, we can conclude that the FD and GDF ansatz equally well reproduce the microscopic HF calculations, and that the biggest source of discrepancy is mainly due to the lack of shell effects, inherent to the ETF approach. We have already mentioned that the FD ansatz is simpler and easier to generalize to the asymmetric case. Therefore in what follows, we will use the FD parametrization, and test its accuracy in asymmetric nuclei and in presence of a nucleon gas.

### II.2.1.b Density profiles for asymmetric nuclei

We now consider the general case of asymmetric  $N, Z$  nuclei, which requires the introduction of two density profiles to consider the independent degrees of freedom of neutrons and protons.

#### i) Fermi-Dirac ansatz

Similarly to the symmetric case, we introduce the neutron  $\rho_n$  and proton  $\rho_p$  density profiles as FD distributions:

$$\rho_p(r) = \frac{\rho_{sat,p}(\delta)}{1 + \exp[(r - R_p)/a_p]} \quad \text{and} \quad \rho_n(r) = \frac{\rho_{sat,n}(\delta)}{1 + \exp[(r - R_n)/a_n]}. \quad (\text{II.38})$$

The parameter  $R_p$  ( $R_n$ ) is determined, similarly to eq. (II.36), by proton (neutron) conservation as

$$R_q = R_{HSq} \left[ 1 - \frac{\pi^2}{3} \left( \frac{a_q}{R_{HSq}} \right)^2 + O \left( \left( \frac{a_q}{R_{HSq}} \right)^4 \right) \right] \quad (\text{with } q = n, p), \quad (\text{II.39})$$

where  $R_{HSp}(\delta) = Z^{1/3}r_{sat,p}(\delta)$  ( $R_{HSn}(\delta) = N^{1/3}r_{sat,n}(\delta)$ ) the equivalent homogeneous proton (neutron) sphere radius,  $r_{sat,q}(\delta) = (\frac{4}{3}\pi\rho_{sat,q}(\delta))^{-1/3}$ , and where we have assumed  $a_q \ll R_q$ .

As for symmetric nuclei, the parameter  $\rho_{sat,p}(\delta)$  ( $\rho_{sat,n}(\delta)$ ) entering eqs. (II.38), corresponds to the density of protons (neutrons) in the limit of infinite homogeneous matter at isospin asymmetry  $\delta = (\rho_{sat,n} - \rho_{sat,p})/\rho_{sat}$ . To evaluate the isospin asymmetry dependence, it is common to make the quadratic approximation in asymmetry  $\delta$  for the energy per particle, introducing the usual symmetry energy density

$$\mathcal{H}_{sym} = \frac{1}{2}\rho^2 \left. \frac{\partial^2 \mathcal{H}}{\partial \rho_3^2} \right|_{\rho_3=0}, \quad (\text{II.40})$$

and then to expand both the isoscalar and isovector parts around the symmetric saturation density  $\rho_{sat}(\delta = 0)$ , such that [Dan09]

$$\begin{aligned} \frac{\mathcal{H}(\rho, \rho_3)}{\rho} &\simeq \frac{\mathcal{H}(\rho_{sat}, 0)}{\rho} + \frac{K_{sat}}{18\rho_{sat}(0)}(\rho - \rho_{sat}(0))^2 \\ &+ \left[ J_{sym} + \frac{L_{sym}}{3\rho_{sat}(0)}(\rho - \rho_{sat}(0)) + \frac{K_{sym}}{18\rho_{sat}(0)}(\rho - \rho_{sat}(0))^2 \right] \delta^2. \end{aligned} \quad (\text{II.41})$$

In this expression,  $J_{sym} = \mathcal{H}_{sym}(\rho)/\rho|_{\rho_{sat}(0)}$  is the symmetry energy per nucleon evaluated at (symmetric) saturation,  $L_{sym} = 3\rho_{sat}\partial(\mathcal{H}_{sym}/\rho)/\partial\rho|_{\rho_{sat}(0)}$  its slope and  $K_{sym} = 9\rho_{sat}^2\partial^2(\mathcal{H}_{sym}/\rho)/\partial\rho^2|_{\rho_{sat}(0)}$  its curvature. The saturation density at a given asymmetry  $\delta$  is determined by the minimisation of eq. (II.41) with respect to  $\rho$ , leading to [Dan09]:

$$\rho_{sat}(\delta) = \rho_{sat}(0) \left( 1 - \frac{3L_{sym}\delta^2}{K_{sat} + K_{sym}\delta^2} \right). \quad (\text{II.42})$$

In [Pap13], the asymmetry dependence of the equilibrium baryonic density given by this formula is shown to well reproduce the asymmetry dependence predicted by HF calculations.

The last parameters of eqs (II.38), the diffusenesses  $a_p$  and  $a_n$ , have been evaluated by a fit on HF calculations [Pap13], in assuming a quadratic dependence on  $\delta$  and no dependence on the nucleus mass:

$$\begin{aligned} a_p &= D_1 + D_2\delta^2 = 0.53 + 0.33\delta^2 \\ a_n &= B_1 + B_2\delta^2 = 0.54 + 1.13\delta^2. \end{aligned} \quad (\text{II.43})$$

The  $\delta$ -quadratic behaviour as well as the mass-independence were verified in [Pap13]. The values of  $D_i$  and  $B_i$  have been found independent of the used Skyrme functional. In part III, we will justify this form in comparing with analytical results.

We can also introduce the total density profile ansatz

$$\rho(r) = \frac{\rho_{sat}(\delta)}{1 + \exp[(r - R)/a]}, \quad (\text{II.44})$$

where the radius parameter  $R$  is given by eq. (II.36), but now depends on  $\delta$ , and the fitted diffuseness is  $a = C_1 + C_2\delta^2 = 0.54 + 1.04\delta^2$  [Pap13].

Let us remark that taking two of the density profiles from eqs. (II.38) and (II.44), the third one cannot be written as a Fermi-Dirac function. Therefore the relation  $\rho(r) = \rho_n(r) + \rho_p(r)$  is not exactly ensured. As a consequence, we cannot consistently use the three ansatz in the same model, and there is an arbitrary choice by using different representations. In that work, we use the total and proton density profiles ansatz, and so define the neutron density as  $\rho_n(r) = \rho(r) - \rho_p(r)$ .

## ii) Isospin asymmetry inhomogeneities

The bulk asymmetry  $\delta = (\rho_{sat,n} - \rho_{sat,p})/\rho_{sat}$  differs from the usual global asymmetry  $I = 1 - 2Z/A$  because of the presence of a neutron skin and Coulomb effects [Dan03]. Taking into account the competing effect of the Coulomb interaction and symmetry energy, which act in opposite directions in determining the difference between the proton and neutron radii, the bulk asymmetry can be related to the global one by [Cen98; War09; Mye80]:

$$\delta = \frac{I + \frac{3a_c}{8Q} \frac{Z^2}{A^{5/3}}}{1 + \frac{9J_{sym}}{4Q} \frac{1}{A^{1/3}}}. \quad (\text{II.45})$$

In this equation,  $Q$  is the surface stiffness coefficient, and  $a_c$  is the Coulomb parameter. We can see that, because of the complex interplay between Coulomb and skin effects, the bulk asymmetry  $\delta$  of a symmetric  $I = 0$  nucleus is not zero, though small. Equation (II.45) highlights the isospin asymmetry inhomogeneities inside a nucleus: the isospin asymmetry distribution  $\rho_3(r)/\rho(r)$  is not uniform. Indeed, the central asymmetry, close to  $\delta$ , is not the same as the global one  $I$ .

The relation between the global asymmetry and the asymmetry in the nuclear bulk, eq. (II.45), is shown for nuclei within the theoretical drip lines in fig. II-3. From this figure we can see that  $\delta$  is a slowly increasing function of the asymmetry. Globally, the interval of  $\delta$  is more restricted than the interval of  $I$ : the values of  $\delta$  increases from  $-0.1$  to  $0.3$  if we consider the ensemble of the medium and heavy nuclei within the drip lines. We also recover from the figure that, for a given  $I$ , the heavier the nucleus is, the closer from  $I$   $\delta$  is: that is the neutron skin effect decreases.

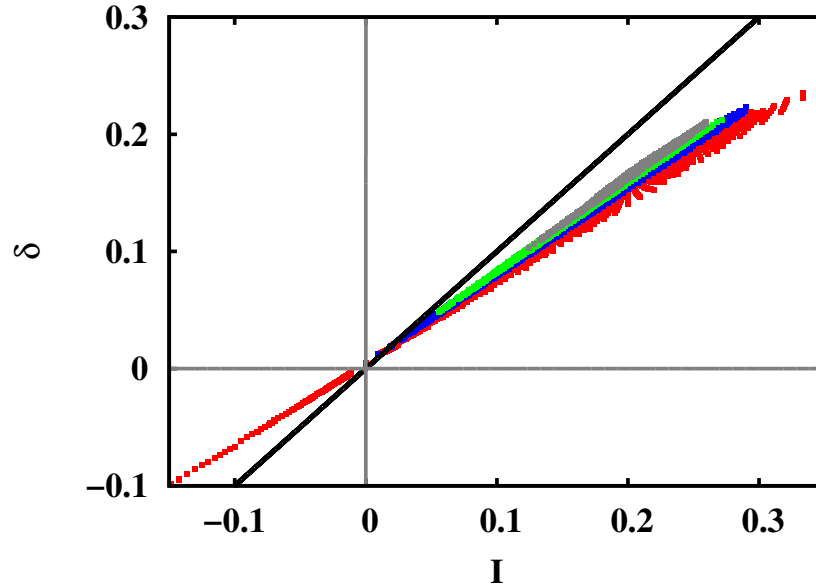


Figure II-3: Bulk asymmetry eq. (II.45) as a function of the global asymmetry  $I$  for nuclei within the theoretical drip lines evaluated from the SLy4 energy functional. The different colors correspond to different intervals in mass number:  $40 \leq A < 100$  in red,  $100 \leq A < 150$  in blue,  $150 \leq A < 200$  in green,  $A \geq 200$  in grey. The function  $y = x$  is also plotted (black). Figure published in [Aym15].

### iii) Comparison to HF calculations

As for symmetric nuclei, we now evaluate the accuracy of our model, comparing it to HF calculations.

In figure II-4, some representative microscopic HF density profiles are compared to the FD ansatz computed with the 2<sup>nd</sup> order ETF. We can see that the level of agreement with the microscopic calculation is comparable to the case of symmetric nuclei, so it does not depend on the exoticity of the nucleus. More specifically, we can notice that the diffuseness of the nuclear surface is well reproduced by our model.

The accuracy of our model is better assessed in fig. II-5 which displays the nuclear ground state energy difference between the (E)TF calculations and the microscopic ones as a function of the neutron number, for a few isotopic chains. The (E)TF energy, calculated with the FD profiles, is

$$E(A, Z) = \int \mathcal{H}[\rho(r), \rho_3(r)] d^3r, \quad (\text{II.46})$$

with  $\rho_3(r) = \rho(r) - 2\rho_p(r)$ , and where the energy density  $\mathcal{H}[\rho(r), \rho_3(r)]$  is given by eq. (I.68), and by the semi-classical expansions eqs. (II.12) and (II.13). Once again, the

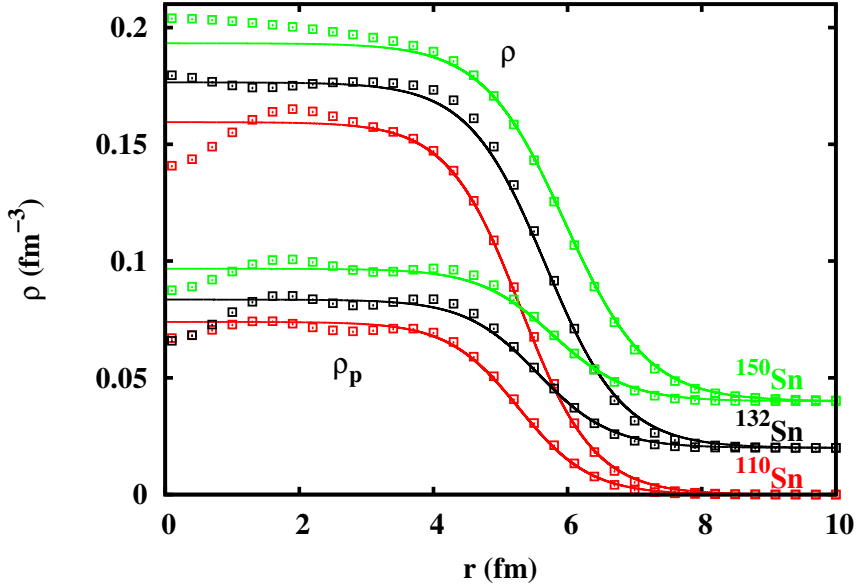


Figure II-4: Total (upper curves) and proton (lower curves) density profiles of different Sn isotopes. Symbols: spherical HF calculations. Full lines: FD model. A vertical shift of  $\delta\rho = 0.02$  ( $0.04$ )  $\text{fm}^{-3}$  is applied to the density profiles of  $^{132}\text{Sn}$  ( $^{150}\text{Sn}$ ), to better separate the different curves. Figure published in [Aym14].

integral in eq. (II.46) is numerically evaluated.

In figure II-5, the filled symbols correspond to the Thomas-Fermi approximation (or LDA) given by eq. (II.12). In this approximation, the spin-orbit term vanishes and the local kinetic energy density at a position  $r$  is the same as for infinite nuclear matter at the local density  $\rho(r)$ ,  $\rho_p(r)$ . We can see that the inclusion of second order terms in the functional (eq. II.13) considerably improves the description (open symbols in fig. II-4). In particular, for the heaviest isotopic chain considered, the average ETF energy very well reproduces the average HF energy. The deviations are comparable to the difference between the HF model and the experimental data (full circles), and can be fully ascribed to the missing shell effects. These effects cannot be accounted for a semi-classical model. For the application to the supernovae and (proto-)neutron star crust, we however do not expect this to be an important point, as shell effects are known to rapidly wash out with increasing temperature.

The use of the simple Fermi-Dirac ansatz in the ETF approach at second order in  $\hbar$  has been found to reproduce with a good accuracy the microscopic HF density profiles as well as the HF binding energies, with an accuracy of the order of 300 keV/nucleon for the lighter nuclei, and which does not exceed 150 keV/nucleon for the heavy ones.

We now come back to the choice of using the FD density profiles for  $(\rho, \rho_p)$  or for

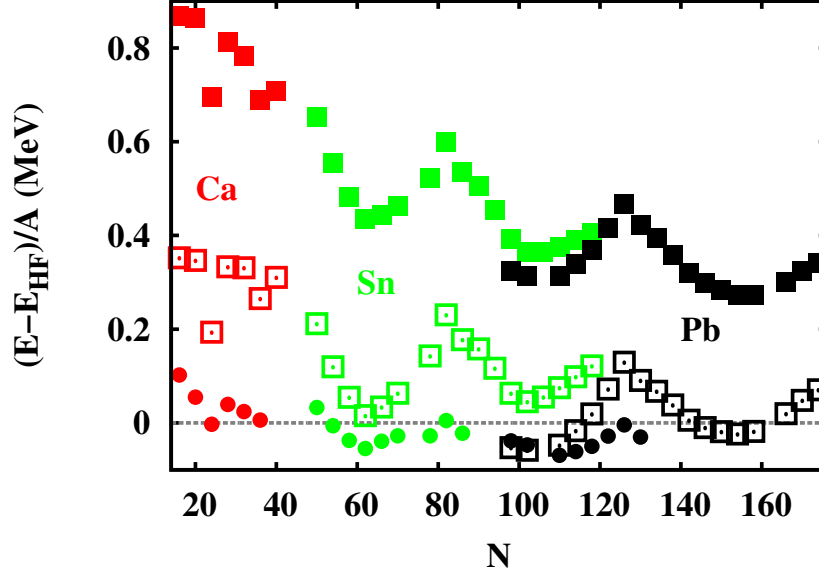


Figure II–5: Difference between the energy per particle calculated in the ETF model and in the HF for the isotopic chain of Ca (red symbols), Sn (green symbols), and Pb (black symbols). Full squares: zeroth order TF approximation. Empty squares: second order ETF. Full circles: experimental data. Figure published in [Aym14].

$(\rho_p, \rho_n)$ . Indeed, we have shown in [i\)](#) that it is not consistent to use the three Fermi-Dirac profiles (of neutron, proton, and total baryon) in the same model. We show in what follows that the two different representations  $(\rho, \rho_p)$  and  $(\rho_p, \rho_n)$  give the same accuracy for the predictions, but cannot be mixed.

Table II–1 gives, for a representative nucleus, the energies per nucleon corresponding to each term of eq. (I.68), calculated with HF, and with the ETF approximation using the representations  $(\rho, \rho_p)$  and  $(\rho_p, \rho_n)$ . We can see that for this chosen nucleus, the two ETF models give the same well reproducing total energies with an overbinding of 20 keV per nucleon.

model	$\langle \mathcal{K}/\rho \rangle$	$\langle \mathcal{H}_{pot}/\rho \rangle$	$\langle \mathcal{H}_{eff}/\rho \rangle$	$\langle \mathcal{H}_{fin}/\rho \rangle$	$\langle \mathcal{H}_{so}/\rho \rangle$	$E/A$
HF	18.7	-36.7	6.4	1.4	-0.3	-10.51
ETF $(\rho, \rho_p)$	18.2	-36.4	6.7	1.4	-0.4	-10.53
ETF $(\rho_p, \rho_n)$	18.3	-36.5	6.8	1.3	-0.4	-10.53

Table II–1: Comparison between HF and ETF with the representations  $(\rho, \rho_p)$  and  $(\rho_p, \rho_n)$  of  $^{236}\text{Pb}$ , for which the total energy is particularly well reproduced. The different columns give in MeV per nucleon, from left to right: the kinetic energy, the potential energy ( $\mathcal{H}_{pot} = \mathcal{H}_0 + \mathcal{H}_3$ ), the effective term energy, the finite-range energy, the spin-orbit interaction energy, and the total energy.

It is interesting to observe that each energy component however is not accurately reproduced. Indeed, differences up to a few hundreds of keV per nucleon between the HF calculations and the ETF models are observed for each term. These discrepancies are observed for any nucleus, but systematically compensate each other, such that the final results are the ones previously discussed in fig. II-5. From table II-1, we can also notice that the ETF models using the  $(\rho, \rho_p)$  representation, or the  $(\rho_p, \rho_n)$  one, differ of  $\sim 100$  keV per nucleon in evaluating each energy component. This shows that different representations cannot be mixed in the calculation of the total energy.

### II.2.1.c Decomposition of the energetics

Before addressing the problem of the energetic beyond driplines, which is the central problem for the astrophysical applications, we are interested in an application of the model to conventional nuclear physics. Given the good reproduction of the smooth part of the microscopic nuclear density, the ETF description can be used to explore the functional form of the nuclear mass. In particular, we study the separation in a bulk and surface term in the isovector and isoscalar parts.

Such a separation is important for the extraction of the largely unknown density behavior of the symmetry energy from nuclear data [EPJ14]. Indeed, while the properties of the energy density close to saturation are constrained by the experimental data of atomic nuclei, little is known about their behavior away from the saturation density of symmetric nuclear matter  $\rho_{sat}(\delta)$ , especially in the isovector sector. As a consequence, the so-called symmetry energy, defined as the curvature of the energy in the isospin direction is presently the object of intense research. This quantity impacts a variety of phenomena, including nuclear masses [Mol12], neutron skin thickness [Abr12], and consequently plays a major role in structure and properties of (proto-)neutron star crust [Ste05; Fat12; Gri12; Gan12; Rad14].

Furthermore, the symmetry energy is thought to be strongly constrained from the measurement of nuclear masses [Mol12]. These estimations give the experimental constraints on the symmetry energy which have at the present smallest uncertainties [Tsa12]. The determination of the symmetry energy from nuclear mass implies that the surface and bulk component of the isospin dependence can be unambiguously distinguished. However, very different values are reported in the literature for the surface symmetry energy coefficient [Dou00; Dan03; Rei06; Nik11]. For this reason, it is important to understand how the surface term of the symmetry energy can be extracted from the global symmetry energy of a finite nucleus.

### i) Surface energy

In a two-component system, there are two possible definitions of the surface energy which depend on the definition of the bulk energy in the cluster [Mye85; Far86; Cen98]. The first one corresponds to identifying the bulk energy of a system of  $N$  neutrons and  $Z$  protons to the energy of an equivalent piece of nuclear matter

$$E_s = S_{\gamma_e} = E - eA, \quad (\text{II.47})$$

where  $e$  is the energy per nucleon of uniform matter. This definition is the standard surface energy of the droplet model [Mye69].

The second definition

$$E_S = S_{\gamma_\mu} = E - \mu_n N - \mu_p Z + pV \quad (\text{II.48})$$

corresponds to the grandcanonical thermodynamical Gibbs definition. It gives the quantity to be minimized in the variational calculation conserving proton and neutron number. It was shown that the sign of the surface symmetry energy depends on the choice between these two possibilities [Mye85; Far86; Cen98]. Moreover it was argued [Mye85] that the case of Liquid Drop Model (LDM) mass formulas, where the bulk energy is a function of the total mass number  $A$  and of the global asymmetry  $I = (N - Z)/A$  only, is closer (though not equal) to the Gibbs definition. This can explain why LDM mass formulas systematically obtain negative (though widely varying) surface symmetry energy coefficients [Dou00; Dan03; Rei06; Nik11].

If the total energy  $E$  is exactly known, the two definitions eqs. (II.47) and (II.48) are in principle exactly equivalent, meaning that the surface symmetry energy is ill-defined. However, the total energy is never exactly known. In the case of empirical mass formulas, it is given by a fit of experimental data. In the case of ETF based functionals, as in the present study, we are seeking for the best possible approximation to the complete variational HF problem within a given effective interaction. Therefore it is important to determine if there is a decomposition which is best suited to the physical question which is being asked. In the case of this work, we want to understand which definition, eq. (II.47) or (II.48), is best suited to reproduce the Hartree-Fock energy. The variational ETF theory imposes the use of local quantities instead of global ones, and it therefore naturally leads to the use of the local asymmetry parameter  $\delta$  instead of  $I$ , that is the use of eq. (II.47). Moreover, in our model, the neutron and proton density profiles are defined by the FD ansatz, which does not contain any variational parameter. For this reason we do not need to introduce the Gibbs surface tension [Mye85], because no energy variation will be performed.. Therefore, we define the surface energy as the quantity deduced from

the total energy after subtraction of the energy the system would have in the absence of the surface:

$$E_s(A, Z) = E(A, Z) - \frac{\mathcal{H}[\rho_{sat}(\delta), \rho_{sat,3}(\delta)]}{\rho_{sat}(\delta)} A, \quad (\text{II.49})$$

with  $\rho_{sat,3}(\delta) = \delta \cdot \rho_{sat}(\delta)$ , and where the total energy  $E(A, Z)$  is given by eq. (II.46).

## ii) Surface symmetry energy

The curvature with respect to  $I$  of equation (II.49) defines the surface symmetry energy. Since the bulk asymmetry  $\delta$  is different from the global one  $I = (N - Z)/A$ , It is clear that this symmetry energy will be different if one replaces the subtracted bulk component evaluated at the bulk asymmetry by the one evaluated at the global asymmetry:

$$E'_s(A, Z) = E(A, Z) - \frac{\mathcal{H}[\rho_{sat}(I), \rho_{sat,3}(I)]}{\rho_{sat}(I)} A. \quad (\text{II.50})$$

Eq. (II.50) amounts to neglecting the spatial distribution of isospin asymmetry, and in particular the possible presence of a neutron skin which creates strong inhomogeneities within the nucleus. However, most mass formulas, both phenomenological [Mye80; Mol12] and microscopically motivated [Dan03; Rei06; Nik11; Dou00], assume that the bulk isospin dependence is given by the global asymmetry variable  $I$ . This is for instance the case of eq. (I.83) where the surface energy is defined as [Dan09],

$$E_s^{LDM}(A, Z) = E_{LDM}(A, Z) - (a_v - a_v^a I^2) A. \quad (\text{II.51})$$

In figure II–6 are compared, as a function of the global asymmetry  $I$ , the energies obtained from eqs. (II.46) and (II.49), referred to as ETF( $\delta$ ), the ones from eqs. (II.46) and (II.50), referred to as ETF( $I$ ), and the ones obtained from eqs. (I.83) and (II.51), referred to as ref. [Dan09]. This comparison is performed for a representative isobaric chain  $A = 200$ . For such heavy nuclei, the curvature terms,  $\propto A^{1/3}$ , play a minor role and the liquid-drop formula (I.83) [Dan09] leads to a nuclear energy very close to the ETF model. However, because of the very different partition between bulk and surface in the models EFT( $\delta$ ) and LDM (II.51), the surface symmetry energy shows an opposite behavior in the two models. As a consequence, the surface energy, and more specifically the surface symmetry energy, depends on the prescription employed to remove the bulk component, cf eqs. (II.49) and (II.50).

It is interesting to notice the very close behavior of the surface energies given by ETF( $I$ ) (II.50) and LDM (II.51) in fig. II–6. This very similar behavior assets the important role of the asymmetry parameters  $\delta$  and  $I$ . Specifically, the isospin dependence of the symmetry energy shown also in fig. II–6 is found to behave in an opposite way between the models EFT( $\delta$ ) and the two other models ETF( $I$ ) and LDM. Consistently

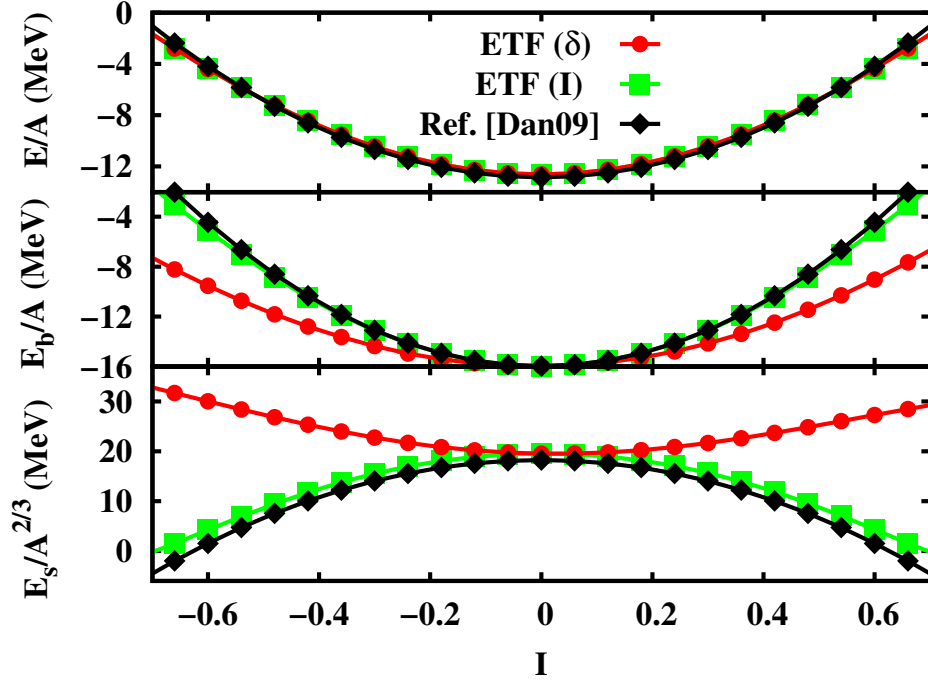


Figure II-6: Total (upper panel) and bulk (central panel) energy per nucleon and surface energy per surface nucleon (lower panel) along the isobaric chain  $A = 200$ . Red circles: ETF calculation including the neutron skin effect eq. (II.49) (see text). Green squares: ETF calculation neglecting the neutron skin effect eq. (II.50). Black diamonds: estimation from eq. (II.51). Figure published in [Aym14].

with Ref. [Mye85], it can be deduced from the curvature (with respect to  $I$ ) of the curves represented in the bottom panel of fig. II-6 that the choice of the asymmetry variable has an important consequence on the sign of the surface symmetry energy.

This effect can be understood analytically. Indeed, neglecting the Coulomb correction, we can approximate the relation between  $\delta$  and  $I$ , eq. (II.45), in the limit of small asymmetries,

$$\begin{aligned} \delta^2 &= \left( \frac{I + \frac{3a_c}{16Q} A^{1/3} (1-I)^2}{1 + \frac{9J_{sym}}{4Q} A^{-1/3}} \right)^2 \\ &\approx I^2 \left[ 1 - \frac{9J_{sym}}{2Q} A^{-1/3} + O\left(\frac{3a_c}{16Q}\right) + O\left(\left(\frac{9J_{sym}}{4Q}\right)^2\right) \right], \end{aligned} \quad (\text{II.52})$$

We can see that the replacement of the asymmetry parameter  $\delta$  by  $I$  in eq. (II.52), induces a correction to the LDM which is proportional to  $A^{-1/3}$ . It means that the ambiguity in defining the proper asymmetry parameter in the bulk term of the LDM propagates to the surface term. Moreover, replacing  $\delta$  by  $I$  in the LDM induces an extra

surface symmetry term with a negative sign, cf eq. (II.52). Since the surface symmetry term is positive in ETF( $\delta$ ), the change of sign in ETF(I) can be related to the negative extra term of eq. (II.52). Indeed, in the parabolic approximation, the bulk part of the ETF energy (II.37) is quadratic in  $\delta$ , so the energy reads

$$E(A, Z) \approx (\lambda_{sat} + J_{sym}\delta^2) A + E_s(A, Z), \quad (\text{II.53})$$

If the same parabolic approximation is employed for the bulk term of eq. (II.50), the energy is

$$E(A, Z) \approx (\lambda_{sat} + J_{sym}I^2) A + E'_S(A, Z). \quad (\text{II.54})$$

Comparing eqs. (II.53) and (II.54), and using eq. (II.52), we immediately get the following relation between the two surface energies,

$$E'_S \approx E_S - \frac{9J_{sym}^2}{2Q} A^{2/3} I^2. \quad (\text{II.55})$$

This same equation was derived in ref. [Mye85] as the difference between the microcanonical ( $\gamma_e$ ) and grandcanonical ( $\gamma_\mu$ ) surface energies, in the limit of small asymmetries. This equation shows that the surface energy  $E'_S$  contains an extra negative symmetry term due to the non-uniformity of the isospin distribution. As a result, and as it is shown in fig. II-6, the surface symmetry energy can change from positive to negative, whether we take into account the neutron skin effect or not.

### iii) Curvature symmetry energy

In spherical symmetry it is well known that the surface energy obtained from eq. (II.49) does not exactly scale as  $A^{2/3}$ , but it contains slower varying terms, the dominant one being a mass curvature term, proportional to  $A^{1/3}$  [Pom13]. In fig. II-7 is displayed the behavior with the mass number  $A$  of the surface energies divided by  $A^{2/3}$ . The red circles represent the  $E_s$  eq. (II.49), where the bulk asymmetry parameter  $\delta$  is employed taking into account the non-uniformity of the isospin asymmetry distribution, the green squares correspond to surface energy  $E'_s$  eq. (II.50), where the bulk asymmetry is approximated by the global asymmetry parameter  $I$ , and the black diamonds stand for the surface energy  $E_s^{LDM}$  LDM (II.51) [Dan09].

The left panel of fig. II-7 shows the isoscalar behavior of the surface energy, where the global asymmetry is fixed to be  $I = 0$ , while the right panel shows the result by fixing the asymmetry parameter to a finite value  $I = 0.4$ . Apart from the LDM (II.51) in the isoscalar case, it is observed that the surface energy  $E_s/A^{2/3}$  is not constant, revealing the presence of a curvature energy in the considered models. We can see that the isoscalar curvature symmetry energy is positive (increasing curves) for the ETF

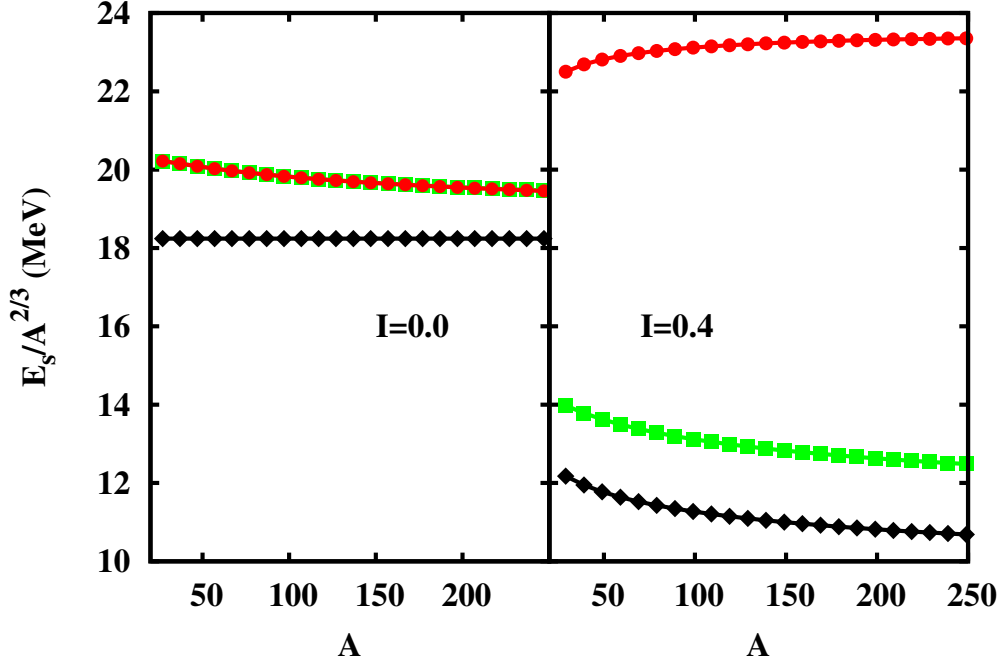


Figure II–7: Surface energy per surface nucleon as a function of the nucleus mass. Red circles: ETF calculation including the neutron skin effect eq. (II.49) (see text). Green squares: ETF calculation neglecting the neutron skin effect eq. (II.50). Black diamonds: estimation from eq. (II.51). Figure published in [Aym14].

models (II.49) and (II.50), and zero for the LDM (II.51). The absence of the curvature energy in the isoscalar part of the functional (II.51) is due to the fact that this LDM formula was motivated by one-dimensional slab calculations [Dan09] which by definition do not contain this term. The absence of a curvature energy is at the origin of the poorer reproduction of nuclear masses for symmetric nuclei, as observed in figure II–2. In this isoscalar case, there is almost no difference between the asymmetry parameters  $I$  and  $\delta$ , therefore the surface energies (II.49) and (II.50) overlap on the left panel of fig. II–7. Indeed, though not exactly equal, the bulk asymmetry  $\delta$  of  $N = Z$ -nuclei is close to zero (cf fig. II–3), leading to almost no difference between  $E_s$  and  $E'_s$ .

On the right panel of fig. II–7 where  $I = 0.4$  the symmetry energy  $E_s$  is shifted up, and the symmetry energies  $E'_s$  and  $E_s^{LDM}$  are shifted down, as expected from fig. II–6. The curvature in the case  $I = 0.4$  is given by a mixture of isoscalar and isovector contributions. The effect of the isovector term in the case of the surface energy (II.49) is however sufficiently negative to overcome the isoscalar contribution. We can therefore deduce from fig. II–7 that the curvature energy is positive and the symmetry curvature energy is negative in the case of  $E_s$ , eq. (II.49). In the case of the model (II.50), the isovector term goes in the same direction as the isoscalar term, and the trend of the

surface symmetry is similar to the one from the LDM (II.51). Therefore, similarly to the surface symmetry energy, the sign of the curvature symmetry term is opposite in the ETF models  $E_s$  and  $E'_s$ , and the ETF model neglecting the neutron skin effect  $E'_s$  has the same behavior as the mass formula (II.51).

To summarize this discussion, we have shown that neglecting the non-uniform isospin density distribution, induced by neutron skin and Coulomb repulsion, a positive symmetry curvature energy is obtained, while taking into account the non-uniformity of the isospin density distribution, a negative sign is found. The question then naturally arises of which is the most correct decomposition.

#### iv) Hints from Hartree-Fock

Since, from the same total energy, we can extract two different expressions for the surface energy (cf eqs. (II.49) and (II.50)), an ambiguity exists in the definition and also in the sign of the surface symmetry energy, as well as of the curvature symmetry energy. This ambiguity arises from the fact that the bulk asymmetry of nuclei  $\delta$  differs from their global asymmetry  $I$  because of the presence of a neutron skin and, to a minor extent, to the distortion of the density profile due to the Coulomb interaction. Since  $I = \delta$  at the thermodynamic bulk limit, a priori both  $E_s$  (II.49) and  $E'_s$  (II.50) can be proposed as a definition of the surface energy, and one may conclude that the surface symmetry energy is ill-defined.

However, at the level of the ETF approximation, these two equations are not equivalent and only eq. (II.49) is theoretically justified. Indeed, as we have discussed in section II.2.1.a, if we consider only ground state configurations, the ETF approximation is equivalent to the solution of a set of coupled local Euler-Lagrange equations. In the idealized situation of a system with a locally constant density profile ( $\rho'_q(r) = \rho''_q(r) = 0$  for a given value of  $r = r_0$ ), these equations simply read

$$\lambda_q = \frac{\partial h}{\partial \rho_q}(r_0). \quad (\text{II.56})$$

This equation admits the simple local bulk solution  $\rho_q(r_0) = \rho_{sat,q}$ , where the saturation density  $\rho_{sat,q}$  has to be calculated at the asymmetry  $\delta(r_0) = 1 - 2\rho_p(r_0)/\rho(r_0)$ , that is the local asymmetry. This reasoning implies that the bulk energy has to be calculated with the local bulk asymmetry  $\delta$ .

Another argument going in the same direction comes from a comparison to HF calculations. Indeed, for the quantity  $E'_s$ , defined in eq. (II.50) to vanish at the bulk limit, the  $\rho_{sat,q}$  parameters entering the proton and neutron density profiles have to be identified with  $\rho_{sat,q} = (1 \pm I)/2\rho_{sat}(I)$ , and the one entering the total isoscalar density should read  $\rho_{sat} = \rho_{sat}(I)$ . Replacing these quantities in eqs. (II.38) and (II.44) leads

A	$I$	$\delta$	$\bar{r}_p(HF)$	$\%(I)$	$\%(\delta)$	$E_{HF}/A$	$\%(I)$	$\%(\delta)$
180	0.09	0.08	5.31	-0.5	-1.1	-12.25	-0.3	-0.4
196	0.16	0.13	5.40	+0.8	-0.5	-11.93	+0.4	-0.1
216	0.24	0.19	5.50	+2.7	+0.4	-11.34	+1.8	+0.5
236	0.31	0.25	5.67	+3.4	+0.0	-10.51	+1.8	-0.2
256	0.36	0.29	5.77	+5.0	+0.6	-9.81	+3.6	+0.7
$\langle \rangle$	0.23	0.19	5.53	+2.3	-0.1	-11.17	+1.4	+0.1

Table II–2: Comparison between HF and ETF along the Pb isotopic chain. The different columns give, from left to right: the mass number of the isotope, the average isospin asymmetry, the bulk isospin asymmetry, the mean HF proton radius, the percentage deviation in the mean proton radius between HF and the ETF(I) and the ETF( $\delta$ ) models, the HF energy per nucleon, the percentage deviation in the energy per nucleon between HF and the ETF(I) and the ETF( $\delta$ ) model. The last line gives the arithmetic average along the isotopic chain.

to a different model both for the density profiles and for the ETF energy according to eq. (II.46). This alternative model, noted ETF(I) to distinguish it from the ETF( $\delta$ ), can be compared to HF calculations using the same Skyrme functional. This comparison is shown in table II–2 for the representative case of the total energy per nucleon and proton mean radius along the Pb isotopic chain.

We can see that the ETF( $\delta$ ) model systematically gives a better reproduction of HF results, and the deviation between ETF( $\delta$ ) and ETF(I) increases with increasing difference between bulk  $\delta$  and global  $I$  asymmetry parameters. The HF result supports the intuitive idea behind eq. (II.44) which is related to the local character of the Euler-Lagrange variational equations: the density in the bulk of a heavy nucleus is related to the saturation density corresponding to the local bulk asymmetry, and not to the global asymmetry of the nucleus.

In conclusion, these two arguments show that the model EFT( $\delta$ ) is better justified both from a theoretical point of view and from a comparison to HF calculations. In the rest of this work, the bulk energy shall therefore be parameterized in terms of the bulk asymmetry, and the surface symmetry energy in the corresponding LDM shall be positive.

## II.2.2 Nuclei embedded in a nucleon gas

In this section, we generalize the previous model developed in section II.2.1, in considering nuclei embedded in a nucleon gas. After presenting the generalized density profiles, we discuss the decomposition of the total Wigner-Seitz cell energy in order to extract the in-medium correction energy of an arbitrary nucleus ( $A, Z$ ) embedded in a nucleon gas with arbitrary density and composition  $(\rho_g, \delta_g)$ .

### II.2.2.a Density profiles and associated energy

We consider  $N_{WS}$  neutrons and  $Z_{WS}$  protons in a Wigner-Seitz (WS) cell. The lattice structure of the Wigner-Seitz cell [Neg73] imposes that the density is maximum in the center of the WS cell and more dilute at the extremity. Therefore, we can split the nucleons ( $N_{WS}, Z_{WS}$ ) into a cluster and a more dilute gas at density  $\rho_g$  and isospin asymmetry  $\delta_g$ . As explained in section I.2, there are two different ways to make this separation, leading to two different definitions of what a cluster is: (coordinate-space)  $r$ -clusters and (energy-space)  $e$ -clusters [Pap13].

#### i) Fermi-Dirac density profiles

In the energy-space clustering, we consider the  $e$ -clusters of  $Z_e$  protons and  $N_e$  neutrons, as the bound nucleons, independently of their localization in the WS cell. As a consequence, the  $e$ -gas is made of the particles in the continuum states. These unbound wave functions occupy the entire (infinite) space and so the gas density in the WS cell is a constant. Furthermore, the high nuclear incompressibility implies that excited nuclei keep the same bulk density as nuclei in their ground states (the Giant Monopole Resonance, that is the collective excitation mode which corresponds to a modification of the bulk density, lies at very large energies, of the order of 20 MeV excitation energy). As a consequence, we can assume that the density of the WS cell center is not modified by the occupation of unbound particle states, such that the particle density center of the WS cell is close to  $\rho_{sat}(\delta)$ , like in section II.2.1. This assumption is confirmed by finite temperature HF calculations [Pap13]. Therefore the WS cell density profiles read, choosing a Fermi-Dirac distribution for the  $e$ -cluster part  $\rho_{q,e}^{cl}(r)$ ,

$$\rho_q(r) = \rho_{q,e}^{cl}(r) + \rho_{g,q} = \frac{\rho_{sat,q}(\delta) - \rho_{g,q}}{1 + \exp[(r - R_q)/a_q]} + \rho_{g,q}, \quad (\text{II.57})$$

where  $\rho_{g,q}$  are the neutron and proton gas densities, considered uniform. We can observe that eq. (II.57) can be equivalently written as:

$$\rho_q(r) = \rho_{q,r}^{cl}(r) + \rho_{q,r}^{gas}(r) = \frac{\rho_{sat,q}(\delta)}{1 + \exp[(r - R_q)/a_q]} + \frac{\rho_{g,q}}{1 + \exp[-(r - R_q)/a_q]}. \quad (\text{II.58})$$

This equation can be interpreted as an equivalent decomposition of the cell in terms of  $r$ -cluster (and consequently  $r$ -gas), where we can see that the  $r$ -cluster excludes its volume to the  $r$ -gas. This decomposition is also very intuitive, as we now briefly discuss. In the coordinate-space clustering, the  $r$ -clusters of  $Z$  protons and  $N$  neutrons, occupy a volume in space and are surrounded by a  $r$ -gas of light particles. So, in contrast with the energy-space representation, at the center of the Wigner-Seitz cell, there are only

nucleons of the  $r$ -cluster and at its extremity, there is only the  $r$ -gas. The  $r$ -clusters and the  $r$ -gas are separated in space by a frontier located at the place where the nuclear density decreases drastically. From microscopic calculations, this frontier is a narrow region of  $\sim 1$ -2 fm, where the  $r$ -clusters and the  $r$ -gas overlap [Pap13]. Neglecting this area, the nucleons of the  $r$ -gas are located at the exterior of the  $r$ -cluster, without modifying the  $r$ -cluster density profile  $\rho_{q,r}^{cl}(r)$ . Therefore it is natural that  $\rho_{q,r}^{cl}(r)$  is given by the same Fermi-Dirac functional as in section II.2.1. To obtain the WS cell density profile, we add a reverse FD function corresponding to the increasing  $r$ -gas density profile  $\rho_{q,r}^{gas}(r)$ , which leads to eq. (II.58), where we can see that the same radii and diffusenesses parameters enter in the definition of  $\rho_{q,r}^{cl}(r)$  and of  $\rho_{q,r}^{gas}(r)$ .

It is important to insist on the fact that though they correspond to two different representations, the WS cell density profiles eq. (II.57) and eq. (II.58) are analytically equal. In one Wigner-Seitz cell, we can arbitrary choose any of the two representations. However, as explained in section I.2, the chosen representation has important consequences in terms of allowed excited states and excluded volume in a Nuclear Statistical Equilibrium model.

The diffusenesses  $a_q$  entering eq. (II.58) are given by eq. (II.43). They have been fitted on HF calculations of both nuclei in vacuum and neutron-rich clusters in nucleon gas [Pap13]. For this work, only ground states have been considered. As a consequence, there were no unbound proton, and the fit performed to obtain eq. (II.43) has been made on clusters embedded in a pure neutron gas. For NSE applications where protons are present in the nucleon gas due to finite temperature, this might be a limitation of the model, and one can wonder if the functional form (II.43) as well as the numerical values of the  $(C_i, D_i, B_i)$  parameters would not change in such a generalized situation. However, we will see in part III that the impact of the diffuseness in the energetics is a minor one, such that we can safely use the fit (II.43).

In integrating  $\rho_{q,r}^{cl}(r)$ , the radii parameters ensure the particle numbers conservation of the  $r$ -cluster  $(Z, N)$ . So, as for nuclei in vacuum, the parameters  $R_q$  are given by eqs. (II.39). We recall the relation between  $r$ -cluster nucleon numbers  $(Z, N)$  and  $e$ -cluster  $(Z_e, N_e)$  nucleon numbers developed in section I.2:

$$Z_e = \left[ 1 - \frac{\rho_{g,p}}{\rho_{sat,p}(\delta)} \right] Z \ ; \ N_e = \left[ 1 - \frac{\rho_{g,n}}{\rho_{sat,n}(\delta)} \right] N. \quad (\text{II.59})$$

Similarly, we can also define the total FD density profile

$$\begin{aligned} \rho(r) &= \rho_e^{cl}(r) + \rho_q = \frac{\rho_{sat}(\delta) - \rho_g}{1 + \exp[(r - R)/a]} + \rho_g \\ &= \rho_r^{cl}(r) + \rho_r^{gas}(r) = \frac{\rho_{sat}(\delta)}{1 + \exp[(r - R)/a]} + \frac{\rho_g}{1 + \exp[-(r - R)/a]}, \end{aligned} \quad (\text{II.60})$$

with  $\rho_g = \rho_{g,n} + \rho_{g,p}$ , and the  $e$ -cluster baryon number

$$A_e = \left[ 1 - \frac{\rho_g}{\rho_{sat}(\delta)} \right] A. \quad (\text{II.61})$$

As for nuclei in vacuum section II.2.1, we cannot use the three density FD profiles independently because in that case  $\rho(r) \neq \rho_p(r) + \rho_n(r)$ , meaning that  $A \neq N + Z$ . This means that we cannot use the three relations eqs. (II.59) and (II.61) in the same model, but, for consistency, have to use the same representation as the one chosen for FD profiles, namely  $(\rho, \rho_p)$ .

## ii) Bulk isospin asymmetry

As we have already discussed, the quantity  $\delta$  entering eqs. (II.57–II.61) is the bulk isospin asymmetry corresponding to the density of the WS cell center. Therefore,  $\delta$  is the local asymmetry in the bulk of the  $r$ -cluster. However, the relation between bulk and global asymmetries eq. (II.45) is obtained from a liquid drop model [Cen98; War09; Mye80], which is only valid for bound nuclei. This is why we can apply that formula to the  $e$ -cluster (and not to the  $r$ -cluster where unbound nucleons are present):

$$\delta_e = \frac{I_e + \frac{3a_c}{8Q} \frac{Z_e^2}{A_e^{5/3}}}{1 + \frac{9J_{sym}}{4Q} \frac{1}{A_e^{1/3}}}, \quad (\text{II.62})$$

where we have introduced the  $e$ -cluster global asymmetry  $I_e = (N_e - Z_e)/A_e$ .

The bulk asymmetry  $\delta$  can be then estimated as a linear combination of the asymmetries coming from the bound and the unbound components [Pap13]:

$$\delta = \left( 1 - \frac{\rho_g}{\rho_{sat}(\delta)} \right) \delta_e + \frac{\rho_g}{\rho_{sat}(\delta)} \delta_g = f(\delta), \quad (\text{II.63})$$

where  $\delta_g = 1 - 2\rho_{g,p}/\rho_g$  is the gas asymmetry. In order to evaluate the bulk asymmetry  $\delta$ , we have to solve  $\delta - f(\delta) = 0$ . Apart from the ideal case of homogeneous isospin  $\delta_e = \delta_g$  where the solution is analytical, the equation (II.63) is numerically solved with the Newton-Raphson method.

The function  $\delta - f(\delta)$  is plotted in fig. II-8 for an arbitrary  $e$ -cluster ( $Z_e = 30, N_e = 40$ ) within different neutron gas densities. From this figure, we can see that eq. (II.63) can have zero, one or two solution(s). The no solution case means that the four quantities  $(Z, N, \rho_{g,n}, \rho_{g,p})$  which determine the Wigner-Seitz cell configuration, are not compatible. For example, in figure II-8, we can see (black dotted lines) that a too high neutron gas density is not compatible with an already neutron rich  $e$ -cluster. From eq. (II.63), we can deduce that for configurations with asymmetries  $\delta_e$  close to  $\delta_g$ , or with low gas densities,

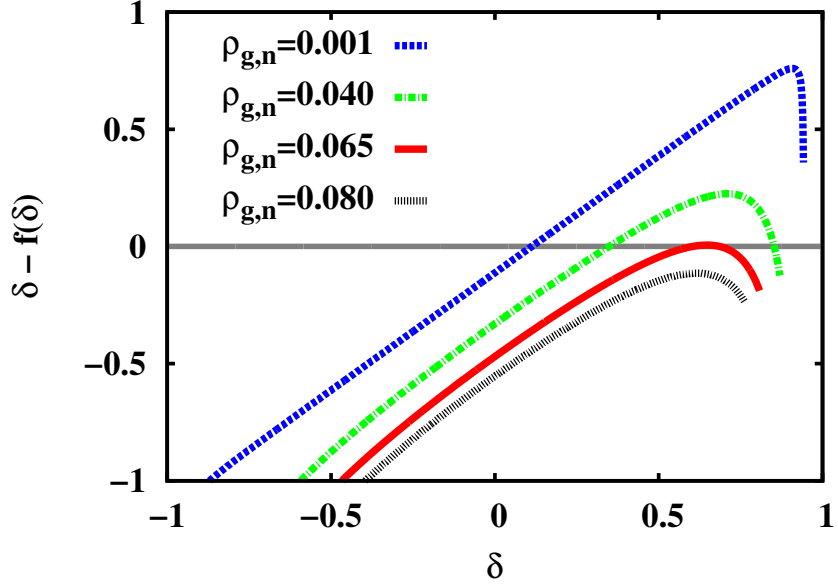


Figure II–8: Function  $\delta - f(\delta)$  eq. (II.63), for four arbitrary configurations of  $Z_e = 30$ ,  $N_e = 40$ ,  $\rho_{g,p} = 0$ , and different neutron gas densities  $\rho_{g,n}$ .

there will be one solution, which is confirmed in fig. II–8 (blue dashed lines). There are also intermediate cases where we can find two solutions for  $\delta$ , one very asymmetric, and a more symmetric one. The Wigner-Seitz cell, defined by the four degrees of freedom  $(Z, N, \rho_{g,n}, \rho_{g,p})$  has thus two possible states, differing in their nucleons distribution. In the very asymmetric case where  $\rho_{sat}(\delta)$  is low, the cluster is very large and more diluted, whereas in the more symmetric state, the cluster is denser and more localized.

In general, the asymmetric configurations have a much higher energy cost than the more symmetric one, such that they are strongly suppressed in the Nuclear Statistical Equilibrium. However, for the sake of completeness, in this study we do not make any restriction about the possible coexistence of nuclei and gas, except the existence of a solution to eq. (II.63). This amounts to considering arbitrarily any excited configurations.

For neutron rich clusters embedded in a pure neutron gas, the quality of this model computed with the Local Density Approximation has been compared to HF calculations in ref. [Pap13]. It was shown that the quality of reproduction of HF results by this model is almost independent of the presence of an external gas. Therefore the general conclusions, concerning the validity of the model for nuclei in vacuum in section II.2.1, can be kept also for the present generalization of clusters embedded in nucleons gas.

### II.2.2.b Decomposition of the energetics: in-medium effects

Computing the energy density eqs. (I.68) and (II.11) with the two density profiles  $\rho_p(r)$  eq. (II.58) and  $\rho(r)$  eq. (II.60), the total energy of a Wigner-Seitz cell is obtained:

$$E_{WS}(A, \delta, \rho_g, \delta_g) = \int \mathcal{H}[\rho(r), \rho_3(r)] d^3r, \quad (\text{II.64})$$

with  $\rho_3(r) = \rho(r) - 2\rho_p(r)$ . Similarly to nuclei in vacuum to obtain eq. (II.49), we define the surface energy of the WS cell as the quantity deduced from the total energy after subtraction of the energy the system would have in the absence of the surface of both the cluster and the gas:

$$E_{s,m}(A, \delta, \rho_g, \delta_g) = E_{WS}(A, \delta, \rho_g, \delta_g) - \mathcal{H}[\rho_{sat}, \rho_{sat,3}] V_{HS} - \mathcal{H}[\rho_g, \rho_g \delta_g] (V_{WS} - V_{HS}), \quad (\text{II.65})$$

where  $V_{WS}$  is the total volume of the Wigner-Seitz cell and  $V_{HS}(\delta) = A/\rho_{sat}(\delta)$  the equivalent hard-sphere volume of the cluster.

The total in-medium modification of the cluster energy  $\delta E$  can be computed by subtracting to the total energy the contribution of the gas alone and of the nucleus alone:

$$\delta E(A, \delta, \rho_g, \delta_g) = E_{WS}(A, \delta, \rho_g, \delta_g) - E(A, Z) - V_{WS} \mathcal{H}[\rho_g, \rho_g \delta_g], \quad (\text{II.66})$$

where  $E(A, Z)$  defined eq. (II.46) is the energy of the nucleus  $(A, Z)$  in the vacuum, with  $Z$  the proton number determined by the variables  $A$  and  $\delta$ :  $Z = Z(A, \delta)$ .

Using eqs. (II.65), (II.66), and (II.49), the in-medium modification energy  $\delta E$  reads

$$\delta E(A, \delta, \rho_g, \delta_g) = \delta E_b(A, \delta, \rho_g, \delta_g) + \delta E_s(A, \delta, \rho_g, \delta_g), \quad (\text{II.67})$$

with

$$\delta E_b(A, \delta, \rho_g, \delta_g) = -\frac{\mathcal{H}[\rho_g, \rho_g \delta_g]}{\rho_{sat}(\delta)} A, \quad (\text{II.68})$$

and

$$\delta E_s(A, \delta, \rho_g, \delta_g) = E_{s,m}(A, \delta, \rho_g, \delta_g) - E_s(A, Z). \quad (\text{II.69})$$

In observing that  $\delta E_b(A, \delta, \rho_g, \delta_g)$  is proportional to the mass number  $A$ , and since  $\delta E_s(A, \delta, \rho_g, \delta_g)$  is a sum of two surface terms, we can then define the bulk and surface

in-medium modified cluster energies as:

$$E_{b,m}(A, \delta, \rho_g, \delta_g) = \left( \mathcal{H}[\rho_{sat}(\delta), \rho_{sat,3}(\delta)] - \mathcal{H}[\rho_g, \rho_g \delta_g] \right) \frac{A}{\rho_{sat}(\delta)}, \quad (\text{II.70})$$

$$E_{s,m}(A, \delta, \rho_g, \delta_g) = E_s(A, Z) + \delta E_s(A, \delta, \rho_g, \delta_g). \quad (\text{II.71})$$

The validity of this decomposition will be explicitly tested in chapter [II.3](#).

## Chapter II.3

# In-medium interactions

In this chapter, the ETF model presented in II.2 is employed to evaluate the in-medium energy shifts in a large variety of excited state configurations. Their dependence on the cluster mass and asymmetry, as well as on the gas density and asymmetry, is presented. More specifically, the case of nuclei immersed in a neutron gas, corresponding to the case of nuclear clusters present in the crust of neutron stars, is examined. The case where the nucleus is in an arbitrary excited state configuration, as it is the case in the finite temperature conditions of supernova matter and proto-neutron stars, is also considered and shown to lead to very different energy shifts.

The bulk and surface energy modifications due to the interactions of the clusters with the nucleon gas are respectively studied in section II.3.1 and II.3.2. Section II.3.3 presents the dependence on the effective interactions in the calculation of the energy shifts with a few chosen Skyrme functionals. In section II.3.4, the impacts of the in-medium corrections on the neutron star inner crust are estimated.

### II.3.1 Modifications of the bulk energy

The in-medium mass-independent bulk energy per nucleon  $E_{b,m}/A$ , defined by eq. (II.70), and computed with the SLy4 interaction is displayed in fig. II-9 as a function of the gas density (left side) for different bulk asymmetries of the nucleus, and as a function of the bulk asymmetry (right side) for different gas densities. Two representative cases are considered: a gas asymmetry equal to the cluster one  $\delta_g = \delta$  (lower panels) and a pure neutron gas  $\delta_g = 1$  (upper panels).

For very neutron rich clusters, the case  $\delta_g = 1$  is relevant both for the ground state of the neutron star inner crust, and for the most representative configurations of neutron rich matter at finite temperature. For nuclei close to isospin symmetry,  $\delta \approx 0$ , the case  $\delta_g = \delta$  corresponds to the most probable configurations at finite temperature. In all

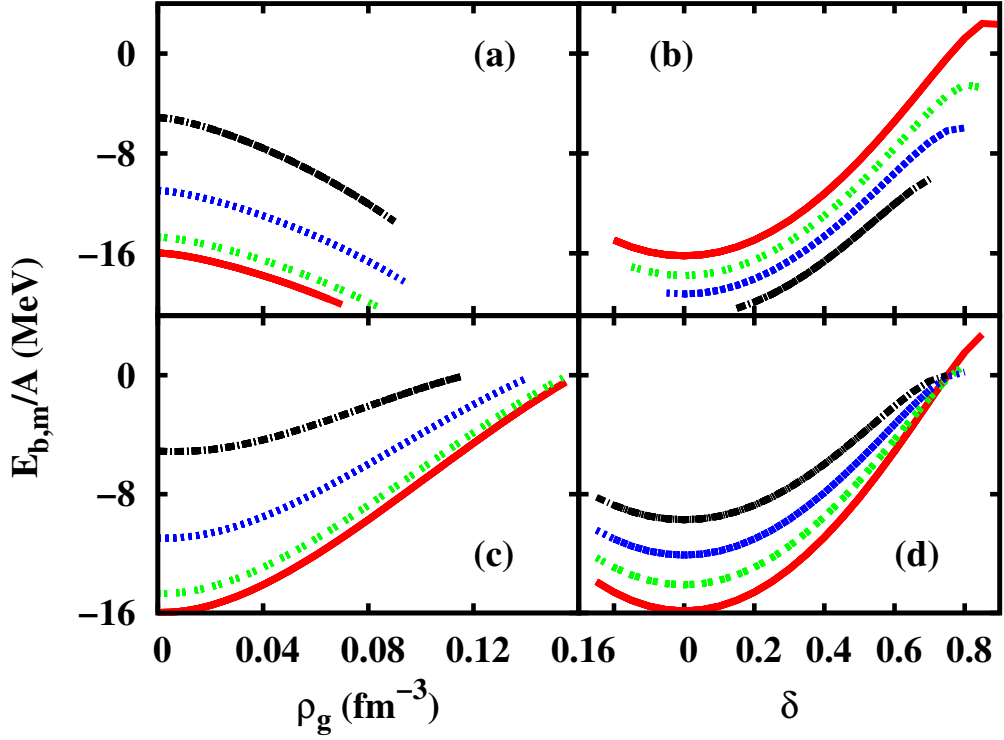


Figure II-9: In-medium bulk energy  $E_{b,m}/A$  eq. (II.70), as a function of the gas density for a fixed bulk asymmetry (left side) and as a function of the bulk asymmetry for a fixed gas density (right side). Upper panels: pure neutron gas ( $\delta_g = 1$ ). Lower panels: gas asymmetry equal to the bulk asymmetry ( $\delta_g = \delta$ ). (a) and (c):  $\delta = 0.0$  (full red),  $\delta = 0.2$  (dashed green),  $\delta = 0.4$  (dotted blue),  $\delta = 0.6$  (dashed-dotted black). (b) and (d):  $\rho_g = 0.01$  (full red),  $\rho_g = 0.04$  (dashed green),  $\rho_g = 0.06$  (dotted blue),  $\rho_g = 0.08$  (dashed-dotted black). Figure published in [Aym14].

cases, increasing gas density corresponds to physical situations at higher density and/or temperature.

Imposing the gas asymmetry to be strictly equal to the cluster asymmetry amounts to disregard isospin effects (isospin fractionation) in the equilibrium. In this case (lower panels) we recover the well known result that the cluster energy is reduced by the presence of the surrounding medium, leading to the dissolution of clusters at the critical Mott density [Typ10; Roe09; Roe11]. The critical Mott density can be defined as the density corresponding to vanishing bulk binding, and is given by the ending point of each curve in fig. II-9(c). It is by construction the saturation density  $\rho_{sat}(\delta)$  and we recover that it monotonically decreases with increasing cluster asymmetry [Pap13].

In the case of stellar matter at  $\beta$ -equilibrium the fractionation effect cannot be neglected, and the gas is systematically more neutron-rich than the clusters. In particular, in the specific case of cold neutron star crust, the uniform gas is uniquely constituted of

neutrons [Neg73; Gul15]. The limiting case  $\delta_g = 1$  is thus close to the physical condition of the low temperature stellar environment. In this case the trend with respect to the density (at fixed asymmetry  $\delta$ ) is reversed.

The reduction of the in-medium bulk energy with respect to the density at fixed  $\delta$  in fig. II-9(a) is simple to understand: the first term in eq. (II.70) is constant at fixed  $\delta$ , as well as the common factor  $1/\rho_{sat}(\delta)$ , while the second term in eq. (II.70) is increasing with the gas density at fixed  $\delta_g = 1$  since neutron matter is unbound.

The consequence of this shift is more interesting to comment in panel (b). Indeed, it is known that in the sequence of nuclei predicted in the crust of neutron stars [Neg73], as the density increases, the bulk asymmetry of the clusters  $\delta$  also increases. This sequence can be understood in part from fig. II-9(b) since as  $\rho_g$  increases, the constant bulk energy path is going towards more and more asymmetric clusters. Taking the sequence of ground state nuclei predicted in the crust of neutron stars [Neg73], the bulk energy departs from a quadratic behavior with respect to  $\delta$  since increasing the gas density shifts down the bulk energy, as shown in figs. II-9(a) and (b). This simple mechanism explains why clusters can survive in environment extremely neutron rich as neutron star crusts.

It is however surprising that for the gas densities considered in fig. II-9, the medium modifications to the bulk energy remain mostly quadratic with respect to  $\delta$  at fixed  $\rho_g$ . Non-quadraticities in  $\delta$  are only observed (right panels) for  $\delta \geq 0.6$ , with or without gas, and disregarding the gas asymmetry. The quadratic dependence of the bulk energy with respect to  $\delta$  is therefore a robust prediction which goes beyond the case of isolated nuclei and can be generalized to dilute nuclei to a large extent.

## II.3.2 Modification of the surface energy

Figure II-10 illustrates the surface tension energy  $E_{s,m}/A^{2/3}$ , defined by eq. (II.71), as a function of the gas density  $\rho_g$  and of the bulk asymmetry  $\delta$  for the same gas compositions as for figure II-9. For each curve, the calculation was done varying the cluster size over a very large domain. The almost perfect scaling with  $A^{2/3}$  shows that indeed the residual in-medium binding energy shift is mainly a surface effect. There are only few cases where the curves acquire a finite width, reflecting a small contributions from curvature terms: in fig. II-10(a) where  $\delta_g = 1$  and for the most neutron rich clusters (black curves), and in fig. II-10(c) where  $\delta_g = \delta$  and here also for the most neutron rich curves (for e.g. black curves at  $\rho_g = 0$ ). The curvature terms have been discussed in section II.2.1.c, and are observed here to be maximal in the most asymmetric clusters as the gas density increases.

Neglecting fractionation effects in fig. II-10(c), the surface energy is reduced as the gas density increases and whatever the cluster asymmetry. It vanishes at the corresponding

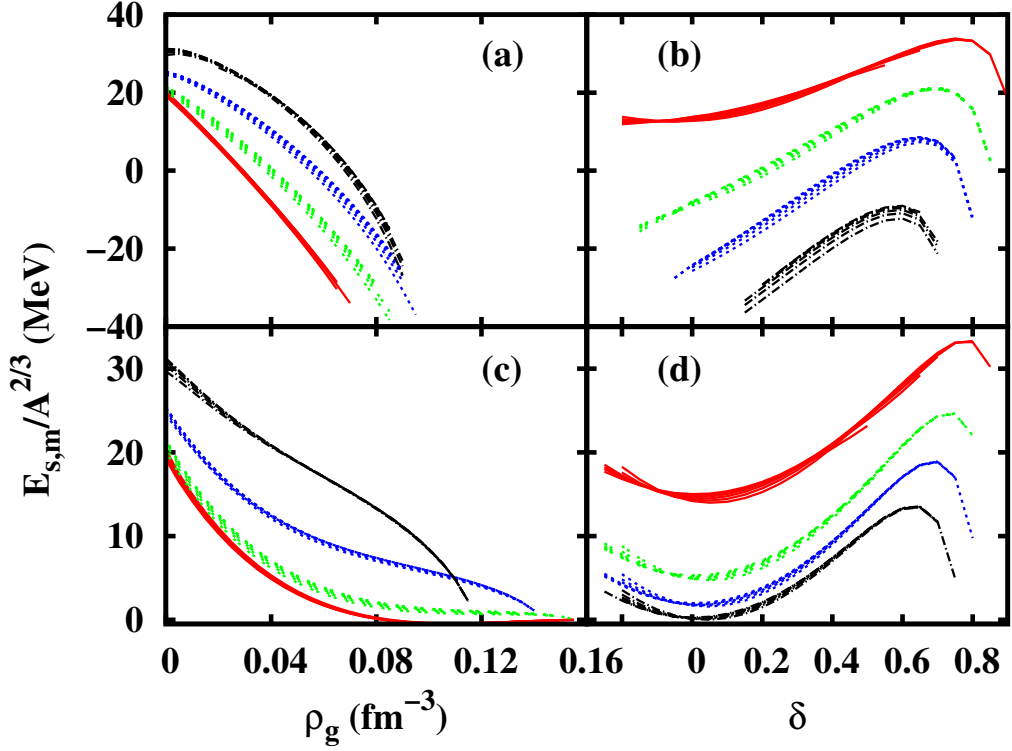


Figure II-10: In-medium surface energy  $E_{s,m}/A^{2/3}$  eq. (II.71), as a function of the gas density for a fixed bulk asymmetry (left part) and as a function of the bulk asymmetry for a fixed gas density (right part). Upper panels: pure neutron gas. Lower panels: gas asymmetry equal to the bulk asymmetry. (a) and (c):  $\delta = 0.0$  (full red),  $\delta = 0.2$  (dashed green),  $\delta = 0.4$  (dotted blue),  $\delta = 0.6$  (dashed-dotted black). (b) and (d):  $\rho_g = 0.01$  (full red),  $\rho_g = 0.04$  (dashed green),  $\rho_g = 0.06$  (dotted blue),  $\rho_g = 0.08$  (dashed-dotted black). Figure published in [Aym14].

saturation density  $\rho_{sat}(\delta)$ , showing again the dissolution of clusters in the dense medium. In fig. II-10(d), the dependence of the surface energy with  $\delta$  is mostly quadratic, even for the largest densities considered here. The quadratic behavior of the surface energy is well satisfied up to  $\delta \simeq 0.6$ , as in the case of the bulk energy.

It is quite surprising to find in the case of pure neutron gas, figs. II-10(a) and (b), that the surface energy not only decreases as the gas density increases, but can even become negative. This can be understood from the fact that the surface energy  $E_{s,m}$  as defined by eq. (II.65) represents the interface contribution between the cluster and the gas. At finite gas density, this interface energy contains contributions from both the cluster and the gas. The contribution of the pure neutron gas to the interface region is largely negative, since the interface region is more symmetric than the gas. The negative contribution of the gas dominates as the gas density increases, leading to negative surface

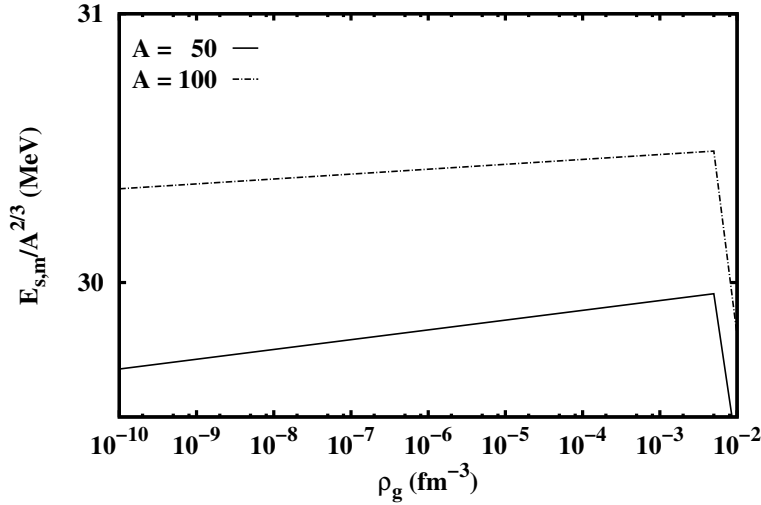


Figure II–11: In-medium surface energy  $E_{s,m}/A^{2/3}$  eq. (II.71), as a function of the pure neutron gas density for a high bulk asymmetry  $\delta = 0.6$ . The different curves correspond to different cluster sizes.

energy as shown in fig. II–10(a). This effect is lowered when the cluster is more neutron rich (see fig. II–10(b)).

It should also be remarked that the density as which the surface energy becomes negative increases as the bulk asymmetry increases. Since the ground state configurations predicted for the crust of neutron stars [Neg73], have increasing  $\delta$  for increasing  $\rho_g$ , we can deduce from fig. II–10(a) that these configurations correspond to systems where the surface energy is positive as discussed in section II.3.4.

Let us also notice that, on the opposite of the results of [Bay71a] for which the asymmetry is disregarded, the surface energy obtained for the highest asymmetry are not monotonic with the gas density. Indeed, the curves of fig. II–11, which stand for neutron rich clusters ( $\delta = 0.6$ ) embedded in a pure neutron gas, show an increase of the surface energy with the gas density, up to  $\sim 5 \cdot 10^{-3} \text{ fm}^{-3}$ .

Concerning the dependence of the surface energy on  $\delta$  in fig. II–10(b), we can see a very different behavior compared with the previous cases: the quadratic approximation in  $\delta$  is completely lost due to the contribution of the gas, which is not quadratic in  $\delta$ , but in  $\delta_g$ .

### II.3.3 Dependence on the effective interaction

In this section, we show that the qualitative behaviors that we have discussed in II.3.1 and II.3.2 are not modified when a different Skyrme interaction is employed. Further-

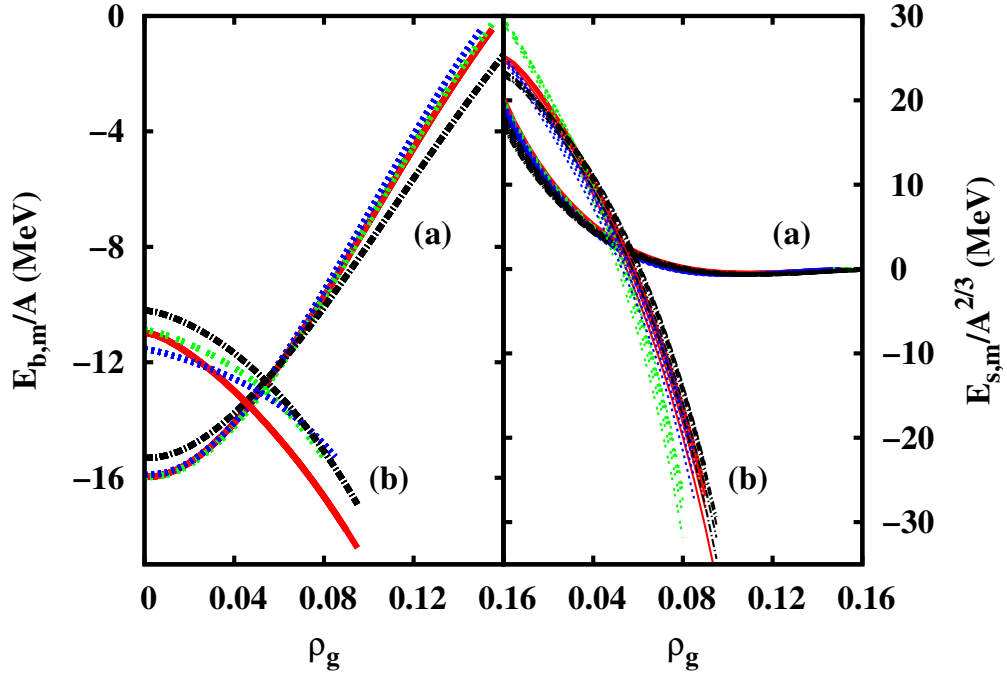


Figure II–12: In-medium bulk (left panel) and surface (right panel) energy as a function of the gas density. (a): clusters with bulk asymmetry  $\delta = 0$  immersed in a symmetric gas. (b): clusters with  $\delta = 0.3$  immersed in a pure neutron gas. Different models are considered: Sly4 [Cha98] (full red), SkI3 [Rei95] (dashed green), SGI [Gia81] (dotted blue), LNS [Cao06b] (dashed-dotted black). Figure published in [Aym14].

more, we show that the positive sign of the surface symmetry energy, discussed in section II.2.1.c, does not depend on the particular effective interaction. However the quantitative values of the clusters bulk and surface energies obviously depend on the effective interaction parameters, and for a realistic treatment of the stellar matter equation of state it is very important to consistently treat within the same effective interaction both the cluster and the nucleon gas [Pap13; Rad14].

To study how the in-medium effects depend on the model, we represent in fig. II–12 two representative situations of a symmetric nucleus in a symmetric gas (a), and a neutron rich nucleus in a pure neutron gas (b), with different Skyrme models. We have chosen these specific interactions in order to span the present uncertainties in the bulk parameters. These latter are reported in table II–3.

We can see from figure II–12 that the qualitative behavior of the different models is the same. A more complete study of the effective interactions parameter space is needed to reach sound conclusions on the quantitative model dependence, but from the representative chosen interactions we can dress some tentative partial interpretation. The differences in bulk energy directly reflect the uncertainties in present models of the

Interaction	$\rho_{sat}(0)$ ( $\text{fm}^{-3}$ )	$K_{sat}$ (MeV)	$J_{sym}$ (MeV)	$L_{sym}$ (MeV)	$K_{sym}$ (MeV)
SLY4 [Cha98]	0.1595	230.0	32.00	46.0	-119.8
SkI3 [Rei95]	0.1577	258.2	34.83	100.5	+ 73.0
SGI [Gia81]	0.1544	261.8	28.33	63.9	- 52.0
LNS [Cao06b]	0.1746	210.8	33.43	61.5	-127.4

Table II-3: Bulk and surface nuclear properties for the different Skyrme interactions examined in this section.

bulk properties of matter. These uncertainties are very small in the isoscalar part, and the curves of the bulk symmetric systems, see curves labelled (a) on the left panel, are indistinguishable except LNS (dashed-dotted black lines). The LNS Skyrme model is known to have a saturation density larger than the expected one, see tab. II-3, which is reflected in the fact that at  $\rho_g = 0$ , the LNS bulk energy is different from the others. It also leads to slightly reduced in-medium modification, as observed in fig. II-12. Concerning medium modifications to the bulk energy in the neutron rich system, see curves labelled (b) on the left panel, it is observed that SLy4 Skyrme interaction (full red) leads to slightly more important binding energy shift. This is due to a non-trivial interplay of slightly different values of  $J_{sym}$ ,  $L_{sym}$ ,  $K_{sym}$ . Concerning the surface energies, the behavior appears very stable. The only exception is the gas density behavior of the neutron rich system, curves (b) in the right panel, calculated with SkI3 (dashed green). This steep in-medium modification is probably due to the very stiff isovector properties of this effective interaction.

To conclude, we can see that, independently of the model, the in-medium modifications are not negligible and should be accounted for in a realistic equation of state. Due to the simple expression (II.69), the surface corrections can be tabulated as a function of  $(A, I, \rho_{g,n}, \rho_{g,p})$  and straightforwardly introduced in the NSE model (see part I), as a consistent modification of the cluster energy functional (I.83), with no extra computational cost. However, the modifications depend on four variables which have to span the very large variety of excited state configurations accessible in supernovae and proto-neutron stars. Moreover, to be complete, the in-medium modifications should also take into account the entropy of nucleons, which amounts to consider the total free energy corrections as a function of  $(A, I, \rho_{g,n}, \rho_{g,p})$ , as well as of the temperature. That is why these corrections have not been directly implemented in the NSE code yet, but in the next section, we show results perturbatively obtained at (almost) zero temperature and  $\beta$ -equilibrium. Finally, it is important to stress that these in-medium modifications have been obtained in the ETF approximation, which is a good approximation for heavy nuclei but worsens for lighter ones. In particular in the case of light particles in the Wigner-Seitz cell, we do not expect this formalism to be realistic. It would be very interesting

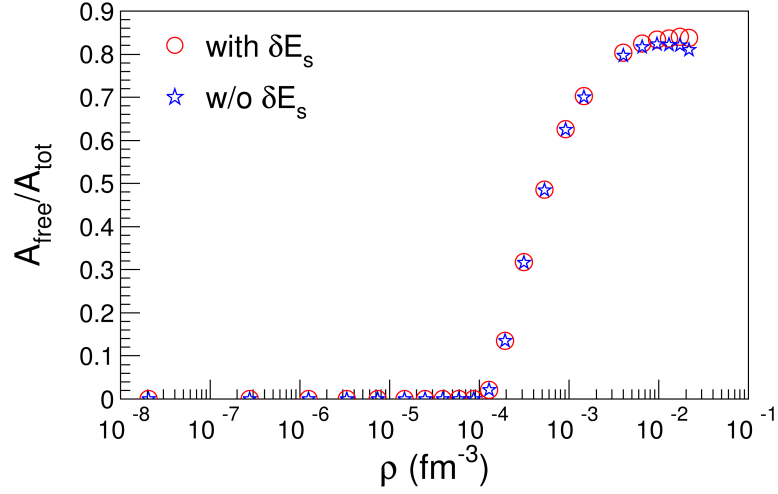


Figure II–13: Percentage of unbound particles along the beta-equilibrium path at  $T = 0$  MeV as a function of total baryonic density. Figure published in [Rad14].

to compare these results with more microscopic and realistic calculations [Sed06; Typ10; Hem11].

### II.3.4 Effects of the in-medium corrections on neutron stars

In order to estimate the extent of the surface in-medium effects on the related quantities to the crust-core transition of a neutron star, we have first calculated the Wigner-Seitz cells characteristics ( $A_{WS}, Z_{WS}, V_{WS}$ ) at the different baryon densities provided by the NSE (part I) at  $T = 0.5$  MeV and at the  $\beta$ -equilibrium path without the inclusion of the surface correction terms, with the effective interaction SLy4. We have verified that the results do not change much by further decreasing the temperature and can thus be considered as representative of the zero temperature situation.

To compare these results where we have ignored the surface in-medium effects, to the ones which take them into account, we proceed as follows. In the simplified situation presented above, we can safely consider a pure neutron gas and, for each density  $\rho$ , we can assume that matter is well described with the Single Nucleus Approximation (SNA). To take into account the in-medium effects, we associate one single representative Wigner-Seitz cell by numerically minimizing the WS energy (eq. (I.106) at zero temperature), with respect to the cluster size  $A$ . In this exploratory calculation, we have assumed that the surface in-medium corrections do not change the cluster proton number, nor the  $\beta$ -equilibrium such that the neutron gas density  $\rho_g$  remains the same with and without  $\delta E_s$ . Moreover, the in-medium surface corrections  $\delta E_s$  have been calculated within the simple Thomas-Fermi approximation. The inclusion of the 2<sup>nd</sup> order ETF corrections is

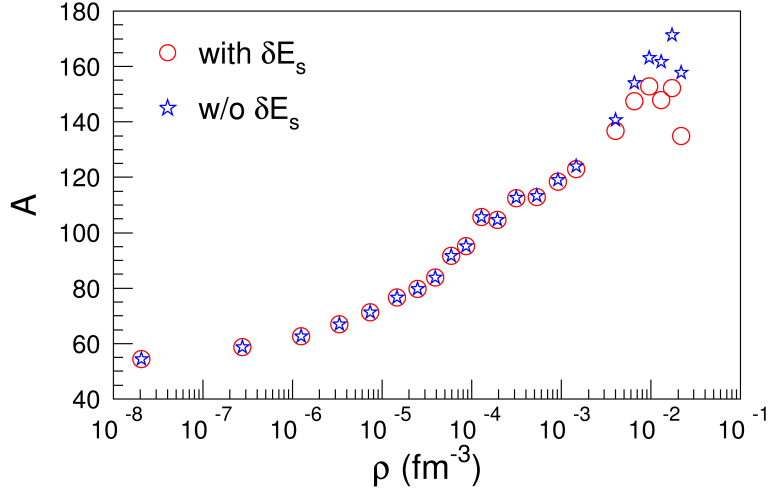


Figure II-14: Cluster size along the beta-equilibrium path at  $T = 0$  MeV as a function of total baryonic density. Figure published in [Rad14].

not expected to change the qualitative trends nor the main deduced conclusions.

Figure II-13 displays the percentage of unbound particles  $A_{free}/A_{tot} = \rho_g/\rho$  along the  $\beta$ -equilibrium at zero temperature, as a function of the average baryonic density  $\rho$  both for the case where in-medium effects are accounted for (red circles), and the one in which they are ignored (blue stars).

Over the considered density range, the percentage of unbound particles increases from 0 to  $\sim 1$ . This confirms that at low densities, matter is made out of clusters without gas, while at high densities it rather consists of uniform matter in strong interaction. As density increases, the system becomes globally more and more neutron-rich due to the  $\beta$ -equilibrium (see part I). We can see the specificity of zero temperature which is the discontinuous behavior of the number of unbound nucleons which is strictly zero before the neutron drip line, at  $\rho \sim 10^{-4} \text{ fm}^{-3}$  in fig. II-13, and monotonically increases afterwards, allowing to clearly distinguish the inner crust from the outer crust. As we have seen in part I, this clear distinction is not possible at finite temperature, because of the presence of continuum states in the whole density domain.

Concerning the in-medium effects, fig. II-13 indicates that they are sizable only at the densities corresponding to the inner part of the inner crust,  $\rho \gtrsim 5 \cdot 10^{-3} \text{ fm}^{-3}$ , and they act in the sense of reducing the cluster size (fig. II-14), meaning that the in-medium correction  $\delta E_s$  is positive. This is in agreement with figure II-11 which presents configurations close of the ones in neutron stars inner crust, that is very neutron-rich clusters.

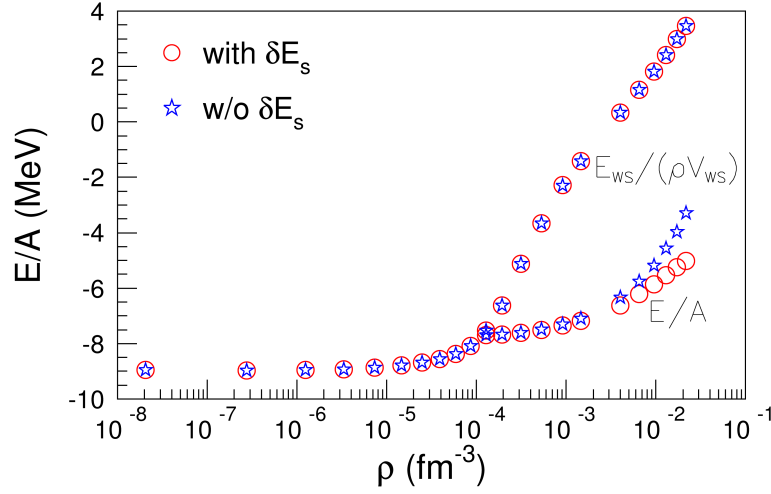


Figure II–15: Total energy per nucleon and cluster energy per nucleon along the beta-equilibrium path at  $T = 0$  MeV as a function of total baryonic density. Figure published in [Rad14].

Figure II–15 shows the total and cluster energy in the Wigner-Seitz cell. We can clearly see the separation between outer and inner crust at the neutron drip at  $\rho \sim 10^{-4} \text{ fm}^{-3}$ . We observe that the energy per nucleon is reduced when we consider the in-medium surface effects. This is simply explained by the reduction of the cluster size which implies an increase of the proton fraction since the proton number is assumed to be the same whether we take into account or ignore the surface corrections. So the clusters being less asymmetric, they gain binding which even overcomes the repulsive energy coming from  $\delta E_s$ .

In the inner crust the unbound component is dominant as it can be seen from fig. II–13. This is why the total energy in the Wigner-Seitz cell is not affected by the in-medium surface corrections in fig. II–15.

To conclude, the effect of the in-medium modification appears globally small in the neutron stars inner crust. This is due to the fact that, at the densities where free nucleons can be found, zero temperature matter in  $\beta$ -equilibrium corresponds to the exclusive configuration of extremely neutron-rich clusters in neutron gas.

From section II.3.2, we have seen that the in-medium modifications have very different behaviors depending on the configuration  $A, Z, \rho_g, \delta_g$ . Thus we expect that in supernova conditions the effects will be more important since at finite temperature all the channels are opened, and the  $\beta$ -equilibrium is not necessary satisfied. Moreover we have to stress that many simplifications have been done in this exploratory calculation, and it will be important to check if the results are the same consistently including the in-medium

effects in the variational problem.

# Part conclusions

In this part, we have considered a quasi-analytical modelling of the nuclear density profiles allowing to calculate nuclear binding energies within the Extended-Thomas-Fermi approximation at the second order in  $\hbar$ . Through a comparison to HF calculations for some representative nuclei, we have shown that a simple Fermi-Dirac profile is sufficient to reach a precision in the energy of the order of 100-200 keV/nucleon, and the widening of the variational space considering Generalized FD trial densities does not introduce any sizeable improvement of the predictive power of the model.

With this model, we have first explored the definitions of the bulk and surface part of the symmetry energy of finite nuclei in vacuum, which is important for the extraction of equation of state parameters for astrophysical applications. We have shown that the variational character of the ETF formalism suggests that the bulk part of the nuclear energy depends on the central bulk asymmetry  $\delta$  rather than on the global asymmetry of the nucleus  $I$  which is usually considered in Liquid Drop Models. This statement, which is confirmed by a detailed comparison to HF calculations, implies that the surface symmetry energy contributes positively to the total symmetry energy of the nucleus. The choice of the global asymmetry parameter  $I$  considered in LDM, while not consistent with ETF, can explain the ambiguities reported in the literature concerning the sign of the surface symmetry energy.

We have extracted and evaluated the in-medium energy shift which is experienced by a nucleus immersed in the gas of its continuum states, as it is the case in supernova matter and in the inner crust of (proto-)neutron stars. We have shown that the presence of an external gas induces both a bulk and a surface energy shifts, which depend in a highly complex and non-linear way on the asymmetry of the cluster, and the asymmetry and density of the gas. The estimations of these effects at zero temperature and  $\beta$ -equilibrium show that the surface in-medium corrections may be neglected when modelling neutron stars crust matter. However, since the absolute values of the energy shifts can be comparable or higher than the nuclear binding energy, the coexistence of nuclei and free particles in hot and/or out  $\beta$ -equilibrium stellar matter are not expected to be modeled as a mixture of non-interacting nuclear species.

# Résumé de la partie II

Les approches semi-classiques de Thomas Fermi -également appelé approximation de densité locale- et Thomas-Fermi étendue de la théorie de la fonctionnelle de densité étaient largement utilisées dans les années 80 pour la structure nucléaire [Bra85; Tre86; Cen90] ainsi que pour les applications astrophysiques [Sur84; Pi86]. Deux motivations pour rechercher des approximations de la théorie microscopique de champ moyen utilisant des interactions effectives étaient avancées. D'une part, cette théorie semi-classique est quasi-analytique et présente donc l'avantage de mettre en évidence la dépendance fonctionnelle des énergies nucléaires et des profils de densité. Cela permet d'obtenir des formules explicites et donc de comprendre des propriétés physiques de l'énergétique des noyaux, ce qui ne peut pas être réalisé en résolvant numériquement les équations de Hartree-Fock. D'autre part, les ressources de calcul à ce moment-là impliquaient que des calculs systématiques d'Hartree-Fock étaient très difficiles à effectuer avec des barres d'erreur numériques fiables. En raison de la progression exponentielle du calcul numérique dans les deux décennies suivantes, cette motivation est devenue obsolète, et de nos jours, des calculs de structure nucléaire à grande échelle de champ moyen et au-delà [Was12] sont régulièrement effectués.

Toutefois, dans les dernières années, un intérêt renaissant envers la théorie de Thomas-Fermi étendue est apparu [Ons08; Pot13; Lee10], en particulier dans le cadre de la description de la matière stellaire. Ceci est largement dû aux nouveaux défis et besoins pour une description microscopique des espèces nucléaires très exotiques qui devraient exister dans la matière stellaire. En effet, comme expliqué dans la partie I, une description complète et microscopique de la matière stellaire à densités sous-saturées et à température finie implique l'évaluation d'une très grande base de données d'états fondamentaux et de configurations nucléaires excitées, qui ne sont pas directement accessibles aux calculs variationnelle Hartree-Fock, ou sont numériquement trop coûteux pour des calculs à grande échelle [New09].

Ainsi, les approches microscopique de moyen-champ ou au-delà ne peuvent pas être raisonnablement effectuées pour une description de la matière stellaire à température finie. De plus, les modèles récents qui prennent en compte la distribution statistique

des noyaux utilisent plutôt des données expérimentales ou de simples formules de goutte liquide pour les masses nucléaires. Ce faisant, ils ne considèrent pas les modifications de milieu de l'énergie nucléaire des agrégats [Hem10; Buy13; Fur13]. En effet, dans ces modèles, en dehors d'un volume exclu, les agrégats ne sont pas affectés par les autres nucléons du milieu, c'est-à-dire que l'énergie de leur état fondamental est la même dans le milieu stellaire que dans le vide. Cette approximation est évidemment très forte à des densités comparables à la densité de saturation. Par conséquent, l'approche plus simple de Thomas-Fermi étendue peut être considérée comme un compromis intéressant pour inclure correctement les effets de milieu aux propriétés du noyau et, en même temps, fournir des expressions quasi-analytiques qui peuvent être implémentées dans une modélisation complète du problème de la matière stellaire.

Dans cette partie, nous avons considéré une modélisation quasi-analytique des profils de densité nucléaire permettant de calculer les énergies de liaison nucléaires, en utilisant l'approximation de Thomas-Fermi étendue au second ordre en  $\hbar$ . Grâce à une comparaison à des calculs Hartree-Fock pour quelques noyaux représentatifs, nous avons montré qu'un simple profil de Fermi-Dirac est suffisant pour atteindre une précision en énergie de l'ordre de 100-200 keV/nucleon, et que l'élargissement de l'espace variationnel en considérant un profil de densité de type Fermi-Dirac généralisé ne présente aucune amélioration importante.

Avec ce modèle, nous avons d'abord exploré les définitions de la partie de volume et de surface de l'énergie de symétrie de noyaux finis dans le vide. Ces différents termes sont importants afin d'extraire les paramètres de l'équation d'état pour des applications astrophysiques. Nous avons montré que le caractère variationnel du formalisme de Thomas-Fermi étendu suggère que la partie de volume de l'énergie nucléaire dépend de l'asymétrie de volume au centre du noyau ( $\delta$ ) plutôt que de l'asymétrie globale du noyau  $I$  qui est généralement considéré dans les modèles de goutte liquide. Cette observation est confirmée par une comparaison détaillée avec des calculs Hartree-Fock. Nous avons montré que cette dépendance implique que l'énergie de symétrie de surface contribue de façon positive à l'énergie totale de symétrie du noyau. Le choix du paramètre global d'asymétrie  $I$  considéré dans les modèles de goutte liquide, qui n'est pas compatible avec un modèle de Thomas-Fermi étendu, peut expliquer les ambiguïtés rapportées dans la littérature en ce qui concerne le signe de l'énergie de symétrie de surface.

Nous avons également extrait et évalué les modifications de l'énergie de milieu d'un noyau immergé dans le gaz de ses états du continuum, comme c'est le cas dans la matière de supernova et dans celle de la croûte interne des (proto-)étoiles à neutron. Nous avons montré que la présence d'un gaz externe induit une modification des énergies de volume et de surface, qui dépendent d'une manière très complexe et hautement non-linéaire de l'asymétrie de l'agrégat, ainsi que de l'asymétrie et de la densité du gaz de nucléons. Les

estimations de ces effets à température nulle et en équilibre  $\beta$  montrent que les corrections de milieu de surface peuvent être négligées lors de la modélisation de la matière de la croûte des étoiles à neutrons. Cependant, étant donné que les valeurs absolues des modifications d'énergie peuvent être comparables ou supérieures à l'énergie de liaison nucléaire, la coexistence des noyaux et de particules libres dans la matière chaude et/ou hors équilibre  $\beta$  ne devrait pas être modélisée comme un mélange d'espèces nucléaires sans interaction.



Part III:

**Analytical mass formula**

# Part introduction

In order to implement in the Nuclear Statistical Equilibrium the in-medium effects investigated in part II, it is highly desirable to have analytical expressions of the Extended-Thomas-Fermi (ETF) integrals. The development of systematic approximations to analytically integrate the ETF functional in the presence of a gas is a delicate issue. Therefore, we mainly focus on nuclei in vacuum between the drip lines in this part, and only sketch the generalization to the Wigner-Seitz cell energy at the end of this part. Coherently with the rest of this thesis, we only consider Skyrme functionals.

As we have already discussed, Skyrme functionals have been widely used to describe nuclear structure properties, with different level of sophistication in the many-body treatment, from the simplest Thomas-Fermi [Bra85] to modern multi-reference calculations [Was12]. The most basic observable accessible to the functional treatment is given by nuclear mass, allowing the analysis of the different mass components in terms of bulk and surface properties, as well as isovector and isoscalar properties. The theoretical prediction of nuclear mass is not only important in itself, but it is also a fundamental tool to optimize the different functional forms and associated parameters, for an increasing predictive power of density functional calculations [Gor13]. Indeed mass predictions from microscopic density functionals are nowadays very accurate and can even equalize the most precise phenomenological mass formulas available in the literature [Liu11; Mol95; Duf95].

For practical applications in nuclear structure or nuclear astrophysics problems, different parametrizations of nuclear masses fitted on density functional calculations with Skyrme forces have been proposed [Abo95; Dan09; Lee10; Nik11]. In particular, the one proposed in [Dan09] has been extensively used in the calculations we have presented in part I. The limitation of these works is that the different coefficients are not analytically calculated but they result from the fit to the numerically determined nuclear masses. As a consequence, the fit has to be performed again each time that the functional is improved by adding further constraints from the rapidly improving experimental data. Moreover, the absence of an analytical link between the Skyrme parameters and the coefficients of the mass formula implies no unambiguous correlation between the differ-

---

ent parts of the mass functional and the physical properties of the effective interaction can be established. For these reasons, it appears interesting to search for an analytical expression of the mass formula coefficients, directly linked to the functional form and parameters of the Skyrme interaction. The derivation of such an analytical formula is the purpose of this part.

An especially appealing formalism when seeking for analytical expressions is the semi-classical Extended-Thomas-Fermi (ETF) approach, which is based on an expansion in powers of  $\hbar$  of the energy functional, as introduced in part II. As we have seen, the advantage of the ETF approximation is that the energy functional solely depends on the local particle densities and their gradients, and the energy of any arbitrary nuclear configuration can be calculated if the density profiles are given through a parametrized form. On the other side, the well known limitation of ETF is that only the smooth part of the nuclear mass can be addressed, and shell effects have to be added on top, for instance through the well known Strutinsky method [Pea12]. As in part II, we will consider here an ETF expansion up to the second  $\hbar^2$ -order, and thus limit ourselves to the smooth part of the mass functional.

The plan of the part is as follows. Chapter III.1 addresses the problem of symmetric nuclei. In this simplified case, the ETF integrals can be analytically integrated leading to a very transparent form for the surface and curvature terms of the nuclear energy. Unlike previously, this approach also allows to express the surface diffuseness as a function of parameters of the Skyrme interaction. The more general problem of isospin asymmetric nuclei is studied in chapter III.2. We first demonstrate that the bulk isospin asymmetry  $\delta$  introduced in part II takes into account a large part of the isospin dependence. The residual isovector surface symmetry energy density term is not analytically integrable, meaning that approximations have to be performed. We propose two different approximations and critically discuss their validity in comparing them to both numerical integration of the ETF functional and to complete Hartree-Fock (HF) calculations using the same functional. Finally, the complete mass formula that we propose is used with different representative Skyrme functionals which allow to discuss the qualitative behavior of the different energy components, that is the surface, curvature and higher order terms decomposed into isovector and isoscalar parts, and local and non-local parts. In chapter III.3, we sketch the generalization of the previous study to clusters embedded in a nucleon gas, where nuclei beyond drip lines have to be considered as well as its interaction with the gas.

## Chapter III.1

# Symmetric nuclei

Let us first consider the idealized case of a common density profile for protons and neutrons, which has the advantage of leading to exact formulas for the nuclear binding energy. In section III.1.1, we develop the analytical expressions of the ETF integrals using a Fermi function. This allows to disentangle in a non-ambiguous way, bulk, surface, curvature as well as higher order terms, and to determine exact relations connecting the different energy components to the parameters of the energy functional. We focus on the surface diffuseness in sec. III.1.2, which leads to an analytical expression. These developments allow to study the decomposition of the surface energy presented in sec. III.1.3. More specifically, we retrieve that in a one-dimensional geometry, the local and non-local terms are related, and the surface tension can be consequently be expressed as a function of the local terms only [Tre86]. This remarkable property however breaks down in spherical symmetry, and any, even slight approximation to the exact variational profile, for instance the use of parametrized densities, increases the difference between local and non-local contributions to the surface energy. As a consequence, using parametrized density profiles, the contribution of non-local terms has to be carefully calculated independently of the local part, and the two separate contributions must be summed up to obtain the surface energy and the surface tension.

In this chapter we will use the notations introduced in chapter II.2. In particular, the energy density is given by the Skyrme symmetric functional eq. (II.15). To integrate the energy density, we use a density profile  $\rho(r)$  given by a simple Fermi function eq (II.35) since we have seen in part II that it succeeds in reproducing the density profiles and the corresponding energy calculated with the spherical HF model. As previously, the radius parameter  $R$  ensures the particle number conservation with eq. (II.36). However, no assumption is made for the value of the diffuseness parameter  $a$  which will be variationally expressed in sec. III.1.2.

### III.1.1 Ground state energy

As in part II, the total energy  $E$  of a nucleus of a mass  $A$  is

$$E(A) = \int_0^\infty dr \mathcal{H}[\rho(r)], \quad (\text{III.1})$$

from which we can distinguish the bulk energy

$$E_b(A) = \frac{\mathcal{H}_{sat}}{\rho_{sat}} A = \lambda_{sat} A, \quad (\text{III.2})$$

and the corresponding surface energy as the total energy after the bulk is removed:

$$E_s = E(A) - E_b(A) = 4\pi \int_0^\infty dr \left\{ \mathcal{H}[\rho(r)] - \lambda_{sat} \rho(r) \right\} r^2. \quad (\text{III.3})$$

In these equations,  $\lambda_{sat}$  is, as in part II, the energy per nucleon in saturated nuclear (symmetric) matter

$$\lambda_{sat} = \frac{h(\rho_{sat})}{\rho_{sat}} = C_{kin} \frac{m}{m_{sat}^*} \rho_{sat}^{2/3} + C_0 \rho_{sat} + C_3 \rho_{sat}^{\alpha+1}, \quad (\text{III.4})$$

with  $C_{kin} = \frac{3}{5} \hbar^2 / (2m)(3\pi^2/2)^{2/3}$  and  $m_{sat}^* = m^*(\rho_{sat})$  the effective mass at saturation density. In the previous part, we have seen that the finite size contribution  $E_s$  eq. (III.3) scales with  $A$  with a dependence slower than linear, but the dependence is different from  $A^{2/3}$  because of curvature and higher order terms [Pom13]. The analytical expressions developed in what follows will confirm this statement.

In the energy density  $\mathcal{H}[\rho]$  eq. (II.15), we can distinguish the non-local terms which depend on the density derivatives and are pure finite-size effects, from the local energy density  $h(\rho)$  which only depends on the equation of state and on the density profile. We then write the surface energy as  $E_s = E_s^L + E_s^{NL}$ , with  $E_s^L$  the local part and  $E_s^{NL}$  the non-local one:

$$E_s^L(A) = 4\pi \int_0^\infty dr \left\{ h[\rho(r)] - \frac{h(\rho_{sat})}{\rho_{sat}} \rho(r) \right\} r^2, \quad (\text{III.5})$$

$$E_s^{NL}(A) = 4\pi \int_0^\infty dr \left\{ \frac{\hbar^2}{2m} f(r) \tau_2[\rho(r)] + \left( C_{fin} + V_{so} \frac{\rho(r)}{f(r)} \right) (\nabla \rho(r))^2 \right\} r^2, \quad (\text{III.6})$$

with  $f = m/m^* = 1 + \kappa\rho$  and  $\tau_2 = \tau_2^l + \tau_2^{nl}$  given by eqs. (II.18a) and (II.18b). Let us notice just for clarity that this latter decomposition of  $\tau_2$  into local and non local parts is not the same and has not the same signification as in eqs. (III.5) and (III.6). We can naturally define the local  $\mathcal{H}_s^L(\rho)$  and non-local  $\mathcal{H}_s^{NL}[\rho]$  surface energy density as the integrand of the corresponding energy. Since the local energy density eq. (II.16) is

in the form of  $h(\rho) = \sum_{\gamma} c_{\gamma} \rho^{\gamma}$  (with  $\gamma > 0$ ), the surface local energy eq. (III.5) can be expressed as differences of Fermi functions  $F(r) = (1 + e^{(r-R)/a})^{-1}$ :

$$E_s^L = 4\pi \sum_{\gamma} c_{\gamma} \rho_{sat}^{\gamma} \int_0^{\infty} dr \{F^{\gamma}(r) - F(r)\} r^2 = \sum_{\gamma} c_{\gamma} \rho_{sat}^{\gamma-1} \Delta I_{\gamma,1}, \quad (\text{III.7})$$

where  $\Delta I_{\gamma,1} = 4\pi \rho_{sat} \int dr (F^{\gamma}(r) - F(r)) r^2$  can be analytically calculated (see appx. A). In equation (III.6), the integrand is proportional to the square of the density gradient. Indeed, in integrating by parts and considering  $\nabla \rho = 0$  and  $\Delta \rho = 0$  at the boundary conditions, the Laplace derivatives  $\Delta \rho = (1/r^2) \frac{d}{dr} (r^2 \nabla \rho)$  entering the kinetic energy density  $\tau_2$ , either vanish when alone:  $\int dr r^2 \Delta \rho = [r^2 \nabla \rho]_0^{\infty} = 0$ , either turn into gradient when multiplied by  $\rho^{i \geq 1}$ :  $\int dr r^2 \rho^i \Delta \rho = - \int dr r^2 \rho^{i-1} (\nabla \rho)^2$ . Thus, eq. (III.6) reads

$$E_s^{NL}(A) = 4\pi \int_0^{\infty} dr \left\{ \frac{\hbar^2}{2m} \frac{1}{6} \left( \frac{1}{6\rho} - \frac{7}{3}\kappa + \frac{1}{2} \frac{\kappa}{f} \right) + C_{fin} + V_{so} \frac{\rho}{f} \right\} r^2 (\nabla \rho)^2. \quad (\text{III.8})$$

Then using the properties of Fermi functions which allow to express their derivatives as Fermi functions,  $\nabla F = (F^2 - F)/a$ , the non-local surface energy can be put in the following form

$$\begin{aligned} E_s^{NL} &= 4\pi \sum_{\gamma} d_{\gamma} \int dr \{(\nabla \rho)^2 \rho^{\gamma-2}(r)\} r^2 \\ &= \frac{4\pi}{a^2} \sum_{\gamma} d_{\gamma} \rho_{sat}^{\gamma} \int dr \left\{ (F^{\gamma+2} - F^{\gamma+1}) - (F^{\gamma+1} - F^{\gamma}) \right\} r^2 \\ &= \frac{1}{a^2} \sum_{\gamma} d_{\gamma} \rho_{sat}^{\gamma-1} [\Delta I_{\gamma+2, \gamma+1} - \Delta I_{\gamma+1, \gamma}] \end{aligned} \quad (\text{III.9})$$

(with  $\gamma > 0$ ). The integrals  $\Delta I_{\gamma, \gamma'}$  entering eqs. (III.7) and (III.9) are shown in appendix A to be analytically integrable and lead to the formula (A.8). Basically, making a simple variable change, the originally 3-dimensional integral  $\int d\mathbf{r}$  can be turned into the sum of three 1-dimensional integrals  $\int_{-\infty}^{+\infty} dx$ . Then a very accurate approximation, that is with an error less than  $(\exp(-5a/3R) - \exp(-a/R))$ , allows to analytically integrate the differences of Fermi functions. Using eq. (A.8), the local and non-local energy can thus be written as a function of the effective interaction parameters as:

$$E_s^L = \mathcal{C}_{surf}^L \frac{a(A)}{r_{sat}} A^{2/3} + \mathcal{C}_{curv}^L \left( \frac{a(A)}{r_{sat}} \right)^2 A^{1/3} + \mathcal{C}_{ind}^L \left( \frac{a(A)}{r_{sat}} \right)^3, \quad (\text{III.10})$$

$$E_s^{NL} = \frac{1}{a^2(A)} \left[ \mathcal{C}_{surf}^{NL} \frac{a(A)}{r_{sat}} A^{2/3} + \mathcal{C}_{curv}^{NL} \left( \frac{a(A)}{r_{sat}} \right)^2 A^{1/3} + \mathcal{C}_{ind}^{NL} \left( \frac{a(A)}{r_{sat}} \right)^3 \right]. \quad (\text{III.11})$$

In these equations, the expansion of  $a/(A^{1/3} r_{sat})$  has been truncated, such that the

residual terms are equal to  $O\left((a/r_{sat})^4 A^{-1/3}\right)$ . Moreover, the coefficients  $C_{surf(curv)(ind)}^{L(NL)}$  depend on the saturation density  $\rho_{sat}$  and on the Skyrme parameters  $C_0$ ,  $C_3$ ,  $C_{eff}$ ,  $\alpha$ ,  $C_{fin}$  and  $C_{so}$ , and we have anticipated the (slight)  $A$ -dependence of the diffuseness in the most general case (see section III.1.2).

The coefficients  $C_i^L$  and  $C_i^{NL}$  corresponding to the local and non-local energy components read:

$$C_{surf}^L = 3 \left\{ C_{kin} \rho_{sat}^{2/3} \left[ \eta_{5/3}^{(0)} \frac{m}{m_{sat}^*} - \frac{3}{5} \delta m_{sat} \right] - C_0 \rho_{sat} + C_3 \rho_{sat}^{\alpha+1} \eta_{\alpha+2}^{(0)} \right\}, \quad (\text{III.12})$$

$$C_{curv}^L = 6 \left\{ C_{kin} \rho_{sat}^{2/3} \left[ \left( \eta_{5/3}^{(1)} - \frac{\pi^2}{6} \right) \frac{m}{m_{sat}^*} - \frac{3}{5} \eta_{5/3}^{(0)} \delta m_{sat} \right] + C_3 \rho_{sat}^{\alpha+1} \left( \eta_{\alpha+2}^{(1)} - \frac{\pi^2}{6} \right) \right\}, \quad (\text{III.13})$$

$$C_{ind}^L = 3 \left\{ C_{kin} \rho_{sat}^{2/3} \left[ \left( \eta_{5/3}^{(2)} - \frac{2\pi^2}{3} \eta_{5/3}^{(0)} \right) \frac{m}{m_{sat}^*} - \frac{2}{5} \left( 3\eta_{5/3}^{(1)} - \pi^2 \right) \delta m_{sat} \right] + \frac{\pi^2}{3} C_0 \rho_{sat} + C_3 \rho_{sat}^{\alpha+1} \left( \eta_{\alpha+2}^{(2)} - \frac{2\pi^2}{3} \eta_{\alpha+2}^{(0)} \right) \right\}, \quad (\text{III.14})$$

$$C_{surf}^{NL} = 3 \left\{ \frac{\hbar^2}{2m} \frac{1}{6} \left( \frac{1}{12} - \frac{11}{36} \delta m_{sat} - \frac{1}{2} \sum_{i=0}^{i_{max}} (-1)^i \frac{(\delta m_{sat})^{i+2}}{(i+3)(i+4)} \right) + \frac{1}{6} C_{fin} \rho_{sat} + V_{so} \rho_{sat}^2 \sum_{i=0}^{i_{max}} (-1)^i \frac{(\delta m_{sat})^i}{(i+3)(i+4)} \right\}, \quad (\text{III.15})$$

$$C_{curv}^{NL} = 6 \left\{ \frac{\hbar^2}{2m} \frac{1}{6} \left( \frac{1}{12} - \frac{1}{2} \sum_{i=0}^{i_{max}} (-1)^i \frac{(\delta m_{sat})^{i+2}}{(i+3)(i+4)} \left[ \eta_{i+2}^{(0)} + 1 \right] \right) + V_{so} \rho_{sat}^2 \sum_{i=0}^{i_{max}} (-1)^i \frac{(\delta m_{sat})^i}{(i+3)(i+4)} \left[ \eta_{i+3}^{(0)} + 1 \right] \right\}, \quad (\text{III.16})$$

$$C_{ind}^{NL} = 6 \left\{ \frac{\hbar^2}{2m} \frac{1}{6} \left( -\frac{1}{12} \frac{\pi^2}{6} + \frac{11}{36} \left( 1 + \frac{\pi^2}{6} \right) \delta m_{sat} - \frac{1}{2} \sum_{i=0}^{i_{max}} (-1)^i \frac{(\delta m_{sat})^{i+2}}{(i+3)(i+4)} \left[ \eta_{i+2}^{(1)} + \eta_{i+2}^{(0)} - \frac{\pi^2}{3} \right] \right) - \frac{1}{6} \left( 1 + \frac{\pi^2}{6} \right) C_{fin} \rho_{sat} + V_{so} \rho_{sat}^2 \sum_{i=0}^{i_{max}} (-1)^i \frac{(\delta m_{sat})^i}{(i+3)(i+4)} \left[ \eta_{i+3}^{(1)} + \eta_{i+3}^{(0)} - \frac{\pi^2}{3} \right] \right\}, \quad (\text{III.17})$$

with  $\delta m_{sat} = (m - m_{sat}^*)/m_{sat}^*$ , and where we have introduced the coefficients  $\eta_\gamma^{(k)}$  defined by equation (A.2). Their numerical values are given in the same appendix. Let us notice that for  $(\gamma, k) \in \mathbb{N}^2$ , their values have been analytically expressed. We have also used the recursive relation (A.4) to reduce the number of different coefficients entering the local and non-local terms. The coefficients  $\eta_{5/3}^{(k)}$  and  $\eta_{\alpha+2}^{(k)}$  ( $k = \{0, 1, 2\}$ ) have to be numerically calculated. In order to have an analytical expression, we have made in eqs. (III.15)-(III.17) a Taylor expansion of the effective mass inverse  $f^{-1} = \sum_{i=0}^{\infty} (-1)^i (\delta m)^i$ . This expansion is rapidly convergent: a truncation at  $i_{max} = 7$  produces an error  $\sim 1\%$  on the considered term, at the highest possible density  $\rho_{sat} = 0.16 \text{ fm}^{-3}$  in the case of the SLy4 interaction.

Equations (III.10) and (III.11) show that the dominant surface effect in the symmetric nucleus energetics is, as expected, a term  $\propto A^{2/3}$ . As it is well known, this term fully exhausts the finite-size effects given by the presence of a nuclear surface in the one-dimensional case of a semi-infinite slab geometry [Tre86; Dan09]. Indeed in this case the surface energy is given by

$$E_s^{slab} = \int_{-\infty}^{+\infty} dx \{ \mathcal{H}[\rho(x)] - \lambda_{sat} \rho(x) \}, \quad (\text{III.18})$$

and its evaluation, similar to the 3-dimensional case by using eq. (A.5) with  $k = 0$  only, leads to the same  $\propto A^{2/3}$  term as in the spherical geometry, with a modified form factor  $4\pi R_{HS}^2$ :

$$\sigma = \lim_{A \rightarrow \infty} \frac{E_s^{slab}}{A^{2/3}} = \sigma^L + \sigma^{NL} = \left( \mathcal{C}_{surf}^L + \frac{1}{a^2} \mathcal{C}_{surf}^{NL} \right) \frac{a}{4\pi r_{sat}^3}. \quad (\text{III.19})$$

The form factor difference between the surface energy of the slab and the one in spherical symmetry signs the difference of geometry: the spherical surface energy is the surface area multiplied by the energy per unit area of the infinite tangent plane. Let us notice that since the mass cannot be defined in the semi-infinite medium, the diffuseness in eq. (III.19) is a constant.

In a three-dimensional geometry, the existence of a surface leads to additional finite-size terms, even in the spherically symmetric case, as shown by eqs. (III.10) and (III.11). The terms proportional to  $A^{1/3}$  are the so-called curvature terms which correct the surface energy with respect to the slab tangent limit. It is interesting to notice that we also have  $A$ -independent terms, which are rarely accounted for in the literature but turn out to be important for light nuclei [Pom13]. Higher order terms are of the order  $\propto A^{-1/3}$  and are systematically neglected in this work. This Taylor expansion is known in the literature as the leptodermous expansion [Mye85; Pom13]. It is interesting to observe that both local and non-local plane surface, curvature, and mass independent energy

components arise even if no explicit gradient term is included in the functional. As a consequence, surface properties are determined by a complex interplay between equation of state properties and specific finite nuclei properties like spin-orbit and finite range. Using the definitions of the energy per particle at saturation  $\lambda_{sat} = h/\rho|_{\rho_{sat}} = \partial h/\partial \rho|_{\rho_{sat}}$  and the nuclear symmetric matter incompressibility  $K_{sat} = 9\rho_{sat}^2 \partial^2(h/\rho)/\partial \rho^2|_{\rho_{sat}}$ , we can express the local energy eqs. (III.12), (III.13) and (III.14) as a function of nuclear matter properties only, using the following expressions:

$$\alpha = -\frac{K_{sat} + 9\lambda_{sat} - C_{kin}\rho_{sat}^{2/3} \left( \frac{m}{m_{sat}^*} + 3\delta m_{sat} \right)}{9 \left[ \lambda_{sat} - C_{kin}\rho_{sat}^{2/3} \left( \frac{m}{3m_{sat}^*} - \delta m_{sat} \right) \right]}, \quad (\text{III.20})$$

$$C_3\rho_{sat}^{\alpha+1} = \frac{9 \left[ \lambda_{sat} - C_{kin}\rho_{sat}^{2/3} \left( \frac{m}{3m_{sat}^*} - \delta m_{sat} \right) \right]^2}{K_{sat} + 9\lambda_{sat} - C_{kin}\rho_{sat}^{2/3} \left( \frac{m}{m_{sat}^*} + 3\delta m_{sat} \right)}, \quad (\text{III.21})$$

$$C_0\rho_{sat} = \left[ K_{sat} + 9\lambda_{sat} - C_{kin}\rho_{sat}^{2/3} \left( \frac{m}{m_{sat}^*} + 3\delta m_{sat} \right) \right]^{-1} \cdot \left[ \lambda_{sat}K_{sat} - C_{kin}\rho_{sat}^{2/3}K_{sat} \frac{m}{m_{sat}^*} - C_{kin}\rho_{sat}^{2/3}\lambda_{sat} \left( 4\frac{m}{m_{sat}^*} + 21\delta m_{sat} \right) - 9C_{kin}^2\rho_{sat}^{4/3}\delta m_{sat} \right]. \quad (\text{III.22})$$

The expression of the coefficients  $C_i^{(N)L}$  greatly simplifies if we consider a simplistic Zamick-type interaction [Zam73], with  $\alpha = 1$  and  $m = m^*$ :

$$C_{surf}^L = \left( \frac{9}{5}\eta_{5/3}^{(0)} + \frac{3}{2} \right) e_{sat}^F - \frac{3}{2}\lambda_{sat}, \quad (\text{III.23})$$

$$C_{surf}^{NL} = \frac{1}{24} \frac{\hbar}{2m} + \frac{1}{2} C_{fin}\rho_{sat}, \quad (\text{III.24})$$

where we have introduced the Fermi energy per nucleon at saturation  $e_{sat}^F = \frac{5}{3}C_{kin}\rho_{sat}^{2/3}$ . We can see that even in this oversimplified model the nuclear surface properties cannot be simply reduced to EoS parameters.

We can also gather the local and non-local terms in order to classify finite-size effects according to the rank of the Taylor expansion. Thus we introduce the surface  $E_{surf}$ , curvature  $E_{curv}$  and  $A$ -independent  $E_{ind}$  energy components:

$$E_{surf} = \left[ C_{surf}^L + \frac{1}{a^2(A)} C_{surf}^{NL} \right] \frac{a(A)}{r_{sat}} A^{2/3}, \quad (\text{III.25})$$

$$E_{curv} = \left[ C_{curv}^L + \frac{1}{a^2(A)} C_{curv}^{NL} \right] \left( \frac{a(A)}{r_{sat}} \right)^2 A^{1/3}, \quad (\text{III.26})$$

$$E_{ind} = \left[ C_{ind}^L + \frac{1}{a^2(A)} C_{ind}^{NL} \right] \left( \frac{a(A)}{r_{sat}} \right)^3. \quad (\text{III.27})$$

We can see that all terms are multiplied by a power of the diffuseness except the non-local curvature part which is not. The role of the diffuseness on the surface properties thus depends on the rank of the Taylor expansion (surface, curvature, independent,...) and is not the same for the local or the non-local part. The functional difference between the local and non-local terms comes from the squared density gradient appearing in the non-local energy and can be clearly seen in eq. (III.9). Globally, if the diffuseness is high, the local energy dominates over the non-local one, see eqs. (III.25)-(III.27). This is easy to understand: in the limit of a purely local energy functional, the optimal configuration corresponds to a homogeneous hard sphere at saturation density, given by  $a = 0$ . The existence of a finite diffuseness for atomic nuclei is due to the presence of non-local terms in the functional, because of both explicit gradient interactions and of quantum effects on the kinetic energy density. Let us notice that these two latter effects are present even in the simplified eqs. (III.23), (III.24).

### III.1.2 Analytical expression for the diffuseness

The ground state energy of this model for symmetric nuclei is given by the minimization of the energy per nucleon  $\delta(E/A) = 0$  with the constraint of a given mass number  $A$ . We have seen in section III.1.1 that the only unconstrained parameter of the model is the diffuseness parameter  $a$ . Though it does not play any role in the bulk energy, it is an essential ingredient for the surface energy  $E_s$  given by eqs. (III.10), (III.11). The diffuseness parameter can therefore be obtained from the variational equation [Tre86]:

$$\frac{\partial E_s}{\partial a} = 0. \quad (\text{III.28})$$

In principle, one should also add the surface Coulomb energy into  $E_s$ , which would change the variational equation. However, the resulting correction on  $a$  is very small [Pap13].

Equation (III.28) turns out to be particularly simple in the one-dimensional case of semi-infinite matter, or equivalently neglecting curvature and  $A$ -independent terms when considering nuclei. Indeed, in this case, eq. (III.19) leads to an analytical solution, already obtained in Ref. [Tre86]:

$$a = \sqrt{\frac{C_{surf}^{NL}}{C_{surf}^L}}. \quad (\text{III.29})$$

This equation shows that the slab diffuseness  $a$  is determined by the balance between the

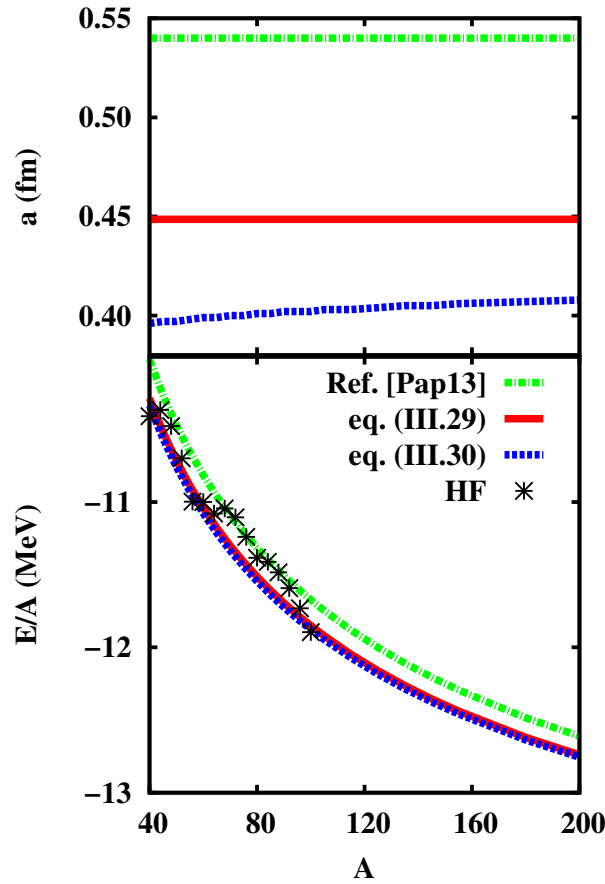


Figure III–1: Diffuseness (upper panel) and energy per nucleon (lower panel) of symmetric nuclei as a function of the mass number. Full red lines: calculations using the slab diffuseness eq. (III.29). Dashed blue lines: calculations using the spherical diffuseness eq. (III.30). Dashed-dotted green lines: calculations using the diffuseness fitted from HF density profiles [Pap13]. Star symbols: full Hartree-Fock calculations in spherical symmetry. Figure published in [Aym15].

local terms, which favour low diffuseness values corresponding to a hard sphere of matter at saturation density, and non-local terms which favour a large diffuseness corresponding to matter close to uniformity.

The complete spherical case leads to the following 4<sup>th</sup> degree polynomial equation:

$$\begin{aligned}
 & 3 \mathcal{C}_{ind}^L \left( \frac{a}{r_{sat}} \right)^4 + 2\mathcal{C}_{curv}^L A^{1/3} \left( \frac{a}{r_{sat}} \right)^3 \\
 & + \left( \mathcal{C}_{surf}^L A^{2/3} + \frac{1}{r_{sat}^2} \mathcal{C}_{ind}^{NL} \right) \left( \frac{a}{r_{sat}} \right)^2 - \frac{1}{r_{sat}^2} \mathcal{C}_{surf}^{NL} A^{2/3} = 0.
 \end{aligned} \tag{III.30}$$

which has to be solved numerically. Let us notice that the coefficient  $\mathcal{C}_{curv}^{NL}$  does not

contribute to this equation since, as already mentioned, it does not depend on  $a$ , cf. eq. (III.26). The solution of this equation, as well as the slab approximation eq. (III.29), are shown in the case of the SLy4 interaction in the upper panel of figure III-1. We can see that the mass dependence of the diffuseness parameter  $a$  in the general case (blue dashed lines) is very small. This agrees with the findings of ref. [Pap13] (green dashed-dotted lines), used in part II, where the diffuseness parameter was extracted from a fit of Hartree-Fock density profiles. Considering only the surface term we get  $a \approx 0.45$  fm, while we can observe that taking into account terms beyond surface (curvature and mass independent), the diffuseness is shifted to lower values of the order of  $a \approx 0.4$  fm. This relatively large effect is due to the fact that the non-local curvature term does not contribute to the diffuseness (see eq. (III.26)). Therefore the effect of the curvature energy is to increase the local component, which tends to favor a low diffuseness.

The energy per nucleon is shown in the lower panel of fig. III-1, for the three models considered in the upper panel, and in comparison to HF calculations (black symbols). We can see from this figure that the variational approach systematically produces more binding than the use of a fitted value for the diffuseness, as we could have anticipated. Indeed the value of ref. [Pap13] was obtained from a fit of the density, which does not guarantee a minimal energy. Less expected is the fact that the energies calculated with the three different choices for the diffuseness are very close, though the value of the diffuseness are quite different. Specifically, implementing the different diffusenesses into eq. (III.1), the resulting total energy reproduces the Hartree-Fock nuclear energies with very similar accuracy.

We can then conclude that introducing higher order terms in the variational derivation of the diffuseness, as it has been done in equation (III.30), does not significantly improve the predictive power of the model. Therefore we will preferentially use the simpler expression of the slab diffuseness given by equation (III.29). This choice is made in all the following figures, unless explicitly specified.

### III.1.3 Decomposition of the surface energy

In this section, we study the functional behavior of the analytical formulas of section III.1.2.

In order to verify the accuracy of the analytical expression for the surface energy  $E_s$ , we compare in figure III-2 the energy  $E_s$  given by the sum of eqs. (III.25)-(III.27) with the numerical integration of eq. (III.3), as a function of the nucleus mass. We can see that the analytical expressions (full red line) very well reproduce the numerical values of  $E_s$  (black circles). An error smaller than 50 keV per nucleon is obtained for the lightest considered nuclei, which rapidly vanishes with increasing mass. The deviation for light

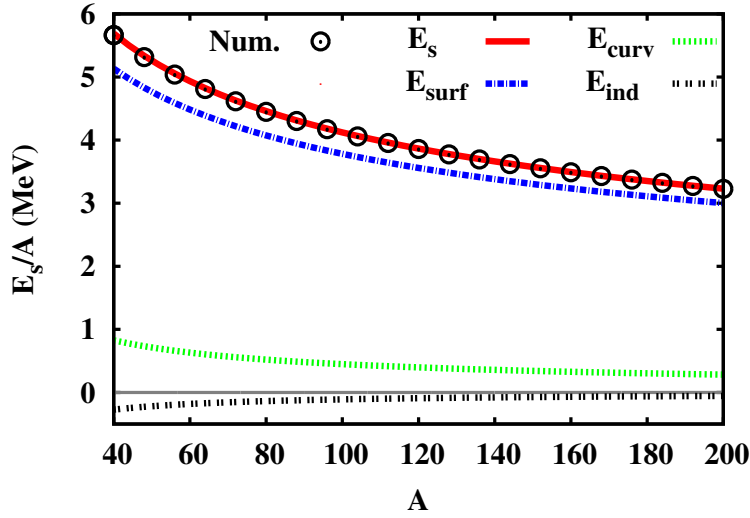


Figure III-2: Numerical (black circles) and analytical (full red line) surface energy per nucleon, and its analytical decomposition into plane surface ( $\propto A^{2/3}$ , dashed-dotted blue line), curvature ( $\propto A^{1/3}$ , dotted green line), and mass independent (double dotted black line) components (eqs (III.25), (III.26), (III.27)) of symmetric nuclei, as a function of the mass number. Figure published in [Aym15].

nuclei comes from the approximation in the relation between the radius  $R$  and the mass  $A$ . Indeed, the expansion of the radius parameter eq. (II.36) leads to an expansion up to  $A^{1/3}(a/r_{sat})$  for  $E_s$ . The missing terms  $\propto A^{-1/3}(a/r_{sat})^4$  rapidly vanish with  $A$ , explaining the excellent reproduction of the exact numerical integral.

Figure III-2 also shows the plane surface, curvature and  $A$ -independent energy per nucleon components, respectively defined in eqs. (III.25), (III.26) and (III.27). Comparing the total surface energy  $E_s$  (full red line) with  $E_{surf}$  (dashed-dotted blue line), we can see that the  $A^{2/3}$  dependence dominates over the whole mass table. However, the curvature part (dotted green line), which represents the energetic cost of a spherical geometry, cannot be neglected even for heavy nuclei, impacting the total energy of  $\gtrsim 300$  keV per nucleon for the heaviest nuclei. For lighter nuclei ( $A \lesssim 100$ ), the curvature contribution to the total finite-size effects is of the order of 20%. Though the  $A$ -independent energy (black dotted line) can be neglected for  $A \gtrsim 100$ , for which  $E_{ind}/A \lesssim 50$  keV, it should be taken into account for light nuclei if high accuracy is requested. Indeed, for  $A = 40$ , the  $A$ -independent term contributes  $\sim 5\%$  of the total surface energy.

We now turn to the decomposition of the surface energy into a local and a non-local component. It was shown in ref. [Tre86] that the local and non-local terms are expected to be exactly equal in the case of symmetric matter in a semi-infinite slab geometry. To obtain this result, we multiply by  $\rho' = d\rho/dx$  the 1-dimensional Euler-Lagrange

equation (II.21), which gives the Euler-Lagrange first moment

$$\rho'(x) \frac{dh}{d\rho}(x) - \lambda_{sat} \rho'(x) = -C_{\nabla}(\rho(x)) \rho'^3(x) - C_{\Delta}(\rho(x)) \rho'(x) \rho''(x), \quad (\text{III.31})$$

with  $C_{\nabla}$  and  $C_{\Delta}$  given by eqs. (II.22). Integrating from  $+\infty$  where  $\rho(+\infty) = 0$  and  $\rho'(+\infty) = 0$  to  $x$ , eq. (III.31) leads to, in integrating by parts the the term  $C_{\nabla} \rho'^3$ ,

$$h[\rho] - \lambda_{sat} \rho = \left[ \frac{\hbar^2}{2m} \frac{1}{6} \left( \frac{1}{6\rho} - \frac{7}{3} \kappa + \frac{1}{2} \frac{\kappa}{f} \right) + C_{fin} \rho'^2 + V_{so} \frac{\rho(x)}{f} \right] \rho'^2, \quad (\text{III.32})$$

where we recognize the local  $\mathcal{H}_s^L$  and non-local  $\mathcal{H}_s^{NL}$  surface energy density defined by the integrands of eqs. (III.5) and (III.8). This equality means that, if the density profile is the exact solution of the Euler-Lagrange variational equation, the contribution of the local term in the surface energy density is at each point of space equal to the contribution of the non-local term, leading to the global equality between the local and non-local slab surface tensions:

$$\sigma^L = \sigma^{NL}. \quad (\text{III.33})$$

Extended to finite nuclei, this result would imply that only the local properties of the interaction (that is: the Equation of State) are needed to predict the surface properties of finite nuclei.

In this study, we do not solve the Euler-Lagrange equation since we impose a given density profile, but we do use a variational approach in minimising the energy to obtain the diffuseness parameter. Therefore, it is easy to show that our model verifies the previous theorem in the one-dimensional case. Indeed, using the slab diffuseness eq. (III.29), equation (III.19) reads,

$$\sigma^L = \sigma^{NL} = \lim_{A \rightarrow \infty} \frac{1}{2} \frac{E_s^{slab}}{A^{2/3}} = \frac{1}{4\pi r_{sat}^3} \sqrt{\mathcal{C}_{surf}^L \mathcal{C}_{surf}^{NL}}. \quad (\text{III.34})$$

At first sight this result might look surprising since we have reduced the full variational problem to the variation of a single variable, which represents a very poor variational approach. Equality (III.34) simply means that verifying the Euler-Lagrange first moment is equivalent to minimising the energy with respect to a single free parameter. That is, the density derivative is well described by the same parameter, here the diffuseness  $a$ , as the density itself.

Unfortunately, this elegant theorem cannot be extended to the case of a spherical geometry. The differences compared with the semi-infinite matter case lies in the Laplace operators which, in spherical symmetry, contain a gradient term:  $r^2 \Delta \rho = \partial/\partial r (r^2 \rho') =$

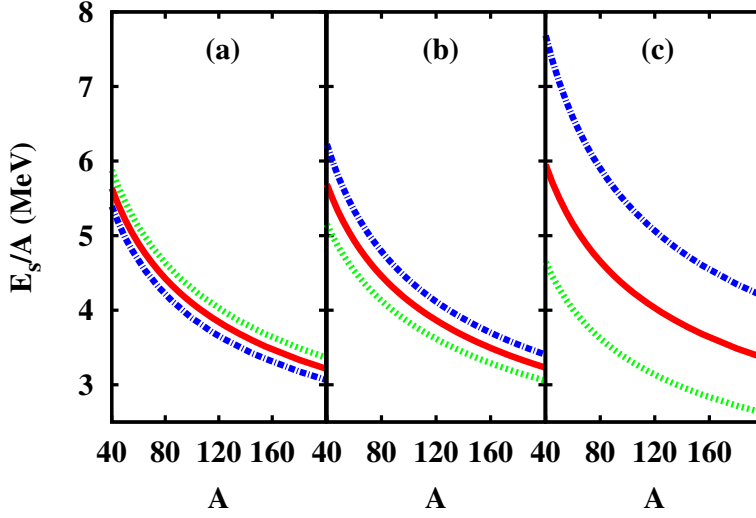


Figure III–3: Surface energy per nucleon of symmetric nuclei using different choices for the diffusivity parameter  $a$ . Panel a): variational diffuseness including finite size effects from eq. (III.30); panel b): variational diffuseness neglecting curvature terms from eq. (III.29); panel c): diffuseness fitted from HF calculations in ref. [Pap13]  $a = 0.54$  fm. Red lines: total surface energy per nucleon. Blue (green) lines: local (non-local) part multiplied by two. Figure published in [Aym15].

$\rho'' + (2/r)\rho'$ . Therefore integrating the 3-dimensional Euler-Lagrange first moment (i.e. eq. (II.21) multiplied by  $\nabla\rho$ ) from  $r$  to  $\infty$  gives extra gradients terms. The previous global equality in the semi-infinite slab geometry thus turns into the following strict inequality

$$E_s^L - E_s^{NL} = 4 \int_0^\infty dr \int_\infty^r dr' \frac{\mathcal{H}_s^{NL}(r')}{r'} < 0. \quad (\text{III.35})$$

The addition of this negative integral due to the gradient part ( $\propto 1/r$ ) of the spherical Laplace operator, comes from the difference between the plane and the spherical geometry, that is the spatial curvature. Eq. (III.35) shows that in a three-dimensional geometry the equality between the local and non-local terms is violated for all components of the surface energy, including the term  $\propto A^{2/3}$ .

The left panel of figure III–3 displays the decomposition of the surface energy between local (dashed-dotted blue line) and non-local (dotted green line) components, when the diffuseness of the density profile is consistently obtained from the numerical solution of the variational equation (III.30). We can see that the local surface energy is indeed less than the non-local one, though the difference is small. This absolute difference is amplified if the ansatz for the density profile deviates from the variational one. As an example, the central panel in figure III–3 shows the surface energy obtained if the simpler

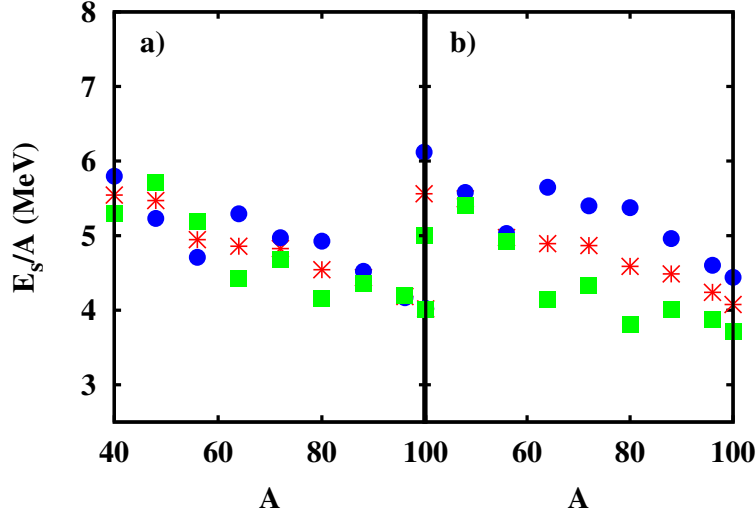


Figure III–4: Hartree-Fock calculations. Surface energy per nucleon (red stars) and its local (blue circles) and non-local (green squares) components multiplied by 2, for symmetric nuclei, as a function of the mass number. Left (right) panel: Coulomb energy excluded (included). Figure published in [Aym15].

expression eq. (III.29) for the diffuseness is employed. The diffuseness of [Pap13], used in part II, is employed in the right panel. We can see that the difference between local and non-local terms is increased as we consider density profiles increasingly deviating from the exact variational result.

As we have already remarked, a higher diffusivity (from a) to c)) trivially leads to a globally higher surface energy. More interesting, the increased deviation from the exact variational result from a) to c) leads to a considerable increase of the local energy over the non-local one. This is a direct consequence of eqs. (III.25)-(III.27). However, in the case of using the slab diffuseness eq. (III.29), the difference remains small (though opposite). This is due to the fact that, in this case, the plane surface energies  $E_{surf}^L = 4\pi R_{HS}^2 \sigma^L$  and  $E_{surf}^{NL} = 4\pi R_{HS}^2 \sigma^{NL}$  are equal according to eq. (III.34). Thus the difference observed in panel (b) only comes from the curvature and  $A$ -independent terms, which are smaller than the plane surface energy.

From eq. (III.35), it is clear that the degree of violation of equality (III.33) will depend on the functional, as well as on the variational model. This point is illustrated in figure III–4, which shows again the decomposition of the surface energy  $E_s$  into local (blue circles) and non-local (green squares) parts, calculated numerically from spherical Hartree-Fock calculations. All the HF results presented in this thesis were kindly provided by J. Margueron. In the calculations presented in the left panel, the Coulomb energy, which breaks the symmetry  $\rho_n = \rho_p$  and thus implies to consider two coupled

Euler-Lagrange equations, is artificially switched off.

We can see that the Euler-Lagrange result in the slab geometry eq. (III.33) is reasonably well verified within 10%, especially for medium-heavy nuclei  $A \gtrsim 90$ . This shows that the approximate equality between local and non-local terms is not limited to the ETF variational principle, but it is also verified by the Hartree-Fock variational solution. However, if the Coulomb interaction is included (right panel), the self-consistent modification of the Hartree-Fock density profile due to Coulomb is sufficient to lead to a strong violation of the equality between local and non-local terms, going up to 50%.

This discussion shows that the exact shape of the density profile, and in particular the exact value of the diffuseness parameter, are not important for the determination of the global surface energy, but are crucial for a correct separation of local and non-local components. In practice it is very difficult to extract precisely the diffuseness coefficient from theory or experiment: as we have seen in fig. III-1, the diffuseness extracted from the Hartree-Fock variational density profile is very different from the ETF value, though the energies are close. Moreover the equality theorem is violated both because of curvature effects and of isospin symmetry breaking terms which cannot be neglected even in symmetric nuclei because of the Coulomb interaction. For all these reasons, the contribution from non-local terms cannot be estimated from the local part making use of eq. (III.33). As a consequence, nuclear surface properties cannot be understood without mastering the gradient and spin-orbit terms of the energy functional.

## Chapter III.2

# Asymmetric nuclei

We now turn to examine the more general problem of an ETF analytical mass model for asymmetric nuclei, which requires the introduction of the proton and neutron density profiles as two independent degrees of freedom. In this general case, the ETF energy integral cannot be evaluated analytically. The usual approach in the literature consists in calculating the integral numerically, with density profiles which are either parametrized [Pot13; Lee10; Pap13], or determined with a variational calculation [Cen90; Cen98; War09; De12]. The limitation of such approaches is that the decomposition of the total binding energy into its different components (isoscalar, isovector, surface, curvature, etc.) out of a numerical calculation is not unambiguous nor unique as we have seen in part II. Moreover, a numerical calculation makes it hard to discriminate the specific influence of the different physical parameters (EOS properties, finite range, spin orbit, etc) on quantities like the surface symmetry energy or the neutron skin.

As a consequence, correlations between observables and physical parameters require a statistical analysis based on a large set of very different models. In this way, one may hope that the obtained correlation is not spuriously induced by the specific form of the effective interaction [Duc10]. The correlation may also depend on several physical parameters and the statistical analysis becomes quite complex [Duc11].

Earlier approaches in the literature have introduced approximations in order to keep an analytical evaluation possible [Kri83]. These approximations however typically neglect the presence of a neutron skin, and more generally of inhomogeneities in the isospin distribution [Lee10]. As a consequence, the results are simple and transparent, but their validity out of the stability valley should be questioned.

In section III.2.1, we show that the bulk asymmetry  $\delta$  introduced in the density profiles naturally takes a large part of the isospin dependence. The residual surface symmetry part is then defined in terms of the isovector density which is not analytically integrable. Two different approximations for this term are fully developed in section III.2.2.

The corresponding diffusenesses are analytically calculated as well. The results are compared to Hartree-Fock (HF) calculations using the same functional. The first approximation is based on neglecting the neutron skin. Surprisingly enough, this very crude approximation leads to an overestimation of Hartree-Fock energies of medium-heavy and heavy nuclei of no more than 200-400 keV per nucleon even for the most extreme drip line nuclei. Again, such an accuracy can be obtained only if both local and non-local terms in the energy functional are separately calculated, meaning that the symmetry energy does not only depend on bulk nuclear matter properties. This might be at the origin of the well known ambiguities in the extraction of the symmetry energy from density functional calculations of finite nuclear properties [Nik11; Dan03; Rei06; Dou00]. A better accuracy for neutron rich nuclei is obtained if isospin fluctuations are accounted for, in approximating the surface symmetry energy density as a Gaussian peaked at the nuclear surface. The complete mass formula is calculated for different representative Skyrme functionals in section III.2.3. The qualitative behavior of the different energy components, that is the surface, curvature and higher order terms decomposed into isovector and isoscalar parts, and local and non-local parts, is discussed.

### III.2.1 Decomposition of the nuclear energy

Asymmetric nuclei imply the introduction of an additional density profile corresponding to the additional degree of freedom. As in part II, we work with the isoscalar density profile  $\rho(r)$ , given by the Fermi function eq. (II.44) and the proton density profile  $\rho_p(r)$ , expressed as an independent Fermi function eq. (II.38). These profiles depend on the isospin asymmetry with their respective saturation densities given by eq. (II.42) and their radii parameters eqs. (II.39). The diffusenesses  $a$  and  $a_p$  will be calculated in section III.2.2 by a minimization of the surface energy, as it has been done for symmetric nuclei in section III.1.2, where  $a_p = a$ .

Let us recall that the nuclei bulk isospin asymmetry  $\delta = 1 - 2\rho_{sat,p}/\rho_{sat}$  differs from the global one  $I = 1 - 2Z/A$  because of the competing effect of the Coulomb interaction and symmetry energy which are taken into account in eq. (II.45). Figure III-5 shows in the  $(N, Z)$  plane the heavy and medium-heavy measured nuclei, the theoretical neutron and proton drip lines evaluated from the SLy4 energy functional, and some iso- $\delta$  lines. We can see that all  $A \lesssim 40$ -isotopes ever synthesized in the laboratory lay between  $\delta \approx 0$  and  $\delta \approx 0.2$ . Furthermore, the theoretical neutron drip line well matches with the iso- $\delta$  line  $\delta \approx 0.3$ , which roughly corresponds to  $I \approx 0.4$ . Therefore, in order to correctly reproduce the energetics of in-vacuum asymmetric nuclei which is the purpose of this section, we will be interested in approximations producing reliable formulae up to  $\delta \approx 0.3$ .

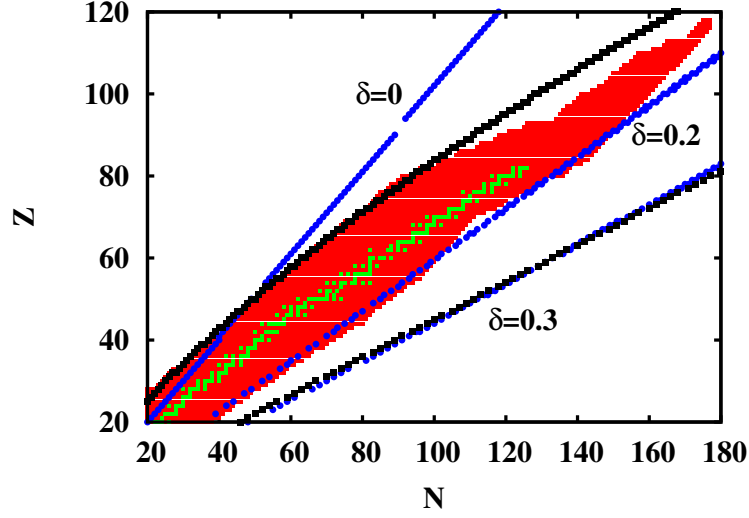


Figure III-5: Stable nuclei (green), unstable nuclei synthesized in the laboratory [NuD14] (red), theoretical neutron and proton drip lines evaluated from the SLy4 energy functional (black squares) and some iso- $\delta$  lines (blue dots) are plotted in the  $N, Z$  plane. Figure published in [Aym15].

Concerning the energy functional, it is customary to split it into an isoscalar and an isovector component. We thus write the energy density eq. (I.68) as

$$\mathcal{H}[\rho, \rho_3] = \mathcal{H}^{IS}[\rho, \rho_3 = 0] + \mathcal{H}^{IV}[\rho, \rho_3], \quad (\text{III.36})$$

with:

$$\begin{aligned} \mathcal{H}^{IS}[\rho, \rho_3] &= \frac{\hbar^2}{2m}\tau + C_{eff}\rho\tau + (C_0 + C_3\rho^\alpha)\rho^2 \\ &+ C_{fin}(\nabla\rho)^2 + C_{so}\mathbf{J} \cdot \nabla\rho, \end{aligned} \quad (\text{III.37})$$

$$\begin{aligned} \mathcal{H}^{IV}[\rho, \rho_3] &= \mathcal{H}^{IS}[\rho, \rho_3] - \mathcal{H}^{IS}[\rho, \rho_3 = 0] \\ &+ D_{eff}\rho_3\tau_3 + (D_0 + D_3\rho^\alpha)\rho_3^2 \\ &+ D_{fin}(\nabla\rho_3)^2 + D_{so}\mathbf{J}_3 \cdot \nabla\rho_3. \end{aligned} \quad (\text{III.38})$$

In equation (III.37), the isoscalar energy density also depends on  $\rho_3$  because of the presence of the kinetic densities  $\tau = \tau_n + \tau_p$  which cannot be written as a function of  $\rho$  only. Therefore, to truly obtain the isoscalar part in eq. (III.36), we have to consider  $\mathcal{H}^{IS}[\rho, \rho_3 = 0]$ . The isovector energy density eq. (III.38) contains therefore terms which explicitly depend on the isovector densities, but also an isovector contribution of the so-called isoscalar component  $\mathcal{H}^{IS}$ .

As in part II, we can define the bulk energy in asymmetric matter in following the

same procedure as for the symmetric case:

$$E_b(A, \delta) = \mathcal{H}[\rho_{sat}(\delta), \rho_{sat,3}(\delta)] V_{HS}(A, \delta), \quad (\text{III.39})$$

where  $V_{HS}(A, \delta) = 4/3\pi R_{HS}^3(A, \delta) = A/\rho_{sat}(\delta)$  is the equivalent homogeneous sphere volume.

The surface energy  $E_s(A, \delta)$  corresponding to finite-size effects can be decomposed, as in the symmetric case in chapter III.1, into the plane surface, the curvature, and the higher order terms. It is defined as the difference between the total and the bulk  $E_b(A, \delta)$  energy,

$$\begin{aligned} E_s(A, \delta) &= \int d\mathbf{r} \mathcal{H}[\rho, \rho_3] - \mathcal{H}[\rho_{sat}(\delta), \rho_{sat,3}(\delta)] V_{HS}(\delta) \\ &= 4\pi \int_0^\infty dr \left\{ \mathcal{H}[\rho, \rho_3] - \frac{\mathcal{H}[\rho_{sat}(\delta), \rho_{sat,3}(\delta)]}{\rho_{sat}(\delta)} \rho \right\} r^2. \end{aligned} \quad (\text{III.40})$$

Using the decomposition of the energy density into an isoscalar (only depending on the total density) and an isovector component (depending on  $\rho$  and  $\rho_3$ ), we get from eqs. (III.37) and (III.38):

$$E_s = E_s^{IS} + E_s^{IV}, \quad (\text{III.41})$$

with

$$\begin{aligned} E_s^{IS} &= 4\pi \int_0^\infty dr \left\{ \mathcal{H}^{IS}[\rho, \rho_3 = 0] - \frac{\mathcal{H}^{IS}[\rho_{sat}, \rho_{sat,3} = 0]}{\rho_{sat}(\delta)} \rho \right\} r^2 \\ &= 4\pi \int_0^\infty dr \left\{ \mathcal{H}[\rho, \rho_3 = 0] - \frac{\mathcal{H}[\rho_{sat}, \rho_{sat,3} = 0]}{\rho_{sat}(\delta)} \rho \right\} r^2, \end{aligned} \quad (\text{III.42})$$

$$\begin{aligned} E_s^{IV} &= 4\pi \int_0^\infty dr \left\{ \mathcal{H}^{IV}[\rho, \rho_3] - \frac{\mathcal{H}^{IV}[\rho_{sat}, \rho_{sat,3}]}{\rho_{sat}(\delta)} \rho \right\} r^2 \\ &= 4\pi \int_0^\infty dr \left\{ \mathcal{H}[\rho, \rho_3] - \frac{\mathcal{H}[\rho_{sat}, \rho_{sat,3}]}{\rho_{sat}(\delta)} \rho \right\} r^2 - E_s^{IS}. \end{aligned} \quad (\text{III.43})$$

Let us first concentrate on the isoscalar surface energy. The dependence of the surface energy on the bulk asymmetry  $\delta$  implies that its decomposition into an isoscalar and an isovector part is not straightforward. Indeed, although the isoscalar energy  $E_s^{IS}$  does not depend on the isospin asymmetry profile  $\rho_3(r)$ , it does depend on the bulk isospin asymmetry  $\delta$  through the isospin dependence of the saturation density  $\rho_{sat}(\delta)$  appearing in the density profile  $\rho$  eq. (II.44). Moreover, in eq. (III.42) the isoscalar bulk term which is removed depends directly on  $\delta$  too, because of the equivalent volume  $V_{HS} = A/\rho_{sat}(\delta)$ . The quantity  $E_s^{IS}$  has therefore an implicit dependence on isospin asymmetry  $\delta$ .

The isoscalar surface energy can be calculated exactly for any nucleus of any asymmetry, with the expressions developed in chapter III.1. In particular we can distinguish a plane surface, a curvature, and a mass independent term:

$$E_s^{IS} = E_{surf}^{IS} + E_{curv}^{IS} + E_{ind}^{IS} + O\left(\left(\frac{a(A, \delta)}{r_{sat}(\delta)}\right)^4 A^{-1/3}\right), \quad (\text{III.44})$$

with an identical result as in eqs. (III.25), (III.26), (III.27), namely:

$$E_{surf}^{IS} = \left[ C_{surf}^L + \frac{1}{a^2(A, \delta)} C_{surf}^{NL} \right] \frac{a(A, \delta)}{r_{sat}(\delta)} A^{2/3}, \quad (\text{III.45})$$

$$E_{curv}^{IS} = \left[ C_{curv}^L + \frac{1}{a^2(A, \delta)} C_{curv}^{NL} \right] \left( \frac{a(A, \delta)}{r_{sat}(\delta)} \right)^2 A^{1/3}, \quad (\text{III.46})$$

$$E_{ind}^{IS} = \left[ C_{ind}^L + \frac{1}{a^2(A, \delta)} C_{ind}^{NL} \right] \left( \frac{a(A, \delta)}{r_{sat}(\delta)} \right)^3. \quad (\text{III.47})$$

The local  $C_i^L$  and non-local  $C_i^{NL}$  functions are given by eqs. (III.12)-(III.17), where the saturation density now depends on asymmetry  $\rho_{sat} = \rho_{sat}(\delta)$  through eq. (II.42). The other difference with respect to the case of symmetric nuclei eqs. (III.25), (III.26), (III.27), is that now the diffuseness depends on the asymmetry  $\delta$ .

Since the analytical expressions of the isoscalar surface energy  $E_s^{IS}$  are the same as in symmetric nuclei, the same accuracy and conclusions as in chapter III.1 are dressed: we can variationally evaluate the isoscalar diffuseness  $a$ , solving equation (III.30), or using equation (III.29) which amounts to neglecting terms varying slower than  $A^{2/3}$ . Though we have considered only isoscalar terms, the diffuseness  $a$  does depend on the isospin asymmetry  $\delta$  because of the  $\delta$  dependence of the saturation density. These results, as well as the fit from HF density profiles [Pap13], where mass independence and quadratic behaviour in  $\delta$  is assumed (that is:  $a = C_1 + C_2\delta^2$ ), are shown in fig. III-6. Concerning the mass-dependence of eq. (III.30) (blue lines labelled “eq. (III.30)”), we observe a slight spread for masses from  $A = 50$  to  $A = 400$ , corroborating both the mass independence assumption in the HF fit [Pap13] and the previous conclusions in section III.1.2: to obtain the diffuseness we can neglect the mass dependence and limit to terms  $\propto A^{2/3}$  (red line, labelled “eq. (III.29)”). However, one can see that the dependence found from the variational equation is opposite to the one exhibited by the fit to HF results: the diffuseness decreases with  $\delta$  instead of increasing. It is difficult to believe that such a huge and qualitative difference might come from the difference between ETF and HF. The discrepancy rather suggests that the variational procedure should include the isovector energy to obtain the correct behaviour of the diffuseness with the isospin asymmetry. Indeed, we will see in section III.2.2 that adding the isovector part reverses the trend.

This discussion shows that, in the case of asymmetric nuclei, eq. (III.29) which only

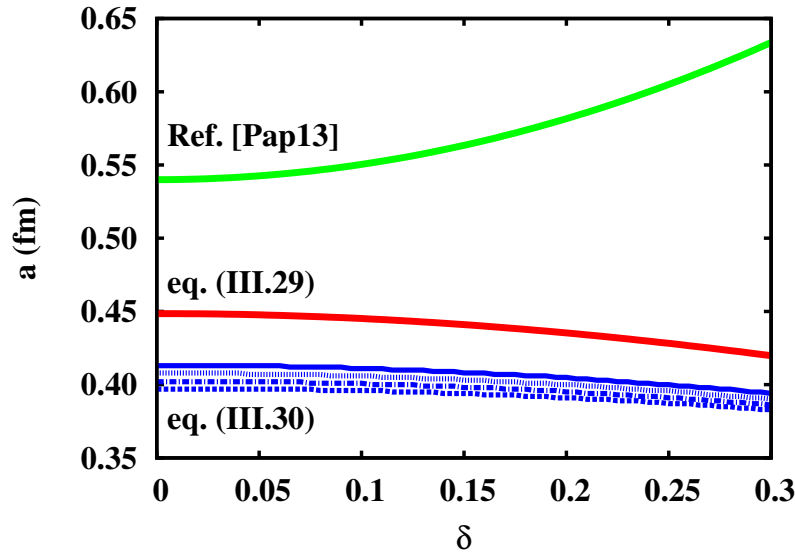


Figure III–6: Diffuseness as a function of the isospin asymmetry, for four isobaric chains ( $A = 400$ : full lines,  $A = 200$ : dotted lines,  $A = 100$ : dashed-dotted lines,  $A = 50$ : dashed lines). Red lines: calculations using the slab diffuseness eq. (III.29). Blue lines: calculations using the spherical diffuseness eq. (III.30). Green lines: calculations using the quadratic diffuseness, fitted from HF density profiles in ref. [Pap13]. Figure published in [Aym15].

takes into account the isoscalar terms, is not a good approximation to find the diffuseness. This statement is confirmed by fig. III–7, where the isoscalar surface energy per nucleon is plotted for different isobaric chains and for different prescriptions for the diffuseness. The full red and the dashed-dotted lines stand for the diffuseness given by eq. (III.29) and eq. (III.30) respectively. There is almost no difference in the isoscalar surface energy for these two prescriptions. In addition, the observed  $\delta$  dependence is extremely weak. The isoscalar surface energy evaluated with the quadratic diffuseness [Pap13] is represented in dashed green line. A qualitative and quantitative difference is observed with respect to the two other curves. This indicates again that the isoscalar and isovector components of the surface energy cannot be treated separately, and the correct  $\delta$  dependence of the isoscalar surface energy, as well as of the isoscalar diffuseness, requires to consider the total surface energy in the variational principle.

As discussed in part II, the positive  $\delta$ -dependence of the surface symmetry energy which contrasts with studies based on liquid-drop parametrizations of the nuclear mass [Dan09; Mye80; Mol12; Rei06; Nik11; Dou00], is due to our choice of definition of the surface in a two component system.

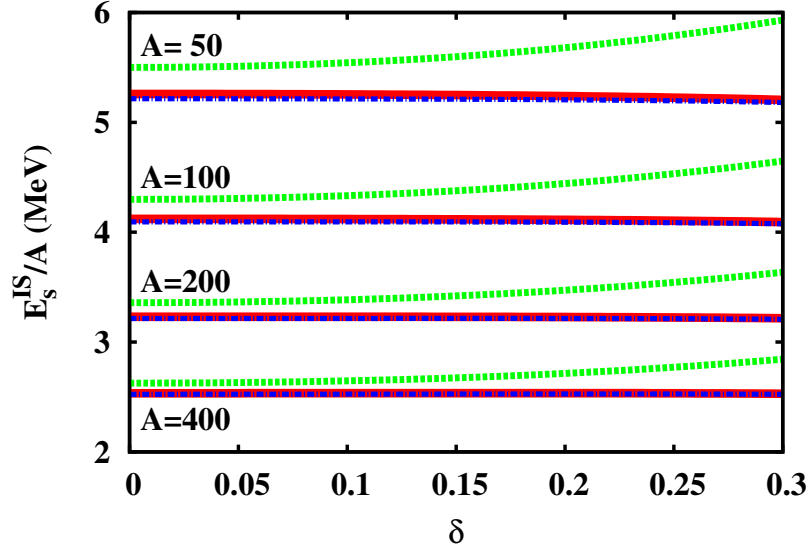


Figure III–7: Isoscalar surface energy per nucleon as a function of the isospin asymmetry, for four isobaric chains. Full red lines: calculations using the slab diffuseness eq. (III.29). Dashed-dotted blue lines: calculations using the spherical diffuseness eq. (III.30). Dashed green lines: calculations using the quadratic diffuseness, fitted from HF density profiles in ref. [Pap13]. Figure published in [Aym15].

### III.2.2 Approximations for the isovector energy

In this section, we focus on the residual isovector surface part  $E_s^{IV}$  defined by eq. (III.43), which cannot be written as integrals of Fermi functions as in the previous sections. Indeed, the isovector density  $\rho_3$  appearing in the energy density is not a Fermi function, meaning that it cannot be analytically integrated to evaluate  $E_s^{IV}$ . Approximations are needed to develop an analytical expression for this part of the energy, and we will consider in what follows two different approaches. At the end, we will verify the accuracy of our final formulae, in comparing the analytical expressions with HF calculations.

#### III.2.2.a No skin approximation

As a first approximation, we neglect all inhomogeneities in the isospin distribution in the same spirit as ref. [Kri83]. This simplification consists in replacing the isospin asymmetry profile  $\rho_3(r)/\rho(r)$  in eq. (III.43) by its mean value  $\langle\delta\rangle$ . Within this approximation, the local isovector energy only depends on the total baryonic density profile  $\rho(r)$ , and the non-local isovector part, involving gradients  $\nabla\rho_3$ , is identically zero. So this approximation amounts neglecting the non-local contribution to the isovector surface energy.

In integrating in space the equality  $\rho_3(r) = \langle\delta\rangle\rho(r)$ , we immediately obtain that the

mean value of the isospin distribution is given by the global asymmetry of the nucleus:

$$\langle \delta \rangle = \frac{N - Z}{A} = I. \quad (\text{III.48})$$

In particular, in this approximation, the bulk isospin asymmetry  $\delta$  is equal to the global asymmetry  $I$ , at variance with the more elaborated relation between  $\delta$  and  $I$  given by eq. (II.45). In neglecting isospin inhomogeneities, we indeed neglect both neutron skin and Coulomb effects which are responsible for the difference between  $\delta$  and  $I$ . Consequently in this section, the saturation density  $\rho_{sat}$  of asymmetric matter is still given by eq. (II.42), but replacing  $\delta$  by  $I$ . As we have seen in part II, this no-skin approximation modifies the bulk energy eq. (III.39), and the isoscalar energy eq. (III.3). Though it only slightly worsens the predictive power of the total ETF energy with respect to Hartree-Fock calculations, the relative weight between bulk and surface energies is drastically modified. In particular, this change of variable switches the sign of the symmetry surface energy. However, the obvious advantage is that analytical results can be obtained without further approximations than the ones developed in chapter III.1, as we now detail.

Replacing  $\rho_3(r)$  by  $I\rho(r)$  and  $\rho_{sat,3}(\delta)$  by  $I\rho_{sat}(I)$  in eq. (III.43), allows to express the energy density as a function of  $\rho(r)$  only. Thus we can follow the same procedure as for symmetric nuclei in section III.1.1, and analytically integrate the energy density using the appendix equation (A.8). Making a quadratic expansion in  $I$  for the kinetic densities  $\tau_3$  gives the following expressions:

$$\begin{aligned} E_s^{IV} = & \left[ \mathcal{C}_{surf}^{IV} \frac{a(A, I)}{r_{sat}(I)} A^{2/3} + \mathcal{C}_{curv}^{IV} \left( \frac{a(A, I)}{r_{sat}(I)} \right)^2 A^{1/3} + \mathcal{C}_{ind}^{IV} \left( \frac{a(A, I)}{r_{sat}(I)} \right)^3 \right] I^2 \\ & + O \left( \left( \frac{a(A, I)}{r_{sat}(I)} \right)^4 A^{-1/3} \right), \end{aligned} \quad (\text{III.49})$$

where the coefficients  $\mathcal{C}_i^{IV}$  depend on the saturation density  $\rho_{sat}(I)$  and on the effective interaction parameters  $C_{eff}$ ,  $D_{eff}$ ,  $\alpha$ ,  $D_0$  and  $D_3$ , appearing in the isovector local terms. The coefficients  $\mathcal{C}_i^{IV}$  are given by:

$$\begin{aligned} \mathcal{C}_{surf}^{IV} = & 3 \left\{ C_{kin} \left[ \frac{5}{3} \eta_{5/3}^{(0)} \left( \frac{m}{3m_{sat}^*} + \Delta m_{sat,3} \right) - \left( \frac{\delta m_{sat}}{3} + \Delta m_{sat,3} \right) \right] \right. \\ & \left. - D_0 \rho_{sat} + D_3 \rho_{sat}^{\alpha+1} \eta_{\alpha+2}^{(0)} \right\}, \end{aligned} \quad (\text{III.50})$$

$$\mathcal{C}_{curv}^{IV} = 6 \left\{ C_{kin} \left[ \frac{5}{3} \left( \eta_{5/3}^{(1)} - \frac{\pi^2}{6} \right) \left( \frac{m}{3m_{sat}^*} + \Delta m_{sat,3} \right) - \eta_{5/3}^{(0)} \left( \frac{\delta m_{sat}}{3} + \Delta m_{sat,3} \right) \right] \right\}$$

$$+ D_3 \rho_{sat}^{\alpha+1} \left( \eta_{\alpha+2}^{(1)} - \frac{\pi^2}{6} \right) \Big\}, \quad (\text{III.51})$$

$$\begin{aligned} \mathcal{C}_{ind}^{IV} = & 3 \left\{ C_{kin} \left[ \frac{5}{3} \left( \eta_{5/3}^{(2)} - \frac{2\pi^2}{3} \eta_{5/3}^{(0)} \right) \left( \frac{m}{3m_{sat}^*} + \Delta m_{sat,3} \right) \right. \right. \\ & \left. \left. - \frac{2}{3} \left( 3\eta_{5/3}^{(1)} - \pi^2 \right) \left( \frac{\delta m_{sat}}{3} + \Delta m_{sat,3} \right) \right] \right. \\ & \left. + \frac{\pi^2}{3} D_0 \rho_{sat} + D_3 \rho_{sat}^{\alpha+1} \left( \eta_{\alpha+2}^{(2)} - \frac{2\pi^2}{3} \eta_{\alpha+2}^{(0)} \right) \right\}, \quad (\text{III.52}) \end{aligned}$$

where  $m/m_{sat}^* = (m/m_{sat,n}^* + m/m_{sat,p}^*)/2$ ,  $\delta m_{sat} = (\delta m_{sat,n} + \delta m_{sat,p})/2$ ,  $\Delta m_{sat,3} = (m/m_{sat,n}^* - m/m_{sat,p}^*)/(2I) = (\delta m_{sat,n} - \delta m_{sat,p})/(2I)$ , and where the values of the coefficients  $\eta_{\gamma}^{(k)}$  defined by eq. (A.2) are given in table A.1.

As for the isoscalar energy, eq. (III.49) shows that the dominant finite-size effect is a surface term ( $\propto A^{2/3}$ ). Additional finite-size terms, which would be absent in a slab configuration, are found in spherical nuclei. As we have only considered the local part of the isovector energy, we recover the same diffuseness dependence as in the local isoscalar terms eqs. (III.10) and (III.11).

We have seen in section III.1.2 that the diffuseness  $a$  can be obtained by minimization of the energy per nucleon with respect to its free parameters. In this no-skin approximation, the only non-constrained parameter of the model is again the diffuseness parameter  $a$ , as for symmetric nuclei. Therefore, we can apply eq. (III.28) in order to obtain the ground state energy. If we neglect the curvature and mass independent terms, we obtain an expression similar to eq. (III.29):

$$a = \sqrt{\frac{\mathcal{C}_{surf}^{NL}(I)}{\mathcal{C}_{surf}^L(I) + \mathcal{C}_{surf}^{IV}(I)I^2}}, \quad (\text{III.53})$$

where the coefficients  $\mathcal{C}_{surf}^i$  depend on the saturation density  $\rho_{sat}(I)$ . This expression corresponds to the diffuseness of one-dimensional semi-infinite asymmetric matter. Considering all the terms of eq. (III.49), the diffuseness corresponding to the complete variational problem is given by the solution of the following equation, similar to eq. (III.30):

$$\begin{aligned} & 3 \left( \mathcal{C}_{ind}^L + \mathcal{C}_{ind}^{IV} I^2 \right) \left( \frac{a}{r_{sat}} \right)^4 + 2 \left( \mathcal{C}_{curv}^L + \mathcal{C}_{curv}^{IV} I^2 \right) A^{1/3} \left( \frac{a}{r_{sat}} \right)^3 \\ & + \left( \left( \mathcal{C}_{surf}^L + \mathcal{C}_{surf}^{IV} I^2 \right) A^{2/3} + \frac{1}{r_{sat}^2} \mathcal{C}_{ind}^{NL} \right) \left( \frac{a}{r_{sat}} \right)^2 \\ & - \frac{1}{r_{sat}^2} \mathcal{C}_{surf}^{NL} A^{2/3} = 0. \end{aligned} \quad (\text{III.54})$$

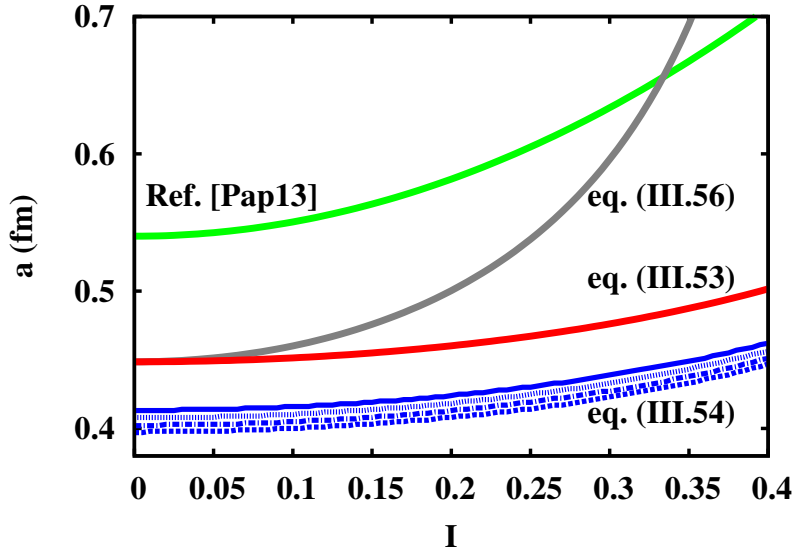


Figure III–8: Diffuseness as a function of the global asymmetry, for four isobaric chains ( $A = 400$ : full lines,  $A = 200$ : dotted lines,  $A = 100$ : dashed-dotted lines,  $A = 50$ : dashed lines). Red lines: calculations using the slab diffuseness eq. (III.53). Blue lines: calculations using the spherical diffuseness eq. (III.54). Green line: calculations using the quadratic diffuseness fitted from HF density profiles [Pap13]. Grey line: calculations using the diffuseness eq. (III.56), based on [Kri83]. Figure published in [Aym15].

Figure III–8 displays the results of eqs. (III.53) and (III.54). At variance with fig. III–6 where we only took into account the isoscalar energy, we can clearly see that adding the isovector energy to the variational procedure leads to the expected behavior of a diffuseness increasing with asymmetry. This behavior shows the importance of the isovector part to correctly determine the isoscalar diffuseness  $a$ . As for symmetric nuclei, we observe again that the mass dependence of the diffuseness calculated in the spherical case is negligible (only a slight spread of the blue curves).

The corresponding analytical total surface energy  $E_s = E_s^{IS} + E_s^{IV}$  per nucleon, given by eqs. (III.10), (III.11) and (III.49), is plotted on fig. III–9, for different isobaric chains. The results using the slab diffuseness (full red curves) are very close to the ones obtained by solving eq. (III.54) (dashed-dotted blue curves), and to the ones using the numerical fit to HF calculations of ref. [Pap13] (dashed green curves), even if the corresponding values for the parameter  $a$  are very different. The conclusions are thus the same as in section III.1.2: although curvature (and mass independent) terms are important to reproduce the energetics, they are not required to determine the diffuseness. Therefore this latter can be well determined by the simplest expression, eq. (III.53).

For completeness, we also compare our results to the approximation for the surface

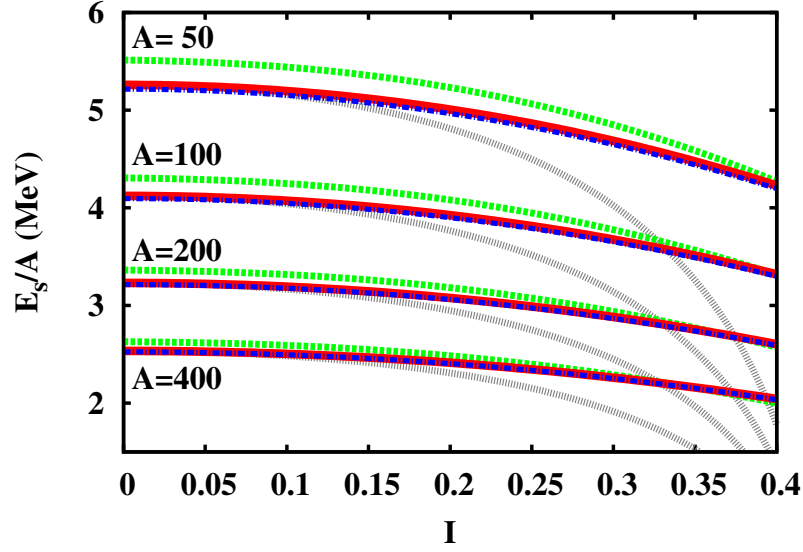


Figure III–9: Total surface energy per nucleon as a function of the global asymmetry, for four isobaric chains. Full red lines: calculations using the slab diffuseness eq. (III.53). Dashed-dotted blue lines: calculations using the spherical diffuseness eq. (III.54). Dashed green lines: calculations using the quadratic diffuseness fitted from HF density profiles [Pap13]. Dotted grey lines: calculations using the diffuseness eq. (III.56), based on [Kri83]. Figure published in [Aym15].

energy proposed in [Kri83], and represented by grey curves in figs. III–8 and III–9:

$$E_s = E_s^{IS}(I=0) + 2 \left[ \frac{E_s^{IS}(I=0)}{A^{2/3}} \frac{L_{sym}}{K_{sat}} - \frac{a \left( L_{sym} - \frac{K_{sym}}{12} \right)}{r_{sat}(I=0)} \right] A^{2/3} I^2. \quad (\text{III.55})$$

In ref. [Kri83], no expression for the diffuseness was proposed. For consistency, we have determined the  $a$  parameter entering eq. (III.55) by minimizing the surface energy given by the same equation, leading to:

$$a = \sqrt{\frac{C_{surf}^{NL}(I=0) \left( 1 + \frac{2L_{sym}}{K_{sat}} I^2 \right)}{C_{surf}^L(I=0) \left( 1 + \frac{2L_{sym}}{K_{sat}} I^2 \right) - 2 \left( L_{sym} - \frac{K_{sym}}{12} \right) I^2}}. \quad (\text{III.56})$$

To obtain eq. (III.55), the authors of ref. [Kri83] did the same approximation  $\rho_3(r) = I\rho(r)$  as we made, neglected the curvature and constant terms, but assumed the equality  $E_s^L = E_s^{NL}$  for the isovector part in order to evaluate the non-local isovector energy. As we have shown in section III.1.3, this property fails in a three-dimensional system. As a consequence, the diffuseness which is determined by the balance between local and

non-local parts, is overestimated as we can see in fig. III–8, finally leading to a largely underestimated energy, as shown in fig. III–9.

To check the accuracy of our analytical no-skin expression given by eqs. (III.44), (III.49) and (III.53), we will quantitatively compare our analytical results with Hartree-Fock calculations in section III.2.2.c.

### III.2.2.b Gaussian approximations

To take into account isospin inhomogeneities, we develop in this section alternative Gaussian approximations to the isovector surface energy. In particular, as in section III.2.1, we will distinguish the bulk asymmetry  $\delta$  eq. (II.45) from the global one  $I$ , which allows considering skin and Coulomb effects. This approximation is therefore expected to be more realistic than the no-skin procedure developed in section III.2.2.a.

#### i) Global Gaussian approximation

Since the isovector component  $E_s^{IV}$  is a surface energy, the corresponding energy density

$$\mathcal{H}_s^{IV}[\rho, \rho_3] = \mathcal{H}^{IV}[\rho, \rho_3] - \frac{\mathcal{H}^{IV}[\rho_{sat}, \rho_{sat3}]}{\rho_{sat}(\delta)} \rho \quad (\text{III.57})$$

is negligible at the nucleus center, where  $\rho \rightarrow \rho_{sat}$ . This is shown in fig. III–10 (red full lines), which displays this quantity for several nuclei in a representative calculation using the diffusenesses  $a$  and  $a_p$  from ref. [Pap13], and with the interaction SLy4. Moreover, as it is a surface energy, the maximum is expected to be close to the surface radius  $R$ , that is the inflection point of the Fermi function eq. (II.44), where  $\rho(R) = \rho_{sat}(\delta)/2$ . Thus we approximate the isovector energy density by a Gaussian peaked at  $r = R$ :

$$\mathcal{H}_s^{IV}(r) \simeq \mathcal{G}_{tot}(r) = \mathcal{A}(A, \delta) \exp\left(-\frac{(r - R)^2}{2\sigma^2(A, \delta)}\right), \quad (\text{III.58})$$

where  $\mathcal{A}$  is the amplitude of the Gaussian at  $r = R$  (thus assumed to be the maximum) and  $\sigma^2$  its variance at the same point  $r = R$ :

$$\mathcal{A}(A, \delta) = \mathcal{H}_s^{IV}[\rho(R), \rho_3(R)], \quad (\text{III.59})$$

$$\sigma^2(A, \delta) = -\mathcal{A}(A, \delta) \left( \frac{d^2 \mathcal{H}_s^{IV}}{dr^2} \right)_{r=R}^{-1}. \quad (\text{III.60})$$

Fig. III–10 shows the quality of this Gaussian approximation eq. (III.58) on the energy density profile for several nuclei. Each panel corresponds to a different representative value of  $\delta$ :  $\delta = 0.1$  (upper left) corresponds to most stable nuclei (see fig. III–5); medium-

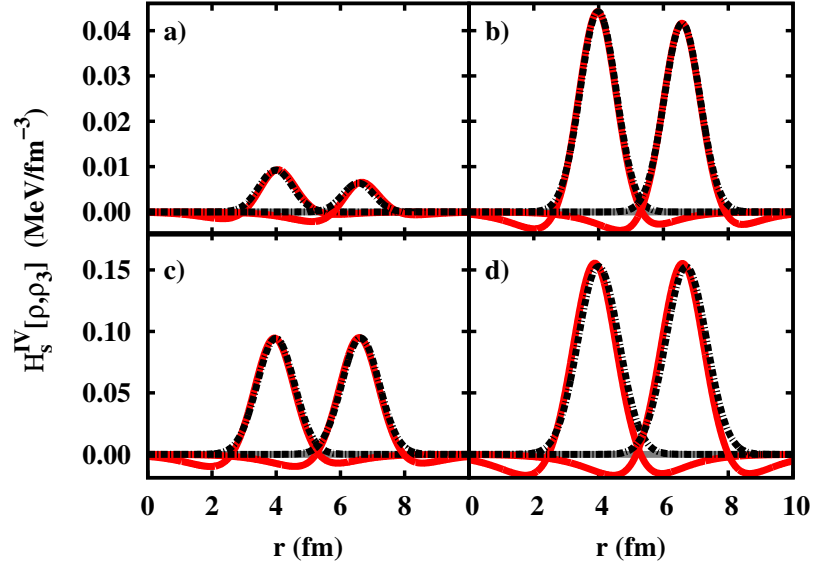


Figure III-10: Numerical isovector energy density profile (red full lines) and Gaussian approximation eq. (III.58) (black dashed-dotted lines) for two masses  $A = 50$  (left curves of each panel) and  $A = 200$  (right curves of each panel). a)  $\delta = 0.1$ ; b)  $\delta = 0.2$ ; c)  $\delta = 0.3$ ; d)  $\delta = 0.4$ . Figure published in [Aym15].

heavy neutron rich nuclei synthesized in modern radioactive ion facilities lay around  $\delta = 0.2$  (upper right); the (largely unexplored) neutron drip-line closely corresponds to  $\delta = 0.3$  (lower left); the higher value  $\delta = 0.4$  (lower right) is only obtained beyond the drip line, that is for nuclei embedded in a nucleon gas. We can see that for all these very different asymmetries, the exact energy density (full red lines) is indeed peaked at the radius  $R$ . However, we can notice that the profiles have small negative components. We thus expect that the Gaussian approximation will overestimate the isovector energy part.

Since Gaussian functions and their moments are analytically integrable, the approximation eq. (III.58) allows obtaining an analytical expression for the isovector energy  $E_s^{IV} \approx 4\pi \int r^2 \mathcal{G}_{tot}(r) dr$ . Indeed, neglecting the terms  $\sim e^{-R^2/(2\sigma^2)}$ , we obtain (see appendix B):

$$E_s^{IV} = 2(2\pi)^{3/2} \sigma(A, \delta, a, a_p) \mathcal{A}(A, \delta, a, a_p) r_{sat}^2(\delta) \cdot \left[ A^{2/3} + \frac{\sigma^2(A, \delta, a, a_p)}{r_{sat}^2(\delta)} - \frac{2\pi^2}{3} \left( \frac{a(A, \delta)}{r_{sat}(\delta)} \right)^2 + O\left( \left( \frac{a}{r_{sat}} \right)^4 A^{-2/3} \right) \right], \quad (\text{III.61})$$

where we have highlighted the dependence on the nuclear mass number  $A$ , bulk asymmetry  $\delta$ , and diffusenesses  $a(A, \delta)$  and  $a_p(A, \delta)$  when they explicitly appear. The neglected terms are of the order  $(a/r_{sat})^4 A^{-2/3}$ . We can notice that the curvature term ( $\propto A^{1/3}$ ) is

missing. This is due to our approximation. Indeed, we have assumed that the isovector energy is symmetric with respect to the inflection point  $R$  for which the curvature is zero, such that the curvature is disregarded by construction.

## ii) Other Gaussian approximations

Before going further in the previous global Gaussian approximation, we briefly give and comment some other possible approximations also based on Gaussian functions.

Since we have noticed that the surface isovector energy density profile eq. (III.57) has both positive and negative components, a natural attempt to improve the global Gaussian approximation of the previous section is to use two Gaussian functions  $\mathcal{G}_\pm$  according to the sign of the energy terms:

$$\mathcal{H}_s^{IV}(r) = \mathcal{H}_+^{IV}(r) + \mathcal{H}_-^{IV}(r) \simeq \mathcal{G}_+(r) + \mathcal{G}_-(r), \quad (\text{III.62})$$

with  $\mathcal{H}_+^{IV}$  the positive part of the isovector energy density, standing for the kinetic and potential terms, and  $\mathcal{H}_-^{IV}$  the remaining negative components, that is the effective, finite-range, and spin-orbit terms. Let us notice that this decomposition is based on the sign of the integrated quantities, but the corresponding density profiles can have small components of the opposite sign. This especially happens with the gradient terms, or at high asymmetry beyond drip lines. With the decomposition eq. (III.62), the corresponding surface isovector energy has two components as well:

$$E_s^{IV} = E_+^{IV} + E_-^{IV}, \quad (\text{III.63})$$

for which  $E_\pm^{IV} \approx 4\pi \int r^2 \mathcal{G}_\pm(r) dr$  can be analytically integrated, following appendix B, and making again the assumption that the positive and negative Gaussian are peaked at the nuclear surface  $R$ .

Fig. III-11(a) displays the positive  $\mathcal{H}_+^{IV}$  and negative  $\mathcal{H}_-^{IV}$  isovector energy density profiles (red full lines) and their associated Gaussian approximations  $\mathcal{G}_+$  and  $\mathcal{G}_-$  (black dashed-dotted lines) for two nuclei at the limit of the drip line  $\delta = 0.3$ . We can see that the positive component is extremely well reproduced by the Gaussian assumption. However, the approximation on the negative part leads to a very large overestimation of the component. This comes from the fact that the negative isovector energy density turns out to not having a Gaussian profile-like. Indeed, because of the small positive contributions mainly coming from the gradients, the profile has a more complex structure. On the other side, the minimum of this energy density is shifted from the nuclear surface  $R$ . As a consequence, the Gaussian profile  $\mathcal{G}_-(r)$  is calculated with a larger variance  $\sigma^2(R)$ , leading to the observed disagreement in fig. III-11(a). In conclusion, this approximation based on two opposite Gaussian profiles worsens the results with respect to eq. (III.58).

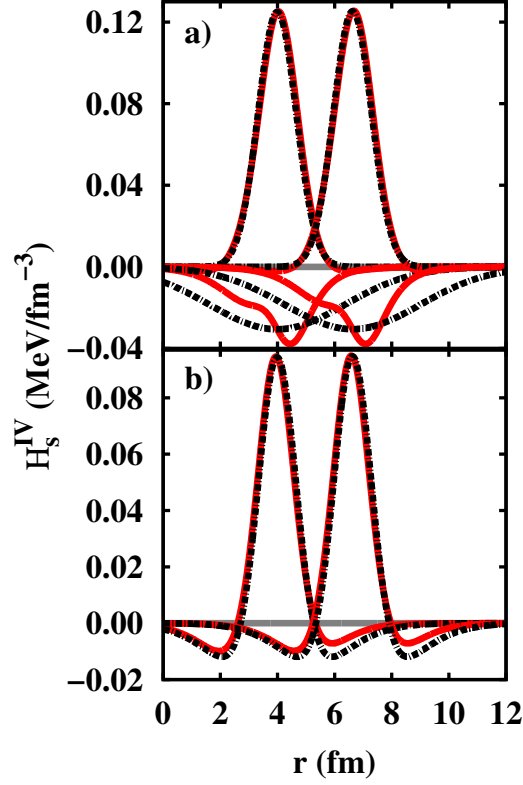


Figure III-11: Numerical isovector energy density profiles (red full lines) and Gaussian approximations (black dashed-dotted lines) eq. (III.62) (upper panel) and eq. (III.64) (lower panel) for two masses  $A = 50$  (left curves of each panel) and  $A = 200$  (right curves of each panel), both at  $\delta = 0.3$ . Upper panel a): positive and negative components of the isovector energy density profile; Lower panel b): total isovector energy density profile.

A second natural attempt to improve the global Gaussian approximation of the previous section, in taking into account the negative components, is to treat each energy term separately:

$$\mathcal{H}_s^{IV}(r) = \sum_t \mathcal{H}_t^{IV}(r) \simeq \sum_t \mathcal{G}_t(r), \quad (\text{III.64})$$

where  $t$  stands for the 7 different terms of the energy, that is 0<sup>th</sup> and 2<sup>nd</sup> order of the kinetic and effective terms, as well as the potential, finite-range, and spin-orbit energy densities. As previously, in assuming that the Gaussian functions are peaked at the nuclear surface  $R$ , we can analytically integrate eq. (III.64) according to appx. B, leading to

$$E_s^{IV} = \sum_t E_t^{IV}. \quad (\text{III.65})$$

The result of the approximation eq. (III.64) is shown in fig. III–11(b) which displays the surface isovector energy density profile (red full lines) and the sum of the Gaussian approximations  $\sum_t \mathcal{G}_t(r)$  (black dashed-dotted lines), again for two nuclei at  $\delta = 0.3$ . We can see that the approximated profile very well reproduce the energy density profile  $\mathcal{H}_s^{IV}(r)$ . More specifically, it succeeds in taking into account the negative components though a little overestimated. This approximation based on Gaussian profiles for each energy term is thus expected to improve the previous global Gaussian approximation eq. (III.58).

However, though the Gaussian integrals of both the global approximation eq. (III.61) and the per term approximation eq. (III.64) are analytical expressions, the explicit derivation of the amplitudes and of the variance leads to formulae far from being transparent (see appendix C). In particular, it is not clear how the different physical ingredients of the energy functional (compressibility, effective mass, symmetry energy) and of the nucleus properties (neutron skin, diffuseness) affect the isovector surface properties. For this reason, we need to develop a further approximation for the isovector energy part  $E_s^{IV}$ . In the case of the global Gaussian approximation, we will see in the following section iii) that expansions of the total symmetry energy density lead to much more transparent expressions in terms of the nuclear matter coefficients  $J$ ,  $L$  and  $K$ , and of the neutron skin thickness. Moreover, these approximations will allow to find a simple analytical expression for the diffuseness. In the case of the per term Gaussian approximation, such expressions related to the properties of the total energy functional are more arduous to obtain since we have precisely decomposed the energy functional. This is why in what follows, we will focus on the global Gaussian approximation eq. (III.61).

### iii) Isovector energy expression

Making the usual quadratic assumption for the symmetry energy

$$\mathcal{H}^{IV}[\rho, \rho_3] = \mathcal{H}_{sym}[\rho] \left( \frac{\rho_3}{\rho} \right)^2, \quad (\text{III.66})$$

the amplitude  $\mathcal{A}(A, \delta)$  eq. (III.59) reads

$$\mathcal{A}(A, \delta) = \mathcal{H}_{sym}[\rho(R)] \left( \frac{\rho_3(R)}{\rho(R)} \right)^2 - \mathcal{H}_{sym}[\rho_{sat}(\delta)] \frac{\rho(R)}{\rho_{sat}(\delta)} \delta^2. \quad (\text{III.67})$$

In order to have a simpler explicit expression, we make a density expansion of the symmetry energy per nucleon  $e_{sym}[\rho] = \mathcal{H}_{sym}[\rho]/\rho$  around a density  $\rho_*$ , such that:

$$\mathcal{H}_{sym}[\rho] = \rho \left[ J_* + \frac{L_*}{3\rho_*} (\rho - \rho_*) + \frac{K_*}{18\rho_*^2} (\rho - \rho_*)^2 \right], \quad (\text{III.68})$$

where  $J_* = \mathcal{H}_{sym}[\rho_*]/\rho_*$ ,  $L_* = 3\rho_*\partial(\mathcal{H}_{sym}/\rho_*)/\partial\rho|_{\rho_*}$  and  $K_* = 9\rho_*^2\partial^2(\mathcal{H}_{sym}/\rho_*)/\partial\rho^2|_{\rho_*}$ . As we can see in eq. (III.67), we need to evaluate the symmetry energy at two different densities: at  $\rho_{sat}(\delta)$  and at the surface radius where  $\rho(R) = \rho_{sat}(\delta)/2$ . For this reason, we will apply eq. (III.68) to two different densities  $\rho_* = \rho_{sat}(0)$  and  $\rho_* = \rho_{sat}(0)/2$ . At  $\rho_* = \rho_{sat}(0)$ , the coefficients ( $J_*$ ,  $L_*$ ,  $K_*$ ) are the usual symmetry energy coefficients ( $J_{sym}$ ,  $L_{sym}$ ,  $K_{sym}$ ). Their values for the Skyrme interaction SLy4 are  $J_{sym} = 32$  MeV,  $L_{sym} = 46$  MeV, and  $K_{sym} = -119.8$  MeV. At one half of the saturation of symmetric nuclear matter,  $\rho_* = \rho_{sat}(0)/2$ , we label the corresponding coefficients ( $J_{1/2}$ ,  $L_{1/2}$ ,  $K_{1/2}$ ) which, for the Skyrme interaction SLy4, are  $J_{1/2} = 22.13$  MeV,  $L_{1/2} = 38.6$  MeV, and  $K_{1/2} = -74$  MeV.

Using the expansion around  $\rho_* = \rho_{sat}(0)/2$  for the first term of eq. (III.67), and around  $\rho_* = \rho_{sat}(0)$  for the second one, we obtain, at second order in  $\delta$ :

$$\begin{aligned} \frac{\mathcal{A}(A, \delta)}{\rho_{sat}(0)} &= \frac{J_{1/2}}{8} \left( \frac{\Delta R(a)}{a(A, \delta)} \right)^2 + \frac{J_{1/2}}{2} \left[ \frac{\Delta R(a)}{a(A, \delta)} - \frac{1}{2} \left( \frac{\Delta R(a)}{a(A, \delta)} \right)^2 \right] \delta \\ &+ \frac{J_{1/2}}{2} \left[ \left( 1 - \frac{J_{sym}}{J_{1/2}} \right) - \frac{\Delta R(a)}{a(A, \delta)} - \frac{1}{4} \left( 1 + \frac{L_{sym}L_{1/2}}{J_{1/2}K_{sat}} \right) \left( \frac{\Delta R(a)}{a(A, \delta)} \right)^2 \right] \delta^2. \end{aligned} \quad (\text{III.69})$$

Notice that the  $K_{sym}$  parameter does not appear in this equation because of the truncation at second order in  $\delta$ . In eq. (III.69), the isospin asymmetry inhomogeneities clearly appear through the quantity  $\Delta R(a) = R(a) - R_p(a)$  which represents the neutron skin thickness:

$$\Delta R(a) = \Delta R_{HS} \left( 1 + \frac{\pi^2}{3} \frac{a^2}{R_{HS}R_{HS,p}} \right), \quad (\text{III.70})$$

where  $\Delta R_{HS}(A, Z) = \Delta R(a = 0, A, Z) = R_{HS}(A) - R_{HS,p}(Z)$  is the neutron skin thickness of nuclei theoretically described by hard spheres. Moreover, we have considered the diffuseness difference  $a - a_p$  as a second order correction with respect to the neutron skin, and have assumed  $a = a_p$  in eq. (III.69). We have also used the following expansion in  $\Delta R(a)/a$  to evaluate  $\rho_3(R)$ :

$$\rho_p(R) = \frac{\rho_{sat,p}(\delta)}{2} \left[ 1 - \frac{\Delta R(a)}{2a} \right] + O \left( \left( \frac{\Delta R(a)}{a} \right)^3 \right). \quad (\text{III.71})$$

Eq. (III.69) gives a relatively simple and transparent expression of the isovector energy density at the nuclear surface, as a function of the EoS parameters. The situation is more complicated for the variance  $\sigma(A, \delta)$  which also enters the isovector energy eq. (III.61). This quantity involves the second spatial derivative of the energy density eq. (III.60),

therefore its explicit expression is not transparent, even with the previous simplifications. Extra approximations are in order.

From fig. III–10, we can observe that the width of the numerical Gaussians, that is the values of  $\sigma^2(A, \delta)$ , is almost independent of the bulk isospin  $\delta$ . This numerical evidence can be understood from the fact that the width gives a measure of the nucleus surface, which is mostly determined by isoscalar properties. It is therefore not surprising that the dominant isospin dependence is given by the amplitude  $\mathcal{A}$  which represents the isovector energy density at the surface. For this reason, we evaluate the variance at  $\delta = 0$ :

$$\sigma(A, \delta) \approx \sigma(A) = \sqrt{\frac{2}{1 - \frac{K_{1/2}}{18J_{1/2}}} a_0} = \sigma_0. \quad (\text{III.72})$$

In this equation,  $a_0$  stands for the diffuseness at  $\delta = 0$ . We recall that this quantity does not depend on the nucleus mass if we do not take into account terms beyond surface in the variational approach discussed in section III.1.2. This approximate mass independence of the variance can be verified in fig. III–10: the width of the two Gaussians corresponding to  $A = 50$  and  $A = 200$  are very close. Neglecting the isovector component at  $\delta = 0$ , the diffuseness is then given by the expression (III.29) valid for symmetric matter:

$$a_0 = \sqrt{\mathcal{C}_{surf}^{NL}(\delta = 0) / \mathcal{C}_{surf}^L(\delta = 0)}. \quad (\text{III.73})$$

Inserting eqs. (III.69) and (III.72) into (III.61), the surface isovector energy can be expressed as a function of the symmetry energy coefficients ( $J_{sym}, L_{sym}, K_{sym}$ ):

$$\begin{aligned} E_s^{IV} &= 3 \sqrt{\frac{\pi}{1 - \frac{K_{1/2}}{18J_{1/2}}} \frac{\rho_{sat}(0)}{\rho_{sat}(\delta)} \frac{a_0}{r_{sat}(\delta)}} J_{1/2} \\ &\times \left\{ \frac{1}{4} \left( \frac{\Delta R(a)}{a(A, \delta)} \right)^2 + \left[ \frac{\Delta R(a)}{a(A, \delta)} - \frac{1}{2} \left( \frac{\Delta R(a)}{a(A, \delta)} \right)^2 \right] \delta \right. \\ &\quad \left. + \left[ \left( 1 - \frac{J_{sym}}{J_{1/2}} \right) - \frac{\Delta R(a)}{a(A, \delta)} - \frac{1}{4} \left( 1 + \frac{L_{sym} L_{1/2}}{J_{1/2} K_{sat}} \right) \left( \frac{\Delta R(a)}{a(A, \delta)} \right)^2 \right] \delta^2 \right\} \\ &\times \left\{ A^{2/3} + \frac{2}{1 - \frac{K_{1/2}}{18J_{1/2}}} \left( \frac{a_0}{r_{sat}(\delta)} \right)^2 - \frac{2\pi^2}{3} \left( \frac{a(A, \delta)}{r_{sat}(\delta)} \right)^2 \right\}. \quad (\text{III.74}) \end{aligned}$$

In principle the surface coefficients ( $J_{1/2}, L_{1/2}, K_{1/2}$ ) can be expressed as a function of the bulk ones ( $J_{sym}, L_{sym}, K_{sym}$ ) by using polynomial expansion in the density. However, we can see from eq. (III.74) that the surface isovector energy  $E_s^{IV}$  is proportional

to the symmetry energy  $J_{1/2}$  evaluated at the surface  $R$ . It is quite natural that the surface energy component is mainly determined by the surface properties of the nuclei, and therefore, the surface symmetry energy is mainly proportional to the isovector parameter  $J_{1/2}$ . For this reason, expressing eq. (III.74) only in terms of bulk quantities ( $J_{sym}, L_{sym}, K_{sym}$ ) would make eq. (III.74) less transparent.

For completely symmetric nuclei, that is  $\Delta R = 0$  and  $\delta = 0$ , the isovector energy is identically zero as it should. However, if we neglect the neutron skin thickness only, that is we consider  $\Delta R = 0$  but  $\delta \neq 0$ , a non-zero isovector surface energy is obtained, given by

$$E_{surf}^{IV, \Delta R=0} = 3 \sqrt{\frac{\pi}{1 - \frac{K_{1/2}}{18J_{1/2}}} \frac{\rho_{sat}(0)}{\rho_{sat}(\delta)} \frac{a_0}{r_{sat}(\delta)}} (J_{1/2} - J_{sym}) \delta^2 A^{2/3}. \quad (\text{III.75})$$

This expression is proportional to the energy density difference between bulk and surface ( $J_{1/2} - J_{sym}$ ), that is to the  $L_{sym}$  parameter. In this approximation, the diffuseness  $a(A, \delta)$  does not appear, which means that the isovector surface energy contributes to the determination of the diffuseness only if we consider the neutron skin.

From a mathematical point of view we can also consider the limit  $\delta = 0$ ,  $\Delta R \neq 0$ , giving:

$$E_{surf}^{IV, \delta=0} = \frac{3}{4} \sqrt{\frac{\pi}{1 - \frac{K_{1/2}}{18J_{1/2}}} J_{1/2} \frac{\Delta R^2(a_0)}{a_0 r_{sat}(0)}} A^{2/3}. \quad (\text{III.76})$$

This expression shows that an isovector surface energy can be induced in asymmetric nuclei even if no asymmetry is present in the bulk. Of course in realistic situations the bulk asymmetry and the difference between neutron and proton radii are not independent variables. In particular, the skin is negligible if  $\delta = 0$ , as we have already assumed in order to obtain eq. (III.73).

Eq. (III.74) shows that even in our rather crude approximation the surface symmetry energy presents a very complex dependence on the physical quantities that measure isospin inhomogeneity, namely the bulk asymmetry  $\delta$  and the neutron skin thickness  $\Delta R$ . In particular we find that  $E_s^{IV}(A, \delta)$  is not quadratic with  $\delta$  but has non-negligible linear components (see also fig. III–16 below). We have also quantitatively tested that both linear and quadratic terms in  $\Delta R$  are required to correctly reproduce the surface isovector energy. It is interesting to notice that the linear components mix  $\delta$  and  $\Delta R$ . Indeed, as we can see in eqs. (III.75) and (III.76), putting to zero one of those variables, which both measure the isospin inhomogeneities, leads to a quadratic behavior with respect to the other variable.

Similar to the previous section, the diffuseness is the only unconstrained parameter

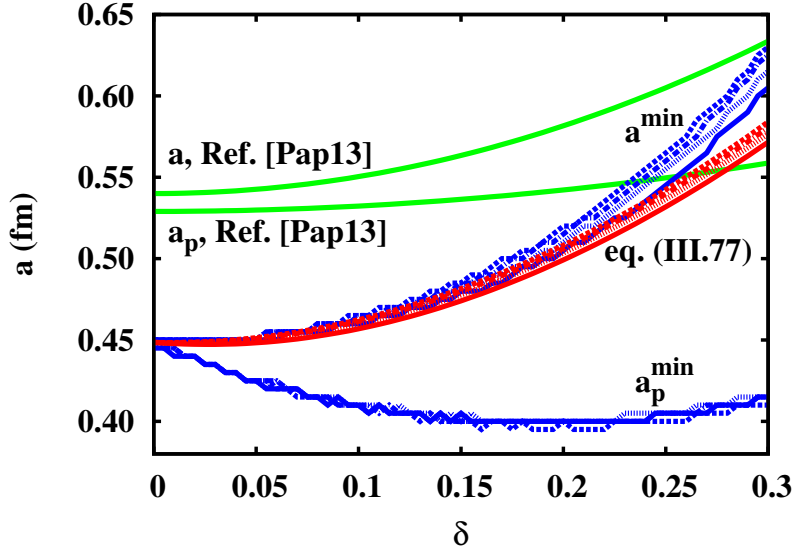


Figure III-12: Diffuseness as a function of the bulk isospin asymmetry. Red lines: eq. (III.77) from the minimization of the Gaussian approximation. Blue lines: minimization of the exact numerically calculated ETF surface energy. Green lines: fit from HF density profiles, taken from [Pap13]. Figure published in [Aym15].

of the model. It can therefore be determined in a variational approach by minimizing the total (isoscalar and isovector) surface energy. In section III.1.2, we have shown that only the dominant  $\propto A^{2/3}$  terms are important to evaluate the diffuseness. For this reason, we neglect again terms beyond plane surface, and we approximate the neutron skin thickness  $\Delta R$  by the hard sphere approximation  $\Delta R_{HS}$ . Neglecting the quadratic terms in the expansion in  $\Delta R_{HS}/a$ , we obtain

$$a^2(A, \delta) = a_{IS}^2(\delta) + \sqrt{\frac{\pi}{1 - \frac{K_{1/2}}{18J_{1/2}}} \frac{\rho_{sat}(0)}{\rho_{sat}(\delta)} \frac{3J_{1/2}(\delta - \delta^2)}{\mathcal{C}_{surf}^L(\delta)}}} a_0 \Delta R_{HS}(A, \delta), \quad (\text{III.77})$$

where  $a_{IS}(\delta)$  is the diffuseness obtained in section III.2.1 by neglecting the isovector component :  $a_{IS}(\delta) = \sqrt{\mathcal{C}_{surf}^{NL}(\delta)/\mathcal{C}_{surf}^L(\delta)}$ . We found in section III.2.1 that  $a_{IS}$  slightly decreases with the isospin asymmetry (fig III-6), which does not appear consistent with the behavior observed in full HF calculations. Now considering in the variational principle the isovector term in addition to the isoscalar one, the diffuseness  $a$  given by eq. (III.77) acquires an additional term which modifies its global  $\delta$  dependence. The complete result eq. (III.77) is displayed in figure III-12 (red curves). We can see that the additional term due to the isovector energy contribution inverses the trend found section III.2.1, as expected. More specifically, though it does not clearly appear in eq. (III.77), the analytical diffuseness is seen to quadratically increase with  $\delta$ , corroborating the assumption

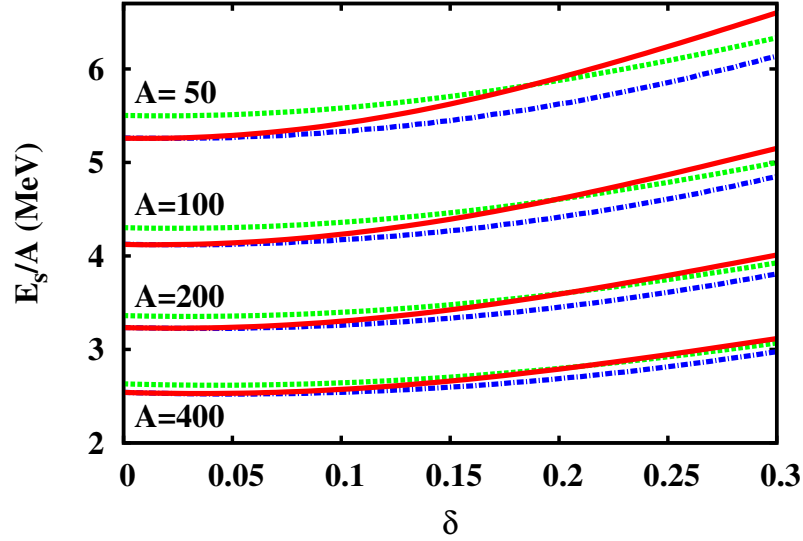


Figure III–13: Lower panel: surface energy per nucleon as a function of the bulk isospin asymmetry for four isobaric nucleus chains. Full red lines: Gaussian approximation using the diffuseness eq. (III.77). Dashed-dotted blue lines: exact numerically calculated ETF surface energy using the optimal diffusenesses ( $a^{min}, a_p^{min}$ ) (see text). Dashed green lines: exact numerically calculated ETF surface energy using the diffusenesses from [Pap13]. Figure published in [Aym15].

made in ref. [Pap13].

Although we only considered terms  $\propto A^{2/3}$ , as in a slab geometry, the results slightly depend on the nucleus mass as shown by the slight dispersion of the different red curves in figure III–12. This is due to the neutron skin since  $\Delta R_{HS}(A, \delta)$  depends on the mass number  $A$ . For comparison, the diffusenesses  $a$  and  $a_p \neq a$  obtained by the fit of HF density profiles of [Pap13] are also represented in figure III–12 (green curves), as well as the numerically calculated pair ( $a^{min}, a_p^{min}$ ) which minimises the energy (blue curves).

As we can see, these diffusenesses significantly differ from each other, but their consequence on the energy is small as we can observe in fig. III–13 which displays the corresponding surface energy  $E_s = E_s^{IS} + E_s^{IV}$  per nucleon, for different isobaric chains. In this figure, the blue curves correspond to a numerical integration of the ETF energy density, using the diffusenesses which minimize the total surface energy. These results can thus be considered as “exact” ETF results. The use of the very different  $a$  and  $a_p$  values fitted from HF (green lines) leads to only slightly different energies, except for the lightest isobar chain. The analytical approximation given by the sum of eq. (III.44) and eq. (III.74), is also plotted (red curves), where the diffuseness is given by the analytical formula eq. (III.77). We can see that our analytical approximation closely follows the “exact” ETF results.

All the curves show a positive surface symmetry energy, which contrasts with the results of fig. III–9. As it has been discussed in part II, this change of sign is due to the choice between the bulk asymmetry  $\delta$  or the global asymmetry  $I$ , in the definition of the bulk energy.

In order to further validate the analytical results of this section, quantitative comparisons with Hartree-Fock calculations are shown in the next section III.2.2.c.

### III.2.2.c Comparison to Hartree-Fock calculations

In this section, we explore the level of accuracy of both the no-skin approximation and the Gaussian approximation, respectively developed in sections III.2.2.a and III.2.2.b.

As previously discussed, the two different approximations lead to two different bulk energetics. Neglecting isospin inhomogeneities implies that the bulk asymmetry  $\delta$  is equalized to the average asymmetry  $I$ . Thus the bulk quantities  $\rho_{sat}$  and  $E_b$  defined by eqs. (II.42) and (III.39) depend on  $I$ , and the total energy of a nucleus  $(A, I)$  within the no-skin approximation is given by

$$E_{NoSkin}(A, I) = E_b(A, I) + E_s^{IS}(A, I) + E_s^{IV}(A, I), \quad (\text{III.78})$$

where  $E_s^{IS}(A, I)$  is given by eq. (III.44) (with  $I$  instead of  $\delta$ ),  $E_s^{IV}(A, I)$  by eq. (III.49), and the diffuseness by eq. (III.53).

On the other hand, the Gaussian approximation allows defining two independent density profiles. Therefore, the bulk energy depends on the bulk asymmetry  $\delta(A, I)$  defined by eq. (II.45) and the total energy of a nucleus  $(A, I)$  within this approximation is given by

$$E_{Gauss}(A, I) = E_b(A, \delta) + E_s^{IS}(A, \delta) + E_s^{IV}(A, \delta), \quad (\text{III.79})$$

where  $E_s^{IS}(A, \delta)$  is given by eq. (III.44),  $E_s^{IV}(A, \delta)$  by eq. (III.74), and the diffuseness by eq. (III.77).

In figure III–14, we compare the analytical expressions (III.78) and (III.79) with Hartree-Fock energy calculations, for different isobaric chains. To compare the same quantities, we used the same interaction (SLy4), and we have removed the Coulomb energy from the total HF energetics.

We can see from the figure that the no-skin and the Gaussian approximations predict close values for the total energy. For low asymmetries  $I \lesssim 0.2$  where the two models are almost undistinguishable, they reproduce the microscopic calculations with a very good accuracy, especially for medium-heavy nuclei  $A \gtrsim 100$ . However, for higher asymmetries  $I \gtrsim 0.2$ , where the symmetry energy becomes important, a systematic difference between

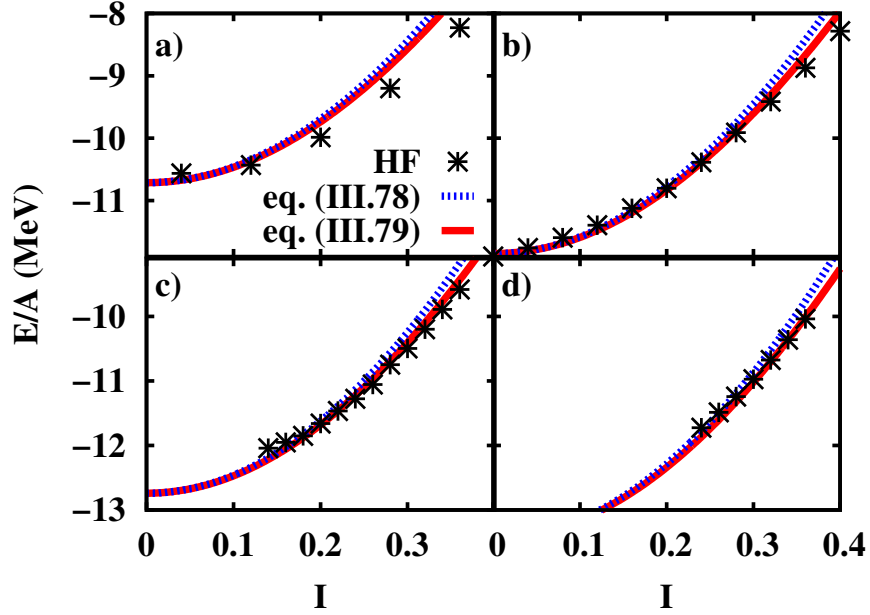


Figure III-14: Total energy  $E = E_b + E_s$  per nucleon as a function of the nucleus asymmetry  $I = 1 - 2Z/A$  calculated within the no-skin approximation, eq. (III.78) (blue dotted lines) and within the Gaussian approximation, eq. (III.79) (red full lines), compared to nuclear Hartree-Fock energy (stars). a)  $A = 50$ ; b)  $A = 100$ ; c)  $A = 200$ ; d)  $A = 400$ . Figure published in [Aym15].

the two models appears and increases up to  $\sim 400$  keV/ $A$  for the highest asymmetries  $I \sim 0.4$ : the Gaussian approximation is systematically closer to the microscopic results than the no-skin model. This observation highlights the importance of taking into account the isospin asymmetry inhomogeneities, considering the neutron skin and at the same time differentiating the bulk asymmetry  $\delta$  from the global one  $I$ , as it has been discussed in part II. Quantitatively, for medium-heavy nuclei, the accuracy of eq. (III.79) is better than  $\sim 200$  keV/ $A$ , which is similar to the predictive power of spherical Hartree-Fock calculations for this effective interaction, with respect to experimental data.

To conclude, the global Gaussian approximation developed in section III.2.2.b provides a reliable analytical formula, especially for the surface symmetry energy. For this reason, we will only use the Gaussian approximation to further study the different components of the nuclei energetics, as we turn to do in the next section.

### III.2.3 Study of the different energy terms

In this section, we use the analytical formulae based on the Gaussian approximation detailed in section III.2.2.b, to study the different components of nuclear energetics. As we have previously discussed throughout this chapter, we can decompose the nucleus

total energy  $E$  into bulk  $E_b$  and surface  $E_s$  parts. Both can be written as sums of isoscalar  $E_i^{IS}$ , that is the part independent of  $\rho_3(r)$ , and isovector  $E_i^{IV}$  terms. The surface energy can be further split into plane surface  $E_{surf} \propto A^{2/3}$ , curvature  $E_{curv} \propto A^{1/3}$  and mass independent  $E_{ind}$  terms. Finally, we can distinguish the local  $E_i^{IS,L}$  and the non-local  $E_i^{IS,NL}$  components of the surface isoscalar part only, since we did not discriminate them in the Gaussian approximation used for the isovector energy. In summary, the energy of a  $(A, I)$  nucleus can be written as

$$E(A, I) = E_b(A, \delta) + E_s(A, \delta), \quad (\text{III.80})$$

$$E_s(A, \delta) = E_s^{IS}(A, \delta) + E_s^{IV}(A, \delta), \quad (\text{III.81})$$

$$E_s^{IV}(A, \delta) = E_{surf}^{IV}(A, \delta) + E_{ind}^{IV}(A, \delta), \quad (\text{III.82})$$

$$E_s^{IS}(A, \delta) = E_{surf}^{IS}(A, \delta) + E_{curv}^{IS}(A, \delta) + E_{ind}^{IS}(A, \delta), \quad (\text{III.83})$$

$$E_{surf}^{IS}(A, \delta) = E_{surf}^{IS,L}(A, \delta) + E_{surf}^{IS,NL}(A, \delta), \quad (\text{III.84})$$

$$E_{curv}^{IS}(A, \delta) = E_{curv}^{IS,L}(A, \delta) + E_{curv}^{IS,NL}(A, \delta), \quad (\text{III.85})$$

where the bijective relation (for a given mass) between  $I$  and  $\delta$  is given by eq. (II.45). The different isoscalar terms  $E_i^{IS,j}$  are defined by eqs. (III.44) to (III.47), with the diffuseness  $a(A, \delta)$  determined within the Gaussian approximation, eq. (III.77). The isovector components  $E_i^{IV}$  are introduced in eq. (III.74), where the curvature term, in this Gaussian approximation, is identically zero by construction.

In what follows, we will study each of these terms, and specifically their dependence with the asymmetry  $\delta$ . For this comparison, we have chosen a representative isobaric chain  $A = 100$  for which the ETF approximation was successfully compared to HF results in fig. III-14, for the SLy4 interaction. For this choice of mass,  $\delta \approx 0$  corresponds to the proton drip line and  $\delta \approx 0.3$  the neutron drip line (see fig. III-5).

Due to our limited experimental knowledge of the isovector properties of the effective interaction, the behavior of the different energy terms with asymmetry is to some extent model dependent. In order to sort out general trends we have considered the same Skyrme functionals as in part II, which approximately span the current uncertainties on the density dependence of the symmetry energy.

The corresponding bulk parameters are reported in table II-3. The calculated surface coefficients  $(J_{1/2}, L_{1/2}, K_{1/2})$  entering eq. (III.74) and (III.77) are given in table III-1. As it is well known [EPJ14], the different interactions are very close at half saturation density, reflecting the fact that all Skyrme parameters have been fitted on ground state properties of finite nuclei, which correspond to an average density of the order of  $\rho_{sat}/2$ . Nevertheless, a considerable spread is already seen at saturation density, showing that the extrapolation of isovector properties to unexplored density domains is still not well controlled [EPJ14].

Interaction	$J_{1/2}$ (MeV)	$L_{1/2}$ (MeV)	$K_{1/2}$ (MeV)
SLY4 [Cha98]	22.13	38.6	-74.0
SkI3 [Rei95]	18.85	46.7	-25.2
SGI [Gia81]	16.75	38.4	-29.7
LNS [Cao06b]	21.10	44.6	-56.8

Table III–1: Surface nuclear properties for the different Skyrme interactions examined in this chapter.

Concerning the LNS interaction, we recall that the parametrization proposed in ref. [Cao06b] corresponds to a too high saturation density which is not realistic. This induces a trivial deviation with respect to the other interactions in both the bulk and surface isovector components. For this reason, only the isovector properties of this functional are of interest for this study.

A more complete study of the effective interactions parameter space would be necessary to reach sound conclusions on the quantitative model dependence, but from the representative chosen interactions, we can already dress some qualitative interpretations.

The bulk energy per nucleon is shown in the upper panel of fig. III–15. At low asymmetries, the curves are indistinguishable reflecting the good present knowledge of symmetric nuclear matter properties. The only exception is given by LNS, which presents a global shift with respect to the other functionals. As already remarked, this is due to the unrealistically high saturation density of this parametrization (tab. II–3). However, we can see that the behaviour with isospin is comparable to the one of the other functionals, reflecting a compatible bulk symmetry energy. For the highest asymmetries  $\delta \gtrsim 0.25$ , we can see that all the parametrizations differ, which reflects the larger uncertainties for asymmetric matter.

The lower panel of figure III–15 displays the surface corrections. We can see that the qualitative behaviour of the different models is the same:  $E_s/A$  increases with the asymmetry, leading to a positive sign of the corresponding symmetry energy, because of the bulk isospin asymmetry  $\delta$ , as discussed previously. The increase rate with isospin is not the same in the different models, reflecting the different surface symmetry energies of the functionals. In particular, the steep behaviour predicted by the SkI3 parametrization is due to the stiff isovector properties of this effective interaction (see  $L_{sym}$  and  $K_{sym}$  in tab. II–3), which lay close to the higher border of the presently accepted values for these parameters [EPJ14]. Moreover, the four considered interactions predict very different values of  $E_s$ . In particular, at  $\delta = 0$  for which the SLy4, SkI3 and SGI models are in perfect agreement on the bulk energy, they however differ from  $\sim 500$  keV per nucleon on the surface energies. We will come back to this surprising result later in this section.

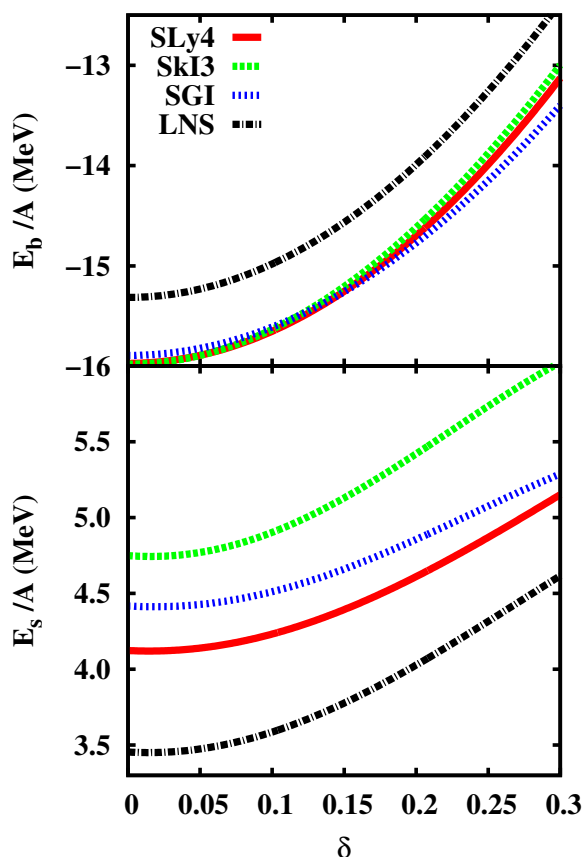


Figure III–15: Bulk (upper panel) and surface (lower panel) energy per nucleon as a function of the bulk asymmetry  $\delta$  for isobaric nuclei  $A = 100$ , predicted by eq. (III.79). Different Skyrme interactions are considered: SLy4 [Cha98] (full red), SkI3 [Rei95] (dashed green), SGI [Gia81] (dotted blue), LNS [Cao06b] (dashed-dotted black). Figure published in [Aym15].

Fig. III–16 shows the energy decomposition of eqs. (III.81) and (III.82). As expected, at  $\delta = 0$ , though not identically zero (see eq. (III.76)), the isovector energy (lower panel) is completely negligible. This a-posteriori justifies the assumption  $E_s^{IV}(0) = 0$  we made in order to obtain  $a_0$  in eq. (III.72). However, for asymmetric systems, though smaller than the isoscalar energy (upper panel), the isovector energy cannot be neglected. Indeed, its dependence with  $\delta$  is much stronger, meaning that the isovector term is the most important term determining the surface symmetry energy. Concerning the mass independent term, we can see that it is negligible compared to the other components, as expected for the medium-heavy nucleus concerned by this picture. Finally, we can observe that the isovector energy is not quadratic with  $\delta$ , thus confirming that the linear terms of eq. (III.74) cannot be neglected.

Fig. III–17 shows the predictions of the different functionals concerning the parame-

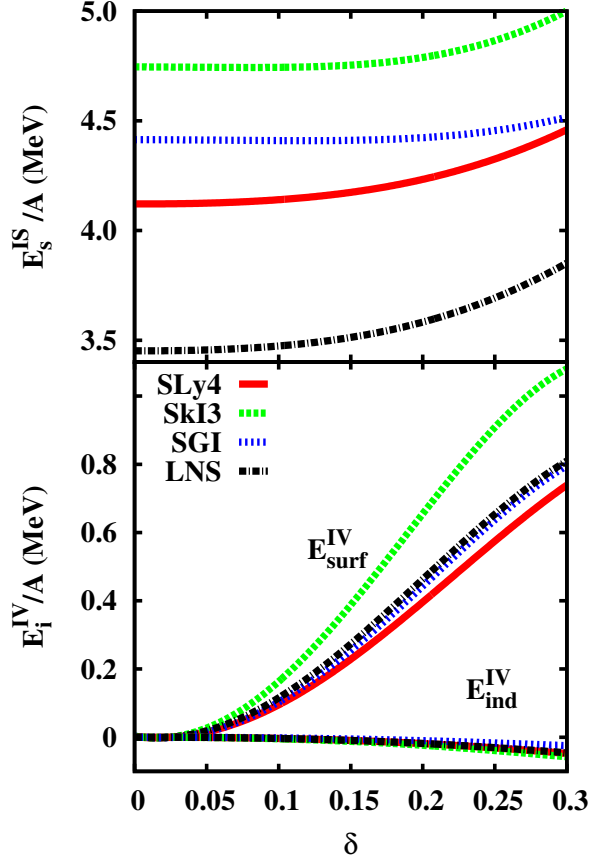


Figure III-16: Isoscalar (upper panel) and isovector (lower panel) surface energy per nucleon as a function of the bulk asymmetry  $\delta$  for isobaric nuclei  $A = 100$ , predicted by eq. (III.79). Different Skyrme interactions are considered: SLy4 [Cha98] (full red), SkI3 [Rei95] (dashed green), SGI [Gia81] (dotted blue), LNS [Cao06b] (dashed-dotted black). Figure published in [Aym15].

ters associated to the density profiles, namely the diffuseness (upper panel), the neutron skin (middle panel) and their ratio (lower panel). We can see that, for a given asymmetry  $\delta$ , the spread of the diffuseness values given by eq. (III.77) is very important, reflecting the poor knowledge of this quantity. These large uncertainties can be understood considering that the diffuseness does not seem to affect the energy in a systematic way. In particular, though SkI3 and SGI models surprisingly give the same diffuseness, the corresponding surface properties systematically differ. Moreover, this similarity of the diffuseness cannot be straightforwardly linked to any specific interaction property or parameter (see tabs. III-1 and II-3). This reflects again the fact that the diffuseness is a delicate balance of all energy components, and is determined by very subtle competing and opposite effects.

The middle part of the figure shows the obvious correlation between  $\Delta R = R - R_p$

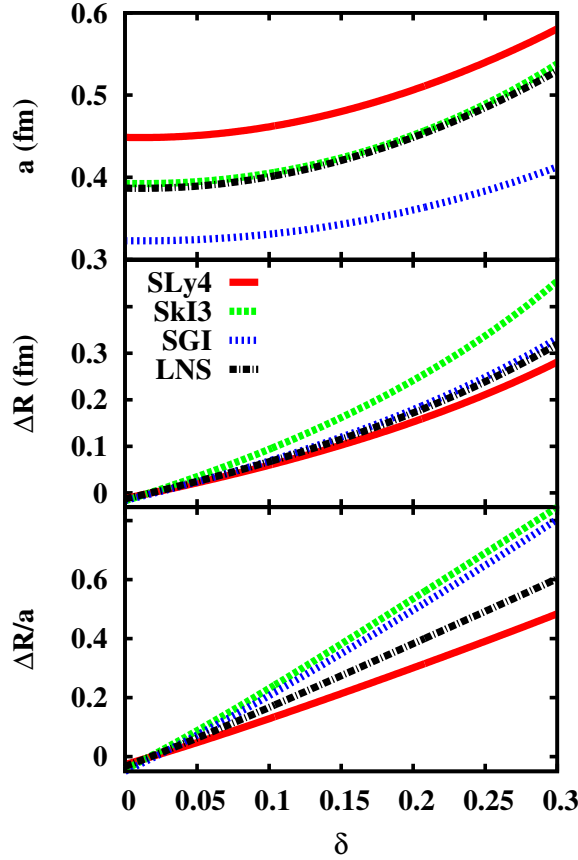


Figure III–17: Diffuseness  $a$  (upper panel), neutron skin thickness  $\Delta R$  (middle panel) and the ratio  $\Delta R/a$  (lower panel) as a function of the bulk asymmetry  $\delta$  for the isobaric chain  $A = 100$ , predicted within the Gaussian approximation (see text). Different Skyrme interactions are considered: SLy4 [Cha98] (full red), SkI3 [Rei95] (dashed green), SGI [Gia81] (dotted blue), LNS [Cao06b] (dashed-dotted black). Figure published in [Aym15].

and  $\delta$ . It is clear from this behavior that quadratic terms in the neutron thickness cannot be neglected to correctly estimate the symmetry energy (see eq. (III.74)). It is interesting to observe that the SGI and LNS models give very close results for this quantity, and the same was true for the isovector part of the surface energy in figure III–16 above. This comes from the fact, already observed in the literature [EPJ14], that  $\Delta R$  is mainly determined by the slope of the symmetry energy  $L_{sym}$  [EPJ14] which are close in the SGI and LNS models. Our work confirms that the neutron thickness can be viewed as a measurement of the  $L_{sym}$  parameter. Indeed,  $\Delta R$  can be well approximated using the equivalent hard spheres radii  $R_{HS}(\delta)$ ,  $R_{HS,p}(\delta)$ , see eq. (III.70). This means that  $\Delta R$  can be seen as a function of the saturation density  $\rho_{sat}(\delta)$ . In turn, the saturation density is given by eq. (II.42) which at first order is quadratic in  $\delta^2$  with the coefficient

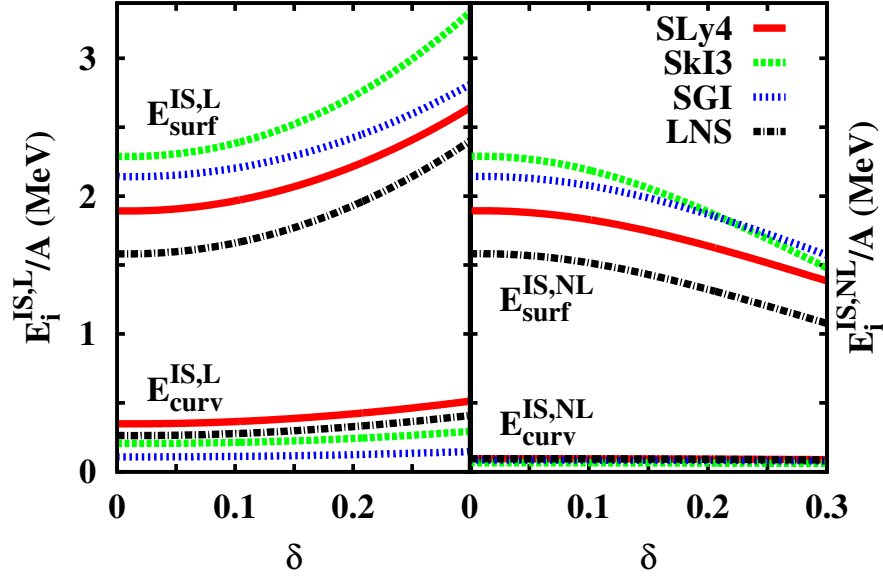


Figure III–18: Decomposition of the local (left) and non-local (right) part of the isoscalar surface energy per nucleon, into its surface and curvature component as a function of the bulk asymmetry  $\delta$  for the isobaric chain  $A = 100$ , as predicted by eq. (III.79). Different Skyrme interactions are considered: SLy4 [Cha98] (full red), SkI3 [Rei95] (dashed green), SGI [Gia81] (dotted blue), LNS [Cao06b] (dashed-dotted black). Figure published in [Aym15].

$L_{sym}/K_{sat}$ . Since  $K_{sat}$  is relatively well constrained, we then understand why  $\Delta R$  is mainly determined by  $L_{sym}$ . In particular, the neutron skin thickness is predicted to be the same in the two specific interactions SGI and LNS. Since the surface isovector energy eq. (III.74) at a given bulk asymmetry mainly depends on the neutron skin, this also explains why we obtain the same energies for the two models in fig. III–16.

This essential role of  $\Delta R$  to determine the symmetry energy is confirmed observing from fig. III–16 and III–17 that Skyrme models which predict thicker neutron skin, that is higher  $L_{sym}$ , give systematically larger values of the isovector surface energy.

The lower part of figure III–17 shows the ratio  $\Delta R/a$  as a function of  $\delta$ . Though it is the quantity which mainly governs the behavior of eq. (III.74), it does not constrain the surface isovector energy  $E^{IV}$ . Indeed, same  $\Delta R/a$  from the functionals SkI3 and SGI lead to different energies (fig. III–16, lower panel), corroborating the above discussion: only the  $L_{sym}$  parameter, or equivalently the neutron skin thickness  $\Delta R$ , is relevant to determine the isovector contribution. This stresses the importance of the experimental measurement of neutron skin thickness as a key quantity for the knowledge of the density dependence of the symmetry energy [EPJ14].

To conclude, we study in figure III–18 the decomposition into local and non-local terms as predicted by the different functionals. Only the isoscalar part of the surface energy is considered because these different terms are mixed up in the Gaussian approximation we have employed for the isovector component.

Again, we can see that the qualitative behavior of the different Skyrme models is the same for each specific term. We can then safely conclude that the non-local curvature component  $E_{curv}^{IS,NL}$  can be neglected for medium-heavy nuclei  $A \gtrsim 100$ , but the local curvature energy has to be taken into account since it represents for these nuclei 10% to 25% of the total surface local energy, depending on the interaction choice and on the asymmetry  $\delta$ .

Concerning the  $\delta$  dependence of the isoscalar surface energies in fig. III–18, we can notice that the local and non-local parts have opposite behaviors, leading to the rather flat curves observed in fig. III–16, upper panel. In section III.1.3, we have shown that the exact equality  $E_{surf}^{IS,L} = E_{surf}^{IS,NL}$  (eq.(III.33)) is obtained only if both curvature and isovector terms are neglected in the determination of the diffuseness. However, the neglect of isovector terms leads to a wrong dependence with  $\delta$  as shown in fig. III–6. Thus, isovector terms cannot be avoided.

The results of figure III–18 clearly show that, once these terms are consistently added in the variational procedure (eq. (III.77)), the equality  $E_{surf}^{IS,L} = E_{surf}^{IS,NL}$  is completely violated for asymmetric systems. Therefore the isoscalar energy strongly depends on the neutron skin thickness, even if it is an indirect dependence through the diffuseness. This shows that, though the energy can be splitted into different terms, these latter cannot be decorrelated and have to be treated altogether.

We have already observed in figure III–15 that the different functionals predict very different surface energy at  $\delta = 0$ , which might be surprising considering that the symmetric nuclear properties are supposed to be well constrained by experimental data. An obvious interpretation would be that the discrepancy comes from the surface properties, that is the non-local gradient terms and the (poorly constrained) diffuseness parameter. However, comparing the different values of the predicted diffuseness at  $\delta = 0$  from Figure III–17, we can see that  $a_{SGI} < a_{LNS} = a_{SkI3} < a_{SLy4}$ . This inequality sequence is not respected for the surface energy  $E_{surf}(\delta = 0)$  in fig. III–18, meaning that the difference of surface energies cannot be ascribed to the diffuseness.

The possible dependence on the couplings of gradient and spin-orbit terms is also excluded. Indeed, we can see from figure III–18 that at  $\delta = 0$ , the isovector part is zero by definition and therefore the equality  $E_{surf}^{IS,L} = E_{surf}^{IS,NL}$  is verified. This means that the total surface energy for symmetric bulk is  $E_{surf} = 2E_{surf}^{IS,L}$ , which does not depend on the non-local terms of the functional, but only depends on the bulk interaction coefficients  $(\rho_{sat}(0), C_0, C_3, C_{eff}, \alpha)$  according to eqs. (III.12)-(III.14).

We can conclude that the differences of the total surface energies observed for  $\delta = 0$ , that is nuclei very close to isospin symmetry, in figure III-15, does not come from the non-local properties but are intrinsically linked to the bulk interaction coefficients ( $C_0, C_3, C_{eff}, \alpha$ ), though the SLy4, SkI3 and SGI models correspond to compatible isoscalar equations of state (that is: compatible values for the saturation density  $\rho_{sat}(0)$ , bulk energy  $E_b(\delta = 0)$ , compressibility  $K_{sat}$  and effective mass). This shows that, at variance with the skin thickness  $\Delta R$  which is strongly correlated to the isovector equation of state, the nuclear surface energy very poorly constrains the equation of state, even for symmetric or quasi-symmetric nuclei.

## Chapter III.3

# Clusters embedded in a nucleon gas

We now turn to the more general problem of clusters embedded in a nucleon gas. As for nuclei, the bulk energy of the Wigner-Seitz cells is analytical so we focus on the in-medium surface energy  $E_{s,m}$  defined in part II by eq. (II.65), which we recall:

$$E_{s,m}(A, \delta, \rho_g, \delta_g) = 4\pi \int dr r^2 \mathcal{H}[\rho(r), \rho_3(r)] - \mathcal{H}[\rho_{sat}(\delta), \rho_{sat,3}(\delta)] V_{HS} - \mathcal{H}[\rho_g, \rho_g \delta_g] (V_{WS} - V_{HS}), \quad (\text{III.86})$$

with  $\rho$  ( $\rho_3$ ) the total isoscalar (isovector) density profile, that is the sum of the cluster and the gas densities. Using the r-cluster definition for the decomposition of the total densities (eqs. (II.58), (II.60)), it is natural to sort out of this expression the surface contribution  $E_s^{cl}$  of the in-vacuum nucleus investigated in the previous chapter III.2:

$$E_{s,m} = E_s^{cl} + E_s^g + \delta E_s', \quad (\text{III.87})$$

with

$$E_s^{cl} = 4\pi \int dr \mathcal{H}[\rho_r^{cl}, \rho_{3,r}^{cl}] r^2 - \mathcal{H}[\rho_{sat}(\delta), \rho_{sat,3}(\delta)] V_{HS}, \quad (\text{III.88})$$

$$E_s^g = 4\pi \int dr \mathcal{H}[\rho_r^{gas}, \rho_{3,r}^{gas}] r^2 - \mathcal{H}[\rho_g, \rho_g \delta_g] (V_{WS} - V_{HS}), \quad (\text{III.89})$$

$$\delta E_s' = 4\pi \int dr \delta \mathcal{H}[\rho, \rho_3] r^2. \quad (\text{III.90})$$

In the latter equation, we have defined the extra surface energy density due to the interaction between the cluster and the gas as follows

$$\delta \mathcal{H}[\rho, \rho_3] = \mathcal{H}[\rho, \rho_3] - \mathcal{H}[\rho_r^{cl}, \rho_{3,r}^{cl}] - \mathcal{H}[\rho_r^{gas}, \rho_{3,r}^{gas}], \quad (\text{III.91})$$

with  $\rho_{3,r}^i = \rho_r^i - 2\rho_{p,r}^i$ , and

$$\rho_r^{cl}(r) = \rho_{sat}(\delta)F(r) = \rho_{sat}(\delta) \left[1 + e^{(r-R)/a}\right]^{-1}, \quad (\text{III.92})$$

$$\rho_r^{gas}(r) = \rho_g \tilde{F}(r) = \rho_g(1 - F(r)) = \rho_g \left[1 + e^{-(r-R)/a}\right]^{-1}. \quad (\text{III.93})$$

Let us notice that, since the surface energy of the gas is included in  $E_s^g$ , the interaction energy  $\delta E'_s$  is not the same as the term  $\delta E_s$  studied in part II.

Obtaining an analytical expression for the WS cell energy eq. (III.87) is a very challenging task. Indeed, we have to analytically approximate each component eqs (III.88)-(III.90). This is a work in progress and consequently, though this chapter gives some approximated general formulae for the total in-medium surface energy, their relevance and accuracy have not been verified yet, and full transparent expressions which may turn up still need to be developed.

The in-vacuum cluster surface energy  $E_s^{cl}$  eq. (III.88) is discussed in section III.3.1. More specifically, we show that we need to reconsider the approach presented in the previous chapter III.2, and use a more sophisticated Gaussian approximation for the isovector energy part of nuclei far beyond drip lines which exist in compact stars. In section III.3.2, we focus on the surface energy of the nucleon gas  $E_s^g$  eq. (III.89) which may be treated with the same approximations used for nuclei in vacuum. At last, the expression for the surface interaction between the cluster and the gas  $\delta E'_s$  eq. (III.90) is developed in section III.3.3 in the case of a symmetric gas.

### III.3.1 Nuclei beyond the drip lines

In chapter III.2, we have considered in-vacuum nuclei only, that is we have verified that our approximations are relevant up to the drip lines,  $\delta \lesssim 0.3$ . However, when embedded in a nucleon gas, the r-clusters can be far beyond, and consequently we need to reinvestigate the validity of the approximated expressions of  $E_s^{cl} = E_s^{IS} + E_s^{IV}$  eqs. (III.44) and (III.61) developed in chap. III.2.

Concerning the isoscalar part, since the results obtained in section III.1.3 are exactly calculated, eqs. (III.45)-(III.47) can be safely extrapolated to any cluster asymmetry, including beyond drip lines. Thus, a large part of the symmetry energy is exactly taken into account.

The approximations developed for the isovector component however have to be reconsidered. Indeed, because of the increasing neutron skin with asymmetry, the isovector energy density profile is modified, as it can be seen in fig. III-19 (red full curves), where clusters at  $\delta = 0.6$  are considered. The negative components are larger, and the profile

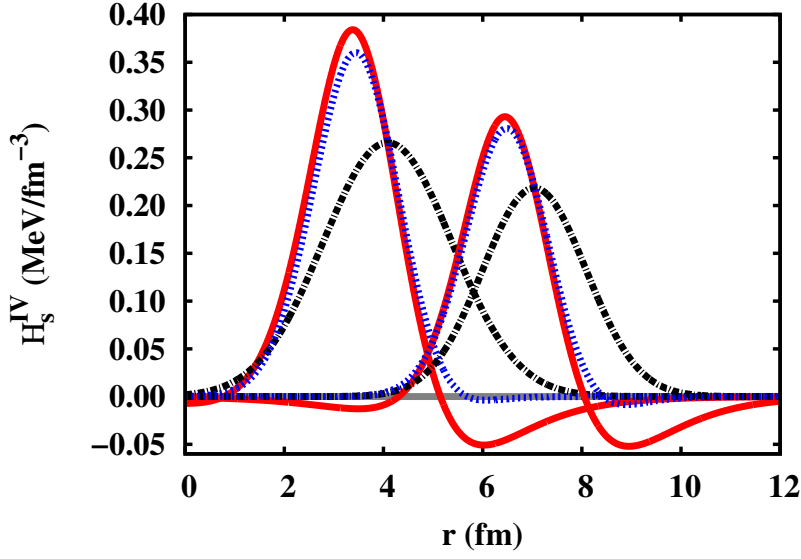


Figure III-19: Numerical isovector energy density profile (red full lines) and Gaussian approximation evaluated at  $r = R$  (black dashed-dotted lines) and at  $r = R_M$  (blue dotted lines), for two masses  $A = 50$  (left curves) and  $A = 200$  (right curves) both at  $\delta = 0.6$ .

is not peaked at the nuclear surface  $r = R$  as it was for nuclei below drip lines, but it is shifted to a smaller radius  $r = R_M = R + \delta R$  ( $\delta R \leq 0$ ). Therefore the previous global Gaussian approximation (black dashed-dotted lines), for which both the amplitude and the variance are evaluated at  $r = R$ , fails to reproduce the correct energy density profile. The corresponding integrated energy is therefore largely overestimated.

To improve the approximation, a natural choice is thus to evaluate the Gaussian at the maximum  $R_M$  of the isovector energy density profile, given by

$$0 = \frac{d}{dr} \mathcal{H}_s^{IV}[\rho_r^{cl}(r), \rho_{3,r}^{cl}(r)] \Big|_{r=R_M} \quad (\text{III.94})$$

$$\begin{aligned} &= \left( \frac{\partial \mathcal{H}_s^{IV}}{\partial \rho} \nabla \rho_r^{cl} \right) \Big|_{r=R_M} + \left( \frac{\partial \mathcal{H}_s^{IV}}{\partial \rho_3} \nabla \rho_{3,r}^{cl} \right) \Big|_{r=R_M} \\ &+ \left( \frac{\partial \mathcal{H}_s^{IV}}{\partial \nabla \rho} \frac{d^2}{dr^2} \rho_r^{cl} \right) \Big|_{r=R_M} + \left( \frac{\partial \mathcal{H}_s^{IV}}{\partial \nabla \rho_3} \frac{d^2}{dr^2} \rho_{3,r}^{cl} \right) \Big|_{r=R_M}. \end{aligned} \quad (\text{III.95})$$

In order to analytically solve this equation, we can make an expansion around  $R$  of the Fermi functions entering the particle density profiles, assuming the shift small enough, that is  $\delta R/a \ll 1$  and  $\delta R/a_p \ll 1$ . To the second order, the Fermi functions  $F$  of the total particle density profile and  $F_p$  of the proton particle density profile read:

$$F(R_M) = \frac{1}{2} \left[ 1 - \frac{1}{2} \frac{\delta R}{a} \right], \quad (\text{III.96})$$

$$F_p(R_M) = \frac{1 - \tanh^2(\Delta R/a_p)}{2} \left[ 1 - \frac{1 + \tanh(\Delta R/a_p)}{2} \frac{\delta R}{a_p} + \frac{1 + \tanh(\Delta R/a_p)}{4} \tanh(\Delta R/a_p) \left( \frac{\delta R}{a_p} \right)^2 \right], \quad (\text{III.97})$$

with  $\Delta R = R - R_p$  the neutron skin. With these equations, and using the Fermi derivative properties  $F' = -F(1-F)/a$ ,  $F'' = -F'(1-2F)/a$ , the shift  $\delta R$  defined by eq. (III.95) amounts to solve a 2<sup>nd</sup> polynomial equation  $\alpha_2(\delta R)^2 + \alpha_1\delta R + \alpha_0 = 0$ , from which the shift can be analytically expressed as  $\delta R = \left[ -\alpha_1 - \sqrt{\alpha_1^2 - 4\alpha_2\alpha_0} \right] / (2\alpha_2)$ . Let us notice that though analytical, the expressions of the coefficients  $\alpha_i$  are far from being transparent, as one can see in appendix C.

With the determination of the energy density profile maximum, we can generalize the Gaussian approximation previously developed in chapter III.2

$$\mathcal{H}_s^{IV}(r) \simeq \mathcal{G}(r) = \mathcal{A}_M(A, \delta) \exp\left(-\frac{(r - R_M)^2}{2\sigma_M^2(A, \delta)}\right), \quad (\text{III.98})$$

where  $\mathcal{A}_M$  and  $\sigma_M^2$  are the amplitude and the variance of the Gaussian defined at the point  $r = R_M$ . The profile based on this Gaussian approximation is displayed in figure III-19 (blue dotted lines) for very asymmetric nuclei. We can see that taking into account the shift  $\delta R \neq 0$  greatly improves the density profile (cf. black dashed-dotted lines for comparison) though the negative components are still not reproduced.

For completeness, we give the isovector energy obtained in integrating the Gaussian profile eq. (III.98), according to appx B:

$$E_s^{IV} = 2(2\pi)^{3/2} \sigma_M \mathcal{A}_M r_{sat}^2 \left[ A^{2/3} + 2 \frac{\delta R}{r_{sat}} A^{1/3} + \frac{\sigma_M^2}{r_{sat}^2} - \frac{2\pi^2}{3} \left( \frac{a}{r_{sat}} \right)^2 + \left( \frac{\delta R}{r_{sat}} \right)^2 - \frac{2\pi^2}{3} \frac{\delta R}{r_{sat}} \left( \frac{a}{r_{sat}} \right)^2 A^{-1/3} + O\left( \left( \frac{a}{r_{sat}} \right)^4 A^{-2/3} \right) \right]. \quad (\text{III.99})$$

We can notice that we find a curvature term  $\propto A^{1/3}$  previously neglected in assuming  $\delta R = 0$ .

### III.3.2 Nucleon gas

In this section, we briefly give the formulas for the surface energy of the gas  $E_s^g$  defined by eq. (III.89), where the gas density profile is describe by a reverse Fermi functions  $\tilde{F} = 1 - F$  eq. (III.93). This problem is thus similar to the in-vacuum clusters previously studied, with the saturation density  $\rho_{sat}$  ( $\rho_{sat,3}$ ) replaced by  $\rho_g$  ( $\delta_g \rho_g$ ) and with the

variable change  $r' = -r + 2R$ . Therefore, similarly to chapter III.2, we can decompose the gas surface energy  $E_s^g$  into isoscalar and isovector terms.

The isoscalar energy can be exactly calculated, as for nuclei, at any asymmetry  $\delta$ , and its local and non-local components read

$$E_s^{g,L} = \left[ \mathcal{C}_{surf}^L \frac{a}{r_{sat}} A^{2/3} - \mathcal{C}_{curv}^L \left( \frac{a}{r_{sat}} \right)^2 A^{1/3} + \mathcal{C}_{ind}^L \left( \frac{a}{r_{sat}} \right)^3 \right] \frac{\rho_g}{\rho_{sat}}, \quad (\text{III.100})$$

$$E_s^{g,NL} = \frac{1}{a^2} \left[ \mathcal{C}_{surf}^{NL} \frac{a}{r_{sat}} A^{2/3} - \mathcal{C}_{curv}^{NL} \left( \frac{a}{r_{sat}} \right)^2 A^{1/3} + \mathcal{C}_{ind}^{NL} \left( \frac{a}{r_{sat}} \right)^3 \right] \frac{\rho_g}{\rho_{sat}}, \quad (\text{III.101})$$

where the coefficients  $\mathcal{C}_i^{L(NL)}$  are given by eqs. (III.12)-(III.17), with  $\rho_{sat}(\delta)$  replaced by  $\rho_g$ . The expressions eqs. (III.100), (III.101) depend on the bulk nuclear asymmetry  $\delta$  because of the dependence of the diffuseness  $a$  and of the saturation density (radius)  $\rho_{sat}$  ( $r_{sat}$ ). The general mass dependence of  $E_s^{g,L(NL)}$  comes from the fact that the surface energy is localized around the same nuclear surface  $r \approx R$  as the nucleus. The expression of  $R$  as a function of the mass  $A$  is also responsible for the additional global factor  $\rho_g/\rho_{sat}(\delta)$ . Since the plane surface energy  $\propto A^{2/3}$  is the surface energy of the 1-dimensional semi-infinite matter (modified by a form factor, see sec. III.1.1), it is natural that we obtain the same expression for a Fermi function or a reverse one. The curvature  $\propto A^{1/3}$  and mass-independent terms are respectively the first and second moment of semi-infinite matter (see appx. A.2, eq. (A.7)). Therefore, the reverse Fermi implying the variable change  $x' = -x$  gives the curvature component with an opposite sign and the same mass-independent energy in eqs. (III.100), (III.101) as in eqs. (III.10), (III.11).

For the isovector energy part  $E_s^{g,IV}$ , the Gaussian approximations developed in sec. III.2 and III.3.1 might be applied. Indeed, though the gas can be made of neutrons only, meaning that its asymmetry  $\delta_g = 1$  can be far from the asymmetry of the clusters, its density  $\rho_g$  replacing the saturation density  $\rho_{sat}(\delta)$  is lower. This low density reduces the values of this energy part and so the error made in approximating it should be reduced as well. A quantitative study on this isovector energy is left for future work.

### III.3.3 In-medium interactions

In this section, we only consider symmetric matter. The generalization to asymmetric matter, and in particular to different asymmetry between the cluster and the gas, is left for future work. In the case of symmetric matter, the interaction energy  $\delta E_s'$  eq. (III.90) can be evaluated with a non-perturbative expansion around  $\rho_r^{cl}(r)$  of the corresponding

energy density  $\delta\mathcal{H}[\rho]$ :

$$\begin{aligned}
\delta\mathcal{H}[\rho] &= \mathcal{H}[\rho] - \mathcal{H}[\rho_r^{cl}] - \mathcal{H}[\rho_r^{gas}] \\
&= \sum_{\ell=1} \frac{(\rho_r^{gas})^\ell}{\ell!} \frac{\partial^\ell \mathcal{H}[\rho]}{\partial \rho^\ell} \Big|_{\rho_r^{gas}=0} \left\{ \left( \frac{\partial \rho}{\partial \rho_r^{gas}} \right)^\ell - \left( \frac{\partial \rho_r^{cl}}{\partial \rho_r^{gas}} \right)^\ell - \left( \frac{\partial \rho_g}{\partial \rho_r^{gas}} \right)^\ell \right\} \\
&\quad + \frac{(\nabla \rho_r^{gas})^\ell}{\ell!} \frac{\partial^\ell \mathcal{H}[\rho]}{\partial \nabla \rho^\ell} \Big|_{\rho_r^{gas}=0} \left\{ \left( \frac{\partial \nabla \rho}{\partial \nabla \rho_r^{gas}} \right)^\ell - \left( \frac{\partial \nabla \rho_r^{cl}}{\partial \nabla \rho_r^{gas}} \right)^\ell - \left( \frac{\partial \nabla \rho_r^{gas}}{\partial \nabla \rho_r^{gas}} \right)^\ell \right\} \\
&\quad + \frac{(\Delta \rho_r^{gas})^\ell}{\ell!} \frac{\partial^\ell \mathcal{H}[\rho]}{\partial \Delta \rho^\ell} \Big|_{\rho_r^{gas}=0} \left\{ \left( \frac{\partial \Delta \rho}{\partial \Delta \rho_r^{gas}} \right)^\ell - \left( \frac{\partial \Delta \rho_r^{cl}}{\partial \Delta \rho_r^{gas}} \right)^\ell - \left( \frac{\partial \Delta \rho_r^{gas}}{\partial \Delta \rho_r^{gas}} \right)^\ell \right\},
\end{aligned} \tag{III.102}$$

where the total density of the Wigner-Seitz cell can be expressed as a function of the Fermi function  $F$  only:  $\rho(r) = \rho_{sat}F(r) + \rho_g\tilde{F}(r) = (\rho_{sat} - \rho_g)F(r) + \rho_g$ . Then, using  $\partial/\partial\rho_r^{gas} = -1/\rho_g \cdot \partial/\partial F$ ,  $\partial/\partial\nabla\rho_r^{gas} = -1/\rho_g \cdot \partial/\partial\nabla F$  and  $\partial/\partial\Delta\rho_r^{gas} = -1/\rho_g \cdot \partial/\partial\Delta F$ , eq. (III.102) reads

$$\begin{aligned}
\delta\mathcal{H}[\rho] &= \sum_{\ell=1} \frac{1}{\ell!} \left( (\rho_r^{gas})^\ell \frac{\partial^\ell \mathcal{H}}{\partial \rho^\ell} \Big|_{\rho_r^{gas}=0} + (\nabla \rho_r^{gas})^\ell \frac{\partial^\ell \mathcal{H}}{\partial \nabla \rho^\ell} \Big|_{\rho_r^{gas}=0} + (\Delta \rho_r^{gas})^\ell \frac{\partial^\ell \mathcal{H}}{\partial \Delta \rho^\ell} \Big|_{\rho_r^{gas}=0} \right) \\
&\quad \left\{ \left( 1 - \frac{\rho_{sat}}{\rho_g} \right)^\ell - \left( -\frac{\rho_{sat}}{\rho_g} \right)^\ell - 1 \right\} \\
&= \sum_{\ell=2} \frac{1}{\ell!} \sum_{k=1}^{\ell-1} \binom{\ell}{k} (-1)^k \rho_{sat}^k \rho_g^{\ell-k} \cdot \\
&\quad \cdot \left( \tilde{F}^\ell \frac{\partial^\ell \mathcal{H}}{\partial \rho^\ell} \Big|_{\rho_r^{gas}=0} + (\nabla \tilde{F})^\ell \frac{\partial^\ell \mathcal{H}}{\partial \nabla \rho^\ell} \Big|_{\rho_r^{gas}=0} + (\Delta \tilde{F})^\ell \frac{\partial^\ell \mathcal{H}}{\partial \Delta \rho^\ell} \Big|_{\rho_r^{gas}=0} \right). \tag{III.103}
\end{aligned}$$

Let us notice that the first non-zero order is as expected the second order  $\ell = 2$ , since we have taken away the linear part in the definition of  $\delta\mathcal{H}$ . Since the Skyrme energy density eq. (II.15) used to evaluate  $\mathcal{H}$  has only linear Laplace terms, the third derivatives term of eq. (III.103) vanish. Similarly, because the energy density is quadratic with the gradient density, the gradient terms are only non-zero at the second order of  $\rho_r^{gas}(r)$ . Therefore eq. (III.103) is simplified as

$$\delta\mathcal{H}[\rho] = \sum_{\ell=2} \frac{1}{\ell!} \sum_{k=1}^{\ell-1} \binom{\ell}{k} (-1)^k \rho_{sat}^k \rho_g^{\ell-k} \tilde{F}^\ell \frac{\partial^\ell \mathcal{H}}{\partial \rho^\ell} \Big|_{\rho_r^{gas}=0} - \rho_{sat} \rho_g \nabla \tilde{F}^2 \frac{\partial^2 \mathcal{H}}{\partial \nabla \rho^2} \Big|_{\rho_r^{gas}=0}. \tag{III.104}$$

Integrating eq. (III.104) leads to the interaction energy

$$\delta E'_s = \sum_{\ell} \delta E_{s-\ell}, \quad (\text{III.105})$$

with  $\delta E_{s-\ell}$  the  $\ell$ th order of the extra surface energy. The first term  $\ell = 2$  reads:

$$\begin{aligned} \delta E_{s-2} = & -\frac{4\pi}{9} \rho_g \int_0^\infty dr \frac{[1-F(r)]^2}{F(r)} \left( K[\rho_r^{cl}(r)] + 6L[\rho_r^{cl}(r)] \right) r^2 \\ & - 4\pi \rho_{sat} \rho_g \int_0^\infty dr \nabla F(r)^2 \frac{\partial^2 \mathcal{H}}{\partial \nabla \rho^2} [\rho_r^{cl}(r)] r^2, \end{aligned} \quad (\text{III.106})$$

with  $L[\rho] = 3\rho \partial(h/\rho)/\partial\rho$  and  $K[\rho] = 9\rho^2 \partial^2(h/\rho)/\partial\rho^2$  the slope and compressibility at a density  $\rho$ .

The next term  $\ell = 3$  is

$$\delta E_{s-3} = -\frac{2\pi}{27} \rho_g \left( 1 - \frac{\rho_g}{\rho_{sat}} \right) \int_0^\infty dr \frac{[1-F(r)]^3}{F(r)^2} \left( Q[\rho_r^{cl}(r)] + 9K[\rho_r^{cl}(r)] \right) r^2, \quad (\text{III.107})$$

with  $Q[\rho] = 27\rho^3 \partial^3(h/\rho)/\partial\rho^3$ . Let us notice that, as expected, the integrand of the interaction energy eqs. (III.106), (III.107) are peaked functions. Using appendix A, we can analytically express the extra surface energy  $\delta E_{s-\ell}$  since they are integrals of the isoscalar density  $\rho$  only.

For asymmetric gas, we can decompose as previously the energy density  $\mathcal{H}$  into an isoscalar part which is analytically given by the previous formulae (with  $\rho_{sat}$  depending on  $\delta$ ), and an isovector component. The study of this residual energy part is left for future work.

# Part conclusions

In this part, we have addressed the problem of the determination of an analytical mass formula with coefficients directly linked to the different parameters of standard Skyrme functionals, in the Extended-Thomas-Fermi (ETF) approximation at second order in  $\hbar$ . The purpose of this effort is twofold. On one side, such a formula is useful for astrophysical applications where extended calculations are needed covering the whole mass table and using a variety of effective interaction to assess the sensitivity of astrophysical observables to the nuclear physics inputs [Com13]. On the other side, analytical expressions of the different coefficients of the mass formula in terms of the Skyrme couplings allow a better understanding of the correlation between these couplings and the different aspects of nuclear energetics, for the construction of optimized fitting procedures of the functionals.

The modelling of Fermi density profiles has allowed an (almost) exact analytical evaluation of the isoscalar part of the nuclear energy, naturally leading to the appearance in the surface energy of a curvature term and a constant term independent of the baryonic number. The diffuseness of the density profile has been variationally calculated within the same formalism, and a simple analytical expression has been given. The relative importance of local and non-local terms has been studied in detail. Non-local energy components arise both from gradient and spin-orbit in the Skyrme functional, and from the higher  $\hbar$  terms in the Wigner-Kirkwood expansion of the kinetic energy. We have shown that in the limit of semi-infinite matter the isoscalar surface energy is  $\propto A^{2/3}$  and solely depends on the local terms. This remarkable property already observed in ref. [Tre86] is however violated in finite nuclei even if spherical symmetry is assumed, and both components contribute in a complex way to the determination of the surface energy. However, the huge dispersion observed on the value of the surface tension for symmetric nuclei in modern Skyrme functionals is essentially due to the local couplings, even if these different functionals correspond to comparable saturation properties of symmetric nuclear matter. This finding means that nuclear matter properties are not sufficient to pin down surface properties of finite nuclei even in the symmetric case.

The extension to isospin asymmetric nuclei is highly non-trivial. No exact analytical

integration of the ETF functional is possible in the presence of isospin inhomogeneities, and approximations have to be done. We have proposed two different approximations for the determination of the surface symmetry energy. The first approximation consists in completely neglecting the difference between the neutron and proton radii, that is the neutron skin  $\Delta R$ . The resulting surface energy shows a quadratic dependence on the isospin asymmetry  $I$ , and consists of local and non-local plane surface, curvature and mass dependent terms which are simple generalizations of the expressions obtained for symmetric nuclei. Surprisingly, this crude approximation reproduces very well numerical Hartree-Fock results for all stable nuclei up to asymmetries of the order of  $I \approx 0.2$ , and leads to a relatively limited overestimation of the order of 400 keV per nucleon close to the drip lines.

A better approximation is obtained if isospin inhomogeneities are accounted for. To this aim, we have introduced a different radius for the neutron and proton distributions, as well as an explicit difference between the global asymmetry  $I$  and the asymmetry in the nuclear bulk  $\delta$ , due to both Coulomb and neutron skin effects. In this more general case, to obtain a mass formula we have made the assumption that the surface energy density is peaked at the nuclear surface, and curvature terms can be neglected. A reproduction of HF results within  $\sim 200$  keV per nucleon at the drip lines has been obtained, and simple expressions have been given for the surface energy and the surface diffuseness parameter. In particular we have shown that both linear and quadratic terms in  $\delta$  and  $\Delta R$  are needed to correctly explain the surface term. Moreover, within this analytical mass formula, we have shown that the neutron skin is essentially determined by the slope of the symmetry energy at saturation, thus confirming earlier numerical results from different groups [EPJ14]. Conversely, the surface symmetry energy has been shown to be due to a complex interplay of all different local and non-local terms in the energy functional. This implies that constraints on the symmetry energy parameters ( $J_{sym}, L_{sym}, K_{sym}$ ) from mass measurements might be model dependent and misleading.

As a further development of this work, we plan to extend the mass formula to the case of nuclei embedded in a nucleon gas. Some expressions have been developed and their validity needs to be verified and quantified.

# Résumé de la partie III

Afin d'implémenter dans le modèle en équilibre statistique nucléaire les effets de milieu étudiés dans la partie II, il est hautement souhaitable de disposer d'expressions analytiques des intégrales de Thomas-Fermi étendues. Le développement d'approximations systématiques pour intégrer analytiquement la fonctionnelle de Thomas-Fermi étendue dans le cas de la présence d'un gaz de nucléons est une question délicate. Par conséquent dans cette partie, nous nous sommes principalement concentrés sur des noyaux dans le vide, entre les ligne de limite de stabilité. La généralisation à l'énergie de la cellule de Wigner-Seitz a seulement été esquissée. De manière cohérente avec le reste de cette thèse, nous ne considérons que les fonctionnelles de Skyrme.

Comme nous l'avons déjà discuté, les fonctionnelles de Skyrme ont été largement utilisées pour décrire les propriétés de structure nucléaire, avec différents niveaux de sophistication dans le traitement à  $N$ -corps, du plus simple Thomas-Fermi [Bra85] à des calculs modernes multi-références [Was12]. La plus simple observable accessible au traitement fonctionnel est donné par la masse nucléaire, permettant l'analyse des différentes composantes de la masse en termes des propriétés de volume et de surface, ainsi que des propriétés isovectorielle et isoscalaires. La prédiction théorique de la masse nucléaire est non seulement importante en soi, mais c'est aussi un outil fondamental pour optimiser les différentes formes fonctionnelles et leurs paramètres associés, pour améliorer le pouvoir prédictif des calculs de la fonctionnelle de densité [Gor13]. En effet, les prédictions de masse par les fonctionnelles de densité sont aujourd'hui très précises et peuvent même égaliser la plus précise des formules de masse phénoménologiques disponibles dans la littérature [Liu11; Mol95; Duf95].

Pour les applications pratiques de la structure nucléaire ou les problèmes de l'astrophysique nucléaire, différentes paramétrisations des masses nucléaires ajustées sur des calculs de fonctionnelle de la densité avec les forces de Skyrme ont été proposées dans la littérature [Abo95; Dan09; Lee10; Nik11]. En particulier, nous avons utilisé dans la partie I celle proposé dans [Dan09]. La limitation de ces travaux est que les différents coefficients ne sont pas calculés analytiquement mais résultent de l'ajustement des masses nucléaires déterminées numériquement. En conséquence, l'ajustement doit être effectué

à nouveau à chaque fois que la fonctionnelle est améliorée, en ajoutant des contraintes supplémentaires à partir des données expérimentales. En outre, l'absence d'un lien analytique entre les paramètres de Skyrme et les coefficients de la formule de masse implique qu'aucune corrélation univoque entre les différentes parties de la masse fonctionnelle et les propriétés physiques de l'interaction effective ne puisse être établie. Pour ces raisons, il semble intéressant de rechercher une expression analytique des coefficients de la formule de masse, directement reliée à la forme fonctionnelle et aux paramètres de l'interaction de Skyrme. La dérivation d'une telle formule analytique a été l'objectif de cette partie.

Un formalisme particulièrement avenant lors de la recherche d'expressions analytiques est l'approche semi-classique Thomas-Fermi étendue, qui est basée sur un développement en puissances de  $\hbar$  de l'énergie fonctionnelle, comme présenté dans la partie II. Comme nous l'avons vu, l'avantage de cette approximation réside dans le fait que l'énergie fonctionnelle dépend uniquement des densités de particules et de leurs gradients, et que l'énergie d'une configuration nucléaire arbitraire peut être calculée si les profils de densité sont donnés par une forme paramétrée. D'autre part, la limitation bien connue de l'approximation Thomas-Fermi étendue est que seule la partie lisse de la masse nucléaire peut être modélisée : les effets de couches doivent être ajoutés a posteriori, par exemple par la méthode Strutinsky [Pea12]. Comme dans la partie II, nous avons examiné ici une expansion de l'approximation Thomas-Fermi jusqu'au second ordre  $\hbar^2$ , et nous nous sommes donc limités à la partie lisse de la fonctionnelle de masse.

La modélisation des profils de densité par des fonctions de Fermi a permis une évaluation analytique (presque) exacte de la partie isoscalaire de l'énergie nucléaire, conduisant naturellement à l'apparition dans l'énergie de surface d'un terme de courbure et d'un terme constant, indépendant du nombre baryonique. La diffusivité du profil de densité a été calculée variationnellement au sein du même formalisme, et une expression analytique simple a été donnée. L'importance relative des termes locaux et non-locaux a été étudiée en détail. Les constituants non-locaux de l'énergie découlent à la fois des gradients et du spin-orbite de la fonctionnelle de Skyrme, ainsi que des plus hauts termes en  $\hbar$  du développement de Wigner-Kirkwood de l'énergie cinétique. Nous avons montré que, dans la limite de la matière semi-infinie, l'énergie de surface isoscalaire est  $\propto A^{2/3}$  et dépend uniquement des conditions locales. Cette propriété remarquable a déjà été observée dans [Tre86], mais est cependant violée dans les noyaux finis, même en symétrie sphérique. Les deux composantes contribuent d'une façon complexe dans la détermination de l'énergie de surface. Cependant, la grande dispersion observée sur la valeur de la tension de surface pour les noyaux symétriques dans les fonctionnelles modernes de Skyrme est essentiellement due à des couplages locaux, même si ces différentes fonctionnelles correspondent à des propriétés similaires de matière nucléaire symétrique saturée. Cette constatation signifie que les propriétés de la matière nucléaire ne sont

pas suffisantes pour cerner les propriétés de surface des noyaux finis, même dans le cas symétrique.

L'extension à des noyaux asymétriques est hautement non-triviale. Les intégrales de Thomas-Fermi (étendu) ne sont pas analytiquement intégrables en présence d'inhomogénéités en isospin, et des approximations doivent donc être effectuées. Nous avons proposé deux approximations différentes pour la détermination de l'énergie de surface de symétrie. La première approximation consiste à négliger complètement la différence entre les rayons de neutron et de proton, c'est-à-dire l'épaisseur de la peau de neutrons  $\Delta R$ . L'énergie de surface résultante montre une dépendance quadratique en asymétrie d'isospin  $I$ , et se décompose en termes (locaux et non-locaux) de surface plane, de courbure, et indépendants de la masse ; ce sont de simples généralisations des expressions obtenues pour les noyaux symétriques. Étonnamment, cette grossière approximation reproduit bien les résultats numériques Hartree-Fock pour tous les noyaux stables jusqu'à des asymétries de l'ordre de  $I \approx 0.2$ , et conduit à une surestimation relativement limitée de l'ordre de 400 keV par nucléon près des lignes de limite de stabilité.

Une meilleure approximation est obtenue si les inhomogénéités en isospin sont prises en compte. Dans ce but, nous avons introduit un rayon différent pour les distributions de neutrons et de protons, ainsi qu'une différence explicite entre l'asymétrie globale  $I$  et l'asymétrie nucléaire de volume  $\delta$ , due aux effets de Coulomb et aux effets de peau de neutrons. Dans ce cas plus général, pour obtenir une formule de masse, nous avons fait l'hypothèse que la densité d'énergie de surface isovecteur est piquée à la surface nucléaire, et que les termes de courbure peuvent être négligés. Une reproduction des résultats Hartree-Fock à  $\sim 200$  keV par nucléon près, aux lignes de limite de stabilité, a été obtenue, et des expressions simples ont été données pour l'énergie de surface ainsi que pour le paramètre de diffusivité. En particulier, nous avons montré que les deux termes linéaires et quadratiques en  $\delta$  et  $\Delta R$  sont nécessaires pour expliquer correctement le terme de surface. En outre, dans cette formule analytique de masse, nous avons montré que la peau de neutrons est essentiellement déterminée par la pente de l'énergie de symétrie à la saturation, confirmant ainsi les résultats numériques antérieures de différents groupes [EPJ14]. Inversement, nous avons montré que l'énergie de symétrie de surface est due à une interaction complexe entre les différents termes locaux et non-locaux de la fonctionnelle d'énergie. Cela implique que les contraintes sur les paramètres d'énergie de symétrie ( $J_{sym}, L_{sym}, K_{sym}$ ) à partir de mesures de masse pourraient dépendre du modèle et donc être artificieuses.

Comme développement ultérieur de ce travail, nous prévoyons d'étendre la formule de masse pour le cas de noyaux immergés dans un gaz de nucléons. Certaines expressions ont été développées et leur validité doit être vérifiée et quantifiée.

# General Conclusions

The aim of this thesis has been to investigate the energy functional of clusters in interaction with a nucleon gas present in sub-saturated matter of supernovae and proto-neutron stars, in the Nuclear Statistical Equilibrium (NSE) framework.

We have considered a NSE model based on the grand-canonical partition sum that can be factorized into its leptonic, photonic, and baryonic components. Since the first ones are very well known, we have focussed on the baryonic sector. Under some assumptions on the Coulomb correlation length in the presence of a screening gas of electrons, this latter can naturally be factorized in independent Wigner-Seitz cell partition functions. In turn, they can be split into a homogeneous component and a cluster. To achieve this latter factorization, the interaction part between nuclei and nucleons must be treated as an in-medium modification of the cluster free energy. The general formalism of the NSE model has been introduced before by different authors in the literature [Eid80; Bot10; Hem10; Rad10; Bli11]. The original part of this thesis essentially consists in the energy modelling of the Wigner-Seitz cell. To model the large variety of clusters taken into account in the NSE, we have introduced quasi-analytical formulas for the different physical quantities entering the free energy. The cluster properties have been directly evaluated by experimental data when they exist. Since nuclei present in compact stars are beyond our experimental knowledge, extrapolated quasi-analytical formulas, consistent with the effective Skyrme interaction used for the homogeneous nucleon gas, are required. The determination of these formulas, and their application in thermodynamic conditions relevant for proto-neutron stars, has been the main subject of the thesis. We have realized this task with different levels of approximation, in the general framework of the (extended) Thomas-Fermi theory. The interaction between the clusters and the free particles, evaluated with the same Skyrme interaction is split in a bulk and a surface part. However, the mean-field entropy being known to give a very poor description of nuclear spectroscopy, the cluster excited states have been estimated on a realistic formula, fitted on a wealth of experimental data.

For the preliminary results shown in part I, only the bulk term has been included, and the nuclear binding energy has been modelled by a liquid-drop-like formula fitted on Skyrme HF calculations in a two-dimensional slab geometry, taken from [Dan09]. Most of the results we have obtained were done using the SLy4 effective interaction. Different conclusions were drawn from this study. First, we have shown that for  $\beta$ -equilibrated matter of proto-neutron star crust, the total proton fraction is mainly determined by the equilibrium condition itself, and therefore does not depend much on the details of the mass model. Concerning matter composition, we have seen that a bimodal cluster size distribution, presenting two comparable peaks corresponding to heavy and light clusters is systematically obtained in almost all thermodynamic conditions. The heavy cluster peak concerns clusters which are typically too neutron rich to be synthesized in the lab.

This means that a theoretical modelling is in order. On the other side, this modelling (based on different level of approximations of the mean-field theory) gives a poor reproduction of the light cluster energy and state density. This means that experimental information is also in order. As a consequence, NSE models need both experimental data and extrapolated parametrizations. The drawback of using two different prescriptions for the energy is that it does not correctly match. It results that for specific thermodynamic conditions where the matter composition corresponds to the limit of the two prescriptions, the model is not reliable and spurious effects in the distribution are present. We have also shown that a wide distribution of clusters survives even at very low temperatures, such that NSE models are required to realistically describe matter of proto-neutron star crust even at low temperatures  $T \sim 500$  keV. Though we did not consider a correct treatment of temperatures below the solid-gas transition temperature, where the entropy associated to the cluster center-of-mass momentum vanishes and vibrational as well as collective excitations are present, we have shown that at very low temperatures, temperature effects should not be neglected since the most probable cluster can change when decreasing temperature. Finally, we have found indications that light clusters are not systematically alpha particles but, because of the low proton fractions which are implied by beta-equilibrium, very asymmetric light resonances might be more favoured. This last conclusion should be taken with caution since the cluster surface in-medium modifications which are expected to be especially important for light nuclei at low temperatures have been disregarded. Moreover the separation itself of in-medium effects between a surface and a bulk component becomes increasingly questionable with decreasing cluster size, and global microscopically calculated in-medium energy shifts should be employed. Further investigations with improved models are highly desirable.

To evaluate the in-medium modifications of the surface tension, we have considered quasi-analytical Fermi nuclear density profiles allowing us to calculate nuclear binding energies within a semi-classical approximation, namely the Extended-Thomas-Fermi (ETF) at the second order in  $\hbar$ . We have verified that this model is sufficient for obtaining precision in the energy of the order of 100-200 keV per nucleon with respect to a complete Hartree-Fock calculation with the same energy functional.

With this model, we have extracted and evaluated the in-medium energy shift at zero temperature, which is experienced by a nucleus immersed in the gas of its continuum states. We have explicitly shown that the presence of an external gas induces both a bulk and a surface energy shifts, which validates the assumption made in our first applications. Both the bulk and the surface term were evaluated and shown to depend on a highly complex and non-linear way on the asymmetry of the cluster, and the asymmetry and density of the gas. The first preliminary results of the implementation of these effects at zero temperature and  $\beta$ -equilibrium show that the surface in-medium corrections may be

neglected when modelling neutron stars crust matter. However, since the absolute values of the energy shifts can be comparable or higher than the nuclear binding energy, the coexistence of nuclei and free particles in hot and/or out  $\beta$ -equilibrium stellar matter are not expected to be modelled as a mixture of non-interacting nuclear species. The most important conceptual result concerning the in-medium effects is that though the bulk energy shift corresponds to steric effects and therefore can be called “excluded volume”, this shift is due to the fact that the gas corresponds to cluster high energy states, in the continuum. As a results, it directly enters the energy in the statistical partition function such that it cannot be expressed as a classical Van der Waals as it is the case in other NSE models. It would be interesting to quantitatively compare results using our bulk energy shift prescription with the more standard excluded volume approximation.

With the same model, we have also explored the definition of the bulk and surface part of the symmetry energy of finite nuclei in vacuum, which is an important issue for devising nuclear mass formulas, as well as for the extraction of equation of state parameters for astrophysical applications. We have shown that the variational character of the ETF formalism suggests that the bulk part of the nuclear energy depends on the central bulk asymmetry  $\delta$  as assumed in the droplet models rather than on the global asymmetry of the nucleus  $I$  which is usually considered in the simpler Liquid Drop Models (LDM). This statement, which is confirmed by a detailed comparison to HF calculations, implies that the surface symmetry energy contributes positively to the total symmetry energy of the nucleus. The choice of the global asymmetry parameter  $I$  considered in LDM, while not consistent with ETF, can explain the ambiguities reported in the literature concerning the sign of the surface symmetry energy.

As discussed above, our first applications were obtained describing nuclear clusters with a simple mass formula with parameters extracted from a slab calculations. The drawback of this approach is that it is not straightforward to implement the in-medium modifications of the surface tension due to the external gas. Moreover, our clusters are systematically overbound which creates an energy discontinuity when shifting from the experimental mass table to the theoretical formulae. In order to implement into the NSE the in-medium effects and more accurate ground state energies compared with the liquid-drop-like formula, we have started to develop analytical mass formulas in the last part of the thesis, with coefficients directly linked to the different parameters of standard Skyrme functionals in the ETF approximation. The task being challenging, we have for now focused on nuclei in vacuum. Such analytical expressions of the different coefficients of the mass formula in terms of the Skyrme couplings also allow for improved understanding of the correlation between these couplings and the different aspects of nuclear energetics, for the construction of optimized fitting procedures of the functionals. This constitutes an extra motivation for this work.

The modelling of Fermi density profiles has allowed an (almost) exact analytical evaluation of the isoscalar part of the nuclear energy, naturally leading to the appearance in the surface energy of a curvature term and a constant term independent of the baryonic number. The diffuseness of the density profile has been variationally calculated within the same formalism, and a simple analytical expression has been given. The relative importance of local and non-local terms has been studied in detail. We have shown that the huge dispersion observed on the value of the surface tension for symmetric nuclei in modern Skyrme functionals is essentially due to the local couplings, even if these different functionals correspond to comparable saturation properties of symmetric nuclear matter. This finding means that nuclear matter properties are not sufficient for pinning down surface properties of finite nuclei even in the symmetric case.

Concerning the surface symmetry energy, we have proposed an approximation based on the assumption that the surface energy density is peaked at the nuclear surface and curvature terms can be neglected. This approximation takes into account the isospin inhomogeneities, required at high asymmetries. A reproduction of HF results within  $\sim 200$  keV per nucleon at the drip-lines has been obtained, and simple expressions have been given for the surface energy and the surface diffuseness parameter. In particular we have shown that both linear and quadratic terms in the bulk nuclear asymmetry  $\delta$  and the neutron skin thickness  $\Delta R$  are needed to correctly explain the surface term. Moreover, within this analytical mass formula, we have recovered the well-known fact that the neutron skin is essentially determined by the slope of the symmetry energy at saturation. Conversely, the surface symmetry energy has been shown to be the result of a complex interplay of all different local and non-local terms in the energy functional. This implies that constraints on the symmetry energy parameters ( $J_{sym}, L_{sym}, K_{sym}$ ) from mass measurements might be model dependent and misleading.

As a further development of this work, we plan to extend the mass formula to the case of nuclei embedded in a nucleon gas, by developing and verifying the validity and accuracy of the expressions sketched in chapter III.3. Such a parametrization will allow for the inclusion of modifications of the nuclear surface energy due to the presence of continuum states in the NSE model. A self-consistent inclusion of pairing effects in the clusters, the homogeneous gas and their interactions, in the local density BCS approximation, using consistent calculations for the mean field and gap equation with the same energy functional, is also in progress [Bur15]. This realistic model will provide data tables for sub-saturated compact stars matter, which are planned to be published at the online service CompOSE [Com13].

# Résumé des conclusions

L'objectif de cette thèse a été d'étudier l'énergie fonctionnelle des agrégats en interaction avec un gaz de nucléons présent dans la matière sous-saturée de supernovæ et de proto-étoiles à neutrons, dans le cadre de l'équilibre statistique nucléaire.

Nous avons considéré un modèle en équilibre statistique nucléaire basé sur l'ensemble statistique grand-canonique qui peut se factoriser en ses composantes leptonique, photonique, et baryonique. Comme les deux premiers sont bien connus, nous nous sommes concentrés sur le secteur baryonique. Sous certaines hypothèses sur la longueur de corrélation des interactions de Coulomb en présence d'un gaz d'électrons écranté, ce dernier peut naturellement être factorisé en fonctions de partition de cellules de Wigner-Seitz indépendantes. À leurs tours, ces fonctions peuvent être divisées en une composante homogène et en un agrégat. Pour obtenir cette dernière factorisation, la partie de l'interaction entre les noyaux et les nucléons doit être considérée comme une modification de milieu de l'énergie libre de l'agrégat. Le formalisme général du modèle en équilibre statistique nucléaire a été introduit par différents auteurs dans la littérature [Eid80; Bot10; Hem10; Rad10; Bli11]. La partie originale de cette thèse consiste essentiellement en la modélisation de l'énergie de la cellule de Wigner-Seitz. Pour modéliser la grande variété d'agrégats pris en compte dans le modèle statistique, nous avons introduit des formules quasi-analytiques pour les différentes grandeurs physiques qui entrent dans l'énergie libre. Les propriétés du cluster ont été directement évaluées par les données expérimentales quand elles existent. Comme les noyaux présents dans les étoiles compactes sont hors de la connaissance expérimentale, des formules quasi-analytiques extrapolées, consistantes avec l'interaction effective de Skyrme utilisée pour le gaz homogène de nucléons, sont requises. La détermination de ces formules, et leur application dans des conditions thermodynamiques pertinentes pour la croûte des proto-étoiles à neutrons, a été le sujet principal de la thèse. Nous avons réalisé cette tâche à différents niveaux d'approximations, dans le cadre général de la théorie de Thomas-Fermi étendue. L'interaction entre les agrégats et les particules libres, évaluée avec la même interaction de Skyrme est divisée en un terme de volume et un de surface. Cependant, l'entropie de champ-moyen étant connue pour donner une description médiocre de la spectroscopie

nucléaire, les états excités de l'agrégat ont été évalués à partir d'une formule réaliste, ajustée sur un grand nombre de données expérimentales.

Pour les résultats préliminaires présentés dans la partie I, seul le terme de volume a été inclus, et l'énergie de liaison nucléaire a été modélisée par une formule sophistiquée de goutte liquide, ajustée sur des calculs Hartree-Fock de Skyrme [Dan09]. La plupart des résultats que nous avons obtenus ont été effectués en utilisant l'interaction effective SLy4. Différentes conclusions ont été tirées de cette étude. Premièrement, nous avons montré que pour la matière en équilibre  $\beta$  de la croûte des proto-étoiles à neutrons, la fraction totale de protons est principalement déterminée par la condition d'équilibre elle-même, et ne dépend donc pas beaucoup des détails du modèle de masse. En ce qui concerne la composition de la matière, nous avons vu qu'une distribution bimodale en taille d'agrégat présentant deux pics comparables, correspondant aux agrégats lourds et légers, est systématiquement obtenue dans presque toutes les conditions thermodynamiques. Les agrégats lourds sont généralement trop riches en neutrons pour être synthétisés au laboratoire. Cela signifie qu'une modélisation théorique est nécessaire puisque les données expérimentales ne sont pas disponibles. D'un autre côté, cette modélisation (basées sur différents niveaux d'approximations de la théorie du champ moyen) donne une mauvaise reproduction des densité d'énergie et d'état des noyaux légers. Cela signifie que les données expérimentales sont également nécessaires. Par conséquent, les modèles en équilibre statistique nucléaire ont besoin à la fois des données expérimentales et de paramétrisations extrapolées. L'inconvénient de l'utilisation de deux prescriptions différentes pour l'énergie est qu'elles ne sont pas égales aux points de raccordement. Il en résulte que, pour des conditions thermodynamiques spécifiques où la composition de la matière correspond à la limite des deux prescriptions, le modèle n'est pas fiable, et des effets spurieux sont présents dans la distribution des agrégats. Nous avons également montré qu'une large distribution d'agrégats survit même à des températures très basses. Les modèles en équilibre statistique nucléaire sont donc nécessaires pour décrire de façon réaliste la matière de la croûte des proto-étoiles à neutrons, même à basse température  $T \sim 500$  keV. Bien que nous ne considérons pas un traitement correct des températures en dessous de la température de transition solide-gaz, où l'entropie associée au moment du centre de masse de l'agrégat disparaît, et où les excitations vibrationnels ainsi que collectives sont présents, nous avons montré qu'à températures très basses, les effets de température ne devraient pas être négligés puisque l'agrégat le plus probable peut être modifié lorsque la température diminue. Enfin, nous avons trouvé que les agrégats légers ne sont pas systématiquement des particules alpha mais, à cause des basses fractions de protons imposées par l'équilibre beta, des petites résonances très asymétriques pourraient être plus favorisées. Cette dernière conclusion doit être prise avec prudence, car les modifications de milieu de surface de l'agrégat qui sont censés être particulièrement

importantes pour les noyaux légers à basses températures ont été ignorées. En outre, la séparation elle-même des effets de milieu en un terme de volume et un terme de surface devient de plus en plus discutable avec la diminution de la taille du noyau, et des calculs microscopiques devraient être effectués. D'autres études avec des modèles améliorés sont fortement souhaitables.

Pour évaluer les modifications de milieu de la tension de surface, nous avons considéré des profils de Fermi menant à des densités nucléaires quasi-analytiques, et permettant de calculer les énergies de liaison nucléaires en utilisant l'approximation semi-classique de Thomas-Fermi étendue au second ordre en  $\hbar$ . Nous avons vérifié que ce modèle est suffisant pour obtenir une précision en énergie de l'ordre de 100-200 keV par nucléon par rapport à un calcul complet Hartree-Fock avec la même fonctionnelle d'énergie.

Avec ce modèle, nous avons extrait et évalué les modifications de milieu de l'énergie, à température nulle, d'un noyau immergé dans le gaz de ses états du continuum. Nous avons explicitement montré que la présence d'un gaz externe induit à la fois une modification des énergies de volume et de surface, ce qui valide l'hypothèse faite dans nos premières applications. Les termes de volume et de surface ont été évalués et nous avons montré qu'ils dépendent, de manière très complexe et hautement non-linéaire, de l'asymétrie de l'agrégat, ainsi que de l'asymétrie et de la densité du gaz. Les premiers résultats préliminaires de l'implémentation de ces effets à température nulle et en équilibre  $\beta$  montrent que les corrections de milieu de surface peuvent être négligées lors de la modélisation de la matière de la croûte des étoiles à neutrons. Cependant, étant donné que les valeurs absolues des modifications d'énergie peuvent être comparables voire supérieures à l'énergie de liaison nucléaire, la coexistence de noyaux et de particules libres dans la matière stellaire chaude et/ou hors équilibre  $\beta$  ne devrait pas être modélisée comme un mélange d'espèces nucléaires sans interaction. Le résultat conceptuel le plus important concernant les effets de milieu est que si la modification de l'énergie de volume correspond à des effets stériques, et peut donc être appelée "volume exclu", cette modification est due au fait que le gaz correspond à des états de haute énergie du noyau, dans le continuum. En conséquence, il entre directement dans l'énergie de la fonction de partition statistique de telle sorte qu'il ne peut pas être exprimé sous la forme classique de Van der Waals comme c'est le cas dans d'autres modèles en équilibre statistique nucléaire. Il serait intéressant de comparer quantitativement les résultats utilisant notre prescription de modification d'énergie de bulk à ceux utilisant l'approximation standard du volume exclu.

Avec le même modèle, nous avons également étudié la définition de la partie de volume et de surface de l'énergie de symétrie des noyaux finis dans le vide, qui est une question importante pour l'élaboration de formules de masses nucléaires, ainsi que pour l'extraction des paramètres de l'équation d'état pour les applications astrophysiques.

Nous avons montré que le caractère variationnel du formalisme de Thomas-Fermi étendu suggère que la partie de volume de l'énergie nucléaire dépend de l'asymétrie d'isospin de volume du centre du noyau  $\delta$ , comme supposé dans les modèles de gouttelettes, plutôt que de l'asymétrie globale du noyau  $I$  qui est généralement considéré dans les modèles plus simples de goutte liquide. Cette observation, confirmée par une comparaison détaillée avec des calculs Hartree-Fock, implique que l'énergie de symétrie de surface contribue de façon positive à l'énergie totale de symétrie du noyau. Le choix du paramètre d'asymétrie globale  $I$  considéré dans les modèles de goutte liquide, non compatible avec Thomas-Fermi étendu, peut expliquer les ambiguïtés rapportées dans la littérature en ce qui concerne le signe de l'énergie de symétrie de surface.

Comme indiqué ci-dessus, nos premières applications ont été obtenues en écrivant les agrégats nucléaires avec une simple formule de masse utilisant des paramètres extraits de calculs semi-infinis. L'inconvénient de cette approche est qu'il est difficile d'implémenter les modifications de milieu de la tension de surface dus au gaz externe. De plus, nos agrégats sont systématiquement plus liés, ce qui crée une discontinuité dans l'énergie lors du passage des masses expérimentales à celles prédites par les paramétrisations. Afin d'implémenter dans le modèle en équilibre statistique nucléaire les effets de milieu et des énergies de l'état fondamentale plus précises par rapport à la formule de goutte liquide, nous avons commencé à développer des formules analytiques de masse dans la dernière partie de la thèse, avec des coefficients directement reliés aux différents paramètres des fonctionnelles de Skyrme standard en utilisant l'approximation Thomas-Fermi étendue. La tâche étant difficile, nous nous sommes pour l'instant concentrés sur des noyaux dans le vide. Ces expressions analytiques des différents coefficients de la formule de masse en termes de couplages de Skyrme permettent également d'améliorer la compréhension de la corrélation entre ces couplages et les différents aspects de l'énergétique nucléaire, pour la construction de procédures d'ajustement optimisées de fonctionnelles. Cela constitue une motivation supplémentaire pour ce travail.

La modélisation des profils de densité de Fermi a permis une évaluation analytique (presque) exacte de la partie isoscalaire de l'énergie nucléaire, conduisant naturellement à l'apparition dans l'énergie de surface d'un terme de courbure et d'un terme constant, indépendant du nombre baryonique. La diffusivité du profil de densité a été calculée variationnellement au sein du même formalisme, et une expression analytique simple a été donnée. L'importance relative des termes locaux et non locaux a été étudiée en détail. Nous avons montré que la grande dispersion observée sur la valeur de la tension de surface pour les noyaux symétriques dans les fonctionnelles de Skyrme modernes est essentiellement due à des couplages locaux, même si ces différentes fonctionnelles correspondent à des propriétés similaires de matière nucléaire symétrique saturée. Cette constatation signifie que les propriétés de la matière nucléaire ne sont pas suffisantes

pour cerner les propriétés de surface des noyaux fins, même dans le cas symétrique.

En ce qui concerne l'énergie de symétrie de surface, nous avons proposé une approximation basée sur l'hypothèse que la densité d'énergie de surface isovecteur est piquée à la surface nucléaire, et que les termes de courbure peuvent être négligée. Cette approximation tient compte des inhomogénéités d'isospin, a priori nécessaires à hautes asymétries. Une reproduction des résultats Hartree-Fock à  $\sim 200$  keV par nucléon près, aux lignes de limite de stabilité, a été obtenue, et des expressions simples ont été données pour l'énergie de surface ainsi que pour le paramètre de diffusivité. En particulier, nous avons montré que les deux termes linéaires et quadratiques en  $\delta$  et  $\Delta R$  sont nécessaires pour expliquer correctement le terme de surface. En outre, dans cette formule analytique de masse, nous avons montré que la peau de neutrons est essentiellement déterminée par la pente de l'énergie de symétrie à la saturation, confirmant ainsi les résultats numériques antérieures de différents groupes [EPJ14]. Inversement, nous avons montré que l'énergie de symétrie de surface est due à une interaction complexe entre les différents termes locaux et non-locaux de la fonctionnelle d'énergie. Cela implique que les contraintes sur les paramètres d'énergie de symétrie ( $J_{sym}, L_{sym}, K_{sym}$ ) à partir de mesures de masse pourraient dépendre du modèle et donc être artificieuses.

Comme développement ultérieur de ce travail, nous prévoyons d'étendre la formule de masse dans le cas de noyaux immergés dans un gaz de nucléons, en développant et en vérifier la validité et l'exactitude des expressions esquissées au chapitre III.3. Un tel paramétrage permettra l'inclusion des modifications de l'énergie nucléaire de surface en raison de la présence d'états du continuum dans le modèle en équilibre statistique nucléaire basé. Les effets d'appariement calculées au sein de l'approximation BCS de densité locale, inclus de façon consistante dans les agrégats, le gaz homogène et leurs interactions, est également en cours de développement [Bur15], Ce modèle réaliste fournira des tables de données pour la matière sous-saturée des étoiles compactes qui sont prévues d'être publiées sur le site internet CompOSE [Com13].

# Appendix A

## Analytical integrals of Fermi functions

We give here the development of the formulae useful to analytically integrate Fermi functions to some power, in order to obtain the local and non-local surface energies eqs. (III.10) and (III.11).

### A.1 General formulae

The Fermi function  $F(r) = (1 + e^{(r-R)/a})^{-1}$  to any power  $\gamma > 0$  can be integrated in any dimension in using the following general formula [Kri81]:

$$\begin{aligned} I_{m,\gamma} &= 4\pi \int_0^{+\infty} dr F^\gamma(r) r^m \\ &\simeq 4\pi \frac{R^{m+1}}{m+1} \left[ 1 + (m+1) \sum_{k=0}^m \binom{m}{k} \eta_\gamma^{(k)} \left(\frac{a}{R}\right)^{k+1} \right], \end{aligned} \quad (\text{A.1})$$

with  $m \in \mathbb{N}$ ,  $\gamma \in \mathbb{R}^{+*}$ , the binomial coefficient  $\binom{m}{k} = m!/(k!(m-k)!)$ , and

$$\eta_\gamma^{(k)} = (-1)^k \int_0^\infty du \left[ \frac{1 + (-1)^k e^{-\gamma u}}{(1 + e^{-u})^\gamma} - 1 \right] u^k. \quad (\text{A.2})$$

One can observe that

$$\eta_{\gamma+1}^{(0)} - \eta_\gamma^{(0)} = -\frac{1}{\gamma} ; \quad \eta_{\gamma+1}^{(k)} - \eta_\gamma^{(k)} = -\frac{k}{\gamma} \eta_\gamma^{(k-1)} \quad (k > 0), \quad (\text{A.3})$$

leading to the recursive relations for  $\gamma \geq 1$ :

$$\eta_{\gamma+2}^{(0)} - \eta_{\gamma+1}^{(0)} - \left( \eta_{\gamma+1}^{(0)} - \eta_\gamma^{(0)} \right) = \frac{1}{\gamma(\gamma+1)},$$

$\eta_\gamma^{(k)}$		$k$		
		0	1	2
$\gamma$	1	0	$\pi^2/6$	0
	5/3	-0.758981245	1.517431001	-2.60168706
	2	-1	$\pi^2/6$	$-\pi^2/3$
	$\alpha + 2$	-1.10223102	1.72183325	-3.59345480
	3	$-3/2$	$1/2 + \pi^2/6$	
	4	$-11/6$	$1 + \pi^2/6$	
	5	$-25/12$	$35/24 + \pi^2/6$	
	6	$-137/60$	$45/24 + \pi^2/6$	
	7	$-49/20$	$203/90 + \pi^2/6$	
	8	$-363/140$	$469/180 + \pi^2/6$	
9	$-761/280$	$29,531/10,080 + \pi^2/6$		
10	$-7,129/2,520$	$6,515/2,016 + \pi^2/6$		

Table A.1: Values of the coefficients  $\eta_\gamma^{(k)}$  calculated via eqs. (A.2) and (A.3).

The calculations for  $\gamma \in \mathbb{N}$  are analytical; numerical otherwise. For the specific  $\eta_\alpha^{(k)}$  which depends on the value of  $\alpha$ , that is of the effective interaction, we show here the result considering the SLy4 interaction ( $\alpha = 1/6$ ). The  $\eta_{i \in \mathbb{N}}^{(k)}$  are given up to the 7<sup>th</sup> order in the spin-orbit Taylor expansion (see text of sec. III.1.1).

$$\begin{aligned}
 \eta_{\gamma+2}^{(1)} - \eta_{\gamma+1}^{(1)} - \left( \eta_{\gamma+1}^{(1)} - \eta_\gamma^{(1)} \right) &= \frac{1}{\gamma(\gamma+1)} \left( \eta_\gamma^{(0)} + 1 \right), \\
 \eta_{\gamma+2}^{(2)} - \eta_{\gamma+1}^{(2)} - \left( \eta_{\gamma+1}^{(2)} - \eta_\gamma^{(2)} \right) &= \frac{2}{\gamma(\gamma+1)} \left( \eta_\gamma^{(1)} + \eta_\gamma^{(0)} \right). \tag{A.4}
 \end{aligned}$$

The values of the coefficients that have been used for this work are given in table (A.1). Equation (A.1) is an approximation for which the tiny error is  $\sim \exp(-R/a)$  [Kri81]. Let us note that it is a finite expansion. This equation allows in particular to obtain the analytical relation between the particle number and the radius parameter, in the case of General Fermi-Dirac function eq. (II.33).

## A.2 Expressions of a 3D integral as 1D integrals

The expression of the difference  $\Delta I_{\gamma',\gamma} = \rho_{sat} (I_{2,\gamma'} - I_{2,\gamma})$  is developed in this section in order to obtain a sum of 1-dimensional integrals.

The moments of the difference between two one-dimensional Fermi functions  $F(x) =$

$(1 + e^{x/a})^{-1}$  to different powers  $\gamma', \gamma$  can be integrated as [Kri81]

$$\int_{-\infty}^{+\infty} x^k \Delta F_{\gamma', \gamma}(x) dx = a^{k+1} \left( \eta_{\gamma'}^{(k)} - \eta_{\gamma}^{(k)} \right), \quad (\text{A.5})$$

with  $\Delta F_{\gamma', \gamma} = F^{\gamma'} - F^{\gamma}$ . Making the change of variable  $x = r - R$ , we can express the 3-dimensional integral  $I_{2, \gamma} = \int \mathbf{dr} F^{\gamma}(r)$  as a sum of three 1-dimensional integrals of moments of Fermi functions  $F(x)$ :

$$\begin{aligned} I_{2, \gamma} &= 4\pi \int_{-R}^{+\infty} (x + R)^2 F^{\gamma}(x) dx \\ &= 4\pi \int_{-\infty}^{+\infty} (x + R)^2 F^{\gamma}(x) dx - 4\pi \int_{-\infty}^{-R} (x + R)^2 F^{\gamma}(x) dx, \end{aligned} \quad (\text{A.6})$$

where we have used the Chasles formula to get integrals over the entire slab-space. Assuming that the bulk is reached in the "negative" region, that is  $F^{\gamma}(x < -R) = 1$ , we can express the difference of two Fermi functions to different powers as

$$\begin{aligned} \frac{\Delta I_{\gamma', \gamma}}{\rho_{sat}} &= 4\pi R^2 \int_{-\infty}^{+\infty} \Delta F_{\gamma', \gamma}(x) dx + 8\pi R \int_{-\infty}^{+\infty} x \Delta F_{\gamma', \gamma}(x) dx \\ &+ 4\pi \int_{-\infty}^{+\infty} x^2 \Delta F_{\gamma', \gamma}(x) dx. \end{aligned} \quad (\text{A.7})$$

Because of the previous approximation, we have spuriously inserted a bulk part in eq. (A.7), but with the very tiny error  $\sim \left( \exp(-\gamma'R/a) - \exp(-\gamma R/a) \right)$ . Computing eq. (A.7) with eq. (A.5) and expanding the radius parameter  $R$  as a series of  $(a/R_{HS})$  until the third order according to eq. (II.36), we finally get at the third order in  $(a/R_{HS})$ :

$$\begin{aligned} \Delta I_{\gamma', \gamma} &= 3 \left( \eta_{\gamma'}^{(0)} - \eta_{\gamma}^{(0)} \right) \frac{a}{r_{sat}} A^{2/3} \\ &+ 6 \left( \eta_{\gamma'}^{(1)} - \eta_{\gamma}^{(1)} \right) \left( \frac{a}{r_{sat}} \right)^2 A^{1/3} \\ &+ 3 \left( \left( \eta_{\gamma'}^{(2)} - \eta_{\gamma}^{(2)} \right) - \frac{2}{3} \pi^2 \left( \eta_{\gamma'}^{(0)} - \eta_{\gamma}^{(0)} \right) \right) \left( \frac{a}{r_{sat}} \right)^3 \\ &+ O \left( \left( \frac{a}{r_{sat}} \right)^4 A^{-1/3} \right), \end{aligned} \quad (\text{A.8})$$

with  $r_{sat} = R_{HS} A^{-1/3} = \left( \frac{4}{3} \pi \rho_{sat} \right)^{-1/3}$ . Let us notice that we can also obtain equation (A.8) using the general formula (A.1).

## Appendix B

# Analytical integrals of Gaussian

We develop here the analytical integral of a 3-dimensional Gaussian  $\mathcal{G}(r)$  peaked at an arbitrary radius  $R_M$  in order to obtain the isovector surface energy as a function of the nucleus mass and of the effective interaction parameters.

The 3-dimensional integral

$$\begin{aligned} E_G &= 4\pi \int_0^\infty dr r^2 \mathcal{G}(r), \\ &= 4\pi \int_0^\infty dr r^2 \mathcal{A} \exp\left(-\frac{(r - R_M)^2}{2\sigma^2}\right) \end{aligned} \quad (\text{B.1})$$

can be expressed as 1-dimensional integrals, making the variable change  $x = r - R_M$ , as for the symmetric energy:

$$\begin{aligned} E_G &= 4\pi \mathcal{A} \int_{-\infty}^{+\infty} dx (x + R_M)^2 \exp\left(-\frac{x^2}{2\sigma^2}\right) \\ &\quad - 4\pi \mathcal{A} \int_{-\infty}^{-R_M} dx (x + R_M)^2 \exp\left(-\frac{x^2}{2\sigma^2}\right). \end{aligned} \quad (\text{B.2})$$

Since we are interested in the surface energy, we assume that the Gaussian  $\mathcal{G}(r)$  is zero at the center of the nucleus, such that the second integral in eq. (B.2) is negligible with an accuracy  $\sim \exp(-R_M^2/(2\sigma^2))$ . Then integrating the Gaussian moments straightforwardly lead to

$$E_G = 2(2\pi)^{3/2} \sigma \mathcal{A} (R_M^2 + \sigma^2). \quad (\text{B.3})$$

To have  $E_G$  as a function of the mass, we just need to express the position  $R_M$  as a

function of  $A$ . If we assume  $R_M = R$ , it reads, using eq. (II.36):

$$E_G = 2(2\pi)^{3/2} \sigma \mathcal{A} r_{sat}^2 \left[ A^{2/3} + \frac{\sigma^2}{r_{sat}^2} - \frac{2\pi^2}{3} \left( \frac{a}{r_{sat}} \right)^2 + O \left( \left( \frac{a}{r_0} \right)^4 A^{-2/3} \right) \right]. \quad (\text{B.4})$$

In the general case, defining  $\delta R = R_M - R$ , we find additional terms, especially curvature:

$$E_G = 2(2\pi)^{3/2} \sigma \mathcal{A} r_{sat}^2 \left[ A^{2/3} + 2 \frac{\delta R}{r_{sat}} A^{1/3} + \frac{\sigma^2}{r_{sat}^2} - \frac{2\pi^2}{3} \left( \frac{a}{r_{sat}} \right)^2 + \left( \frac{\delta R}{r_{sat}} \right)^2 - \frac{2\pi^2}{3} \frac{\delta R}{r_{sat}} \left( \frac{a}{r_{sat}} \right)^2 A^{-1/3} + O \left( \left( \frac{a}{r_{sat}} \right)^4 A^{-2/3} \right) \right]. \quad (\text{B.5})$$

## Appendix C

# Analytical expressions of the energy density derivatives

In this appendix, we give some formulae that are useful for the analytical Gaussian approximations developed in part III. In C.1, we give the analytical expressions of the energy density second derivatives that are involved in the variance  $\sigma$  of eqs. (III.61), (III.64), and (III.99). In C.2, the ingredients used to obtain the analytical shift correction  $\delta R$  of the maximum Gaussian position  $R_M = R + \delta R$  introduced in sec. III.3.1 are expressed.

### C.1 Second derivatives of the energy density

From the Skyrme energy density eq. (I.69), the second derivative terms of the local energy straightforwardly read:

$$\frac{d^2 \mathcal{K}_0}{dr^2} = \frac{\hbar^2}{2m} (3\pi^2)^{2/3} \left[ \rho_n^{2/3} \rho_n'' + \frac{2}{3} \rho_n'^2 \rho_n^{-1/3} + \rho_p^{2/3} \rho_p'' + \frac{2}{3} \rho_p'^2 \rho_p^{-1/3} \right], \quad (\text{C.1})$$

$$\begin{aligned} \frac{d^2 \mathcal{H}_{eff}}{dr^2} &= \frac{3}{5} (3\pi^2)^{2/3} C_{eff} \rho'' \left[ \rho_n^{5/3} + \rho_p^{5/3} \right] + 2 (3\pi^2)^{2/3} C_{eff} \rho' \left[ \rho_n' \rho_n^{2/3} + \rho_p' \rho_p^{2/3} \right] \\ &+ (3\pi^2)^{2/3} C_{eff} \rho \left[ \rho_n^{2/3} \rho_n'' + \frac{2}{3} \rho_n'^2 \rho_n^{-1/3} + \rho_p^{2/3} \rho_p'' + \frac{2}{3} \rho_p'^2 \rho_p^{-1/3} \right] \\ &+ \frac{3}{5} (3\pi^2)^{2/3} D_{eff} \rho_3'' \left[ \rho_n^{5/3} - \rho_p^{5/3} \right] + 2 (3\pi^2)^{2/3} D_{eff} \rho_3' \left[ \rho_n' \rho_n^{2/3} - \rho_p' \rho_p^{2/3} \right] \\ &+ (3\pi^2)^{2/3} D_{eff} \rho_3 \left[ \rho_n^{2/3} \rho_n'' + \frac{2}{3} \rho_n'^2 \rho_n^{-1/3} - \rho_p^{2/3} \rho_p'' - \frac{2}{3} \rho_p'^2 \rho_p^{-1/3} \right], \quad (\text{C.2}) \end{aligned}$$

$$\begin{aligned} \frac{d^2 (\mathcal{H}_0 + \mathcal{H}_3)}{dr^2} &= 2C_0 \left[ \rho \rho'' + \rho'^2 \right] + 2D_0 \left[ \rho_3 \rho_3'' + \rho_3'^2 \right] + (\sigma + 2) C_3 \left[ \rho^{\sigma+1} \rho'' + (\sigma + 1) \rho^\sigma \rho'^2 \right] \\ &+ \sigma D_3 \rho^{\sigma-2} \rho_3 \left[ (\sigma - 1) \rho_3 \rho_3'^2 + \rho_3 \rho \rho'' + 4 \rho \rho' \rho_3' \right] + 2D_3 \rho^\sigma \left[ \rho_3'^2 + \rho_3 \rho_3'' \right], \quad (\text{C.3}) \end{aligned}$$

where  $\mathcal{K}_0$  is the local part of the kinetic energy density, and where  $\rho'_i = d\rho_i/dr$  and  $\rho''_i = d^2\rho_i/dr^2$  (which is not the 3-dimensional Laplace derivative) can be expressed as functions of Fermi-Dirac  $F_i(r)$ :

$$\rho'_i(r) = -\frac{\rho_{sat,i}}{a_i} F_i(r) [1 - F_i(r)] \quad ; \quad \rho''_i(r) = \frac{\rho_{sat,i}}{a_i^2} F_i(r) [1 - 3F_i(r) + 2F_i^2(r)]. \quad (\text{C.4})$$

For the non local terms, we first turn the Laplace derivatives of the kinetic densities (eq. (II.14)) into gradients, which leads to

$$\begin{aligned} \mathcal{H}_{NL} &= \frac{\hbar^2}{2m} \sum_q f_q (\tau_{2q}^L + \tau_{2q}^{NL}) \\ &= \frac{\hbar^2}{2m} \sum_q \left[ \frac{1}{36} \frac{f_q \rho_q'^2}{\rho_q} + \frac{1}{6} \rho_q' f_q' - \frac{1}{12} \frac{\rho_q \rho_q'^2}{f_q} \right] - \frac{1}{2} [C_{eff} \rho'^2 + D_{eff} \rho_3'^2]. \end{aligned} \quad (\text{C.5})$$

Moreover, we can easily gather the spin-orbit energy density  $\mathcal{H}_{so}$  (eq. (I.69)) with the spin-orbit involving in the kinetic densities  $\tau_{2q}^{so}$  (eq. (II.14)) in observing that, without spin-gradient terms,

$$\mathcal{H}_{so} = -2 \cdot \frac{\hbar^2}{2m} \sum_q f_q \tau_{2q}^{so} = -\frac{2m}{\hbar^2} \left[ \frac{\rho_n}{f_n} (C_{so} \rho' + D_{so} \rho_3')^2 + \frac{\rho_p}{f_p} (C_{so} \rho' - D_{so} \rho_3')^2 \right]. \quad (\text{C.6})$$

Then introducing the density third derivatives

$$\rho_i^{(3)}(r) = -\frac{\rho_{sat,i}}{a_i^3} F_i(r) [1 - 7F_i(r) + 12F_i^2(r) - 6F_i^3(r)], \quad (\text{C.7})$$

we obtain the following formulae for the non local energy density second derivatives:

$$\frac{d^2 \mathcal{H}_{fin}}{dr^2} = 2C_{fin} [\rho''^2 + \rho' \rho^3] + 2D_{fin} [\rho_3''^2 + \rho_3' \rho_3^3], \quad (\text{C.8})$$

$$\begin{aligned} \frac{d^2 \mathcal{H}_{NL}}{dr^2} &= \frac{\hbar^2}{2m} \sum_q \frac{1}{36 \rho_q^3} \left[ -2\rho_q \rho_q'^3 f_q' + 4\rho_q^2 \rho_q' f_q' \rho_q'' + \rho_q^2 \rho_q'^2 f_q'' \right. \\ &\quad \left. - 5\rho_q f_q \rho_q'^2 \rho_q'' + 2\rho_q^2 f_q \rho_q''^2 + 2\rho_q^2 f_q \rho_q' \rho_q^{(3)} + 2f_q \rho_q'^4 \right] \\ &\quad + \frac{1}{6} \left[ f_q' \rho_q^{(3)} + 2\rho_q'' f_q'' + \rho_q' f_q^{(3)} \right] \\ &\quad - \frac{1}{12 f_q^3} \left[ -2f_q \rho_q' f_q'^3 + 4f_q^2 \rho_q' f_q' f_q'' + f_q^2 f_q'^2 \rho_q'' \right. \\ &\quad \left. - 5\rho_q f_q f_q'^2 f_q'' + 2\rho_q f_q^2 f_q''^2 + 2\rho_q f_q^2 f_q' f_q^{(3)} + 2\rho_q f_q'^4 \right] \\ &\quad - C_{eff} [\rho''^2 + \rho' \rho^{(3)}] - D_{eff} [\rho_3''^2 + \rho_3' \rho_3^{(3)}], \end{aligned} \quad (\text{C.9})$$

$$\begin{aligned}
 \frac{d^2 \mathcal{H}_{so}}{dr^2} = & -\frac{2m}{\hbar^2} \sum_q \frac{C_{so}^2}{f_q^3} \left[ f_q^2 \rho'^2 \rho_q'' + 4f_q^2 \rho'_q \rho' \rho'' + 2\rho_q f_q^2 \rho''^2 + 2\rho_q f_q^2 \rho' \rho^{(3)} \right. \\
 & \left. - \rho_q f_q \rho'^2 f_q'' - 2f_q \rho'_q f'_q \rho'^2 - 4\rho_q f_q \rho' f'_q \rho'' + 2\rho_q f_q'^2 \rho'^2 \right] \\
 & + \frac{D_{so}^2}{f_q^3} \left[ f_q^2 \rho_3'^2 \rho_q'' + 4f_q^2 \rho'_q \rho'_3 \rho_3'' + 2\rho_q f_q^2 \rho_3''^2 + 2\rho_q f_q^2 \rho_3' \rho_3^{(3)} \right. \\
 & \left. - \rho_q f_q \rho_3'^2 f_q'' - 2f_q \rho'_q f'_q \rho_3'^2 - 4\rho_q f_q \rho_3' f'_q \rho_3'' + 2\rho_q f_q'^2 \rho_3'^2 \right] \\
 & \pm \frac{2C_{so} D_{so}}{f_q^3} \left[ f_q^2 \rho' \rho_3' \rho_q'' + 2f_q^2 \rho'_q \rho_3' \rho'' + 2f_q^2 \rho_q \rho' \rho_3'' + 2\rho_q f_q^2 \rho'' \rho_3' \right. \\
 & \left. + \rho_q f_q^2 \rho_3' \rho^{(3)} + \rho_q f_q^2 \rho' \rho_3^{(3)} - \rho_q f_q \rho' \rho_3' f_q'' - 2f_q \rho'_q f'_q \rho' \rho_3' \right. \\
 & \left. - 2\rho_q f_q f'_q \rho_3' \rho'' - 2\rho_q f_q \rho' f'_q \rho_3'' + 2\rho_q f_q'^2 \rho' \rho_3' \right], \quad (C.10)
 \end{aligned}$$

where  $\pm$  stand for  $q = n$  (above) and  $q = p$  (below), and where we have introduced the effective mass derivatives  $f'_q = df_q/dr$ ,  $f''_q = d^2 f_q/dr^2$  and  $f_q^{(3)} = d^3 f_q/dr^3$ .

## C.2 Expansions of the energy density first derivative

In this section, we develop useful formulae in order to get the position  $R_M = R + \delta R$  of the maximum of the asymmetric part of the energy density. Assuming  $X = \delta R/a \ll 1$  and  $X_p = \delta R/a_p \ll 1$ , we make a 2<sup>nd</sup> order expansions around  $R$  of the basic ingredients, which are the densities involved in the Skyrme functional derivative with respect to  $r$ . In order to shorten the expressions, we introduce  $\Delta R_a = \Delta R/(2a_p) = (R - R_p)/(2a_p)$  and the following notations:

$$\begin{aligned}
 \rho'_{0p} &= \rho_{sat,p} \left[ 1 - \tanh(\Delta R_a) \right] ; & \rho'_{0n} &= \rho_{sat} - \rho'_{0p} ; & \rho'_{03} &= \rho_{sat} - 2\rho'_{0p} ; \\
 \frac{1}{a'_p} &= \frac{1 + \tanh(\Delta R_a)}{a_p} ; & \frac{1}{a'_n} &= \frac{\rho_0}{\rho'_{0n}} \frac{1}{a} - \frac{\rho'_{0p}}{\rho'_{0n}} \frac{1}{a'_p} ; & \frac{1}{a'_3} &= \frac{\rho_0}{\rho'_{03}} \frac{1}{a} - 2 \frac{\rho'_{0p}}{\rho'_{03}} \frac{1}{a'_p} ; \\
 X'_p &= \frac{\delta R}{a'_p} ; & X'_n &= \frac{\delta R}{a'_n} ; & X'_3 &= \frac{\delta R}{a'_3} ; \\
 \frac{1}{\bar{a}_p} &= \frac{\tanh(\Delta R_a)}{a_p} ; \\
 \bar{X}_p &= \frac{\delta R}{\bar{a}_p}, \quad (C.11)
 \end{aligned}$$

and  $\rho_0 = \rho_{sat}$ . Let us notice that if  $\Delta R_a = 0$ , that is without neutron (or proton) skin, all the previous and following quantities are much simplified. We also define the mixing

coefficients

$$\omega_{pn} = \frac{\rho'_{0p} a'_n}{\rho'_{0n} a'_p} \quad ; \quad \omega_{tn} = \frac{\rho_0 a'_n}{\rho'_{0n} a} \quad ; \quad \omega_{p3} = \frac{\rho'_{0p} a'_3}{\rho'_{03} a'_p} \quad ; \quad \omega_{t3} = \frac{\rho_0 a'_3}{\rho'_{03} a}. \quad (\text{C.12})$$

Then we have at the second order in  $(\delta R/a_{(p)})$ :

$$\begin{aligned} \rho &= \frac{\rho_0}{2} \left[ 1 - \frac{1}{2} X \right] \\ \rho_p &= \frac{\rho'_{0p}}{2} \left[ 1 - \frac{1}{2} X'_p + \frac{1}{4} X'_p \bar{X}_p \right] \\ \rho_n &= \frac{\rho'_{0n}}{2} \left[ 1 - \frac{1}{2} X'_n - \frac{1}{4} \frac{\rho'_{0p}}{\rho'_{0n}} X'_p \bar{X}_p \right] \\ \rho_3 &= \frac{\rho'_{03}}{2} \left[ 1 - \frac{1}{2} X'_3 - \frac{1}{2} \frac{\rho'_{0p}}{\rho'_{03}} X'_p \bar{X}_p \right], \end{aligned} \quad (\text{C.13})$$

$$\begin{aligned} \frac{d\rho}{dr} &= -\frac{\rho_0}{4a} \left[ 1 - \frac{1}{4} X^2 \right] \\ \frac{d\rho_p}{dr} &= -\frac{\rho'_{0p}}{4a'_p} \left[ 1 - \bar{X}_p - \frac{1}{4} X_p^2 + \frac{3}{4} \bar{X}_p^2 \right] \\ \frac{d\rho_n}{dr} &= -\frac{\rho'_{0n}}{4a'_n} \left[ 1 + \omega_{pn} \bar{X}_p - \frac{1}{4} (\omega_{tn} X^2 - \omega_{pn} X_p^2) - \frac{3}{4} \omega_{pn} \bar{X}_p^2 \right] \\ \frac{d\rho_3}{dr} &= -\frac{\rho'_{03}}{4a'_3} \left[ 1 + 2\omega_{p3} \bar{X}_p - \frac{1}{4} (\omega_{t3} X^2 - 2\omega_{p3} X_p^2) - \frac{3}{2} \omega_{p3} \bar{X}_p^2 \right], \end{aligned} \quad (\text{C.14})$$

and

$$\begin{aligned} \frac{d^2\rho}{dr^2} &= \frac{1}{2} \frac{\rho_0}{4a^2} X \\ \frac{d^2\rho_p}{dr^2} &= \frac{1}{2} \frac{\rho'_{0p}}{4a_p a'_p} X_p + \frac{\rho'_{0p}}{4a'_p \bar{a}_p} \left[ 1 - \frac{3}{2} \bar{X}_p - X_p^2 + \frac{3}{2} \bar{X}_p^2 \right] \\ \frac{d^2\rho_3}{dr^2} &= \frac{1}{2} \left[ \frac{\rho_0}{4a^2} X - \frac{\rho'_{0p}}{2a_p a'_p} X_p \right] - \frac{\rho'_{0p}}{2a'_p \bar{a}_p} \left[ 1 - \frac{3}{2} \bar{X}_p - X_p^2 + \frac{3}{2} \bar{X}_p^2 \right]. \end{aligned} \quad (\text{C.15})$$

Eqs. (C.13), (C.14) and (C.15) allow to calculate each (asymmetric) term of the Taylor expansion around  $R$  at the second order  $(\delta R)^2$ , such that we obtain first derivative of the potential terms  $(D_0, D_3)$

$$\begin{aligned} \rho_3 \frac{d\rho_3}{dr} &= -\left( \frac{\rho'_{03}}{2} \right)^2 \frac{1}{2a'_3} \left[ 1 - \frac{X'_3}{2} + 2\omega_{p3} \bar{X}_p - \frac{\omega_{t3} X^2 - 2\omega_{p3} X_p^2}{4} - \omega_{p3} X'_3 \bar{X}_p - \frac{\rho'_{0p}}{2\rho'_{03}} X'_p \bar{X}_p - \frac{3\omega_{p3} \bar{X}_p^2}{2} \right] \\ \rho_3 \rho^\alpha \frac{d\rho_3}{dr} &= -\left( \frac{\rho'_{03}}{2} \right)^2 \left( \frac{\rho_0}{2} \right)^\alpha \frac{1}{2a'_3} \left[ 1 - \frac{\alpha}{2} X - \frac{X'_3}{2} + 2\omega_{p3} \bar{X}_p + \frac{\alpha(\alpha-1)}{8} X^2 + \frac{\alpha}{4} X X'_3 \right] \end{aligned}$$

$$\rho_3^2 \rho^{\alpha-1} \frac{d\rho}{dr} = - \left( \frac{\rho'_{03}}{2} \right)^2 \left( \frac{\rho_0}{2} \right)^\alpha \frac{1}{2a} \left[ 1 - \frac{\alpha-1}{2} X - X'_3 + \frac{\alpha(\alpha-3)}{8} X^2 + \frac{X_3'^2}{4} + \frac{\alpha-1}{2} X X'_3 - \frac{\rho'_{0p}}{\rho'_{03}} X'_p \bar{X}_p - \frac{3\omega_{p3}}{2} \bar{X}_p^2 \right] - \frac{\omega_{t3} X^2 - 2\omega_{p3} X_p^2}{4} - \alpha \omega_{p3} X \bar{X}_p - \omega_{p3} X'_3 \bar{X}_p - \frac{\rho'_{0p}}{2\rho'_{03}} X'_p \bar{X}_p - \frac{3\omega_{p3}}{2} \bar{X}_p^2 \Big], \quad (C.16)$$

the kinetic ones

$$\begin{aligned} \rho^{2/3} \frac{d\rho}{dr} &= - \left( \frac{\rho'_0}{2} \right)^{5/3} \frac{1}{2a} \left[ 1 - \frac{X}{3} - \frac{5}{18} X^2 \right] \\ \rho_p^{2/3} \frac{d\rho_p}{dr} &= - \left( \frac{\rho'_{0p}}{2} \right)^{5/3} \frac{1}{2a'_p} \left[ 1 - \frac{X'_p}{3} - \bar{X}_p - \frac{X_p^2}{4} - \frac{X_p'^2}{36} + \frac{X'_p \bar{X}_p}{2} + \frac{3}{4} \bar{X}_p^2 \right] \\ \rho_n^{2/3} \frac{d\rho_n}{dr} &= - \left( \frac{\rho'_{0n}}{2} \right)^{5/3} \frac{1}{2a'_n} \left[ 1 - \frac{X'_n}{3} + \omega_{pn} \bar{X}_p \right. \\ &\quad \left. - \frac{\omega_{tn} X^2 - \omega_{pn} X_p^2}{4} - \frac{X_n'^2}{36} - \frac{\rho'_{0p}}{6\rho'_{0n}} X'_p \bar{X}_p - \frac{\omega_{pn}}{3} X'_n \bar{X}_p - \frac{3\omega_{pn}}{4} \bar{X}_p^2 \right], \quad (C.17) \end{aligned}$$

the effective ones ( $C_{eff}$ )

$$\begin{aligned} \rho^{5/3} \frac{d\rho}{dr} &= - \left( \frac{\rho_0}{2} \right)^{8/3} \frac{1}{2a} \left[ 1 - \frac{5}{6} X - \frac{1}{9} X^2 \right] \\ \rho_p^{5/3} \frac{d\rho_p}{dr} &= - \left( \frac{\rho'_{0p}}{2} \right)^{5/3} \frac{\rho_0}{2} \frac{1}{2a} \left[ 1 - \frac{5}{6} X'_p - \frac{X^2}{4} + \frac{5}{36} X_p'^2 + \frac{5}{12} X'_p \bar{X}_p \right] \\ \rho_n^{5/3} \frac{d\rho_n}{dr} &= - \left( \frac{\rho'_{0n}}{2} \right)^{5/3} \frac{\rho_0}{2} \frac{1}{2a} \left[ 1 - \frac{5}{6} X'_n - \frac{X^2}{4} + \frac{5}{36} X_n'^2 - \frac{5\rho'_{0p}}{12\rho'_{0n}} X'_p \bar{X}_p \right] \\ \rho_p^{2/3} \frac{d\rho_p}{dr} &= - \left( \frac{\rho'_{0p}}{2} \right)^{5/3} \frac{\rho_0}{2} \frac{1}{2a'_p} \left[ 1 - \frac{X}{2} - \frac{X'_p}{3} - \bar{X}_p \right. \\ &\quad \left. - \frac{X_p^2}{4} - \frac{X_p'^2}{36} + \frac{X X'_p}{6} + \frac{X \bar{X}_p}{2} + \frac{X'_p \bar{X}_p}{2} + \frac{3}{4} \bar{X}_p^2 \right] \\ \rho_n^{2/3} \frac{d\rho_n}{dr} &= - \left( \frac{\rho'_{0n}}{2} \right)^{5/3} \frac{\rho_0}{2} \frac{1}{2a'_n} \left[ 1 - \frac{X}{2} - \frac{X'_n}{3} + \omega_{pn} \bar{X}_p - \frac{\omega_{tn} X^2 - \omega_{pn} X_p^2}{4} - \frac{X_n'^2}{36} + \frac{X X'_n}{6} \right. \\ &\quad \left. - \frac{\omega_{pn}}{2} X \bar{X}_p - \frac{\rho'_{0p}}{6\rho'_{0n}} X'_p \bar{X}_p - \frac{\omega_{pn}}{3} X'_n \bar{X}_p - \frac{3\omega_{pn}}{4} \bar{X}_p^2 \right], \quad (C.18) \end{aligned}$$

and ( $D_{eff}$ )

$$\begin{aligned} \rho_p^{5/3} \frac{d\rho_3}{dr} &= - \left( \frac{\rho'_{0p}}{2} \right)^{5/3} \frac{\rho'_{03}}{2} \frac{1}{2a'_3} \left[ 1 - \frac{5}{6} X'_p + 2\omega_{p3} \bar{X}_p \right. \\ &\quad \left. - \frac{\omega_{t3} X^2 - 2\omega_{p3} X_p^2}{4} + \frac{5}{36} X_p'^2 + \frac{5}{3} \left( \frac{1}{4} - \omega_{p3} \right) X'_p \bar{X}_p - \frac{3\omega_{p3}}{2} \bar{X}_p^2 \right] \\ \rho_n^{5/3} \frac{d\rho_3}{dr} &= - \left( \frac{\rho'_{0n}}{2} \right)^{5/3} \frac{\rho'_{03}}{2} \frac{1}{2a'_3} \left[ 1 - \frac{5}{6} X'_n + 2\omega_{p3} \bar{X}_p \right. \\ &\quad \left. - \frac{\omega_{t3} X^2 - 2\omega_{p3} X_p^2}{4} + \frac{5}{36} X_n'^2 - \frac{5\rho'_{0p}}{12\rho'_{0n}} X'_p \bar{X}_p - \frac{5\omega_{p3}}{3} X'_n \bar{X}_p - \frac{3\omega_{p3}}{2} \bar{X}_p^2 \right] \\ \rho_3 \rho_p^{2/3} \frac{d\rho_p}{dr} &= - \left( \frac{\rho'_{0p}}{2} \right)^{5/3} \frac{\rho'_{03}}{2} \frac{1}{2a'_p} \left[ 1 - \frac{X'_p}{3} - \frac{X'_3}{2} - \bar{X}_p \right. \end{aligned}$$

$$\begin{aligned}
 \rho_3 \rho_n^{2/3} \frac{d\rho_n}{dr} = & - \left( \frac{\rho'_{0n}}{2} \right)^{5/3} \frac{\rho'_{03}}{2} \frac{1}{2a'_n} \left[ -\frac{X_p^2}{4} - \frac{X_p'^2}{36} + \frac{X_p' X_3'}{6} + \frac{1}{2} \left( 1 - \frac{\rho'_{0p}}{\rho'_{03}} \right) X_p' \bar{X}_p + \frac{X_3' \bar{X}_p}{2} + \frac{3}{4} \bar{X}_p^2 \right] \\
 & - \frac{1}{2} \left( \frac{\rho'_{0p}}{\rho'_{03}} + \frac{\rho'_{0p}}{3\rho'_{0n}} \right) X_p' \bar{X}_p - \frac{\omega_{pn} X_3' \bar{X}_p}{2} - \frac{\omega_{pn} X_n' \bar{X}_p}{3} - \frac{3\omega_{pn} \bar{X}_p^2}{4} \Big], \tag{C.19}
 \end{aligned}$$

and the finite size part ( $D_{fin}$ )

$$\begin{aligned}
 \frac{d\rho_3}{dr} \frac{d^2\rho_3}{dr^2} = & - \frac{\rho'_{03}}{2} \frac{1}{4a'_3} \left( \frac{\rho_0}{4a^2} X - \frac{\rho'_{0p}}{2a_p a'_p} X_p \right) (1 + 2\omega_{p3} \bar{X}_p) \\
 & + \frac{\rho'_{0p} \rho'_{03}}{8a'_3 a'_p \bar{a}_p} \left[ 1 - \frac{3}{2} \left( 1 - \frac{4\omega_{p3}}{3} \right) \bar{X}_p - \frac{\omega_{t3} X^2 - 2\omega_{p3} X_p^2}{4} - X_p^2 + \frac{3}{2} (1 - 3\omega_{p3}) \bar{X}_p^2 \right]. \tag{C.20}
 \end{aligned}$$



# Bibliography

- [Abo95] Y. Aboussir, J.M. Pearson, A.K. Dutta, and F. Tondeur, ADNDT 61, 127 (1995).
- [Abr12] S. Abrahamyan *et al.*, Phys. Rev. Lett. 108, 112502 (2012).
- [Agr06] B. K. Agrawal, S. K. Dhiman, and R. Kumar, Phys. Rev. C 73, 034319 (2006).
- [Arn77] W. D. Arnett, Astrophys. J. 218, 815 (1977).
- [Aud12] G. Audi *et al.*, Chinese Phys. C 36, 1157, 1287 and 1603 (2012).
- [Ava12] S. S. Avancini, C. C. Barros Jr., L. Brito, S. Chiacchiera, D. P. Menezes, and C. Providência, Phys. Rev. C 85, 035806 (2012).
- [Aym14] F. Aymard, F. Gulminelli, and J. Margueron, Phys. Rev. C 89, 065807 (2014).
- [Aym15] F. Aymard, F. Gulminelli, and J. Margueron, arXiv:1507.05064, accepted in Journal of Physics G (2015).
- [Baa34a] W. Baade and F. Zwicky, Phys. Rev. 45, 138 (1934).
- [Baa34b] W. Baade and F. Zwicky, Phys. Rev. 46, 76 (1934).
- [Bal05] M. Baldo, U. Lombardo, E. E. Saperstein, and S. V. Tolokonnikov, Nucl. Phys. A 750, 409 (2005).
- [Bar57] J. Bardeen, L. Cooper, and J. R. Schrieffer, Phys. Rev. 108, 1175 (1957).
- [Bay71a] G. Baym, H. A. Behte, and C. J. Pethick, Nucl. Phys. A 175, 255 (1971).
- [Bay71b] G. Baym, C. J. Pethick, and P. Sutherland, Astrophys. J. 170, 299 (1971).
- [Ben03] M. Bender, P.-H. Heenen, and P.-G. Reinhard, Rev. Mod. Phys. 75, 121 (2003).
- [Ber91a] S. van den Bergh and G. A. Tammann, Ann. Rev. Astron. Astrophys. 29, 363 (1991).
- [Ber91b] G. F. Bertsch and H. Esbensen, Ann. of Phys. 209, 327 (1991).
- [Bet79] H. A. Bethe, G. E. Brown, J. Applegate, and J. M. Lattimer, Nucl. Phys. A 324, 487 (1979).
- [Bet90] H. A. Bethe, Rev. Mod. Phys. 62, 801 (1990).

- [Bli11] S. I. Blinnikov, I. V. Panov, M. A. Rudzsky, and K. Sumiyoshi, *Astron. & Astrophys.* 535, A37 (2011).
- [Bot10] A. S. Botvina and I. N. Mishustin, *Nucl. Phys. A* 843, 98 (2010).
- [Bra85] M. Brack, C. Guet, and H. B. Hakansson, *Phys. Rep.* 123, 275 (1985).
- [Bur06] A. Burrows, E. Livne, L. Dessart, C. D. Ott, and J. Murphy, *Astrophys. J.* 640, 878 (2006).
- [Bur14] S. Burrello, M. Colonna, and F. Matera, *Phys. Rev. C* 89, 057604 (2014).
- [Bur15] S. Burrello, F. Gulminelli, F. Aymard, M. Colonna, and Ad. R. Raduta, in preparation (2015).
- [Buy13] N. Buyukcizmeci *et al.*, *Nucl. Phys. A* 907, 13 (2013).
- [Cab06] O. L. Caballero, C. J. Horowitz, and D. K. Berry, *Phys. Rev. C* 74, 065801 (2006).
- [Cao06a] L. G. Cao, U. Lombardo, and P. Schuck, *Phys. Rev. C* 74, 064301 (2006).
- [Cao06b] L. G. Cao, U. Lombardo, C. W. Shen, and N. V. Giai, *Phys. Rev. C* 73, 014313 (2006).
- [Cen90] M. Centelles, M. Pi, X. Viñas, F. Garcias, and M. Barranco, *Nucl. Phys. A* 510, 397 (1990).
- [Cen98] M. Centelles, M. Del Estal, and X. Viñas, *Nucl. Phys. A* 635, 193 (1998).
- [Cha05] N. Chamel, *Nucl. Phys. A* 747, 109 (2005).
- [Cha07] N. Chamel, S. Naimi, E. Khan, and J. Margueron, *Phys. Rev. C* 75, 055806 (2007).
- [Cha09] N. Chamel, S. Goriely, and J. M. Pearson, *Phys. Rev. C* 80, 065804 (2009).
- [Cha10] N. Chamel, *Phys. Rev. C* 82, 014313 (2010).
- [Cha31] S. Chandrasekhar, *Astrophys. J.* 74, 81 (1931).
- [Cha32] J. Chadwick, *Nature* 129, 312 (1932).
- [Cha97] E. Chabanat, P. Bonche, P. Haensel, J. Meyer, and R. Shaeffer, *Nucl. Phys. A* 627, 710 (1997).
- [Cha98] E. Chabanat, P. Bonche, P. Haensel, J. Meyer, and R. Shaeffer, *Nucl. Phys. A* 635, 231 (1998).
- [Col60] R. A. Coldwell-Horsfall and A. A. Maradudin, *J. Math. Phys.* 1, 395 (1960).
- [Com13] CompOSE, database (2013), URL: <http://compose.obspm.fr/>.
- [Dan03] P. Danielewicz, *Nucl. Phys. A* 727, 233 (2003).

- [Dan09] P. Danielewicz and J. Lee, Nucl. Phys. A 818, 36 (2009).
- [Dat95] B. Datta, A.V. Thampan, and D. Bhattachaya, J. Astrophys. Astron. 16, 375 (1995).
- [De12] J. N. De, S. K. Samaddar, and B.K. Agrawal, Phys. Lett. B 716, 361 (2012).
- [Dou00] F. Douchin, P. Haensel, and J. Meyer, Nucl. Phys. A 665, 419 (2000).
- [Duc10] C. Ducoin, J. Margueron, and C. Providência, Eur. Phys. Lett. 91, 32001 (2010).
- [Duc11] C. Ducoin, J. Margueron, C. Providência, and I. Vidaña, Phys. Rev. C 83, 045810 (2011).
- [Duf95] J. Duflo and A. P. Zuker, Phys. Rev. C 52, R23 (1995).
- [Dut12] M. Dutra, O. Lourenço, J. S. Sá Martins, A. Delfino, J. R. Stone, and P. D. Stevenson, Phys. Rev. C 85, 035201 (2012).
- [Egi05] T. Von Egidy and D. Bucurescu, Phys. Rev. C 72, 044311 (2005).
- [Egi06] T. Von Egidy and D. Bucurescu, Phys. Rev. C 73, 049901(E) (2006).
- [Eid80] M. F. El Eid and W. Hillebrandt, Astron. & Astrophys. Suppl. Ser. 42, 215 (1980).
- [EPJ14] EPJA, 50, *Special Issue on Symmetry energy* (2014).
- [Fan10] A. F. Fantina, “Supernovae theory: study of electro-weak processes during gravitational collapse of massive stars”, phd thesis (2010).
- [Far86] M. Farine and J. M. Pearson, Phys. Lett. B 167, 259 (1986).
- [Fat12] F. J. Fattoyev and J. Piekarewicz, Phys. Rev. C 86, 015802 (2012).
- [Fay00] S. A. Fayans, S. V. Tolokonnikov, E. L. Trykov, and D. Zawischa, Nucl. Phys. A 676, 49 (2000).
- [Fis67] M. E. Fisher, Physics 3, 255 (1967).
- [For10] M. Fortin, F. Grill, J. Margueron, D. Page, and N. Sandulescu, Phys. Rev. C 82, 065804 (2010).
- [Fur13] Shun Furusawa, Kohsuke Sumiyoshi, Shoichi Yamada, and Hideyuki Suzuki, Astrophys. J. 772, 95 (2013).
- [Gan12] S. Gandolfi, J. Carlson, and Sanjay Reddy, Phys. Rev. C 85, 032801 (2012).
- [Gia81] N. van Giai and H. Sagawa, Phys. Lett. B 106, 379 (1981).
- [Gle82] N. Glendenning, Phys. Lett. B 114, 392 (1982).
- [Gne01] O. Y. Gnedin, D. G. Yakovlev, and A. Y. Potekhin, MNRAS 324, 725 (2001).

- [Gol68] T. Gold, *Nature* 218, 731 (1968).
- [Gor10] S. Goriely, N. Chamel, and J. M. Pearson, *Phys. Rev. C* 82, 035804 (2010).
- [Gor13] S. Goriely, N. Chamel, and J. M. Pearson, *Phys. Rev. C* 88, 061302 (2013).
- [Gra79] B. Grammaticos and A. Voros, *Ann. of Phys.* 123, 359 (1979).
- [Gri11] F. Grill, J. Margueron, and S. S. Avancini, *Phys. Rev. C* 84, 065801 (2011).
- [Gri12] F. Grill, C. Providência, and S. S. Avancini, *Phys. Rev. C* 85, 055808 (2012).
- [Gri14] F. Grill, H. Pais, C. Providência, I. Vidaña, and S. S. Avancini, *Phys. Rev. C* 90, 045803 (2014).
- [Gul12] F. Gulminelli and Ad. R. Raduta, *Phys. Rev. C* 85, 025803 (2012).
- [Gul13] F. Gulminelli, Ad. R. Raduta, M. Oertel, and J. Margueron, *Phys. Rev. C* 87, 055809 (2013).
- [Gul15] F. Gulminelli and Ad. R. Raduta, in preparation (2015).
- [Hem10] M. Hempel and J. Schaffner-Bielich, *Nucl. Phys. A* 837, 210 (2010).
- [Hem11] M. Hempel, J. Schaffner-Bielich, S. Typel, and G. Röpke, *Phys. Rev. C* 84, 055804 (2011).
- [Hew68] A. Hewish, S. J. Bell, J. D. H. Pilkington, P. F. Scott, and R. A. Collins, *Nature* 217, 709 (1968).
- [Hey04] K. Heyde, “Basic Ideas and Concepts in Nuclear Physics: An Introductory Approach”, Institute of Physics, 3rd edition (2004).
- [Hor04] C. J. Horowitz, M. A. Pérez-García, J. Carriere, D. K. Berry, and J. Piekarewicz, *Phys. Rev. C* 70, 065806 (2004).
- [Hov49] L. Van Hove, *Physica* 15, 951 (1949).
- [Jan07] H.-Th. Janka, K. Langanke, A. Marek, G. Martinez-Pinedo, and B. Mueller, *Phys. Rep.* 442, 38 (2007).
- [Kir33] J. G. Kirkwood, *Phys. Rev.* 44, 31 (1933).
- [Kre13] S. Kreim, M. Hempel, D. Lunney, and J. Schaffner-Bielich, *Int. J. Mass Spectrom.* 349, 63 (2013).
- [Kri81] H. Krivine and J. Treiner, *J. Math. Phys.* 22, 2484 (1981).
- [Kri83] H. Krivine and J. Treiner, *Phys. Lett. B* 124, 127 (1983).
- [Lam78] D. Q. Lamb, J. M. Lattimer, C. J. Pethick, and D. G. Rayenhall, *Phys. Rev. Lett.* 41, 1623 (1978).
- [Lan04] K. Langanke and G. Martínez-Pinedo, *Nucl. Phys. A* 731, 365 (2004).

- [Lan32] L. D. Landau, *Phys. Z. Sowjetunion* 1, 285 (1932).
- [Lan80] L. D. Landau and E. M. Lifschitz, “Statistical Physics”, Vol. 5, 3rd edition (1980).
- [Lat01] J. M. Lattimer and M. Prakash, *Astrophys. J.* 550, 426 (2001).
- [Lat85] J. M. Lattimer, C. J. Pethick, D. G. Ravenhall, and D. Q. Lamb, *Nucl. Phys. A* 432, 646 (1985).
- [Lat91] J. M. Lattimer and F. D. Swesty, *Nucl. Phys. A* 535, 331 (1991).
- [Lat94] J. M. Lattimer, K. A. Van Riper, and M. Prakash, *Astrophys. J.* 425, 802 (1994).
- [Lee10] S. J. Lee and A. Z. Mekjian, *Phys. Rev. C* 82, 064319 (2010).
- [Lil01] J. Lilley, “Nuclear Physics: Principles and Applications”, Willey (2001).
- [Lim06] M. Limongi and A. Chieffi, *Astrophys. J.* 647, 483 (2006).
- [Liu11] M. Liu, N. Wang, Y. Deng, and X. Wu, *Phys. Rev. C* 84, 014333 (2011).
- [Mar04] J. Margueron, J. Navarro, and P. Blottiau, *Phys. Rev. C* 70, 028801 (2004).
- [Mar05] T. Maruyama, T. Tatsumi, D. N. Voskresensky, T. Tanigawa, and S. Chiba, *Phys. Rev. C* 72, 015802 (2005).
- [Mar06] A. Marek, H. Dimmelmeier, H.-Th. Janka, E. Müller, and R. Buras, *Astron. & Astrophys.* 445, 273 (2006).
- [Maz79] T. J. Mazurek, J. M. Lattimer, and G. E. Brown, *Astrophys. J.* 229, 713 (1979).
- [Men10] J. Mendoza-Temis, J. G. Hirsch, and A. P. Zuker, *Nucl. Phys. A* 843, 14 (2010).
- [Mig59] A. B. Migdal, *Nucl. Phys.* 13, 655 (1959).
- [Mol12] P. Moller, W. D. Myers, H. Sagawa, and S. Yoshida, *Phys. Rev. Lett.* 108, 052501 (2012).
- [Mol95] P. Moller, J. R. Nix, W. D. Myers, and W. J. Swiatecki, *ADNDT* 59, 185 (1995).
- [Mye69] W. D. Myers and W. J. Swiatecki, *Ann. of Phys.* 55, 395 (1969).
- [Mye80] W. D. Myers and W. J. Swiatecki, *Nucl. Phys. A* 336, 267 (1980).
- [Mye85] W. D. Myers, W. J. Swiatecki, and C. S. Wong, *Nucl. Phys. A* 436, 185 (1985).
- [Neg73] J. W. Negele and D. Vautherin, *Nucl. Phys. A* 207, 298 (1973).
- [New09] W. G. Newton and J. R. Stone, *Phys. Rev. C* 79, 055801 (2009).

- [Nik11] N. Nikolov, N. Schunck, W. Nazarewicz, M. Bender, and J. Pei, *Phys.Rev. C* 83, 034305 (2011).
- [NuD14] NuDat, database (2014), URL: <http://www.nndc.bnl.gov/amdc/>.
- [Oer12] M. Oertel, A. F. Fantina, and J. Novak, *Phys. Rev. C* 85, 055806 (2012).
- [Oer13] M. Oertel, private communication (2013).
- [Ons08] M. Onsi, A. K. Dutta, H. Chatri, S. Goriely, N. Chamel, and J. M. Pearson, *Phys. Rev. C* 77, 065805 (2008).
- [Opp39] J. R. Oppenheimer and G. M. Volkoff, *Phys. Rev.* 55, 374 (1939).
- [Pag06a] D. Page, U. Geppert, and F. Weber, *Nucl. Phys. A* 777, 497 (2006).
- [Pag06b] D. Page and S. Reddy, *Ann. Rev. Nucl. Part. Sci.* 56, 327 (2006).
- [Pap13] P. Papakonstantinou, J. Margueron, F. Gulminelli, and Ad. R. Raduta, *Phys. Rev. C* 88, 045805 (2013).
- [Pas13] A. Pastore, J. Margueron, P. Schuck, and X. Viñas, *Phys. Rev. C* 88, 034314 (2013).
- [Pea11] J. M. Pearson, S. Goriely, and N. Chamel, *Phys. Rev. C* 83, 065810 (2011).
- [Pea12] J. M. Pearson, N. Chamel, S. Goriely, and C. Ducoin, *Phys.Rev. C* 85, 065803 (2012).
- [Pet95] C. J. Pethick and D. G. Ravenhall, *Annu. Rev. Nucl. Part. Sci.* 45, 429 (1995).
- [Pi86] M. Pi, X. Viñas, M. Barranco, A. Perez-Canyellas, and A. Polls, *Astron. & Astrophys. Suppl. Ser.* 64, 439 (1986).
- [Pie14] J. Piekarewicz, F. J. Fattoyev, and C. J. Horowitz, *Phys. Rev. C* 90, 015803 (2014).
- [Pom13] K. Pomorski and J. Dudek, *Phys. Rev. C* 67, 044316 (2013).
- [Pot13] A. Y. Potekhin, A. F. Fantina, N. Chamel, J. M. Pearson, and S. Goriely, *Astron. & Astrophys.* 560, A48 (2013).
- [Pra97] M. Prakash, I. Bombaci, M. Prakash, P. J. Ellis, J. M. Lattimer, and R. Knorren, *Phys. Rep.* 280, 1 (1997).
- [Pro15] C. Providencia, M. Fortin, F. Gulminelli, and Ad. R. Raduta, in preparation (2015).
- [Rad10] Ad. R. Raduta and F. Gulminelli, *Phys. Rev. C* 82, 065801 (2010).
- [Rad14] Ad. R. Raduta, F. Gulminelli, and F. Aymard, *EPJA* 50, 24 (2014).
- [Rei06] P.-G. Reinhard, M. Bender, W. Nazarewicz, and T. Vertse, *Phys. Rev. C* 73, 014309 (2006).

- [Rei95] P.-G. Reinhard and H. Flocard, Nucl. Phys. A 584, 467 (1995).
- [Rin80] P. Ring and P. Schuck, “The Nuclear Many-Body Problem”, Springer (1980).
- [Roe09] G. Roepke, Phys. Rev. C 79, 014002 (2009).
- [Roe11] G. Roepke, Nucl. Phys. A 867, 66 (2011).
- [Sag09] I. Sagert *et al.*, Phys. Rev. Lett. 102, 081101 (2009).
- [Sch00] J. Schaffner-Bielich and A. Gal, Phys. Rev. C 62, 034311 (2000).
- [Sch96] C. Schaab, F. Weber, M. K. Weigel, and N. K. Glendenning, Nucl. Phys. A 605, 531 (1996).
- [Séb11] F. Sébille, V. de la Mota, and S. Figerou, Phys. Rev. C 84, 055801 (2011).
- [Sed06] A. Sedrakian and J. W. Clark, Phys. Rev. C 73, 035803 (2006).
- [She11] H. Shen, H. Toki, K. Oyamatsu, and K. Sumiyoshi, Astrophys. J. Suppl. Ser. 197, 20 (2011).
- [She98] H. Shen, H. Toki, K. Oyamatsu, and K. Sumiyoshi, Nucl. Phys. A 637, 435 (1998).
- [Sky56] T. H. R. Skyrme, Phil. Mag. 1, 1043 (1956).
- [Sou09] S. R. Souza, A. W. Steiner, W. G. Lynch, R. Donangelo, and M. A. Famiano, Astrophys. J. 707, 1495 (2009).
- [Ste05] A. W. Steiner, M. Prakash, J. M. Lattimer, and P. J. Ellis, Phys. Rep. 411, 325 (2005).
- [Sum08] K. Sumiyoshi and G. Röpke, Phys. Rev. C 77, 055804 (2008).
- [Sur84] E. Surand and D. Vautherin, Phys. Lett. B 138, 325 (1984).
- [Tol39] R. C. Tolman, Phys. Rev. 55, 364 (1939).
- [Tre86] J. Treiner and H. Krivine, Ann. of Phys. 170, 406 (1986).
- [Tsa12] M. B. Tsang *et al.*, Phys. Rev. C 86, 015803 (2012).
- [Typ10] S. Typel, G. Roepke, T. Klahn, D. Blaschke, and H. H. Wolter, Phys. Rev. C 81, 015803 (2010).
- [Uhl36] G. E. Uhlenbeck and E. Beth, Physica 3, 729 (1936).
- [Val81] L. Valentin, “Subatomic Physics: Nuclei and Particles”, Elsevier (1981).
- [Vau72] D. Vautherin and D. M. Brink, Phys. Rev. C 5, 626 (1972).
- [War09] M. Warda, X. Viñas, X. Roca-Maza, and M. Centelles, Phys. Rev. C 80, 024316 (2009).

- 
- [Was12] K. Washiyama, K. Bennaceur, B. Avez, M. Bender, P.-H. Heenen, and V. Hellemans, *Phys. Rev. C* 86, 054309 (2012).
- [Wig32] E. Wigner, *Phys. Rev.* 40, 749 (1932).
- [Wig34] E. P. Wigner and F. Seitz, *Phys. Rev.* 46, 509 (1934).
- [Wol13] R. N. Wolf *et al.*, *Phys. Rev. Lett.* 118, 041101 (2013).
- [Woo02] S. E. Woosley, A. Heger, and T. A. Weaver, *Rev. Mod. Phys.* 74, 1015 (2002).
- [Yan52] C. N. Yang and T. D. Lee, *Phys. Rev.* 87, 404 (1952).
- [Zam73] L. Zamick, *Phys. Lett. B* 45, 313 (1973).
- [Zha06] F.-Y. Zhao, R. G. Strom, and S.-Y. Jiang, *Chin. J. Astron. Astrophys.* 6, 635 (2006).

